

Dissertation  
submitted to the  
Combined Faculties for the Natural Sciences and for Mathematics  
of the Ruperto-Carola University of Heidelberg, Germany  
for the degree of  
Doctor of Natural Sciences

presented by  
Diplom-Physicist **Martin Lauer**  
born in St.Ingbert

Oral examination: 20th October 2004



# **Digital Signal Processing for segmented HPGe Detectors Preprocessing Algorithms and Pulse Shape Analysis**

Referees: **Prof. Dr. Dirk Schwalm**  
**Prof. Dr. Rainer Männer**



## Abstract

MINIBALL is an versatile spectrometer consisting of 24 longitudinally six-fold segmented HPGe detectors, build for the efficient detection of rare  $\gamma$  decays in nuclear reactions of radioactive ion beams. MINIBALL was the first spectrometer equipped with digital electronics. Pulse shape analysis algorithms to determine the interaction position of  $\gamma$ -rays were implemented on a Digital Signal Processor and validated in an experiment using a collimated  $\gamma$ -ray source. Emphasis was placed on the properties of the different digital signal processing algorithms, the consequences for the implementation and the applicability for position determination.

The next generation of  $\gamma$ -ray spectrometers will consist of highly segmented HPGe detectors equipped with digital electronics, resulting in a more than ten-fold increase in complexity compared to current spectrometers. To enable the construction of a  $\gamma$ -ray tracking spectrometer, new and powerful digital electronics will be developed. Preprocessing algorithms, giving the  $\gamma$ -ray energy and generating event triggers, were implemented on a VME module equipped with fast A/D converters and tested with different detectors and sources. Emphasis was placed on the detailed simulation and understanding of the algorithms as well as the influence of electronics and detector onto the energy resolution.

## Zusammenfassung

MINIBALL ist ein vielseitiges Spektrometer zum effizienten Nachweis von seltenen  $\gamma$  Zerfällen in Kernreaktionen mit radioactiven Ionenstrahlen, bestehend aus 24 HPGe Detektoren, die der Länge nach sechsfach segmentiert sind. MINIBALL war das erste Spektrometer ausgestattet mit digitaler Ausleseelektronik. Pulsformanalyse-Algorithmen zur Bestimmung des Wechselwirkungsorts wurden für einen digitalen Signalprozessor implementiert und in einem Experiment mit gebündelten  $\gamma$ -Strahlen verifiziert. Die Eigenschaften der Algorithmen wurden deshalb besonders untersucht, sowie die sich daraus ergebenden Konsequenzen für die Implementierung und die Anwendbarkeit zur Positionsbestimmung.

Die nächste Generation von Spektrometer zum Nachweis von  $\gamma$  Strahlung besteht aus hochsegmentierten HPGe Detektoren, die mittels digitaler Elektronik ausgelesen werden, was dazu führt, dass die Komplexität im Vergleich zu aktuellen Spektrometern um mehr als einen Faktor 10 ansteigt. Für den Aufbau eines  $\gamma$ -ray tracking Spektrometers wird neue und leistungsfähige Ausleseelektronik entwickelt. Algorithmen zur Vorverarbeitung der Detektorsignale wurden auf einem VME Modul ausgestattet mit schnellen A/D Wandlern implementiert und mit verschiedenen Detektoren und Quellen getestet. Diese Algorithmen werden zur Detektion und zur Bestimmung der Energie von  $\gamma$  Strahlung benutzt. Schwerpunkt war dabei das genaue Verständnis der Algorithmen durch gezielte Simulationen sowie der Einfluss von Elektronik und Detektor auf die erzielte Energieauflösung.



# Contents

<b>1</b>	<b>Introduction</b>	<b>19</b>
<b>2</b>	<b>Pulse Shape Analysis for HPGe detectors</b>	<b>23</b>
2.1	Detection Process . . . . .	23
2.2	First and Main Interaction . . . . .	24
2.3	Signal Formation in HPGe Detectors . . . . .	24
2.4	The MINIBALL detector . . . . .	26
2.4.1	The MINIBALL electronics . . . . .	30
2.5	$\gamma$ -Energy - Moving Window Deconvolution . . . . .	30
2.5.1	Description of the Algorithm . . . . .	32
2.5.2	Baseline Restoration . . . . .	35
2.5.3	Simulation of the MWD algorithm . . . . .	37
2.5.4	Tests with measured waveforms . . . . .	38
2.6	Timing Algorithms . . . . .	41
2.6.1	Test with measured waveforms . . . . .	45
2.7	Position Determination . . . . .	51
2.7.1	Radial Position $r$ of the Main Interaction . . . . .	53
2.7.2	Angular Position $\varphi$ of the Main Interaction . . . . .	54
2.7.3	Depth of the Main Interaction . . . . .	55
<b>3</b>	<b>Realtime PSA using the XIA DGF-4C CAMAC module</b>	<b>59</b>
3.1	The realtime pulse shape analysis program . . . . .	59
3.2	Experimental setup . . . . .	60
3.3	Tests with measured waveforms . . . . .	62
3.3.1	Comparison with offline analysis . . . . .	62
3.3.2	Investigation of the $r$ and $\varphi$ determination . . . . .	66
3.3.3	Calibration . . . . .	74
3.3.4	Position Resolution . . . . .	83
<b>4</b>	<b>GRT4 VME module</b>	<b>87</b>
4.1	Overview of the hardware . . . . .	87
4.1.1	XILINX Spartan 2 . . . . .	88
4.1.2	Existing GRT4 Firmware . . . . .	90
4.2	Implementation of the VME interface . . . . .	91
4.3	Implementation of the MWD algorithm . . . . .	91
4.4	Implementation of the Baseline Restorer . . . . .	102
4.5	Implementation of the Trigger Algorithm . . . . .	102
4.6	Simulation of VHDL code . . . . .	104

4.7	Measurements . . . . .	106
4.7.1	Measurement of the DNL . . . . .	106
4.7.2	Measurement with a NaI detector . . . . .	111
4.7.3	Measurements with an ORTEC HPGe detector . . . . .	113
4.7.4	Measurements with a MINIBALL HPGe detector . . . . .	116
<b>5</b>	<b>Conclusions and Outlook</b>	<b>125</b>
5.1	Realtime Pulse Shape Analysis . . . . .	125
5.2	Preprocessing Algorithms: MWD and GRT4 . . . . .	126
<b>A</b>	<b>Introduction to Digital Signal Processing</b>	<b>129</b>
A.1	Discrete Linear Time-Invariant Systems . . . . .	129
A.2	Analog-Digital (A/D) Conversion (ADC) . . . . .	130
A.2.1	Quantization . . . . .	130
A.2.2	Discretization: Periodic Sampling . . . . .	131
A.2.3	The Flash ADC Architecture . . . . .	133
A.3	Digital Filter . . . . .	134
A.3.1	Transfer Function . . . . .	134
A.3.2	IIR filter . . . . .	134
A.3.3	FIR filter . . . . .	138
A.4	Numerical Differentiation . . . . .	144
A.4.1	Differentiability of bandwidth limited Signals . . . . .	144
A.4.2	Differentiation Equations . . . . .	144
A.5	Digital Resampling: Decimation and Interpolation . . . . .	148
A.5.1	Decimation . . . . .	149
A.5.2	Upsampling . . . . .	149
A.6	Useful IIR Filters . . . . .	151
<b>B</b>	<b>Details of the MWD implementation</b>	<b>155</b>
B.1	FPGA Design Flow . . . . .	155
B.1.1	Development Environment . . . . .	156
B.1.2	VHDL . . . . .	156
B.1.3	Synthesis . . . . .	157
B.1.4	Translate . . . . .	157
B.1.5	Mapping . . . . .	157
B.1.6	Place and Route (PAR) . . . . .	158
B.1.7	Timing Constraints . . . . .	158
B.1.8	Configuration . . . . .	159
B.2	ADC DNL correction . . . . .	160
B.2.1	Analog Signal Conditioning . . . . .	160
B.2.2	Analog to Digital Converter . . . . .	161
B.2.3	DNL correction coefficients . . . . .	162
B.3	Addressing of the MWD code . . . . .	162
B.4	MWD and double-exponential decaying signals . . . . .	163
B.5	Measurements with a Pulser . . . . .	167
B.5.1	Changing the ADC clock . . . . .	169
B.6	MWD implementation for the DDC-8 module . . . . .	169

<b>C</b>	<b>The MINIBALL User Code</b>	<b>173</b>
C.1	Description of the User Code . . . . .	173
C.1.1	Description of the User code subroutines . . . . .	174
C.2	Input Format . . . . .	185
C.3	Output Format . . . . .	185
C.4	Configuration Software for the User DSP Code . . . . .	185
C.5	Fixed Point Data Formats . . . . .	188
C.6	Event Trigger . . . . .	189
<b>D</b>	<b>Contents of the CD-ROM</b>	<b>193</b>



# List of Tables

2.1	Comparison of DGF-4C with offline MWD energy resolution . . . . .	41
2.2	Time resolution of the Q-EBC algorithm using the $^{152}\text{Eu}$ data set for different time differences of the DGF-4C time stamps . . . . .	51
3.1	Estimate of the average interaction depth from the steepest slope time . .	77
3.2	Influence of the AID $z(E)$ on the true radial interaction position $r(z(E))$ compared to the radial position at the detector front face $r(z(0))$ using equation 3.3 . . . . .	77
3.3	Influence of the interaction depth $z(E)$ on the true angular interaction position $\varphi(z(E))$ compared to the angular interaction position $\varphi(z(0))$ determined by the collimator using equation 3.4. . . . .	78
3.4	Calibration of the angular position information for segment 1 of detector C	79
3.5	Position resolution of the user DSP code . . . . .	85
3.6	Position resolution of the offline analysis for all data points that have been scanned and for the individual radial positions . . . . .	86
3.7	Position resolution of the offline analysis if a scaled MI segment signal is subtracted instead of a linear signal . . . . .	86
4.1	Settings of the MWD CSR register controlling the behavior of the S2U unit.	95
4.2	Possible shaping times with the various clock reduction factors and MA implementation using a single block RAM (256 memory locations). . . . .	95
4.3	Energy resolution before and after ADC DNL correction using an $^{152}\text{Eu}$ source . . . . .	111
4.4	Energy resolution achieved with the ORTEC detector and the GRT4 VME module . . . . .	114
4.5	Relaxation time of the exponential averaging filter for different $\alpha$ . . . . .	121
4.6	Energy resolution achieved with the baseline restorer based on moving average . . . . .	122
B.1	Bitgen options for the generation of bitstream for the ADC FPGA . . . . .	160
B.2	Entries of the ROM that were used for the ADC DNL correction. . . . .	163
B.3	Usage of VME Address Lines . . . . .	164
B.4	Mapping of MWD Register into VME Address Range . . . . .	165
B.5	Description of the MWD CSR register . . . . .	166
B.6	Usage of Common Spare I/O Signals . . . . .	166
B.7	Usage of ADC-DPP Spare Signals as seen from ADC FPGA. . . . .	167

C.1	Usage of the USERIN data array. The data is ordered with respect to the address offset relative to the address of USERIN. . . . .	186
C.2	Size and position in the USERIN array of the user code parameters. . . .	186
C.3	Usage of the PSA Control and Status Register (CSR). . . . .	187
C.4	Usage of the Channel Header information for the User code compared with that of the original XIA DSP code. . . . .	187
C.5	Interpretation of the PSA error codes. . . . .	187
C.6	Dynamic range (DR) and the size of the LSB for three fixed point data formats . . . . .	189
C.7	Time resolution obtained with the CFD trigger implemented in the DGF-4C FiPPI . . . . .	190

# List of Figures

1.1	Picture of the REX-ISOLDE linear accelerator located in the ISOLDE hall at CERN . . . . .	20
2.1	Weighting potentials of the MINIBALL detector . . . . .	25
2.2	Simulated current pulses for a true coaxial HPGe detector of infinite length with an inner radius of 0.5 cm and an outer radius of 3.5 cm operated at 4000 V . . . . .	27
2.3	ADC waveforms of the simulated charge signals and the corresponding derivatives . . . . .	28
2.4	Physical dimensions of the MINIBALL detector. . . . .	29
2.5	Photograph of the MINIBALL detector. . . . .	29
2.6	Picture of the DGF-4C CAMAC module . . . . .	31
2.7	Deconvolution of the preamplifier signal. . . . .	34
2.8	Steps of MWD algorithm leading to the final trapezoidal shape . . . . .	35
2.9	Drift of the pedestal level after power-up of a MINIBALL HPGe detector .	37
2.10	Elimination of ballistic deficit due to the flat top period $M - L$ of the trapezoidal shaper . . . . .	39
2.11	Downsampled waveform and energy spectrum of a $^{60}\text{Co}$ source using the MWD algorithm. . . . .	40
2.12	Sample Signals from the data set with corresponding energy filter response.	42
2.13	Energy spectra of the MWD algorithm. . . . .	43
2.14	Out of range signal. . . . .	44
2.15	Influence of the threshold $T$ and the fraction $f$ on the time resolution of the L-EBC algorithm. . . . .	47
2.16	Influence of the coefficient on the time difference peak shape for the (M)L-EBC method . . . . .	48
2.17	Time resolution of the Steepest Rise timing algorithm using the $^{60}\text{Co}$ data set for different differentiation formulas . . . . .	49
2.18	Time resolution of the Q-EBC algorithm . . . . .	49
2.19	Time resolution of the Q-EBC timing algorithm . . . . .	50
2.20	Influence of the time stamp time difference onto the time difference spectra.	52
2.21	Explanation of the origin of the polarity of the mirror charge signal . . . .	54
2.22	Extraction of the mirror charge amplitude from segment signals. . . . .	57
2.23	Neighboring Segment Event (NSE) . . . . .	58
2.24	Perpendicular and non-perpendicular irradiation geometries for the MINIBALL detector . . . . .	58
3.1	Setup for the collimator measurement . . . . .	61

3.2	Geometry of the collimator measurement setup . . . . .	61
3.3	Steepest slope spectra for three different angular position of the collimator . . . . .	63
3.4	Comparison of the realtime with the offline analysis for the $\log\left(\frac{ q_+ }{ q_- }\right)$ algorithm . . . . .	64
3.5	Confirmation of the validity of the user DSP code approximation for segments that have no access to the timing information of the core channel . . . . .	67
3.6	Risetime $t_{90} - t_0$ of the MINIBALL detector . . . . .	68
3.7	Amplitude of the induced charge for both neighboring segments of the hit segment . . . . .	69
3.8	Influence of the ADC offset on the dynamic range of the induced charge . . . . .	70
3.9	Evolution of the induced charge amplitudes for different radial and angular positions of the collimator . . . . .	71
3.10	Separation of the steepest slope and $\log\left(\frac{ q_+ }{ q_- }\right)$ spectra using the polarity of the mirror charge amplitude . . . . .	73
3.11	Explanation how the irradiation causes ambiguities in the steepest slope spectrum. . . . .	74
3.12	Spectra of the $\log\left(\frac{ q_+ }{ q_- }\right)$ algorithm obtained for three different methods to extract the induced charge from segment signals featuring also a net charge signal. . . . .	75
3.13	Sensitivity of segment 1 of detector C . . . . .	76
3.14	Linear calibration of the steepest slope algorithm for segment 1 of detector C . . . . .	78
3.15	Angular calibration of the $\log\left(\frac{ q_+ }{ q_- }\right)$ algorithm for different radii . . . . .	80
3.16	Reconstructed interaction positions at the detector front face $z(0)$ using the user DSP code . . . . .	81
3.17	Reconstructed interaction positions at $z(0)$ and position resolution in x and y direction for the $\log\left(\frac{ q_{++} }{ q_{--} }\right)$ algorithm . . . . .	82
3.18	Position resolution of segment 1 of detector C obtained with the realtime and the offline analysis . . . . .	84
4.1	Picture of the GRT4 VME module. . . . .	88
4.2	Strongly simplified layout of a Spartan 2 chip. . . . .	89
4.3	Schematic view of the VME interface. . . . .	92
4.4	Overview of the MWD implementation. . . . .	93
4.5	Schematic of the moving average unit (MAU). . . . .	94
4.6	Waveforms that have been acquired with different settings for the S2U unit . . . . .	96
4.7	Schematic of the decimation unit . . . . .	97
4.8	Waveforms that have been acquired with different settings of the decimation unit. . . . .	98
4.9	The structure of the MWD unit . . . . .	98
4.10	Waveforms that have been acquired after deconvolution. . . . .	100
4.11	Layout of the EA and MA baseline restorer . . . . .	103
4.12	Layout of the FIR leading edge trigger module . . . . .	103
4.13	Response of the FIR trigger module to a step input. . . . .	105
4.14	Waveform window of the ModelSim XE Starter software. . . . .	107
4.15	Measured DNL of the AD6645. . . . .	108
4.16	Simulation of the ADC. . . . .	108

4.17	Correlation of the energy peak shift with the ADC offset . . . . .	110
4.18	Effect of the decay time. . . . .	111
4.19	Effect of the DNL correction. . . . .	112
4.20	$^{60}\text{Co}$ spectrum acquired with a GRT4 and a NaI detector . . . . .	113
4.21	Spectra acquired with the GRT4 and the ORTEC detector using two different sources, a $^{60}\text{Co}$ and a $^{152}\text{Eu}$ source . . . . .	114
4.22	Dependence of the energy resolution measured with $^{60}\text{Co}$ and the filter parameter peaking and gap time . . . . .	115
4.23	Signal shape of an analog spectroscopy amplifier ORTEC 671 for shaping times of 3 and 6 $\mu\text{s}$ . . . . .	115
4.24	Energy dependence and linearity of the energy resolution measured with an $^{152}\text{Eu}$ source . . . . .	116
4.25	Adjusting the trigger threshold for the measurements with an $^{152}\text{Eu}$ source	117
4.26	Dependence of the energy resolution on the MWD filter parameters for two $^{152}\text{Eu}$ lines of 121 and 1408 keV . . . . .	119
4.27	Dependence of the energy resolution on the MWD filter parameters measured with a $^{60}\text{Co}$ source . . . . .	120
4.28	The influence of the pileup rejection period parameter on the energy spectra	124
A.1	The pipelined flash ADC . . . . .	135
A.2	Magnitude and phase response of the exponential averaging . . . . .	137
A.3	Impulse and step response of the exponential averaging. . . . .	137
A.4	Transfer functions of the ideal low-pass filter. . . . .	139
A.5	Transfer function of the moving average filter. . . . .	140
A.6	Impulse and step response of the moving averaging filter . . . . .	140
A.7	Magnitude and phase response of the numerical differentiation. . . . .	145
A.8	Transfer function of the numerical second derivative . . . . .	146
A.9	Transfer function of the differentiation filter. . . . .	147
A.10	Transfer function of numerical differentiation formulas. . . . .	148
A.11	Magnitude and phase response of the linear interpolation . . . . .	152
B.1	The Sallen-Key circuit. . . . .	161
B.2	Spice simulation of the analog low-pass filter of the GRT4. . . . .	162
B.3	The MWD algorithm applied to double-exponential decaying signal . . . .	168
B.4	Linearity of the energy spectrum determined with a pulser . . . . .	170
B.5	Changing the ADC clock frequency . . . . .	171
B.6	MWD implementation for the DDC-8 module . . . . .	172
C.1	The data flow of the channel processing. . . . .	175
C.2	The data flow of the run initialization routine. . . . .	177
C.3	The DSP code to determine the baseline of the signal . . . . .	178
C.4	The DSP code to determine the start of the signal . . . . .	179
C.5	The user DSP code that extracts the $t_{90}$ time . . . . .	180
C.6	The user DSP code that extracts the steepest slope time $t_{ss}$ . . . . .	182
C.7	The algorithm for extraction of the mirror charge amplitudes $q^{max}$ from the segments with no charge deposition . . . . .	183
C.8	The algorithm for extraction of the mirror charge amplitudes $q^{max}$ from the segments with charge deposition . . . . .	184
C.9	The constant fraction discriminator . . . . .	191



# List of Symbols and Abbreviations

$\alpha$  Weighting factor for the EA or Angle between collimator and interaction position

**ACC** Accumulator

**ADC** Analog to Digital Converter

**A/D Converter** Analog to Digital Converter

**AID** Average Interaction Depth

**ARC** Amplitude and Risetime Compensation

**a.u.** Arbitrary units or ADC units

**BLR** Baseline Restorer

**BW** Bandwidth

**CAMAC** CAMAC data acquisition standard (IEEE STD 583)

**CsI** Scintillating Crystal of CsI

**CD** Continuous Discharge

**CFD** Constant Fraction Discriminator

**CLB** Configurable Logic Block

**CS** Common Spare bus of the GRT4 module

**CSR** Control and Status Register

$D_M[n]$  Value of the numerical differentiation of length M at sample index n

**DAC** Digital to Analog Converter

**D/A Conversion** Digital to Analog Conversion

**DLL** Delay Locked Loop

**DNL** Differential Non-Linearity

**DPP** Digital Pulse Processing

**DRC** Design Rule Check

**DS** Delay-Subtract Unit

**DSP** Digital Signal Processor

**DUT** Design Under Test

**EA** Exponential Averaging

**EBC** Extrapolated Baseline Crossing

**EDIF** Electronic Data Interchange Format

$E_\gamma$  Energy of a  $\gamma$ -ray

$E_w$  Weighting Field

**FEE** Full Energy Events

**FET** Field Effect Transistor

**FI** First Interaction

**FIFO** First In First Out

**FIR** Finite Impulse Response

**FPGA** Field Programmable Gate Array

**FSR** Full Scale Range

**FWHM** Full Width at Half Maximum

**GUI** Graphical User Interface

**HDL** Hardware Description Language

**h(E)** Distance between source and interaction in z-direction

**HPGe** High Purity Germanium

**H( $\omega$ )** Transfer Function

**IEEE** Institute of Electrical and Electronics Engineers, Inc. (Eye-triple-E)

**IIR** Infinite Impulse Response

**INL** Integral Non-Linearity

**I/O** Input/Output

**IOB** Input Output Block

**L** Length of the MA of the MWD algorithm

**LC** Logic Cell

**LE** Leading Edge

**LSB** Least Significant Bit

**LTI** Linear Time-Invariant System

**LUT** Look-Up Table

**M** Differentiation time of the MWD algorithm

**MA** Moving Average

**MA<sub>M</sub>[n]** Value of a moving average operation of length M at sample index n

**MAP** Program that Maps the design onto the FPGA resources

**MI** Main Interaction

**MSB** Most Significant Bit

**MWD** Moving Window Deconvolution

**NaI** Scintillating Crystal of NaI

**NIM** Nuclear Instrumentation Methods

**NNNS** Next to Nearest Neighbor Segment

**NSE** Neighboring Segment Event

**NSR** Normalized Step Response

**OSE** One Segment Event

**PAR** Program that performs the Place and Route process

**PCF** Physical Constraints File

**PROM** Programmable Read Only Memory

**PSA** Pulse Shape Analysis

$\Phi_w$  Weighting Potential

**$q_+$ ,  $q_-$**  Maximal mirror charge amplitudes in the neighboring segments with higher (+) and lower (-) index

**RAM** Random Access Memory

**RC preamp** Continuous discharge preamplifier

**RTL** Register Transfer Level

**RTPU** Real Time Processing Unit

**SNR** Signal to Noise Ratio

**SS** Steepest Slope

**$S[n]$ ,  $s[n]$**  Slope of the detector current  $i[n]$ , i.e. second derivative of the charge signal  $c[n]$ , at sample index  $n$

**SRAM** Static Random Access Memory

$\tau$  Decay time of a CD preamplifier  $\tau = \frac{1}{RC}$

$t_{cc}$  Charge collection time determine from the difference of the steepest slope and the start of the detector pulse

$t_\gamma$  Event Time

$t_0$ , Event Time determined by PSA

$t_{50}$  Time when the signal reaches 50% of its full height

$t_{90}$  Time when the signal reaches 90% of its full height

**$T_M^L[n]$**  Value of trapezoidal filter at sample index  $n$  using a MA of length  $L$  and a differentiation time of length  $M$

$t_{ss}$  Time of the steepest slope of the current signal

**TFA** Timing Filter Amplifier

**TR** Transistor Reset Preamplifier

**TS** Time Stamp

**UCF** User Constraints File

**VHDL** VHSIC Hardware Description Language

**VME Bus** Versa Module Europa Bus

$\omega_c$  Cut-off frequency of a filter,  $\omega_c = 2\pi f_c$

$\omega_s$  Sampling frequency of a A/D converter,  $\omega_s = 2\pi f_s$

**XST** XILINX Synthesis Technology

**z(0)** AID in the detector for a  $\gamma$  energy  $E = 0$ , i.e.  $z(0)=0$

**z(E)** AID in the detector for for the  $\gamma$  energy  $E$



# Chapter 1

## Introduction

”As the island of our knowledge grows, so does the shore of our ignorance.” -  
John Wheeler

Nuclei far from stability are of key interest at the present time. They provide tests for existing nuclear-structure models and new physics such as halo nuclei and new shell closures. Stable nuclei have been studied in detail for years but an extrapolation of their properties to exotic nuclei, characterized by a large asymmetry in proton  $Z$  and neutron  $N$  number (either neutron rich or neutron deficient) compared to the stable isotope, is impossible. In order to further understand the nucleus, a many body quantum system, and to allow the development of theoretical models, it is mandatory to determine the properties of the exotic nuclei. Despite their fleeting existence, exotic nuclei play a crucial role in understanding the origin of the elements.

New experimental techniques and facilities are required for the study of exotic nuclei. Ideally, such a facility would allow to select nuclei with no restrictions in  $Z$  or  $N$ , enabling the experimentalist to choose the nucleus which amplifies the effect to be studied<sup>1</sup>.

Primarily two different methods for the study of exotic nuclei exist: the ISOL<sup>2</sup> method and fragment separator method, i.e. projectile fragmentation with in-flight separation. The ISOL method is used at the ISOLDE facility at CERN [2], which is in operation since 1992, while the in flight fragmentation method is available at the GSI accelerator facility with the FRS device.

As exotic nuclei can only be studied with **Radioactive Ion Beams (RIB)**, since they are subjected to  $\beta$  decay which makes it impossible to produce targets made of exotic nuclei, the beam has become the target. Due to the high velocity of the reaction products, the emitted  $\gamma$ -rays are subjected to Doppler shifts. In order to correct the Doppler broadening to a tolerable level, a highly granular detector is needed.

As the beam intensities are extremely low, e.g.  $10^4$  particles/s for a  $^{30}\text{Mg}$  beam, high reaction rates and efficient detection have to be assured. In order to efficiently detect  $\gamma$ -rays emitted from a target foil, a large fraction of the solid angle has to be covered by the detectors. In order to achieve high reaction rates thick targets should be used without degrading the energy resolution.  $\gamma$ -ray spectroscopy with a highly granular detector satisfies all criteria and is therefore the method of choice to study exotic nuclei.

---

<sup>1</sup>The importance of the exotic nuclei can also be recognized from the FAIR project of GSI [1], which is a 600 Million Euro project largely devoted to the study of exotic nuclei.

<sup>2</sup>Isotope Separation **On-Line**

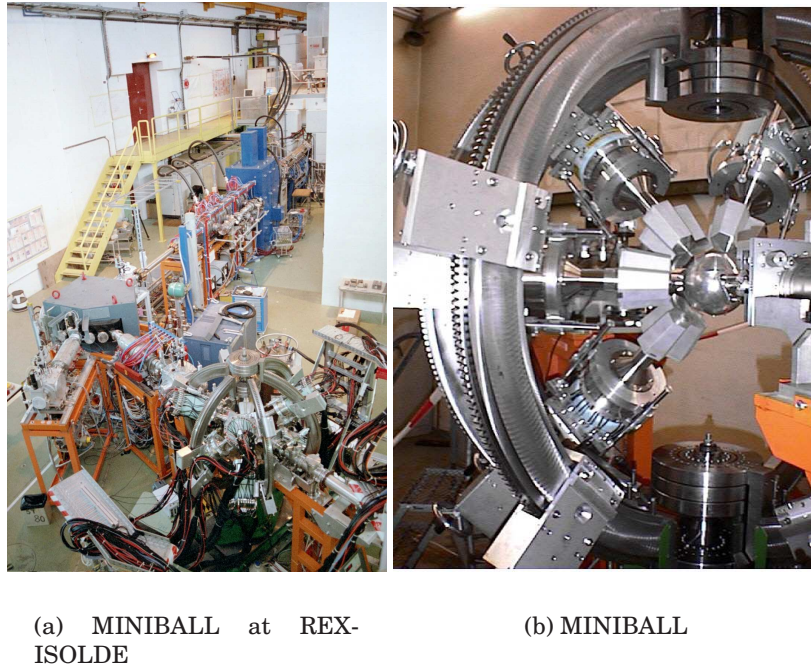


**Figure 1.1:** Panel (a) shows a picture of the REX<sup>3</sup> linear accelerator located in the ISOLDE hall at CERN and the MINIBALL array. The accelerator is followed by a bending magnet, distributing then beam to the experiments. The MINIBALL detector array can be seen at the bottom of the picture in panel (a) and is shown in more detail in panel (b).

In order to increase the detection efficiency the encapsulated detector [3, 4, 5, 6] was invented for the EUROBALL III array [7], combining seven encapsulated HPGe detectors into one *cluster* detector<sup>4</sup> surrounded by a common escape-suppression or anti-compton shield. The encapsulation eases the construction of a multi element detector by protecting the very sensitive intrinsic surface of the HPGe crystal, improving the reliability and allowing an easy annealing after neutron damage. The encapsulated germanium detectors are operated in anti-coincidence with the escape shield, detecting  $\gamma$ -rays which do not deposit their full energy in the detector, in order to improve the peak to background ratio. Furthermore, such a cluster detector can be operated in *add-back* mode, where all the energies of the individual detectors are added and the cluster detector responds as one large germanium detector, with the granularity of the individual detector element.

The first spectrometer equipped with *segmented* germanium detectors was the GAMMASPHERE array [8]. 80 of the 110 crystals feature a two-fold longitudinal segmentation to reduce the Doppler broadening<sup>5</sup> due to the increase in granularity by a factor of two. The GAMMASPHERE array covers the full solid angle (a  $4\pi$  detector) and is in operation since 1995. However, since each of the detectors is surrounded by an anti-compton

<sup>4</sup>In order to minimize the space between the detectors, hexagonal tapered instead of a true coaxial detectors are used.

<sup>5</sup>The segmentation was also used to determine the linear polarization of the  $\gamma$ -rays emitted from spin aligned nuclear states [9].

shield made of BGO<sup>6</sup>, which detects  $\gamma$ -rays that scatter out of (or into) the germanium detector volume, a large fraction of the solid angle cannot be used for  $\gamma$ -ray spectroscopy.

MINIBALL [10] is a highly efficient HPGe detector array optimized for  $\gamma$  spectroscopic studies with radioactive beams mainly by means of Coulomb excitation and (inverse) transfer reactions at REX-ISOLDE [11] and rare  $\gamma$  decay measurements. Since 2002 experiments<sup>7</sup> have been performed with the MINIBALL detector array at the ISOLDE facility at CERN using radioactive beams accelerated with the REX-ISOLDE linear accelerator and also at the tandem accelerator facility at the University of Cologne with stable beams.

The MINIBALL detectors are used to detect  $\gamma$ -rays emitted from nuclei with large recoil velocities. The MINIBALL HPGe detector array currently consists of 8 cluster cryostats containing three individually encapsulated HPGe crystals of the EUROBALL type that feature a sixfold longitudinal electrical segmentation of the outer contact. The crystal is 78 mm long and its diameter varies between 59 mm and 70 mm. In order to achieve a reasonable photopeak efficiency and to cover a large fraction of the solid angle with a small amount of detectors, the detectors can be placed only 10 cm away from the target. Because of the finite opening angle of the detector and the velocity of the radioactive beams of approx. 6 % of the speed of light, it is necessary to extract information not only about the energy, but also about the direction of the emitted  $\gamma$ -ray to achieve a good Doppler correction. In order to improve the granularity beyond that achieved by segmenting the outer contact of the detector module longitudinally, **Pulse Shape Analysis**<sup>8</sup> (PSA) is employed to accomplish the electronic segmentation that is part of the MINIBALL concept. While the segmentation of the outer contact increases the granularity by a factor of six, the electronic segmentation by PSA will further increase the granularity up to about a factor of 100.

All channels are equipped with cold FET<sup>9</sup>, the central contact, where the positive HV is applied, uses an AC-Coupled, charge-sensitive preamplifier, while for the segments DC-Coupled preamplifiers are employed. The preamplifier signal is fed onto the digitizing electronics DGF-4C from X-ray Instrumentation Associates [13]. The digitization of the preamplifier signal is necessary to allow for a further pulse shape analysis (PSA), which is necessary to determine the emission angle  $\Theta$  of a  $\gamma$ -ray.

The ultimate germanium detector [14] would allow in a first step to determine the energy and position of all interactions and then in a second step to correlate interactions belonging to the same initial  $\gamma$ -ray entering the detector. Two  $\gamma$ -ray tracking arrays are currently under development, the GRETA [15] and the AGATA<sup>10</sup> [16] array. Both detectors demand new digital electronics with fast A/D converters and unprecedented processing power. The GRT4 module, presented in chapter 4, is an example of such a module.

The possibility to identify the positions of all interactions enables the extraction of further physical parameters. For a successful correction of the Doppler shift the determination of the position of the first interaction is needed. With the knowledge of the

---

<sup>6</sup>Bismut-Germanat

<sup>7</sup>The REX-MINIBALL collaboration consists of the following Institutes: Instituut voor Kern- en Stralingsfysica, University of Leuven; Ludwig-Maximilians-Universität München; Technische Universität München; Max-Planck-Institut für Kernphysik, Heidelberg; CERN, Geneva; University of Edinburgh; Institut für Kernphysik, Universität Köln; Universität Mainz; Oliver Lodge Laboratory, University of Liverpool; Heavy Ion Laboratory, Warsaw University; Technische Universität Darmstadt

<sup>8</sup>The SeGa [12] array uses a higher segmentation but no PSA to achieve a higher granularity.

<sup>9</sup>Interfet IF1304

<sup>10</sup>Advanced **GA**mma-**T**racking **A**rray

position of the second interaction also a polarization information can be extracted. In addition, the emission angle  $\Theta$  of a  $\gamma$ -ray can be determined from the knowledge of the  $\gamma$ -ray energy and the interaction positions, allowing to locate the  $\gamma$  source, e.g. identify  $\gamma$ -rays emitted from the target [17]. The determination of the interaction positions requires the decomposition of the signals of the individual segments into the components originating from the individual interactions. This process requires a set of basis signals, a grid of single interaction events distributed over the full detector volume. Instead of storing the full basis signals the storage of only a few important parameters describing the pulse shape reduces the memory requirements. The coefficients of a wavelet transform are one example of such a data set [18]. The interaction positions are determined by minimizing the difference between the measured signal and a superposition of basis signals by varying the number, energy and position of interactions. A position resolution of 2.5 mm RMS was achieved in an in-beam experiment [19] and this resolution is considered sufficient for  $\gamma$ -ray tracking [20], since usually the tracking process starts by combining events in close proximity into clusters.

The tracking process identifies interactions belonging to the same  $\gamma$ -ray and allows therewith to distinguish interactions coming from multiple coincident  $\gamma$ -rays entering the detector. The tracking is not limited to a single detector element and should therefore reduce the background caused by  $\gamma$ -rays scattered into neighboring detector elements or into the surrounding environment.

This thesis deals with the development, implementation and test of signal processing algorithms for segmented HPGe detectors equipped with digital electronics. The aim of the pulse shape analysis algorithms is to achieve an increase in granularity of a detector element, allowing for a better Doppler correction. Therefore, knowledge of the energy deposition in the detector and the interaction positions is required.

In chapter 2 the pulse shape analysis algorithms for MINIBALL detectors will be presented. First the interaction process of a  $\gamma$ -ray with the detector material will be shortly presented before the basic concept of PSA for the MINIBALL detector, the main interaction concept, will be introduced. Afterwards, the shape of the detector pulse will be motivated with the help of the weighting field concept. The remaining part of this chapter is dedicated to the PSA algorithms that will be used in the following chapter.

Chapter 3 presents measurements with a collimated source, demonstrating the position sensitivity that can be achieved with the developed DSP code. The realtime analysis will be compared to the offline analysis and the pulse shape will be studied depending on the irradiation position given by the collimator.

Chapter 4 presents the implementation and test of preprocessing algorithms to detect  $\gamma$ -ray interactions and determine their corresponding energies. First the electronics will be introduced followed by a presentation of the implementation and simulation. The measurements with different detectors and sources complete this chapter.

Finally, chapter 5 summarizes the results and gives an outlook on future developments.

## Chapter 2

# Pulse Shape Analysis for HPGe detectors

”If A equals success, then the formula is:  $A = X + Y + Z$ . X is work. Y is play. Z is keep your mouth shut.” - Albert Einstein

The **Pulse Shape Analysis (PSA)** algorithms for the MINIBALL detector were developed and presented in [21, 22, 23, 24, 25] and only the basic concepts will therefore be discussed in this chapter.

Additional information concerning the detector material can be found in [26] and the advances in building large and segmented HPGe detector are compiled in [3, 27]. The properties of the EUROBALL III array were discussed in [28].

### 2.1 Detection Process

The detection of a  $\gamma$ -ray in a semiconductor detector is a two-step process. When a photon interacts with the detector material a fast electron and a Compton scattered  $\gamma$ -ray, or a fast electron-positron pair, are created. These fast charged particles deposit their energy by producing a large number of electron-hole pairs. The electron-hole pairs can be electronically detected, if recombination is prevented by an applied electrical field, by measuring the detector current.

The current pulse is usually a superposition of several pulses due to multiple Compton scattering before the full energy is deposited. Therefore, and due to the finite size of the detector, it is possible and likely that only a fraction of the initial energy of a  $\gamma$ -ray is deposited inside the detector volume.

The most important information, the energy of the incident  $\gamma$ -ray, is contained in the **Full-Energy Events (FEE)** as only for these events the total energy of the initial  $\gamma$ -ray is deposited in the detector. For all other events this important piece of information is not included in the detector pulse, so that they contribute mostly to the background. Therefore, in the following only FEE will be considered. The FEE condition is of great importance, as for instance a  $\gamma$ -ray with 4 MeV energy is most likely to have a Compton as its first interaction whereas the FEEs have a pair production as their first interaction [22].

## 2.2 First and Main Interaction

In order to determine the flight direction of a detected photon the position of the first interaction has to be determined. As  $\gamma$ -rays travel with the speed of light the time between the different interactions in the detector is negligible and cannot be resolved electronically. Hence there is no means to distinguish between the **First Interaction (FI)** from other interactions electronically. The interaction one can expect to locate inside the detector is the interaction where the largest fraction of the initial energy of the photon is deposited, the **Main Interaction (MI)**, as the charge pulse of this interaction will dominate the total detector pulse.

Fortunately, there is a strong correlation between the MI and the FI and one can use the location of the MI as an approximation for the FI since the distance between FI and MI is less than 5 mm for more than 50 % of all interactions [21]. As the detectors of the MINIBALL triple cluster are not individually adjusted onto the target<sup>1</sup> it was shown that it is useful to include also the **Average Interaction Depth (AID)** [22] into the analysis in order to reconstruct the  $\gamma$  emission angle.

## 2.3 Signal Formation in HPGe Detectors

The shape of the detector suggests a determination of the interaction position in cylindrical coordinates. A radial coordinate  $r$  can be extracted from the core pulse and an azimuthal coordinate  $\varphi$  from the segment signals, as defined in figure 2.4 and figure 3.2. The depth  $z$  of an interaction cannot be determined by PSA in case of a MINIBALL detector, which features only a longitudinal segmentation. In order to understand the shape of the detector signals and how this shape evolves with the interaction position it is useful to study the creation of the detector pulses.

The induced current signals on the detector electrodes are calculated using the *weighting field*, depending only on the geometry of the electrode setup and describing the electrostatic coupling between the moving charge and the electrode [29, 30].

The weighing potential  $\Phi_w$  is calculated by setting all electrodes to 0 V except the electrode of interest which is assigned 1 V and neglecting any space charge. The induced charge  $q_{\text{ind}}$  on the electrode of interest is then given by

$$q_{\text{ind}} = -q \cdot \Phi_w \quad (2.1)$$

and the corresponding current signal is obtained from

$$i_{\text{ind}} = -q \vec{E}_w \cdot \vec{v} \quad (2.2)$$

with  $\vec{E}_w = -\vec{\nabla} \Phi_w$  the weighting field and  $\vec{v}$  the actual drift velocity, which depends on the strength of the electrical field at the current position.

In figure 2.1 the weighting potential of the core contact and a segment contact are shown. In addition, three trajectories, labeled 1, 2 and 3, are shown for the segment contact starting at the segment contact and traversing to the inner electrode. The electrode of interest, the sensing electrode, is assigned a potential of 1 V, all other electrodes are set to 0 V. In case of trajectory 2, i.e. the charge is collected in the neighboring segment,

<sup>1</sup>This configuration is called *aligned 3-cluster* and features a higher addback efficiency than the *on-target 3-cluster* [22].

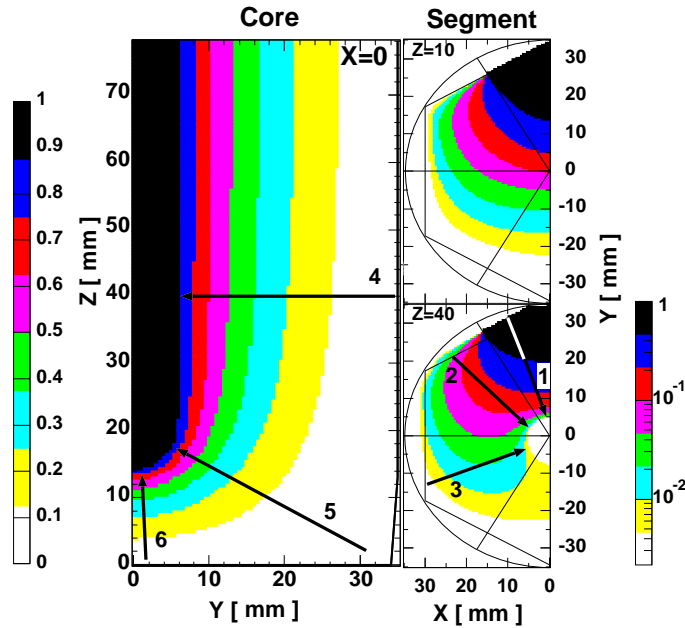


**Figure 2.1:** Weighting potentials of the MINIBALL detector (taken from [22]). The weighting potentials of the core and a segment contact are shown on the left and right side, respectively. Note that the weighting potentials for the segment contact are shown for two different cuts in depth,  $z = 10$  mm (planar part) and  $z = 40$  mm (coaxial part).

only a temporary mirror charge signal is observed, because the slope of the weighting field, and consequently the induced current, changes its sign in the middle between the inner and outer electrode. The same is true for trajectory 3, where the event is located in the segment *next* to the neighboring segment of the sensing electrode. The shape of the mirror charge signal is explained in more detail in figure 2.21. In case of trajectory 1, a net charge signal is observed on the segment contact and with increasing distance from the sensing electrode the induced current decreases due to the decreasing strength of the weighting field.

The total induced charge is simply given by the difference in the weighting potentials of two positions, leading a zero net charge for trajectory 2 since both electrodes are at ground potential and a net charge of  $-q$  for trajectory 1 because of the difference in the weighting potentials of the two electrodes.

For the core contact three trajectories, labeled 4, 5 and 6, are shown in figure 2.1 for MINIBALL detector which is of closed-ended geometry. Due to the complexity of the electric field and the resulting drift path of the charge carriers, the interpretation of the detector pulse shapes from the quasi-planar front part<sup>2</sup> (trajectory 5 and 6) is difficult and this additional complication is usually neglected [17], i.e. the detector is assumed to be a true coaxial detector<sup>3</sup>. The detector current signal for trajectory 4 can be approximated by calculating the pulse shapes of a simple true coaxial detector.

The equations for the electrical field of a true coaxial HPGe detector together with

<sup>2</sup>The MARS detector [31] features a dedicated segment in front of the core contact to take advantage of the planar geometry.

<sup>3</sup>Similarly, the interpretation of the drift time as a radial position information, in fact being proportional to the distance from the contact (compare trajectory 4 and 6), leads to a decrease in position resolution [22].

the corresponding expressions for the drift velocity were used to calculate example pulse shapes for different interaction radii. The simulation of pulse shapes for a coaxial detectors of infinite length is treated in [21, 32] and the detailed simulation of the MINIBALL detector is covered in [22]. The electrical and the weighting field [30] were simulated for an inner and outer radius of 0.5 and 3.5 cm and a voltage of 4000 V and 1 V respectively. Only single interaction events were investigated. The current signals generated by the positive and negative charge carriers, assumed to be point-like, were simulated by calculating the strength of the electrical field at the current position and from this the velocity of the charge carriers was determined. The simulation advanced in time steps of 1 ns and repeated the previous steps for the new positions of the electrons and holes. The final detector current pulse is the sum of the contributions from the positive and negative charge carriers and the resulting current pulses are shown in figure 2.2. The current pulses are then integrated using the equation for a single pole RC integrator leading to the charge signal, which is subsequently discretized and quantized by a virtual 14 bit, 100 MHz ADC as shown in figure 2.3. The sample and hold part of the simulated ADC averages  $T_s$  samples leading to an alias free spectrum.

The numerical differentiation recovers the original current signal, however, the sharp edges have been eliminated due to the finite bandwidth of the preamplifier. In addition, any preamplifier with a linear phase response delays the signal. The second derivative shows a maximum in the beginning (at least for small radii), which corresponds to the beginning of the charge collection process and is an amplitude and position independent time information of the begin of the charge collection process. The absolute minimum of the second derivative is the position of the steepest slope, which corresponds to the end of the charge collection process for the electrons which drift towards the inner contact. The end of the charge collection process for the holes drifting towards the outer contact is hardly visible since the drop in current is much less than for the electrons. The strong increase of the electric field towards the inner contact amplifies the electron contribution and therefore the drift time of the electrons is the best measure for the distance from the electrode [21]. The drift time of the electrons is given by the difference between the time when the charge carriers are created in the detector, i.e. the initial rising edge of the current signal or the steepest of the second derivative and the time when the charge carriers reach to electrode, i.e. the time of the steepest slope of the second derivative.

## 2.4 The MINIBALL detector

The MINIBALL HPGe detector consists of individually encapsulated n-type<sup>4</sup> HPGe crystals of the EUROBALL type, even though the shape of the EUROBALL detectors was optimized for a target-detector distance of 42 cm. The MINIBALL detectors are placed as close as possible to target chamber for a high efficiency arrangement, typically about 10.5 cm away from the target. The encapsulation, using a thin aluminum can, ensures an ultra clean vacuum together with a dedicated getter material. The detectors are operated at the temperature of liquid nitrogen. In order to increase the granularity of the detector, a sixfold longitudinal electrical segmentation of the outer contact was introduced. The crystal is 78 mm long and its diameter varies between 59 mm and 70 mm. To fully deplete the detector (a pin diode) a high voltage of about 4000 V has to be applied

---

<sup>4</sup>The n-type material is less sensitive to neutron damage and allows thin Boron implanted outer contacts.

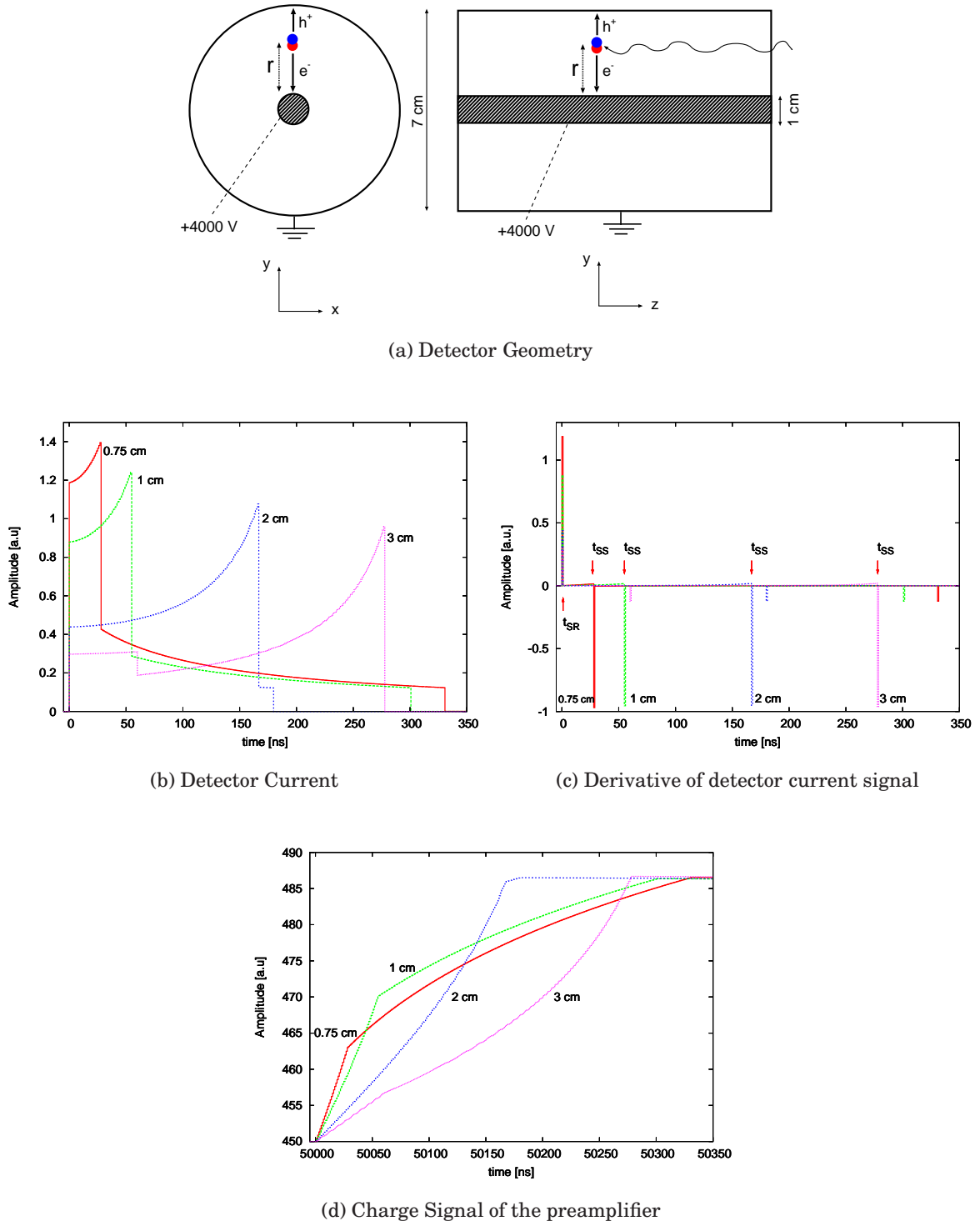


**Figure 2.2:** Simulated current pulses for a true coaxial HPGe detector of infinite length with an inner radius of 0.5 cm and an outer radius of 3.5 cm operated at 4000 V. Panel (a) shows a true coaxial detector of (infinite) length. Four different interaction radii ( $r = 0.75$  cm,  $r = 1$  cm,  $r = 2$  cm and  $r = 3$  cm) have been simulated as shown in panel (b). With increasing distance from the central contact the drift time of the electrons increases and the steepest drop of the current signal happens later after the signal start as visible from panel (c). Panel (d) shows the corresponding output of a charge integrating preamplifier.

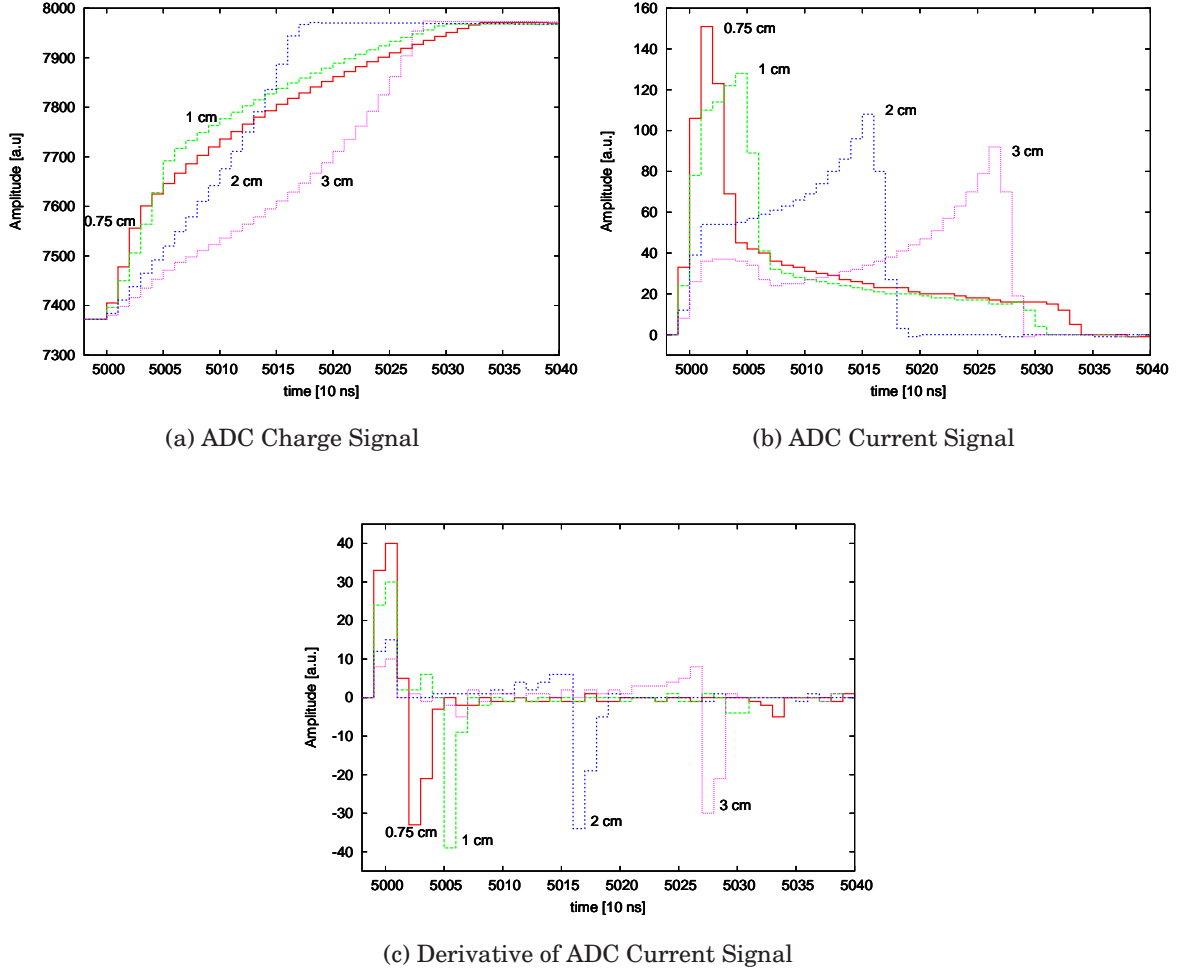


**Figure 2.3:** Panel (a) shows the ADC waveforms of the simulated charge signals, corresponding to the detector signals in figure 2.2. A sampling frequency of 100 MHz was chosen. The times of the steepest slope are derived from the second derivative of the ADC charge signals, which are plotted in panel (c). Panel (b) displays the detector current signals recovered by differentiation of the ADC charge signal.

to the core contact, ensuring that most of the detector volume is sensitive to  $\gamma$ -rays. The exact geometry of the crystal is shown in figure 2.4 together with the detector coordinate system.

Three MINIBALL detector are combined into one triple cluster cryostat to allow for an efficient add-back operation. The cryostat containing the three individually encapsulated crystals is shown in figure 2.5.

The MINIBALL detectors are equipped with digital electronics, the DGF-4C, replacing the conventional analog processing chains. The digital electronics allows a further increase in granularity by pulse shape analysis. A radial position information  $r$  is obtained by analyzing the central contact using the steepest slope algorithm. An angular position information  $\varphi$  is obtained by exploiting the segmentation of the outer contact and analyzing the mirror charge signals present in the neighboring segments of the hit segment.

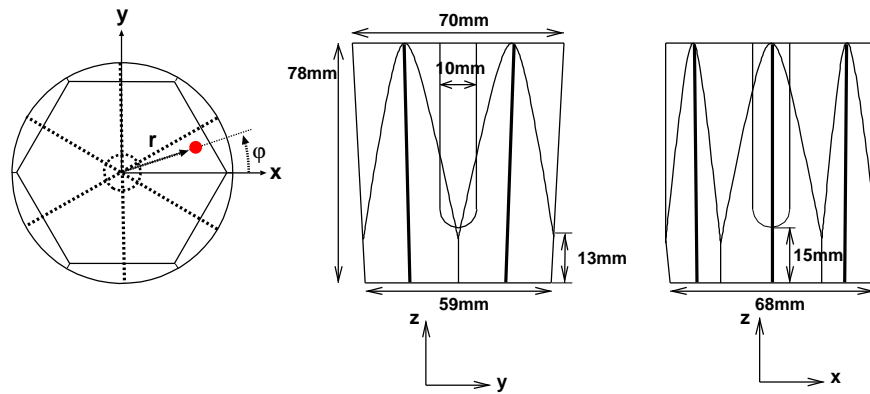


**Figure 2.4:** Physical dimensions of the MINIBALL detector. The detector is 78 mm long and the diameter increases from 59 to 70 mm from the front to the end (taken from [22]).

Three encapsulated, sixfold segmented HPGe Detectors

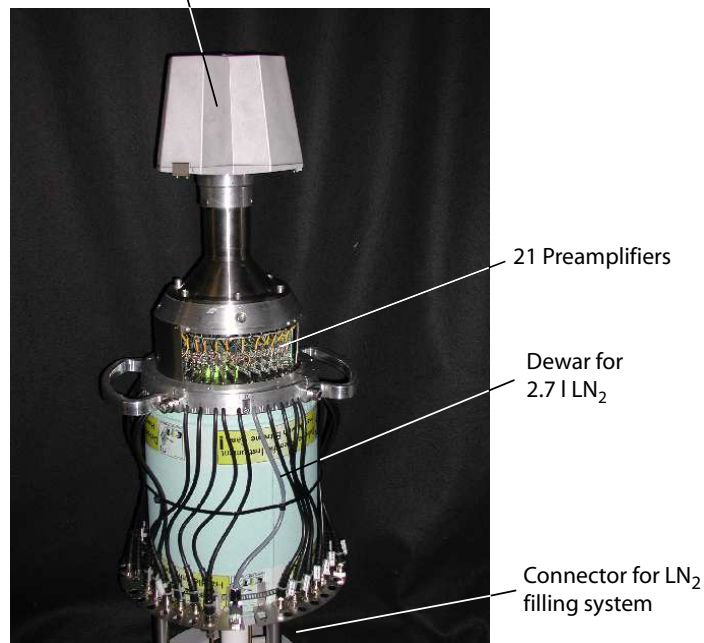


**Figure 2.5:** Photograph of the MINIBALL detector build from six fold segmented HPGe detectors. (taken from [25])

### 2.4.1 The MINIBALL electronics

The DGF-4C CAMAC module [34] from X-Ray Instrumentation Associates (XIA) was the first commercially available digital spectrometer, developed (more than) half a decade after the pioneering work of [35, 36, 37]. It accepts four inputs directly from the charge integrating (either CD or TR) preamplifiers of the detectors. The input signals are digitized, and subjected to first level digital processing, which is implemented in a Spartan XCS40XL FPGA from XILINX, the **Real Time Processing Unit (RTPU)**, which handles the data in real time at the full data rate (40 MHz) of the analog-to-digital converter (ADC). Events which are identified and validated by the internal trigger algorithm are then transferred to a ADSP-2183 **Digital Signal Processor (DSP)** from Analog Devices, where further event processing like ballistic deficit correction and pulse shape analysis takes place. The specification of the DGF-4C is detailed in the data sheet [34].

The ADC data is processed by the RTPU with digital filters that extract energy and trigger information. The RTPU also controls the FIFO for waveform captures of up to 100  $\mu\text{s}$  of data (4096 samples), with programmable pre-trigger delay. In addition the RTPU includes a pile up rejection circuit, a trigger counter and a live time measurement and also supports event validation using logic signals (NIM standard).

The digital signal processor (DSP) on the DGF-4C boards is the ADSP-2183 from Analog Devices which is a 16 bit fixed point DSP with Harvard architecture, featuring separate memories for program code and data storage. The DSP is clocked with the 40 MHz DGF-4C clock. The processor core consists of three independent computational units: An **Arithmetic Logic Unit (ALU)**, an **Multiply ACcumulate unit (MAC)** and a **Shifter** unit. The DSP performs the PSA algorithms.

The ALU is not only used for simple computations like addition or logic operations, but also for divisions.

The MAC unit performs multiplications and the multiply-accumulate instruction. The result of a multiplication operation is stored in a 32 bits wide register and subsequently passed to a 40 bit accumulator. The additional 8 bits of the accumulator are used to allow an intermediate overflow during computations. The shifter unit is mainly used for logical and arithmetic shifts of the data.

The read out takes place over the CAMAC backplane using Fast CAMAC level 1 transfers.

In larger systems, multiple DGFs can operate with a common clock which is distributed via the backplane connector. The common clock system allows accurate identification of coincident events which are *time stamped* with the common clock.

The DGF-4C also includes external memory to store energy spectra on boards. For this a total of 384 kByte of memory was added to the DGF-4C, organized in 4 banks of 32k 24 bit memory locations.

To summarize, the DGF-4C supplies the user with the  $\gamma$ -energy  $E_\gamma$ , a time stamp TS for time of arrival determination and the detector waveform, which can be read out or analyzed on board using the DSP.

## 2.5 $\gamma$ -Energy - Moving Window Deconvolution

The direct digitalization of the charge sensitive preamplifier output with subsequent digital shaping has certain advantages over the analog approach. For high-resolution high-rate  $\gamma$ -ray spectroscopy the most important advantage is the possibility to implement



**Figure 2.6:** Picture of the DGF-4C CAMAC module. The CAMAC connector is located on the left side and is not shown. The (analog) inputs are located on the right side.

trapezoidal shaping, which is the optimal shaping for HPGe detectors [33] and cannot be realized using analog electronics<sup>5</sup>. Another advantage is that only the analog components preceding and including the ADC are subjected to environmental influences, e.g. temperature changes, whereas the performance of the digital filters is unaffected and predictable. On the other hand, if environmental influences, e.g. temperature changes, can be measured by the electronics, e.g. using a temperature sensor, digital corrections can be applied.

**Moving Window Deconvolution (MWD)** [36, 38, 39, 40] is a simple algorithm to calculate the energy of a  $\gamma$ -ray from the digitized charge signal. The basic elements are **Moving Average (MA)** operations and a deconvolution operation. The MWD algorithm transforms the signal from a RC preamplifier (featuring an exponential decaying signal) into a signal which would be obtained from a transistor reset (TR) amplifier (featuring a stair case signal), before a moving average operation removes high frequency noise from the signal and at the same time generates the trapezoidal signal shape.

Moving Window Deconvolution is not the only method for energy determination and various alternative methods have been developed [37, 41, 42, 43, 44, 45, 46, 47, 48, 49, 50]. However, MWD is the most intuitive method and therefore this method was investigated and the results are presented in the following sections.

<sup>5</sup>The analog amplifiers usually features two different shaping techniques, semi-gaussian and quasi-triangular.

### 2.5.1 Description of the Algorithm

The output of a charge integrating preamplifier with continuous discharge<sup>6</sup> is a fast rising step caused by the charge collection followed by an exponential decay due to the discharge of the capacitors over the resistor. The exponential decay reduces the final peak height depending on the signal rise time and in order to accomplish a true ballistic measurement the influence of the preamplifier has to be removed from the signal. This is accomplished by the Moving Window Deconvolution (MWD) algorithm. Ideally, the preamplifier output features a single exponential decay<sup>7</sup> and with the knowledge of the decay time and the start time of the signal the initial amplitude can be determined from any data point of the decaying signal. Starting with the expression for a single exponential decay starting a time  $t_0 = t = 0$

$$f(t) = \begin{cases} A \exp\left(-\frac{t}{\tau}\right) & , t \geq 0 \\ 0 & , t < 0 \end{cases} \quad (2.3)$$

and with the knowledge of amplitude  $f(t_n)$  at time  $t_n$  the initial amplitude can be derived from

$$A = f(t_n) + A - f(t_n) \quad (2.4)$$

$$= f(t_n) + A \left(1 - \exp\left(-\frac{t_n}{\tau}\right)\right) \quad (2.5)$$

$$= f(t_n) + \frac{1}{\tau} \int_0^{t_n} f(t) dt \quad (2.6)$$

$$= f(t_n) + \frac{1}{\tau} \int_{-\infty}^{t_n} f(t) dt. \quad (2.7)$$

Since all computations will be performed in the digital domain, it is useful to go from the continuous to the discrete form

$$A[n] = x[n] + \frac{1}{\tau} \sum_{k=-\infty}^{n-1} x[k] = x[n] - \left(1 - \frac{1}{\tau}\right) x[n-1] + A[n-1]. \quad (2.8)$$

The deconvolution equation 2.7 transforms the continuous discharge preamplifier signal into a signal from a transistor reset preamplifier, which is a staircase signal. The knowledge of the step height is then recovered by differentiation of the deconvoluted signal. At the same time, the differentiation prevents the integration from overflowing, which would be the case for an infinite stair case signal.

Applying a numerical differentiation to the discrete form of the deconvolution equation 2.8 leads to the MWD equation

$$\text{MWD}_M[n] = A[n] - A[n-M] \quad (2.9)$$

$$= x[n] - x[n-M] + \frac{1}{\tau} \sum_{k=n-M}^{n-1} x[k]. \quad (2.10)$$

By setting  $D_M[n] = x[n] - x[n-M]$  and  $\text{MA}_M[n] = \sum_{k=n-M}^{n-1} x[k]$  a simpler expression for the MWD is obtained

$$\text{MWD}_M[n] = D_M[n] + \frac{1}{\tau} \text{MA}_M[n]. \quad (2.11)$$

<sup>6</sup>In short: CD preamp or RC preamp.

<sup>7</sup>Double-exponential decays are treated in section B.4.

The MWD algorithm converts an exponential decaying signal not into an infinitely increasing staircase signal but into a step signal of length  $M$ . It should be noted that the signal is deconvoluted inside the window  $M$  only, in contrast to equation 2.7. A deconvolution operation does not improve the signal to noise ratio [51]. Therefore the delta noise contribution to the MWD signal is reduced by a low-pass filter following the MWD module, implemented as a moving average operation of length  $L$ . At the same time the trapezoidal pulse shape is generated from the MWD signal, since the convolution of two steps signals yields a triangular ( $L = M$ ) or trapezoidal shape ( $L \neq M$ )

$$T_M^L[n] = \text{MA}_L \text{MWD}_M[n]. \quad (2.12)$$

For  $L < M$  the output<sup>8</sup> is a trapezoidal signal shape with a flat top (gap) time of length  $M - L$ , because ideally the moving average operation leads to  $M - L$  times to the same result if the moving average (of length  $L$ ) is moving over the flat top of the MWD signal (of length  $M$ ). The process of MWD is illustrated in figure 2.8. The value of the trapezoidal filter at the end of the flat top period gives the energy information, since at the end of the charge collection period ballistic deficit effects are compensated.

If the incoming ADC data shows a non-zero offset, this will cause an offset of the trapezoidal filter<sup>9</sup>, which in turn leads to an offset of the energy information. The zero  $\gamma$ -energy information will be non-zero, i.e. equal to the trapezoidal filter offset. The effect of a non-zero ADC offset was simulated, showing that the offset of the trapezoidal filter changes in proportion to the ADC offset and furthermore from the output of the filter the actual ADC offset can be determined. In absence of any  $\gamma$  event, the slope of the signal will be zero, i.e.  $D_M[n] = 0$ , and therefore the average ADC offset is given by  $\text{MA}_M[n] = \tau \text{MWD}_M[n] = \frac{\tau}{L} T_M^L[n]$ . In a digital spectroscopy system the pedestal of the filter is subtracted from the energy value on an event-by-event basis; this process is explained in section 2.5.2.

### Remarks concerning adaptive shaping

Adaptive shaping [49] is the process of adjusting the shaping time for each event in order to maximize the throughput of the spectroscopy system, sacrificing, however, energy resolution. An ideal adaptive shaper determines the occurrence of all  $\gamma$  events and optimal filtering is applied to each event based on the available time between the pulses.

A digital spectroscopy system with adaptive shaping is considered for the AGATA tracking array. The simplest implementation would consist of two independent energy channels, one high-resolution channel, where the filter has been set to the optimum shaping time, and one high rate<sup>10</sup> channel, where the shaping times have been reduced to a minimum that allows for an acceptable energy resolution. If the high resolution channel cannot be used because of another event occurring during the shaping period (pile up), then the high rate channels can be used instead to determine the  $\gamma$  energy. Ideally the system should be able to continuously, or in sufficiently small steps, match the shaping time to the current event.

<sup>8</sup>Also for  $L > M$  a trapezoidal shape is obtained. However, such a filter has a different noise residual function and the MA operation is applied to a shorter MWD signal (for equal signal length), but includes also the noisy baseline during the flat top period.

<sup>9</sup>Since the weighting function of the MWD has a non-zero area, any offset at the input of the MWD unit will cause an offset at the output.

<sup>10</sup>High rate means 50 kHz.

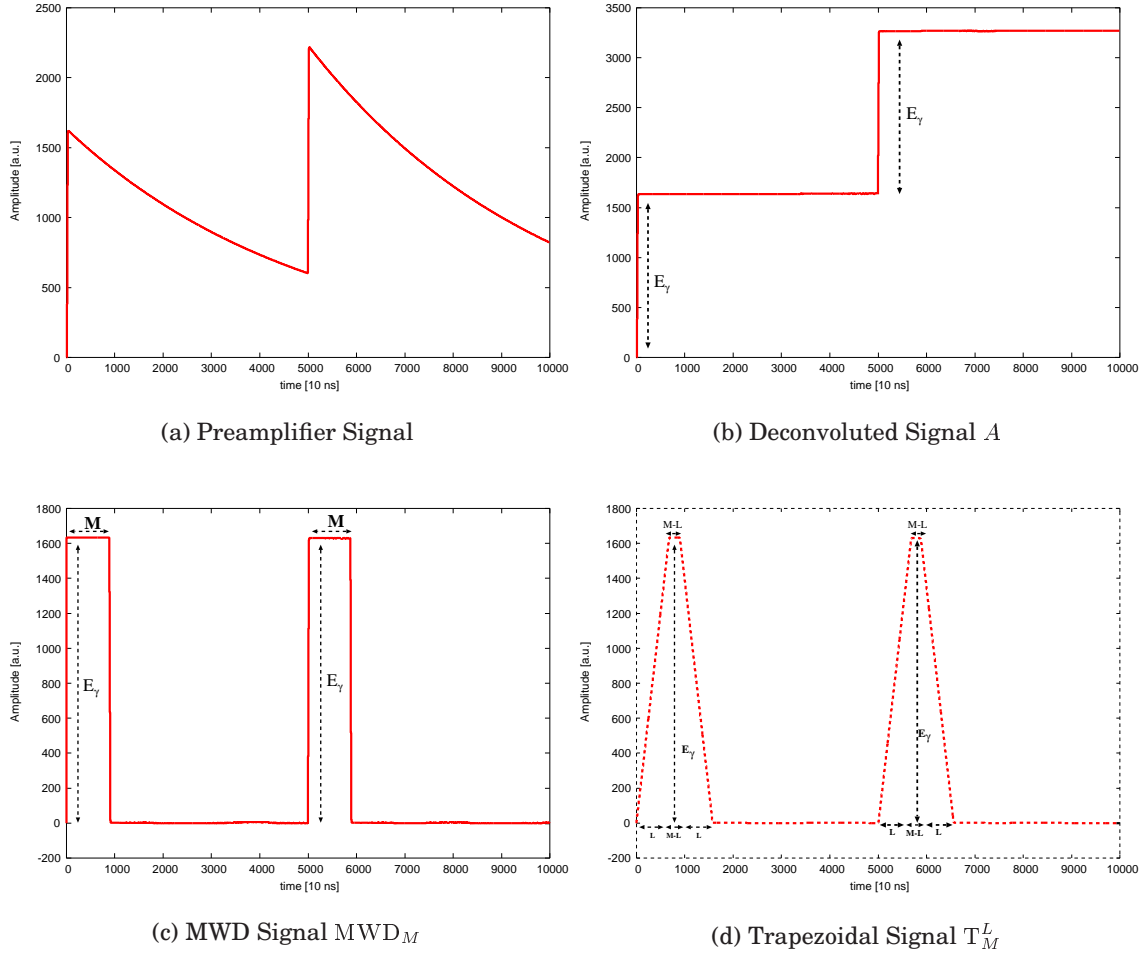
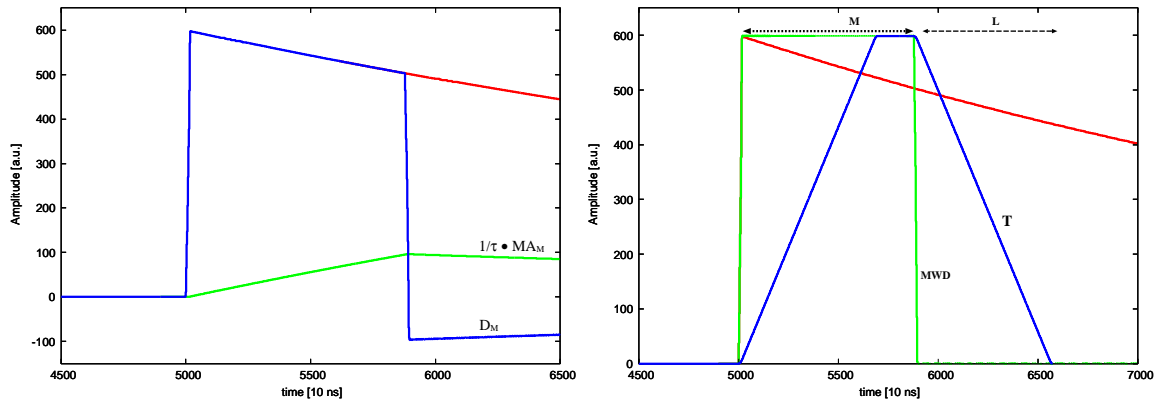


**Figure 2.7:** Deconvolution of the preamplifier signal with subsequent trapezoidal shaping. These are the individual steps of the moving window deconvolution, leading to a trapezoidal signal shape. The amplitude at the end of the flat top period gives the energy information.

The disadvantage of the adaptive shaping system is that the proper shaping time has to be determined from the trigger information of the fast channel<sup>11</sup> before the energy filter can be applied, which requires the storage (delay) of the detector signal. Furthermore, the different shaping times have to be taken into account for the calculation of the baseline average as explained in the previous section. Therefore in an adaptive system, the energy filter values have to be normalized correctly with respect to the MWD parameters  $M$ ,  $L$  and  $\tau$  in order to allow a combination of baseline samples acquired with different MWD parameters. Another solution would be the usage of a dedicated non-adaptive trapezoidal filter for the baseline restorer.

<sup>11</sup>Currently, the trigger information is used only to indicate if the event could be successfully processed with the fixed shaping time or if the event has to be rejected because it is piled up with another event.



(a) Preamplifier signal and the two components of the MWD, the  $D_M[n]$  and  $\frac{1}{\tau}MA_M[n]$  operations.

(b) Preamplifier signal and the deconvoluted step signal plus the trapezoidal energy filter signal.

**Figure 2.8:** Panel (a) shows a typical signal and the result of the two components of the MWD, the numerical differentiation  $D_M[n]$  and the moving average operation  $MA_M[n]$ . Similar to the operation of a standard analog pole-zero cancellation circuit [32], the contribution from the  $MA_M[n]$  compensates the undershoot of the  $D_M[n]$  operation. Panel (b) shows the preamplifier signal together with the deconvoluted step signal  $MWD_M[n]$  and the trapezoidal signal shape  $T_M^L[n]$ . After the  $\gamma$  event, i.e. when the signal features only the exponential decay without leading edge, the trapezoidal filter returns to the baseline value. The dotted line indicates the differentiation period  $M$ , the dashed line the averaging period  $L$  and the difference  $M - L$  determines the flat top period of the trapezoidal signal.

## 2.5.2 Baseline Restoration

The output of an analog pulse shaper typically shows an offset caused by the detector leakage current, the AC coupling and the non-zero area of the weighting function of the shaper, the pedestal or baseline. Additionally, because of noise pickup or variations in the detector leakage current, the baseline shows fluctuations or drifts as visible in figure 2.9.

In an typical analog spectroscopy amplifier a baseline restorer [52] is used to restore a zero baseline value in between events or to store the actual baseline value on a capacitor and subtract it from the shaper output.

The pedestal of the trapezoidal filter gives rise to an offset of the energy spectrum. In case of a noise trigger<sup>12</sup> the output of the filter is non-zero and this event causes a peak at the low end of the energy spectrum, the zero energy or baseline peak. For each normal event the pedestal adds to the filter height. It is obvious that the pedestal has to be subtracted from the filter value for each event.

It is important to note the different meanings of offset and baseline. The actual offset of the signal is defined as the offset before the leading edge of the detector pulse, expressed either in ADC units or mV, which changes for each event especially at high rates when one event is sitting on the exponential decaying signal of the previous event. The baseline or pedestal is the offset the signal will decay to after an infinite amount of

<sup>12</sup>A noise trigger is a false trigger, that happened although there was no  $\gamma$  event.

time.

Equivalently, the offset of the trapezoidal shaper output is a measure of the signal baseline since the trapezoidal shaper output returns to its baseline value when applied to the exponential decaying signal after the leading edge. Therefore the trapezoidal filter baseline is a measure of the offset the preamplifier signal will finally decay to.

The energy information  $E_\gamma$  is the difference between the trapezoidal filter value  $T$  at the end of the flat top and the baseline value  $B$  in front of the trapezoidal  $E_\gamma = T - B$  and therefore the variance of the energy information is then not only determined by the variance of the energy filter height but also by the variance of baseline, i.e.  $\sigma_{tot} \sim \sqrt{\sigma_T^2 + \sigma_B^2}$ . Clearly, if the variance of the baseline is larger than zero the energy resolution will be worsened [29]. In order to decrease the delta noise contribution to the baseline and reduce the baseline variance to a tolerable level, another low-pass filter is applied to the baseline samples. For this the output of the trapezoidal filter, already being the result of a low-pass filter operation, is (re)sampled at a lower rate and send to the baseline filter. Ideally, the baseline should be a constant value and therefore the proper filter for baseline averaging should be of the low-pass type. Two types of low-pass filters have been evaluated in soft- and hardware for the determination of the trapezoidal filter baseline: a moving average filter (MA) and an exponential averaging (EA) filter<sup>13</sup>. Both filters showed equivalent performance in software and are presented in section A.3.

Remembering that the origin of the pedestal of the trapezoidal filter lies in the detector leakage current (source of step noise), the process of baseline restoration can also be understood as separation of the charge created in the  $\gamma$ -ray interaction from the leakage current, whose step noise contribution is subtracted from the total signal, extracting the charge created in the interaction process.

Figure 2.9 demonstrates that the detector leakage current is not constant which sets an lower limit onto the cut-off frequency of the baseline filter. If the baseline would be a constant value plus a delta noise contribution, the optimal baseline filter would simply average *all* baseline samples. The need to track the changes in the detector leakage current, leads to a *windowed* operation where only a certain number of the most recent filter baselines is used for the averaging process.

To summarize, in a digital spectroscopy systems the baseline restorer determines the energy filter baseline value in between events and subtracts the baseline value from the filter value on an event-by-event basis, revealing the charge produced in the  $\gamma$ -ray interaction process. In order to reduce the contribution from the baseline fluctuation to the line width, the baseline restorer averages multiple measurements of the baseline to determine the actual value of the trapezoidal filter baseline with higher precision.

The radiation-free time span is indicated by the absence of any trigger and the fact that the actual filter sample is below a user-defined threshold value. The trigger signal is generated by a filter with a much shorter shaping time and is therefore stronger influenced by the noise. On the other hand, the baseline cut-off value is applied to the trapezoidal filter output and takes advantage of the longer shaping times of the energy filter. This threshold corresponds directly to the maximal energy contribution to the baseline average, limited only by the fluctuations of the baseline. The combination of both methods is used to ensure that the baseline samples are radiation-free, i.e. are due to the detector leakage current only. This is important because in the case of the EA filter a single bad measurement leads to an infinite response of the EA filter, which in

---

<sup>13</sup>In addition any other low-pass filter can be used, e.g. the filters presented in section A.6.

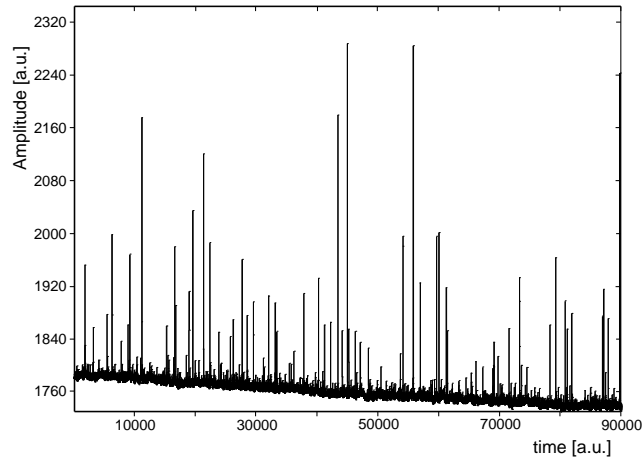


**Figure 2.9:** Drift of the pedestal level after power-up of a MINIBALL HPGe detector. If the average value of the pedestal would not be measured and subtracted from the energy filter output, the position of a  $\gamma$ -ray peak would shift by about two times the FWHM. The spikes are caused by bad baseline measurements due to undetected  $\gamma$  events.

turn degrades the accuracy of the baseline average for a certain period. However, if for example the  $\alpha$  parameter for the EA is  $\ll 1$ , i.e. the EA shows a long impulse response, the contribution of a single sample to the average is small too and if  $\alpha$  is close to 1 the impulse response is very short. Another advantage of the two threshold condition is the possibility to allow for a high fast trigger threshold, with the consequence that low-energy events will not be detected, while at the same time the baseline samples will be acquired only if the energy is (almost) zero.

The frequency of the baseline sampling process is a parameter of the baseline filter module. As mentioned above, the trapezoidal shaper output is the result of a moving average operation applied to the deconvoluted data. From the discussion of the finite duration of the sampling process it is clear that the optimal sampling frequency is the inverse of the length of the moving average window size, i.e  $L$  in case of the MWD. Similarly, the baseline sampler and the moving average operation form a decimation unit (see section A.5) and the properties derived for the decimator apply also to the baseline sampling process. The baseline samples are correlated on the timescale of the peaking time  $L$ .

### 2.5.3 Simulation of the MWD algorithm

The properties of the MWD have been tested with an exponential decaying signal  $f_e(t) = \exp\left(-\frac{t}{\tau}\right)$  with  $\tau = 50 \mu\text{s}$  being the decay time constant.

The charge signal was afterwards processed using the MWD algorithm. The decay time parameter of the algorithm was adjusted such that the deconvoluted and the trapezoidal signal showed a flat top without any slope and further returned to the same baseline value as before the event. This yielded a decay time constant of  $45.4597 \mu\text{s}$  for  $M = 8.8 \mu\text{s}$  and  $L = 6.8 \mu\text{s}$ ; the deviation from the signal decay time is due to additional shaping components and the sampling process. It should be noted that the decay time constant was adjusted with a precision of 1 ns, which is a factor of ten below the time resolution of the ADC. The flatness of the deconvoluted and the trapezoidal signal is illustrated in figure 2.8. At the end of the shaping period, i.e. after  $M + L$ , the trapezoidal

signal returns to the baseline value without any indication of an under- or overshoot.

### Ballistic Deficit

Ballistic deficit is considered to be a major limitation for high-resolution  $\gamma$ -ray spectroscopy with large HPGe detectors with typical signal rise times of about 400 ns. Ballistic deficit arises from the fact that the signal amplitude at the end of the charge collection process differs depending on the charge collection process, which depends on the position(s) of the interaction(s). It is important to note, that the *total area* under the exponential decaying signal is *independent* of the charge collection process<sup>14</sup> and that the deconvolution, according to equation 2.7, removes *any* ballistic deficit effects<sup>15</sup>. Clearly, for measurements with noisy detector signals  $L$  and  $M$  are set to obtain the best energy resolution, e.g.  $L$  for best suppression of delta noise and  $M$  for best ballistic deficit compensation, i.e. the flat top time  $M - L$  increases with increasing need for ballistic deficit compensation.

To illustrate the ballistic deficit compensation pulse shapes with different rise times have been generated using equation<sup>16</sup> (32) from [37]

$$f_{BD}(t) = \frac{A}{\tau_1 - \tau_2} \left( \exp\left(-\frac{t}{\tau_1}\right) - \exp\left(-\frac{t}{\tau_2}\right) \right) \quad (2.13)$$

by setting  $\tau_1 = 50 \mu\text{s}$  and varying  $\tau_2$ . For four different settings the result is shown in figure 2.10, where  $\tau_2$  was set to 100 ns, 200 ns, 300 ns, 400 ns. For the signals with  $\tau_2 = 100$  ns and  $\tau_2 = 200$  ns the ballistic deficit can be corrected and at the end of the flat top period the same filter value is reached. For the other two signals the ballistic deficit cannot be compensated during the flat top period and therefore the energy information cannot be properly determined. Hence, for the filter values chosen, the ballistic deficit of  $\gamma$ -rays with risetimes less than about  $1 \mu\text{s}$ , i.e.  $\tau_2 < 200$  ns, will be compensated.

### 2.5.4 Tests with measured waveforms

The MWD algorithm was compared with the DGF-4C algorithm by comparing the energy resolution obtained offline from the analysis of the waveforms with the energy determined by the DGF-4C module. The MWD algorithm was applied to waveforms of  $100 \mu\text{s}$  length, acquired with the DGF-4C, recording signals of a 12-fold segmented MINIBALL detector irradiated by a  $^{60}\text{Co}$  source. The energy reported by the DGF-4C was stored together with the waveforms. The purpose of this test was to find out if the MWD algorithm achieves the same energy resolution as the algorithms implemented in the DGF-4C. Indeed, the C-code implementation of the MWD algorithm yielded an equivalent energy resolution at the investigated energies and showed that the MWD algorithm is not limiting the energy resolution. The differences stem from the fact that the MWD algorithm works on a shorter data set of  $\pm 50 \mu\text{s}$  around the trigger point whereas the DGF-4C has access to the continuous ADC data and the fact that the MWD algorithm

<sup>14</sup>This can easily be seen from the convolution of the detector current with any normalized preamplifier response.

<sup>15</sup>This can easily be seen from equation 2.7 for  $t_n \rightarrow \infty$  with  $f(t_n) \rightarrow 0$ .

<sup>16</sup>With the condition that the same area, i.e. same charge, should be obtained, i.e.  $A \int \exp(-\frac{t}{\tau_1}) = C \int (\exp(-\frac{t}{\tau_1}) - \exp(-\frac{t}{\tau_2}))$  it follows that  $C = \frac{\tau_1 A}{\tau_1 - \tau_2}$ .

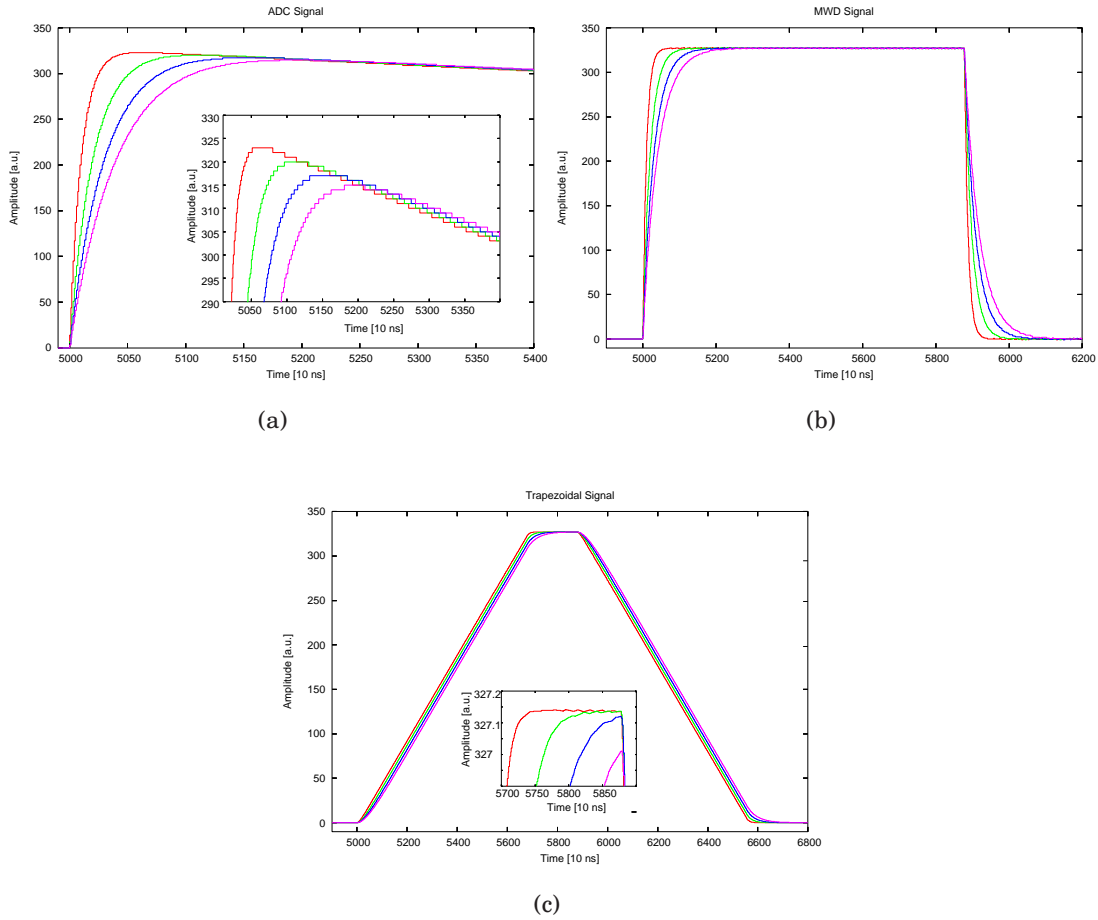


**Figure 2.10:** Elimination of ballistic deficit due to the flat top period  $M - L$  of the trapezoidal shaper. Four different rise times have been simulated as shown in panel (a). The different rise times also show up at the edges of the MWD step signal, which is plotted in panel (b). The trapezoidal signal in panel (c) reaches the maximum amplitude at the end of the end of the flat top period, which is no longer flat due to the finite rise time of the detector signal. The flat top period  $M - L$  is too short to compensate the ballistic deficit for the two signals with the longest risetimes.

uses floating point computations which is not possible with the fixed-point DSP of the DGF-4C.

In order to determine the  $\gamma$  energy with the MWD method, the data was resampled from 40 to 5 MHz to speed up the calculations. A moving average operation was applied to the data, before resampling. Without the MA operation the energy resolution decreased strongly from 2 to 8 keV due to aliasing, as visible from figure 2.11.

The trigger signal was derived from the differentiated and decimated data after application of a fixed threshold. The positions of all triggers were stored. The recorded trace was centered around the trigger point with a  $50 \mu\text{s}$  pre-trigger delay and had a total length of  $100 \mu\text{s}$ . The event trigger was identified by its position, which was required to be inside a  $6 \mu\text{s}$  time interval around the middle of the waveform.<sup>17</sup>

<sup>17</sup>Pile up rejection is accomplished by the DGF-4C and two events cannot happen closer than a about  $9 \mu\text{s}$ . Consequently, since the same peaking and flat top times where used for the offline analysis, pile up

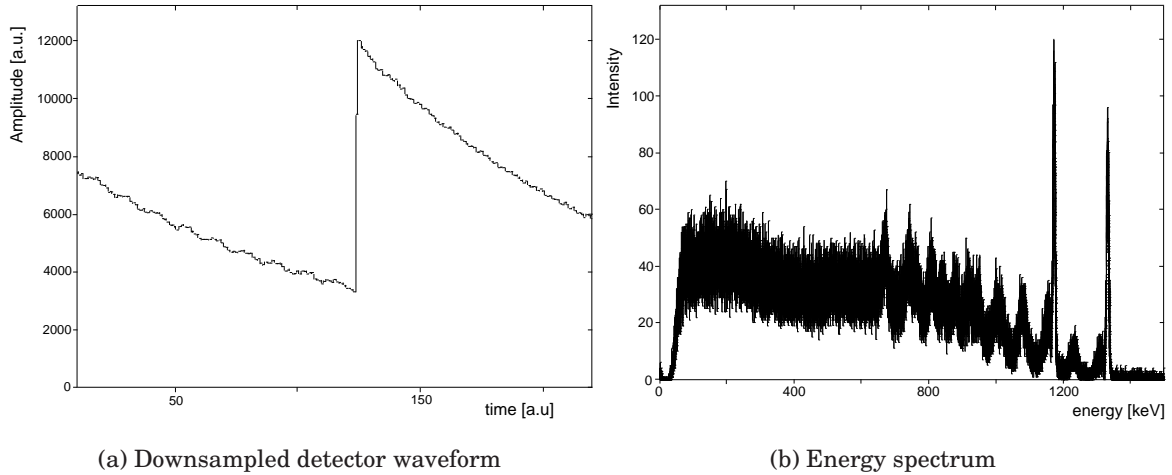


**Figure 2.11:** Downsampled waveform and energy spectrum of a  $^{60}\text{Co}$  source using the MWD algorithm obtained without using an anti-alias filter for the downsampling operation. An increased noise is already observable in the waveform. The energy resolution at 1.3 MeV is about 8 keV.

The  $\gamma$  energy is given by the trapezoidal filter value at the end of the flat top period. Since the digital shaper always leads to the same trapezoidal shape for the same parameters  $M$  and  $L$ <sup>18</sup> this can be accomplished by latching the filter value a *fixed* time after a trigger. The precision of the trigger time determines the precision of the peak sampling process, but since the time resolution in the energy/slow branch is much smaller than that of the trigger/fast branch, the jitter of the trigger does not influence the energy resolution. Additionally, the flat top part of the trapezoidal shaper is usually chosen much larger than then the maximal risetime of the detector. Therefore, even if the sampling point varies by one or two decimated samples, the peak sampling will still happen in the flat part of the trapezoidal signal. Since the flat top is determined by the parameter  $M$  and  $L$  of the MWD, the proper delay<sup>19</sup>  $D$  for the peak sampling process was determined by varying a delay parameter  $t_d$ , which was added to  $M$ <sup>20</sup>, i.e.  $D = M + t_d$ . The best energy resolution was obtained for  $t_d = -800$  ns.

The next step is the determination of the baseline value with both baseline restoration methods and also without any baseline restoration. The baseline module uses the trigger information, generated before, to remove the parts that are due to  $\gamma$  events from the trapezoidal shaper waveform. The region  $[-2\mu\text{s}, M+L+2\mu\text{s}]$  around a trigger is removed, where a safety time of  $2\mu\text{s}$  was added to take into account that the trigger happens *after* the event and that the trapezoidal shaper can show an under- or overshoot at the end of the trapezoidal pulse. This means that for each event the full trace, i.e. before and after the trigger, was used for baseline analysis. The remaining parts of the shaper waveform were sampled with a certain frequency which was set to  $2\mu\text{s}$  for

effects were ignored.

<sup>18</sup>In standard analog system usually the maximum value of the shaper output is latched, but the position of the maximum can depend on the detector pulse shape.

<sup>19</sup>The energy is given by the trapezoidal filter value at the end of the flat top period, i.e.  $M$  after signal start. In order to take into account the trigger generation and other latencies of the implementation, the parameter  $t_d$  was introduced.

<sup>20</sup> $M$  is the differentiation time and corresponds to peaking time plus flat top time.

Algorithm	$E_\gamma = 1173.2 \text{ keV}$	$E_\gamma = 1332.5 \text{ keV}$
DGF-4C	$2.04 \pm 0.02 \text{ [keV]}$	$2.18 \pm 0.01 \text{ [keV]}$
MWD+MA	$1.97 \pm 0.02 \text{ [keV]}$	$2.09 \pm 0.02 \text{ [keV]}$
MWD+EA	$2.07 \pm 0.09 \text{ [keV]}$	$2.16 \pm 0.01 \text{ [keV]}$
MWD	$3.01 \pm 0.09 \text{ [keV]}$	$3.05 \pm 0.02 \text{ [keV]}$

**Table 2.1:** Comparison of DGF-4C with offline MWD energy resolution (FWHM). DGF and MWD use the same shaping times, a peaking time of  $6.8 \mu\text{s}$  and a flat top time of  $2 \mu\text{s}$ . The baseline averaging parameter in the DGF was set to 4. The MA baseline module determines the baseline from the average of all baseline samples for each event ( $\pm 50 \mu\text{s}$ ). The EA BLR module was used with  $\alpha = 2^{-3}$ .

the analysis.

The MA module takes the average of all baseline events that were extracted from this event. If no baseline samples could be acquired, then the previous baseline average value is kept.

The EA module starts with the previous baseline average value and calculates the new baseline average for each acquired baseline sample according to equation A.25. This means that the EA module also uses baseline samples from previous events, however, the most recent baseline sample contributes most to the baseline average. Typical waveforms together with their corresponding energy filter responses are shown in figure 2.12.

Table 2.1 highlights the results of this comparison. The energy resolution without baseline restoration is worse by 50 %, clearly demonstrating the need for baseline averaging with HPGe detectors. This is also visible from figure 2.13, where the  $^{60}\text{Co}$  energy lines are plotted for the MWD algorithm with and without BLR. The MWD algorithm together with the EA BLR module achieves the same energy resolution that was obtained with the DGF-4C. Since the DGF-4C uses such an averaging scheme to determine the baseline average, it can be concluded that the MWD algorithm performs equally as the DGF-4C algorithm. The combination of the MWD algorithm with the MA BLR module, which was originally proposed in [38], yields the best energy resolution.

Another important effect has been observed, which influenced the implementation of the MWD algorithm. At some point in the measurement the baseline average changed suddenly into a negative value, which was due to changes in the detector current, changing the preamplifier offset such, that the signal exceeds the ADC range. An example signal is shown in figure 2.14.

The implementation of the preprocessing algorithm to determine the  $\gamma$ -energy will be presented in chapter 4. The next sections present the pulse shape analysis algorithms for the MINIBALL detector.

## 2.6 Timing Algorithms

A precise determination of the event time  $t_\gamma$  is important for pulse shape analysis and coincidence measurements. The 25 ns granularity of the XIA DGF-4C waveform data is insufficient for timing applications since the time resolution of a HPGe detector is about a factor of two lower than the sampling period and therefore methods employing an interpolation between samples have been evaluated in order to determine the beginning of the detector signal  $t_0 \approx t_\gamma$ .

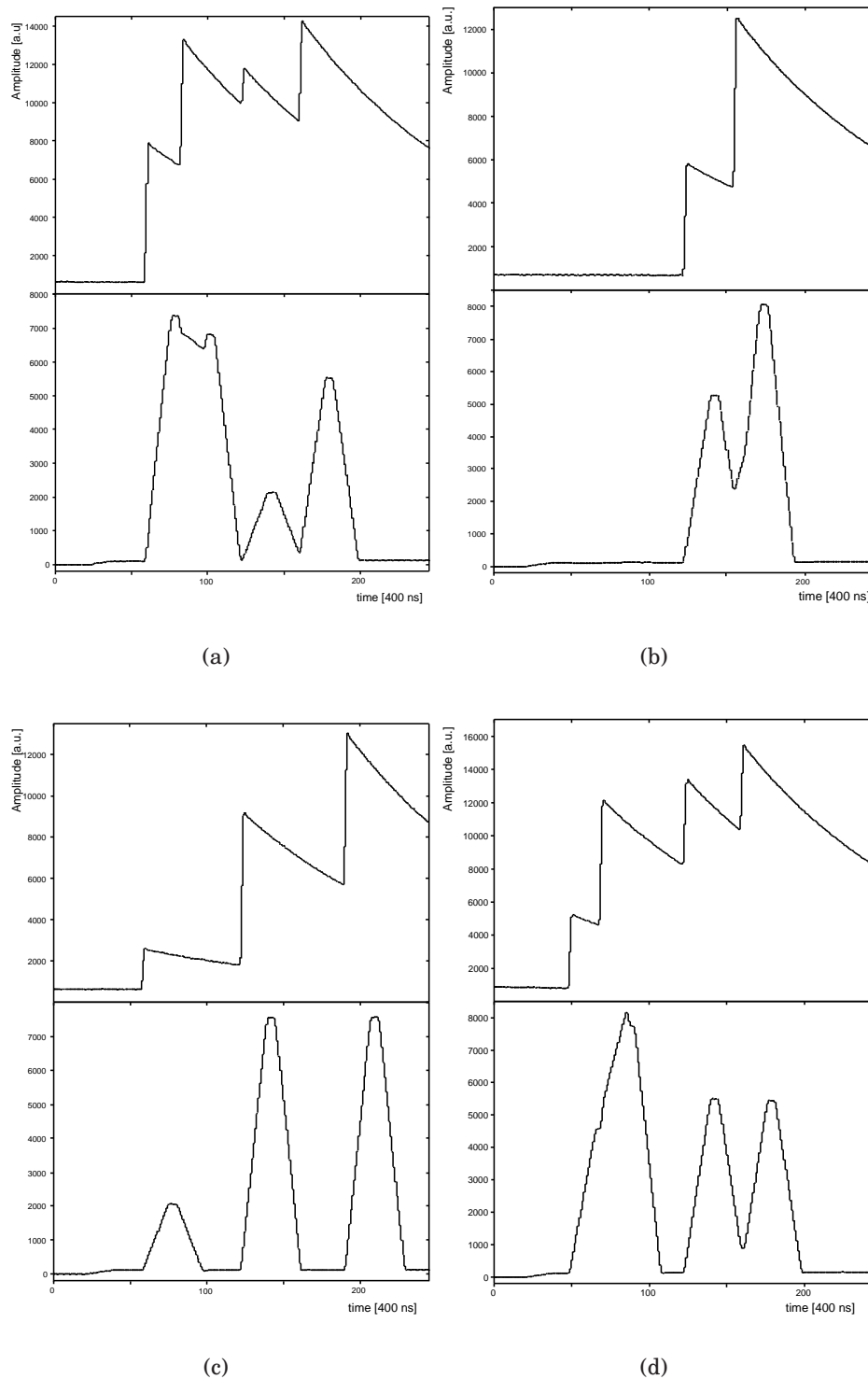


**Figure 2.12:** Sample Signals from the data set (upper panels) with corresponding energy filter response (lower panels). Only events with more than 1 event inside the  $100 \mu\text{s}$  window are shown. In (c) the trapezoidal signals are well separated, i.e. it is possible to acquire baseline samples in between the events. In (d) the first two events are probably piled up, i.e. the second event happens during the flat top period of the previous event. In (a) and (b) the events are well separated, but do not allow for a acquisition of baseline samples in between the events, since the filter does not return to the baseline. In order to be able to acquire baseline samples an additional MWD unit could be implemented, running with much shorter peaking (and gap) time. The output of this dedicated MWD unit could then be used to determine the baseline as explained in section 2.5.1.

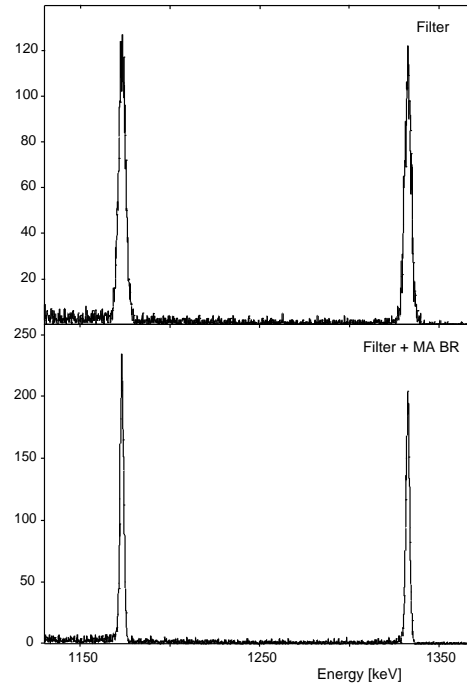


**Figure 2.13:** Energy spectra of the core contact obtained using the MWD algorithm with and without MA baseline restoring. The improvement in energy resolution from 3 to 2 keV is clearly visible.

Due to the finite risetime of the preamplifier the shape of the detector pulse in the very beginning of the signal is determined by the preamplifier only [53] and is independent of the charge collection process. The signal slope during the first 50 ns of the signal is small (see figure 2.22, note the difference between core and segment 2 signal), limiting the performance of any threshold discriminator caused by an increased sensitivity to amplitude variations due to noise. This leads to a *lowest practical threshold* [29], which is defined as the threshold where the signal still features high slope needed for the discriminator. The important parameter for timing algorithms depending on a threshold discrimination is therefore the *slope-to-noise ratio* [29] and not the signal to noise ratio, which is important for energy determination. As a consequence, the best time resolution is obtained when the signal features its steepest rise and not when the signal rise is limited by the preamplifier (see also figure 2.2).

One approach to determine the beginning of the signal is a fit to the detector pulse<sup>21</sup>. A fit would be difficult to implement on the digital signal processor (DSP) of the DGF-4C, nevertheless this method was developed and evaluated previously [25]. Similarly, if the measured detector signal can be fit with simulated detector waveforms for PSA [15], a timing information can be obtained too.

The simplest approach is the linear extrapolation using a sample at the beginning of the signal, the slope  $S$  at that position and the baseline  $B$  in front of the signal, the **Linear Extrapolated Baseline Crossing** (L-EBC) method. For this algorithm to work, the signals should feature a sufficient range that extrapolates to the same origin [29]. Clearly, the pulse shape variations of large HPGe detectors limit the useful range. The

<sup>21</sup>In [54] a fit of the detector signal was used to determine the  $\gamma$ -energy, but the energy resolution was twice the resolution obtained with the MWD algorithm.

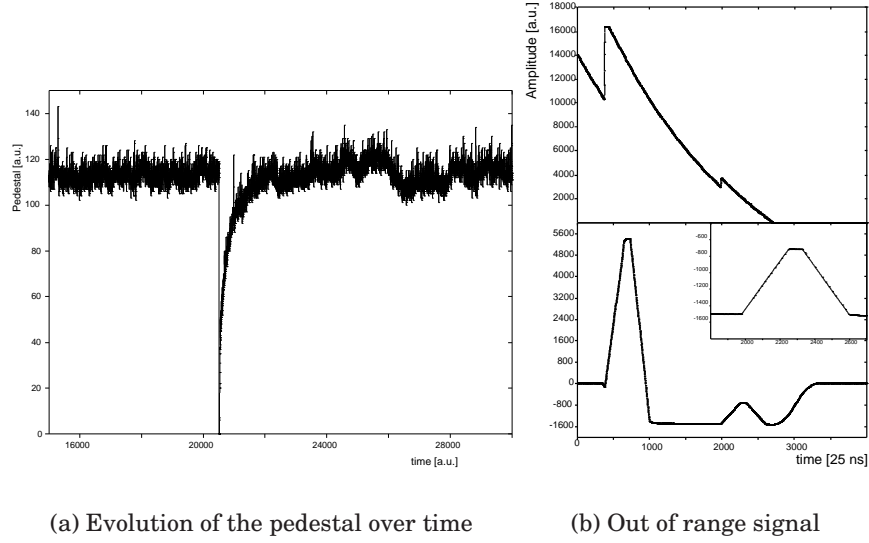


**Figure 2.14:** Panel (a) shows the pedestal, i.e. the baseline, of the energy filter, which features a sharp drop which was due to a strange behavior of the preamplifier. Afterwards the baseline recovers slowly to the previous value. Panel (b) shows an example of such a signal that goes out of the ADC range on both sides, first at the upper end and, after a valid event, the signal continues to decay, leaving the lower end of the ADC range. Consequently, the energy filter shows a negative offset and therefore negative filter values have to be taken into account for the implementation.

numerical value of the baseline  $B$  in front of the detector pulse is determined by averaging over an adjustable amount of samples<sup>22</sup>. The slope  $S$  is determined between adjacent samples  $S[n] = x[n+1] - x[n]$ . The sample  $M$  to start the extrapolation is found using the **Leading Edge (LE)** method, by looking for a sample whose ADC value exceeds baseline  $B$  plus a threshold value  $T$ , i.e.  $x[M] \geq B + T$  and  $x[M-1] < B + T$ . To find  $M$  it is advantageous to go backwards starting from a position during the leading edge of the detector pulse since this approach is less sensitive to baseline noise. Alternatively, to be independent of the signal amplitude the sample  $M$  can also be determined using the **Fractional Timing (FT)** algorithm, by searching for a certain fraction  $f$  of the signal amplitude  $A$ , i.e.  $x[M] = B + f \cdot A$ . The beginning of the signal is then determined by extrapolating to the baseline, i.e. to the starting position of the detector signal, which is assumed to be linear

$$t_0 = M - \frac{x[M] - B}{S} = M - \frac{x[M] - B}{x[M+1] - x[M]}, \quad (2.14)$$

with  $B = \sum_{k=0}^{<M} x[k]$  representing the baseline average  $B$  in front of the leading edge of the signal. Linear interpolation is simple and therefore fast, but the quality of the interpolated data is not sufficient to achieve a good time resolution. In addition, the time difference spectra (see figure 2.16) show side peaks at about half of the sampling interval.

However, it was shown that it is possible to achieve very good results with linear interpolation by help of a simple modification [55]. In order to improve the time resolution,

<sup>22</sup>Note that the DGF-4C has to be set up such that sufficient pre-trigger data is acquired.

an additional factor  $c$  was introduced leading to the **Modified L-EBC (ML-EBC)**

$$t_0 = M - c \frac{x[M+1] - B}{S} = M - c \frac{x[M+1] - B}{x[M+1] - x[M]}, \quad (2.15)$$

which removes the additional side peaks and ensures an almost gaussian peak shape in the coincidence spectrum.

Since the linear extrapolation is not an accurate<sup>23</sup> description of the detector signal<sup>24</sup>, this method has been extended to allow for higher order approximations. Assuming a function that rises with a power of  $(t_0 - t)$  as approximation for the pulse shape  $f(t) = A(t - t_0)^n$  and calculating the delay information  $t_d(t)$

$$t_d(t) = \frac{f'(t)}{f''(t)} = \frac{t - t_0}{n - 1} \quad (2.16)$$

it is obvious that by subtracting  $(n - 1) \cdot t_d$  from the time  $t_M$  given by the sample  $x[M]$  the start position of the detector pulse is obtained

$$t_\gamma = t_M - (n - 1) \cdot t_d = t_M - (t_M - t_0) = t_0, \quad (2.17)$$

i.e.  $t_d(t)$  gives the delay between the actual time  $t$  and the signal start time  $t_0$ . The  $\frac{f'(t)}{f''(t)}$  algorithm features a better approximation of the pulse shape, while maintaining the simplicity of the linear interpolation. In addition, the knowledge of the baseline  $B$  is not required. Usually a value of  $n = 2$  gives best results, leading to the **Quadratic Extrapolated Baseline Crossing (Q-EBC)** method. Both algorithms are easy to implement on a DSP and are therefore used in the MINIBALL User DSP code which will be presented in chapter 3. A FPGA implementation of a **Constant Fraction Discriminator (CFD)** for online triggering purpose is presented in section C.6.

### 2.6.1 Test with measured waveforms

The time resolutions that can be obtained with these algorithms were determined with two different data sets by analyzing the signal from the central contacts. Data set A [23] was acquired using a  $^{60}\text{Co}$  source with two encapsulated detectors, but one detector was equipped with the original preamplifier from Eurisys<sup>25</sup>. Both detectors were connected to two channels of a DGF-4C, which was setup such that the first channel triggering stopped the waveform FIFOs. Since in this configuration a common clock is ensured automatically, time stamp information was not available in the data set. The dynamic range of the DGF-4C was set to about 1.5 MeV, just above the 1.3 MeV line of  $^{60}\text{Co}$ . The  $\gamma$  energies investigated were located at 1173.2 and 1332.5 keV for detector C and B, respectively and in addition also the time resolution over the full dynamic range, allowing any  $\gamma$  energy, was investigated. The time resolution was determined by taking the difference between the start times of detector C and B, i.e.  $t_C - t_B$ .

Data set B [25] was acquired using a  $^{152}\text{Eu}$  source irradiating a MINIBALL triple cluster detector. In this setup the core signals of the detectors were connected to different DGF modules and a common clock was distributed. The time stamp information TS is

<sup>23</sup>However, for this algorithm to work, only a subrange of the signal has to extrapolate to the same origin.

<sup>24</sup>In [18] the beginning of the detector signal is described by  $S(t) = t - \frac{\sqrt{\pi}T_r}{2\sqrt{1.3}} \operatorname{erf}\left(\frac{1.3t}{T_r}\right)$

<sup>25</sup>The EURISYS preamplifiers are usually replaced by preamplifiers especially designed for the MINIBALL detectors.

necessary, since the waveform FIFO is stopped by each individual trigger and the PSA timing information, which is extracted from the waveform is therefore correlated with the time stamp of the triggering channel. In data set B, the dynamic range was set to about 3 MeV, in addition the 12 bit ADC data is reported as 14 bit number by the DGF. The  $\gamma$  energies investigated were located at 344.3 and 778.9 keV. The time resolution was determined by taking the difference between the start times of detector C and B taking into account the time of arrival TS, i.e.  $(TS_C + t_C) - (TS_B + t_B)$ .

First, the influence of the initial sample index  $M$  onto the time resolution was investigated, through variation of the threshold  $T$ . Figure 2.15 shows the influence of the threshold  $T$  on the time resolution, which is important for the setup of the corresponding user DSP code parameter. The optimal threshold  $T$  for the L-EBC method using data set A is about 150 ADC units, which translates into a fractional threshold  $f$  of about 4-5 % of the signal height (FEE of 1.33 and 1.17 MeV). Due to the different dynamic range in data set B, the optimal threshold  $T = 150$  equals also a fractional threshold of  $f \approx 4$  %, i.e. in order to obtain the best time resolution with the L-EBC a fractional threshold  $f$  of about 5 % of the signal height should be used. A time resolution of 16 ns and 30 ns was obtained for data set A and B, respectively. The difference in time resolution is caused by the different dynamic range together with the different energies of the  $\gamma$ -lines (all energies in data set A are above 1 MeV), the different noise levels in the data sets and the different setup of the digital electronics.

The time resolution of the ML-EBC is shown in figure 2.16. In the coincidence spectrum for the L-EBC ( $c = 1$ ) additional side peaks at half of the sampling period are visible, indicating that an upsampling by more than a factor of two is impossible with the L-EBC setting the lower limit for the bin size of the spectrum. However, using the factor  $c$  allows higher upsampling ratios, i.e. smaller bins, as can be seen from figure 2.16. By increasing the factor  $c$  from 1.0 to 1.75, the side peaks disappear and an almost gaussian coincidence peak is obtained. It is important to note that the time resolution improves only slightly for data set A, i.e. the ML-EBC method improves mainly the *shape* of the coincidence peak.

In addition to the algorithms implemented in the user DSP code, the FT algorithm was evaluated<sup>26</sup>. The time resolution is shown in figure 2.17 for data set A. The best time resolution of 23 ns is obtained for  $f = 10$  % if an energy gate is used. If the full energy range is analyzed, the best time resolution of 38 ns is obtained for  $f = 5$  %.

The time of the **Steepest Rise** (SR) of the current signal, which is important for the Q-EBC algorithm, was evaluated as a timing method, since the position of the steepest rise should be independent of the charge collection process and determined by the preamplifier transfer function only. The time resolution that can be obtained by determination of the position of the steepest rise is shown in figure 2.17 for different differentiation formulas (see section A.4.2). For data set A, a time resolution between 18 and 22 ns is obtained, depending on the differentiation equation and corresponding transfer function, which are presented in section A.4. Since the three point differentiation is an average of the two point formula, the higher frequencies are consequently suppressed compared to the two point formula. Increasing the number of data points for the differentiation further, amplifies the higher frequency components. Therefore the three point formula gives the worst results.

Finally, the time resolution of the Q-EBC algorithm was studied. In figure 2.18 the

---

<sup>26</sup>A similar timing algorithm is part of the DGF firmware.

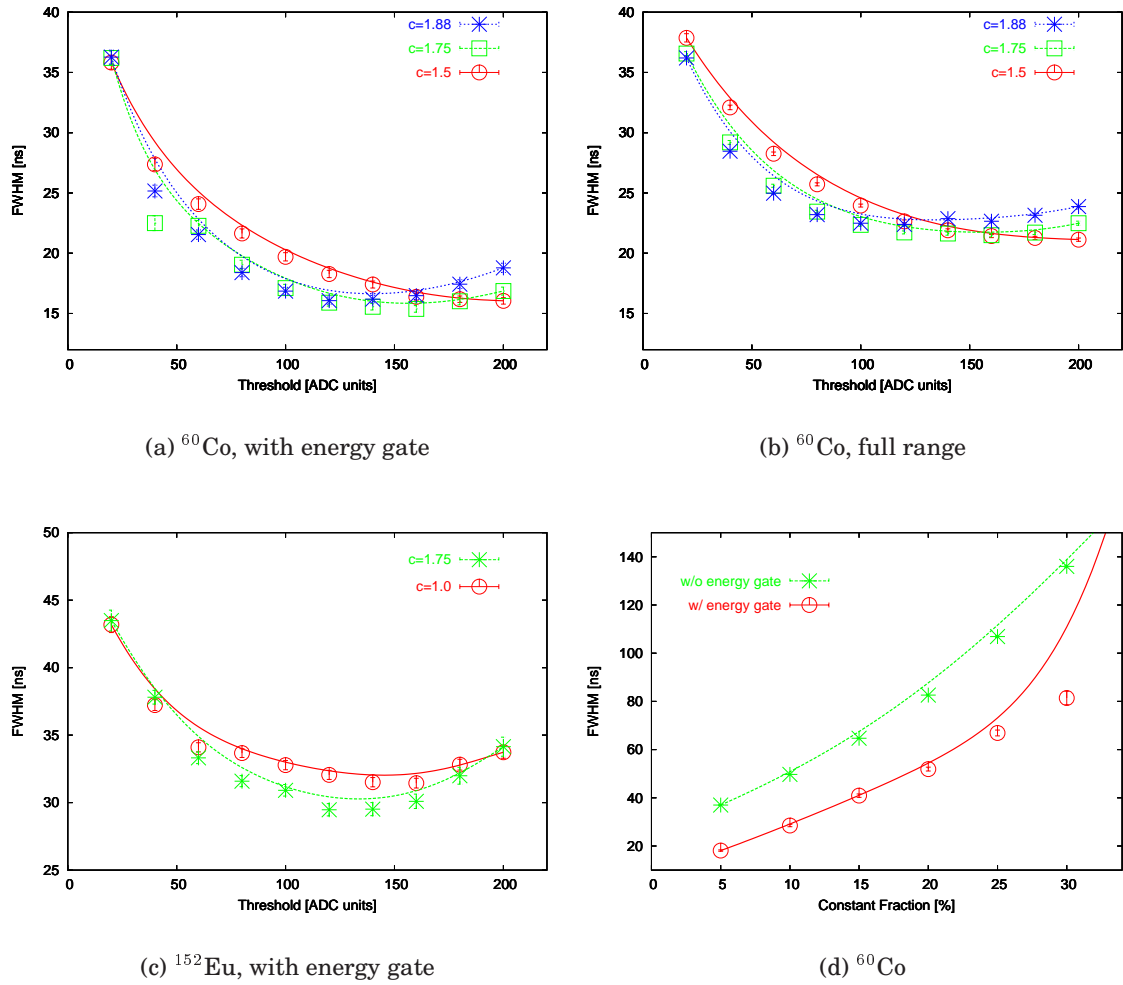


**Figure 2.15:** Panel (a), (b) and (c) show the influence of the threshold  $T$  on the time resolution (FWHM) of the L-EBC, while panel (d) shows the results for a fractional threshold  $f$ . Due to a change in the DGF-4C firmware, one ADC unit for the  $^{60}\text{Co}$  data equals four ADC units in the  $^{152}\text{Eu}$  data. The time resolution obtained for the  $^{60}\text{Co}$  data is about twice the resolution obtained with the  $^{152}\text{Eu}$  data. An energy of 1.17 and 1.33 MeV for detector C and B, respectively, was required in case of the energy gate for the  $^{60}\text{Co}$  data. An energy of 344 and 779 keV for detector C and B, respectively, was required in case of the energy gate for the  $^{152}\text{Eu}$  data.

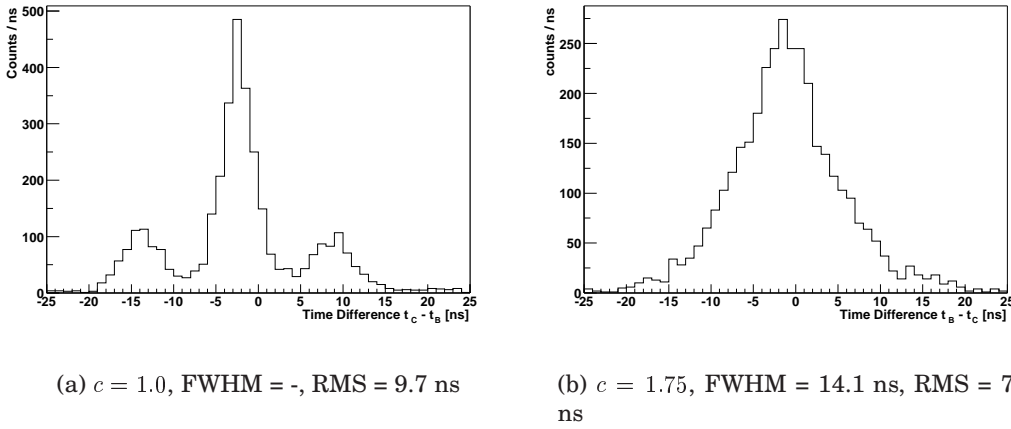


**Figure 2.16:** Influence of the coefficient on the time difference peak shape for the (M)L-EBC method. With increasing  $c$  from 1 to 1.75 for the  $^{60}\text{Co}$  data set, the additional side peak are removed from the spectrum and the main peak gets wider. The time resolution of the linear extrapolation method does improve slightly by using the factor  $c$ .

time resolution obtained with the  $\frac{f'(t)}{f''(t)}$  algorithm is shown for two different differentiation formulas using three or nine data points. The improvement in time resolution is about 2 ns if nine data points are used instead of three. Since the improvement is small and not valid under all operating conditions, the user DSP code uses the three point formula.

Figure 2.19 displays the time resolution of the Q-EBC method for different differentiation equations. In addition, two methods to determine the initial sample index  $M$ , a leading edge discriminator (LE) with a threshold  $T$  and the position of the steepest rise (SR), have been evaluated. An improvement by more than a factor of two in time resolution, compared to the sampling frequency, can be achieved. For data set B a time resolution of 23 ns is achieved for  $n = 2$ . The sensitivity of the Q-EBC algorithm to noise can be seen from the fact that the best time resolution is obtained for the three point formula, which suppresses the higher<sup>27</sup> frequency components of the signal. On contrary, in data set A, the best time resolution of 9.5 ns is obtained for the two point formula.

It's important to note, that the efficiency, i.e. fraction of events inside a  $\pm 30$  ns window ( $3\sigma$ ), of the algorithm improves from only about 50 % to 86 % if the position of the steepest rise (SR) is used instead of the leading edge (LE) discriminator position for data set B, demonstrating the importance of the slope-to-noise ratio.

To further understand the difference in the time resolution between data set A and B, the effect of the DGF-4C time stamp information is summarized in table 2.2 for the  $\frac{f'(t)}{f''(t)}$  algorithm. In the coincidence spectra the position of the coincidence peak shifts by about 3 ns in proportion to the time stamp difference  $\Delta\text{TS} = \text{TS}_B - \text{TS}_C$ <sup>28</sup>, i.e. the shift can be expressed as  $3 \text{ ns} \cdot (|\Delta\text{TS}| + 1)$ . Therefore, coincidence conditions should be applied depending on  $|\Delta\text{TS}|$  and it is expected that such an effect is not present in data

<sup>27</sup>The frequency components in the upper half of the bandwidth.

<sup>28</sup>Since the energies are fixed, the time stamp difference  $\Delta\text{TS}$  does only depend on the pulse shape, e.g.  $\Delta\text{TS}$  is correlated with the steepest slope time  $t_{ss}$  of detector C (344 keV).

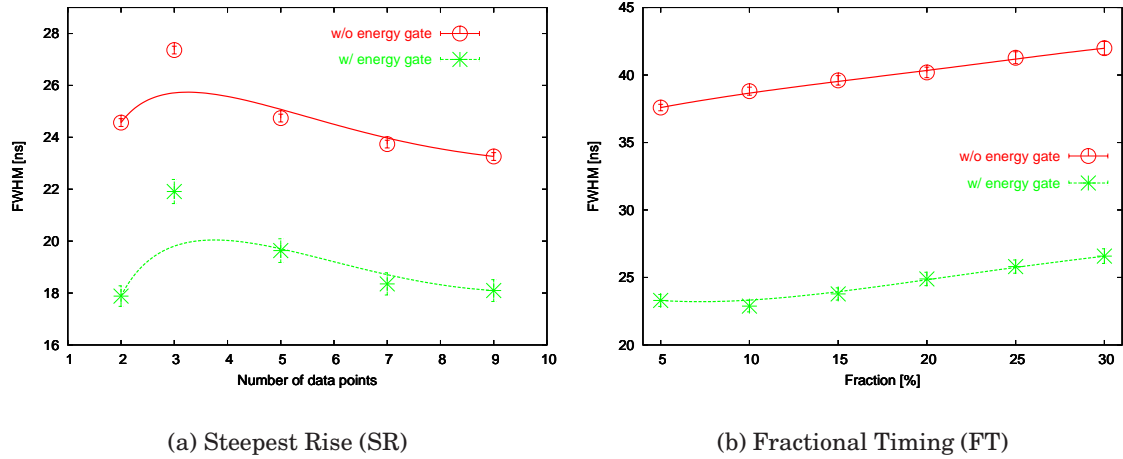


**Figure 2.17:** Panel (a) shows the time resolution of the steepest rise (SR) timing algorithm using the  $^{60}\text{Co}$  data set for different differentiation formulas using 2 to 9 data points. The worst time resolution is obtained for the three-point formula due to the stronger damping of the higher frequency content as explained in section A.4. Panel (b) shows the time resolution of the fractional timing (FT) algorithm using a quadratic interpolation obtained with the  $^{60}\text{Co}$  data set.

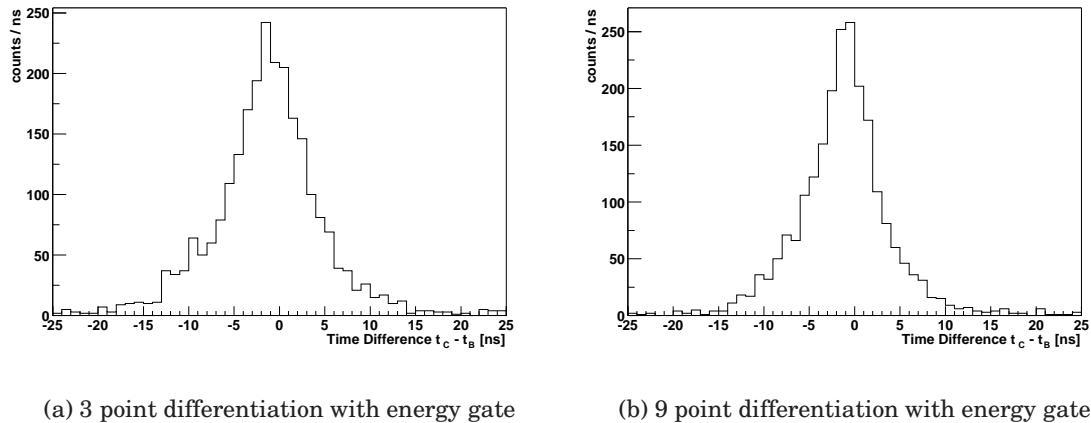


**Figure 2.18:** Time resolution of the Q-EBC algorithm for two differentiation formulas using three or nine data points, plotted for an energy gate onto the 1173.2 and 1332.5 keV lines of  $^{60}\text{Co}$  source for detector C and B, respectively. The time resolution improves from 12.1 in case of the three point differentiation formula to 10.4 ns in case of the nine point formula.

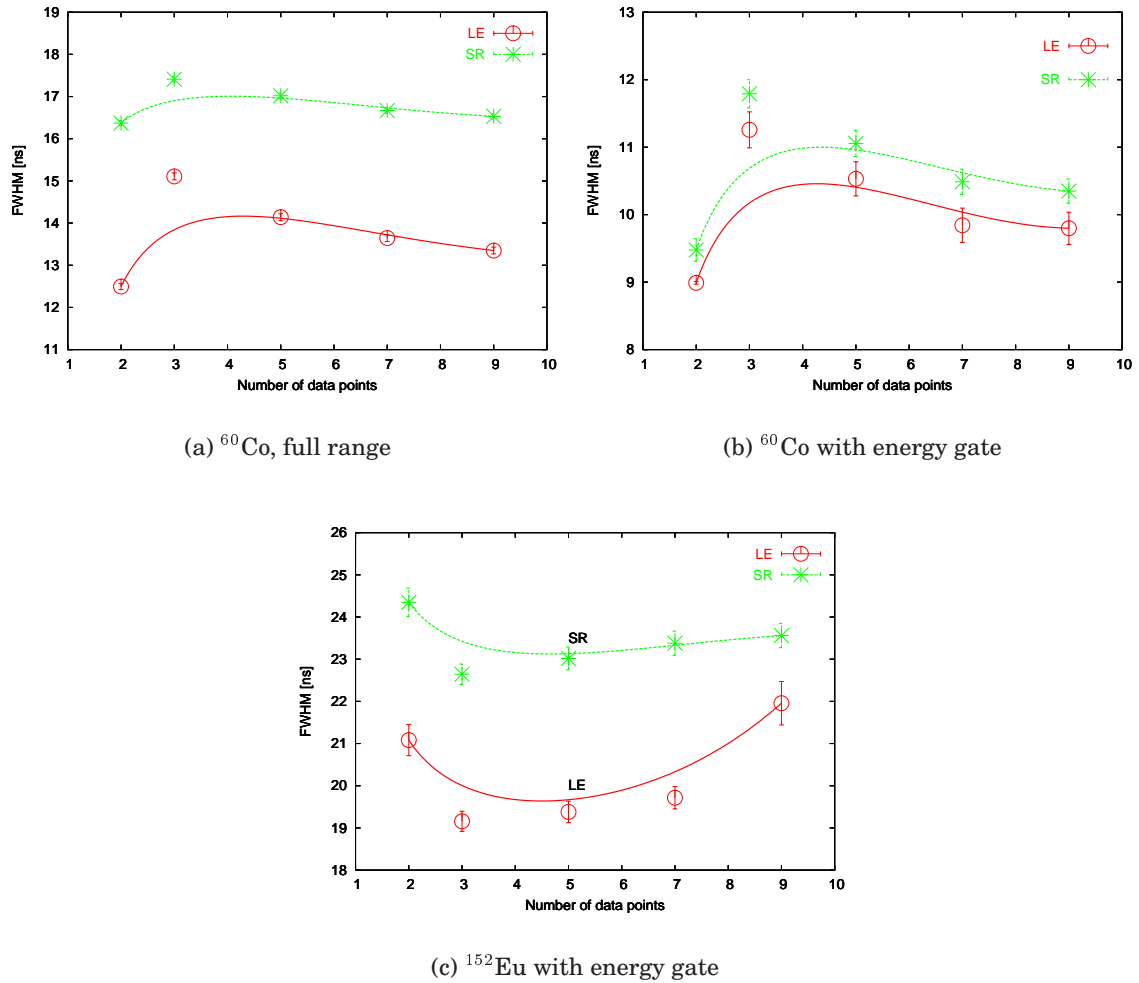


**Figure 2.19:** Panel (a) and (b) show the time resolution of the Q-EBC algorithm for data set A versus the number of data points used for the differentiation. Panel (c) shows the time resolution for data set B. The starting point  $M$  is very important for an efficient application of this algorithm. In addition, if more data points are used for the derivative, the time resolution improves for data set A compared to the three point formula, due to the damping of high frequency components. The inverse is true for data set B, suggesting the application of a low-pass filter before applying the timing algorithm.

$\Delta$ TS	FWHM [ns]	Position [ns]	Entries
$ \Delta\text{TS}  = 0$	16.8	3.7	880
$ \Delta\text{TS}  = 1$	16.6	6.4	2887
$ \Delta\text{TS}  = 2$	20.3	9.3	2477
$ \Delta\text{TS}  = 3$	22.9	13.8	557
$ \Delta\text{TS}  \leq 1$	17.0	5.8	3767
$ \Delta\text{TS}  \leq 2$	18.4	7.1	6244
$ \Delta\text{TS}  \leq 3$	19.0	7.4	6801

**Table 2.2:** Time resolution of the Q-EBC algorithm using the  $^{152}\text{Eu}$  data set for different time differences of the DGF-4C time stamps. The shift of the peak position causes an additional broadening of the time difference spectrum and in addition the time resolution decreases with increasing time stamp difference. There is a phase shift in the coincidence spectra of about  $3 \text{ ns} \cdot (|\Delta\text{TS}| + 1)$ .

set A, stopping the waveform FIFOs with a common trigger. The effect is shown in panel (c) and (d) of figure 2.20 for the Q-EBC algorithm and the fit to the detector pulse.

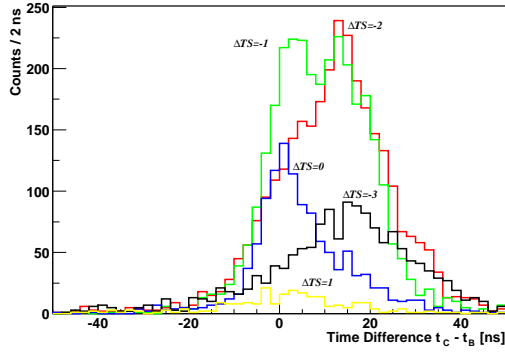
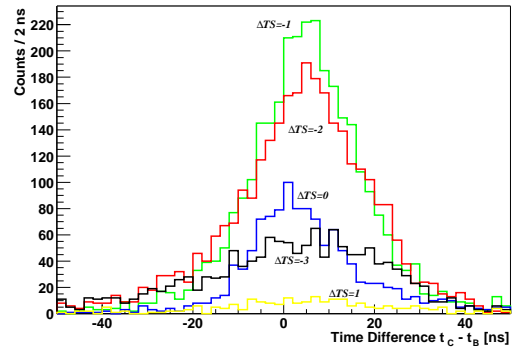
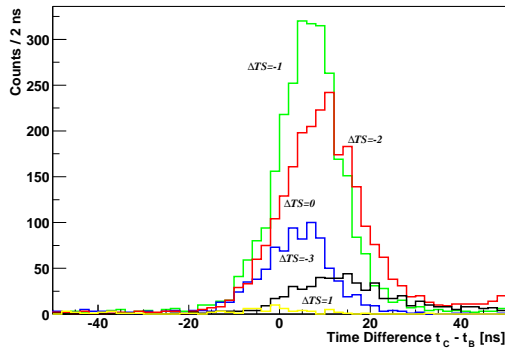
The behavior of the linear extrapolation algorithm for different  $\Delta\text{TS}$  is plotted in panel (a) and (b) of figure 2.20 for  $c = 1.0$  and  $c = 1.75$ , respectively. For  $\Delta\text{TS} = 0$  the coincidence peak is centered around 3 ns in the time difference spectrum. For  $\Delta\text{TS} = -1$  the peak shows two contributions centered at about 3 ns and 15 ns, i.e. separated by half of the sampling period. In the  $\Delta\text{TS} = -2$  spectrum the 3 ns contribution is suppressed and not visible in the  $\Delta\text{TS} = -3$  spectrum, which is centered around 15 ns time difference. Using the linear extrapolation with a factor  $c = 1.75$  centers the coincidence spectra for all  $\Delta\text{TS}$  value and also improves the total time resolution slightly from 31.5 to 29.5 ns. The linear extrapolation algorithm is strongly influenced by effects caused by the sampling and time stamping. This effect is less severe for non-linear approximations, like the  $\frac{f'(t)}{f''(t)}$  algorithm, which are therefore the preferred timing algorithms. Fortunately, the uncertainty introduced by the sampling process will decrease with increasing sampling rates already available now.

The L-EBC and the Q-EBC algorithm were implemented for the DGF-4C using a LE method to determine the initial sample index  $M$ . The performance of the L-EBC together with the PSA algorithm is presented in chapter 3.

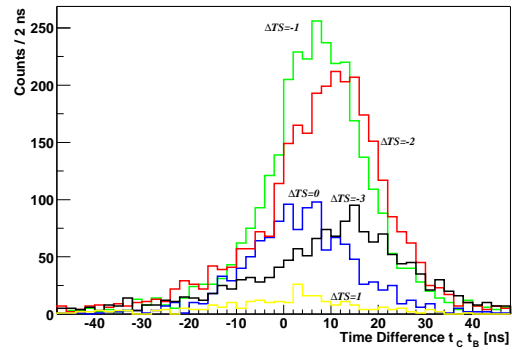
## 2.7 Position Determination

The determination of the emission angle of a  $\gamma$ -ray from the target is based on the determination of the **Main Interaction (MI)** position as approximation for the **First Interaction (FI)** position. The segment with the highest energy deposition is assumed to contain the main interaction (a detailed analysis of the segment hit pattern for position determination is given in [22]) and therefore the first step of the position determination is the identification of the segment containing the MI<sup>29</sup>.

<sup>29</sup>To be precise, the segment *collecting* the charge of the MI is determined. The fact that the charge is not collected in the hit segment poses a problem for  $\gamma$ -ray tracking detectors.

(a) L-EBC algorithm ( $c = 1.0$ )(b) ML-EBC algorithm ( $c = 1.75$ )

(c) Q-EBC algorithm



(d) Fit to leading edge of detector pulse

**Figure 2.20:** Influence of the time stamp time difference onto the time difference  $t_C - t_B$  using the (M)L-EBC methods, the Q-EBC method and the fit to the waveform. For the linear extrapolation the results are shown for two settings 1 and 1.75 of the coefficient  $c$ . The time stamp difference ( $\Delta TS = TS_B - TS_C$ ) of 1, 0, -1, -2, -3 samples are indicated for the corresponding time difference spectra. The effect of the coefficient for the linear extrapolation is that the individual spectra are shifted such that the peaks are at the same position, which is not the case for any other method.

### 2.7.1 Radial Position $r$ of the Main Interaction

The interpretation of the detector current signal of the core contact can be demonstrated best assuming a single interaction event. As can be seen from figure 2.2, the signals feature a steep rise in the beginning, when the charge is created inside the detector. The current signal is a superposition of the minority and majority charge carrier current contributions. After one charge carrier type has reached a detector electrode, the remaining signal is determined by a single kind of charge carrier only. The individual contribution to the sum signal depends on the strength of the weighting field, i.e. on the position of the drifting charges.

For a radial interaction position of 1 cm the electron contribution in the beginning of the signal is about two times larger than the hole contribution. Since the distance from the core is only 0.5 cm but the distance to the segment contact is 2.5 cm, the electrons reach the contact first. After an initial steep rise while approaching the contact, the steepest slope of the current happens when the electrons reach the central contact, i.e. a short time after the beginning of the pulse. The remaining part of the signal shows the continuously decreasing current of the holes while drifting towards the outer contact.

For a radial distance of 2 cm both charge carriers reach their contacts almost at the same time, resulting in a short total charge collection time and an intermediate steepest slope time.

In case of a radial interaction position of 3 cm, the holes reach the segment contact before the electrons reach the core, resulting in a long steepest slope time.

Since the steepest slope time increases linearly with the distance from the core contact, i.e. the drift time of the electrons, the steepest slope of the detector current signal is used to determine the radial interaction position  $r$  of the MI.

For multiple interactions, the situation is more complicated. However, the steepest slope of the current signal [21] is in any case determined by the majority charge carriers and the MI. The MI contributes most to the detector pulse and in addition the strength of the weighting field  $E_w$  increases strongly with decreasing distances from the the central contact .

The steepest slope algorithm determines the drift times of the electrons from the signal of the core contact. The drift time is determined by the velocity of the charge carriers, being at saturation level (0.1 mm/ns) almost everywhere in the detector volume, and by the drift direction, determined by the electric field and the orientation of the crystal lattice. The interpretation of the steepest slope, being proportional to the *distance* from the core, as radial position information is only valid for a true coaxial detector. This leads to distorted drift time spectra for the planar part of the detector, which cannot be resolved due to the unknown depth of the interaction.

The implementation of the steepest slope algorithm is straight forward. First, the second derivative of the charge signal  $S[n] = x[n] - 2x[n-1] + x[n-2]$  has to be calculated. Then the minimum has to be found. The charge collection time  $t_{cc}$  of the majority charge carriers is then the difference between steepest slope time  $t_{ss}$  and the start time  $t_0$  of the detector pulse  $t_{cc}^e = t_{ss} - t_0$ . A quadratic interpolation can be used for further refinement of the steepest slope time

$$t_{ss} = \frac{(2n-1)S[n+1] - 2nS[n] + (2n+1)S[n-1]}{2(S[n+1] - 2S[n] + S[n-1])}. \quad (2.18)$$

The interpolation is necessary to overcome the 25 ns granularity of the ADC samples.

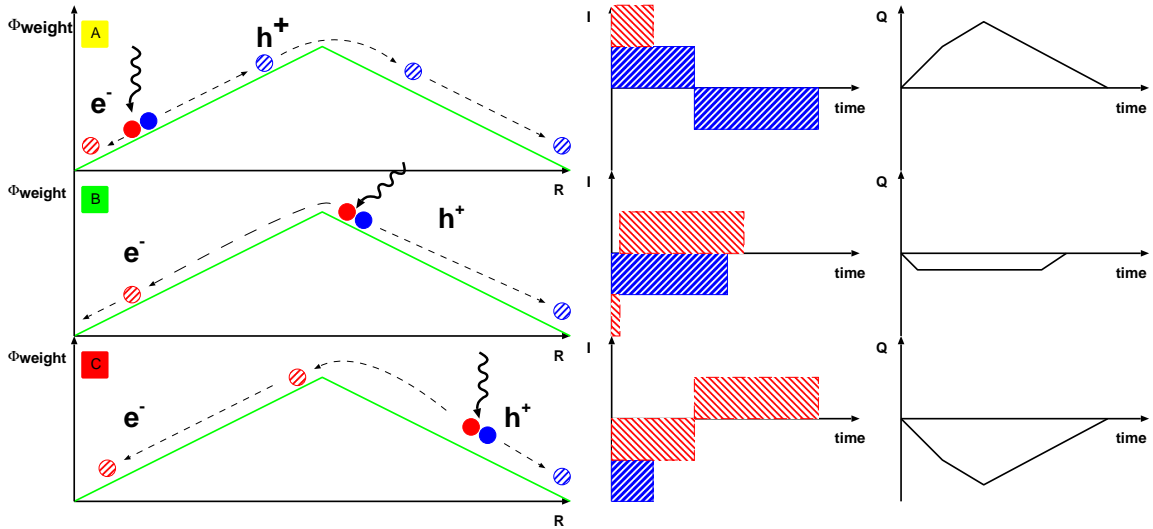


**Figure 2.21:** Explanation of the origin of the polarity of the mirror charge signal. The radial distribution of the weighting potential of a spectator electrode, i.e. a neighbor of the MI segment, is schematically shown together with the location of the charge carrier production (holes are blue and electrons are red). The detector current is given by the weighting field  $E_w(r) = \frac{d\Phi_w}{dr}$ , the moving charge  $q$  and its velocity  $v = \frac{dr}{dt}$ . The charge and direction of movement differs for the charge carriers. The slope of the weighting potential also changes its sign in the middle between the contacts. The resulting current ( $i = -qE_w v$ ) and charge signals are shown on the right. It should be noted that the maximum amplitude of the mirror charge signal depends on the distance from the maximum of the weighting potential and not on the radial distance  $r$  from the core contact. It should also be noted that the weighting potential (see segment weighting potential at  $z=0$  mm in figure 2.1) and the drift path (see trajectories 5 and 6 in figure 2.1) in the planar part do not allow a similar simple explanation of the pulse shapes.

### 2.7.2 Angular Position $\varphi$ of the Main Interaction

In contrast to the steepest slope algorithm giving a radial position by analyzing the current signal of the core contact, the angular position information is extracted from the segment signals by analyzing the induced signals on neighboring segments of the segment containing the MI. The sixfold segmentation already allows a coarse determination of the angular position of the MI, given by the segment with the highest energy deposition. This method is detailed in [22].

To illustrate the algorithm used it is best to consider events, where the charge is collected by a single segment only. The net charge of an induced signals has to be zero. An induced signal is seen while the hole and electron charge clouds in the segment are moving towards the outer or inner contacts. In case of the MINIBALL detector, these induced signals are used to determine the angular position of the MI [22]. The shape of the induced signals depends on the position of the (main) interaction in the detector volume, as explained in figure 2.21. The sign of the induced charge depends on whether the current is mainly due to the minority or the majority charge carriers and hence depends on the position of the MI with respect to the maximum of the weighting field.

A single interaction close to the central contact in the coaxial part of the detector will produce a positive mirror charge signal, since in this case the detector current is domi-

nated by the hole contribution. On the other hand, a single interaction close to a segment contact will produce a negative mirror charge signal, because the neighboring segments see an induced signal that decreases until the drifting electron cloud reaches the maximum of the weighting field and after that increases until the electrons have reached the central contact. Midways between the segment and core contact the smallest amplitudes are observed because the electron and hole contribution cancel each other. The maximum of the weighting field can be found at a larger distance from the core close to the hit segment (large intra-segment angle) and at a smaller distance at the opposite side of the neighboring segment (small intra-segment angle). Therefore also combinations where one neighbor has a positive and the other one has a negative induced charge exist if the MI is located midway between the inner and outer electrode.

From the explanations above it is clear that the detailed shape of the induced charge can only be understood with the help of the developed simulation [22]. It is, however, not necessary to analyze the shape in detail, since an angular position information can be determined from the maximum amplitude of the mirror charge signal. The mirror charge amplitudes are determined from the detector signal as shown in panel (a) of figure 2.22. From the calculated weighting fields it is apparent that the maximum of the weighting field decreases with increasing distance from the spectator segment, as show in figure 2.1. If an interaction happens close to the shared segmentation line, the induced charge (assuming a fixed distance from the core) will be larger than if the interaction happens far away from the shared segmentation line. To overcome the radial dependence of the height of the induced charge the ratio the logarithmic ratio of the mirror charge amplitudes is calculated [22]

$$\varphi \propto \log \left( \frac{|q_+|_{\max}}{|q_-|_{\max}} \right) \quad (2.19)$$

$|q_-|_{\max}$  and  $|q_+|_{\max}$  being the maximal absolute values of the height of the induced charge of the neighboring segments. The logarithmic ratio  $\log \left( \frac{|q_+|_{\max}}{|q_-|_{\max}} \right)$  is linearly correlated with the angular position  $\varphi$  of the MI inside the MI segment and is used to determine the position of the MI inside the MINIBALL detector.

In case that charge has also been deposited in the neighboring segments, the induced charge signal is not directly accessible. It was shown previously in [23] that a linear approximation for the segment signals is sufficient and the position resolution decreases only by about a factor of two compared to the single segment events. The induced signal is extracted by subtracting a linear rising signal, starting and ending at the same time as the detector pulses and being of the same height as the corresponding segment signal, from the regarded segment signal. The difference between these measured and the generated signals is assumed to be due to induced currents. The process is schematically shown in figure 2.23.

The extracted mirror charge amplitude is then subjected to the same analysis as a segment without energy deposition. With this scheme it is possible to apply PSA to all events.

### 2.7.3 Depth of the Main Interaction

In case of an irradiation of the MINIBALL detector perpendicular to the detector surface, the knowledge of the interaction depth is not required since the radial and angular

positions  $r$  and  $\varphi$  of the (first) interaction do not differ from the radial and angular position of the point where the  $\gamma$ -ray enters the detector, the entry position  $r(z(0))$ ,  $\varphi(z(0))$ . Therefore, the positions from the PSA can be referenced directly to the front face of the detector ( $z(0)$ ) as shown in figure 2.24.

In case of a non-perpendicular irradiation of a single MINIBALL detector the entry position and the interaction position do also differ in radial and angular direction. If the PSA position is referenced to the **Average Interaction Depth (AID)**  $z(E)$  the entry position of the  $\gamma$ -ray can be reconstructed with the knowledge of the source position as shown in figure 2.24.

As the MINIBALL detector lacks an additional segmentation in depth, an experimental determination of the depth of the MI impossible. Since the knowledge of the interaction depth is necessary for the reconstruction of the interaction position, it has to be inserted into in the analysis as an external parameter. The average interaction depth (AID) of the first  $\langle z_{\text{FI}}(E_\gamma) \rangle$  and main  $\langle z_{\text{MI}}(E_\gamma) \rangle$  interaction was determined for various energies in a Monte-Carlo simulation [22]. These values are then put into a look-up table that is used to determine the average interaction depth. The AID determines the effective distance between detector and target, e.g. at an energy of 1 MeV the effective target-detector distance increases from 10.5 cm to about 13.5 cm.

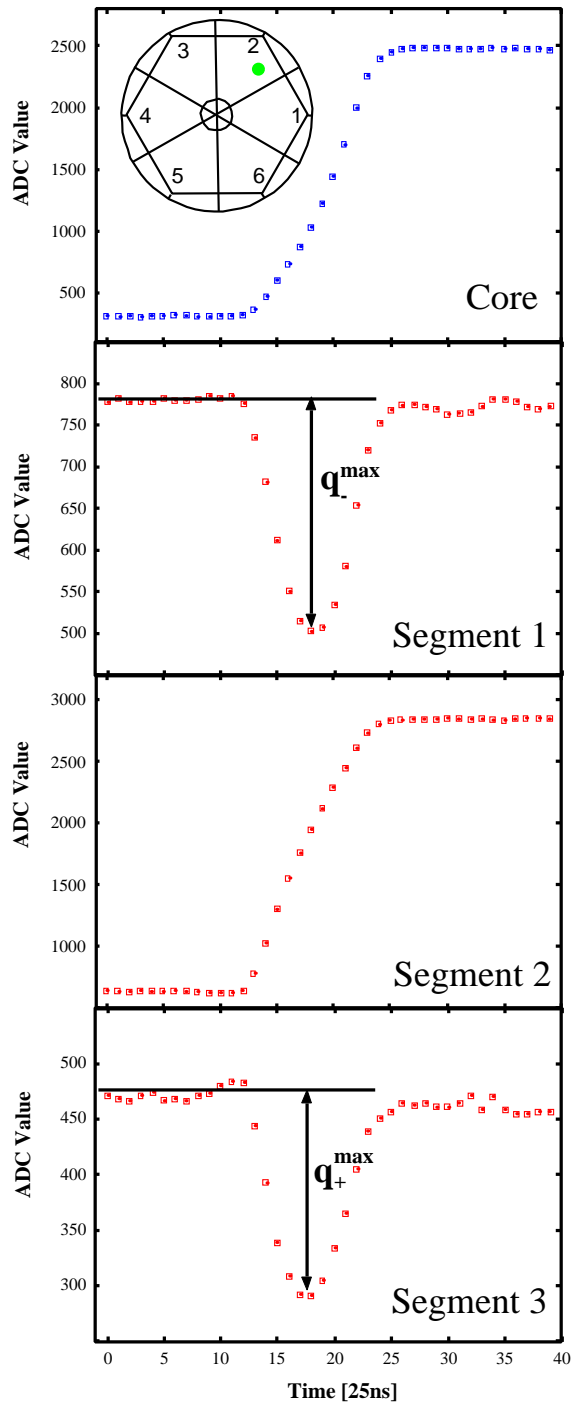


**Figure 2.22:** The plot shows the extraction of the mirror charge amplitude from segment signal showing induced signals only, a one segment event (OSE). The maximum mirror charge amplitude  $|q^{\max}|$  can be determined directly from the detector waveform. The mirror charge amplitude varies between 5 and 15 % of the net charge signal amplitude.

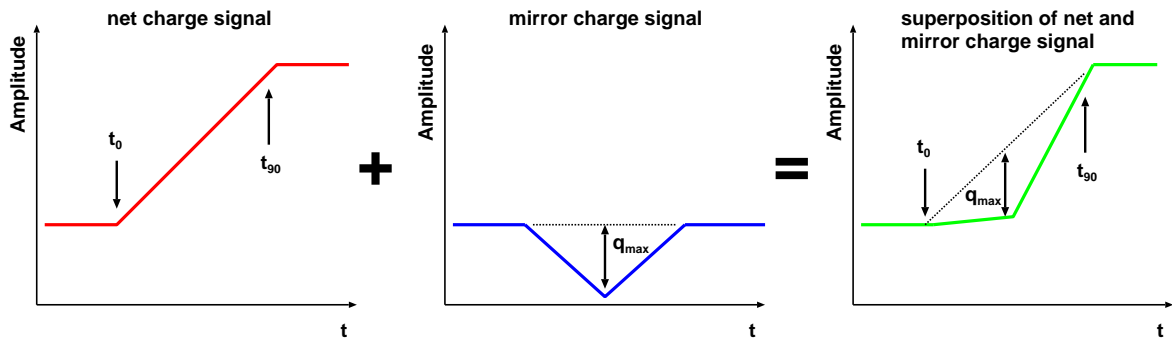


**Figure 2.23:** The extraction of the mirror charge amplitude for the case of a neighboring segment event (NSE) is schematically shown. The net charge signal is approximated by a linear signal using the timing parameters  $t_0$  and  $t_{90}$  determined from the core contact. The difference between the approximation and the segment signal gives the mirror charge signal.

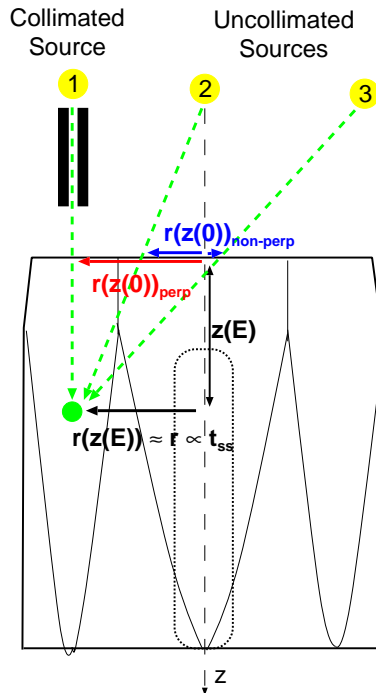


**Figure 2.24:** Perpendicular and non-perpendicular irradiation geometries for the MINIBALL detector for a single interaction event, i.e. first and main interaction do coincide. Three different locations for  $\gamma$ -ray sources are indicated (1, 2 and 3). In case of a perpendicular irradiation using a collimated source (1) the entry position does not differ from the (first) interaction position in radial and angular direction. In case of a non-perpendicular irradiation (2 and 3), the entry and (first) interaction positions differ also in radial and angular direction and therefore the positions obtained from the pulse shape analysis have to be referenced to the AID  $z(E)$ .

## Chapter 3

# Realtime Pulse Shape Analysis using the XIA DGF-4C CAMAC module

”Great spirits often meet violent opposition with mediocre minds” - Albert Einstein

In this chapter the realtime pulse shape analysis used for the MINIBALL project, using a digital electronics, namely the DGF-4C module from XIA [13], will be presented. The purpose of the realtime PSA<sup>1</sup> is a further reduction in data that has to be read out and stored. Instead of the detector waveform (40 parameters per channel at 40 MHz sampling rate) only a handy set of parameters (five per channel) is needed to characterize a  $\gamma$  event in the MINIBALL detector. A measurement with a collimated  $\gamma$ -ray source was performed to verify (and identify) the relationship between the detector pulse shape, i.e. the PSA parameters, and the collimator position.

### 3.1 The realtime pulse shape analysis program

The developed realtime PSA program, the user DSP code, was implemented for the digital signal processor of the DGF-4C module. The details of the implementation are compiled in appendix C.

As the FPGA on the DGF-4C board (RTPU) performs the first level processing, delivering  $\gamma$ -energy  $E_\gamma$  and time of arrival TS, the DSP collects this information event-by-event in its internal buffers together with the waveform of the leading edge of the detector pulse, read from a separate FIFO, to perform further pulse shape analysis and ballistic deficit compensation.

The developed program performs the MINIBALL PSA algorithms presented in section 2.7, delivering the steepest slope time  $t_{ss}$  and the maximum height of the induced charge  $q_{max}$ . In addition, the L-EBC and the Q-EBC timing algorithms (implemented using a LE method to determine the initial sample index  $M$ ) can be performed giving the signal start time  $t_0^{EBC}$  and replacing the FT algorithm parameter  $t_0^{FT}$  determined by the

---

<sup>1</sup>Consider preprocessing as first level processing, PSA as second level processing.

DGF-4C module<sup>2</sup>. Additionally, the rise time  $t_{90}$ , the sample index of  $q_{max}$ , i.e.  $t(q_{max})$  and a parameter specifying the PSA module reporting an error condition are supplied<sup>3</sup>.

The segment containing the MI is identified by searching for the segment with the highest energy deposition. Using the PSA parameters, the drift time of the electrons is given by  $t_{cc}^{e-} = t_{ss}^{true} = t_{ss}^{dsp} - t_0^{dsp}$  with  $t_{ss}^{dsp}$  the steepest slope parameter of the central contact from which the start time of the detector pulse  $t_0$  has to be subtracted to obtain the time-to-steepest-slope  $t_{ss}^{true}$ . The radial interaction position is then given by  $r = a \cdot t_{cc} + b$ , with  $a$  and  $b$  the calibration parameters that have to be determined. The angular interaction position (the segment angle) is given by  $\varphi = c \cdot \log\left(\frac{|q_+|}{|q_-|}\right) + d$ , with  $c$  and  $d$  the calibration parameters and  $|q_+|$  and  $|q_-|$  the absolute value of the maximum mirror charge amplitude in the neighboring segments of the MI segment<sup>4</sup>. Together with the AID  $z(E_\gamma)$ , the position of the (main) interaction inside the detector has been determined by PSA. With the knowledge of the source position the entry position at the detector front face can be calculated.

In order to verify the functionality of the user DSP code, implementing the MINIBALL PSA algorithms, the response of a MINIBALL cluster detector to a collimated  $\gamma$ -ray source was determined.

## 3.2 Experimental setup

The scanning apparatus that was used for the measurement was developed previously and the specification can be found in [25]. The distance between the source and the detector front face was designed to be 10.5 cm and the resolution should be less than  $\Delta\theta = 4^\circ$  [23] (the simulated beam spot size of 6 mm at a distance of 150 mm corresponds to  $\Delta\theta = 2.3^\circ$  [25]). To facilitate an irradiation similar to the experimental conditions a gimbal mounted setup was chosen. The collimator was manufactured from Hevimet, which resulted in a compact system. The data acquisition was fully automated, scanning every position for 20 minutes using a  $^{60}\text{Co}$  source with an activity of 3.7 MBq. For the analysis only FEE with an energy of 1332.5 keV were considered. The distance between the measurement positions was chosen to be 5 mm in radial direction and  $5^\circ$  in angular direction at the detector front face ( $z(0)$ ). A lead shield, which was already available [56], was used, reducing the background rate to 80 Hz. The collimator can be moved with the help of two step motors controlled by a PC via the RS232 interface. All software for the setup of the measurement were previously developed in our group [25]. The setup is shown in figure 3.1, showing the correlation between the channels of the DGF and segments of the detector. Figure 3.2 explains the geometry of the irradiation of segment 1 of detector C, which is an unfavorable geometry to demonstrate the position resolution of the detector but allows the validation of the developed DSP code and an investigation of the limits of PSA.

<sup>2</sup>Depending on the configuration of the DGF-4C and the user DSP code, it is possible the readout  $t_0^{FT}$ ,  $t_0^{EBC}$ , as well as the PSA information  $t_{ss}$  and  $q_{max}$ .  $E_\gamma$  and TS are always read out.

<sup>3</sup>The "Bad Energy" information was no longer available to the user DSP code with release 3.0 of the DGF-4C firmware.

<sup>4</sup> $q_+$  and  $q_-$  denote the neighboring segments of the MI segment with the higher and lower index (e.g. segment 2 and 6 in case of segment 1 as the MI segment), respectively.

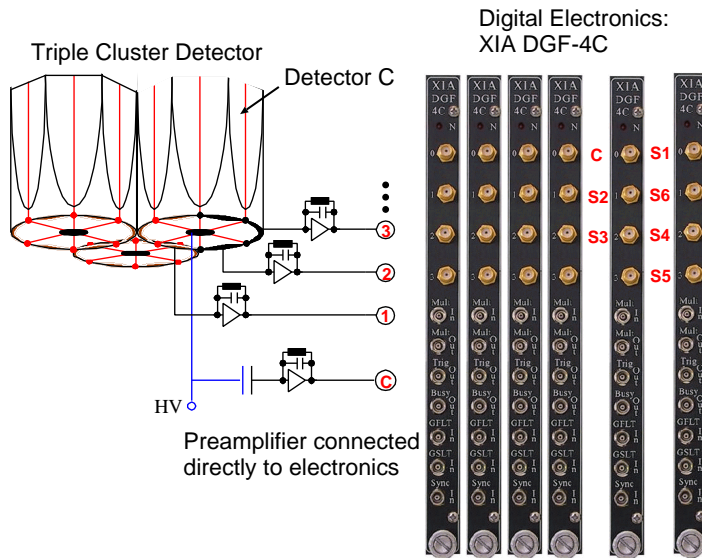


**Figure 3.1:** Setup for the collimator measurement. Six DGF modules are necessary to readout the triple cluster detector. The detector preamplifiers are directly connected to the digital electronics. The segment numbers of detector C are shown together with their corresponding DGF channels.

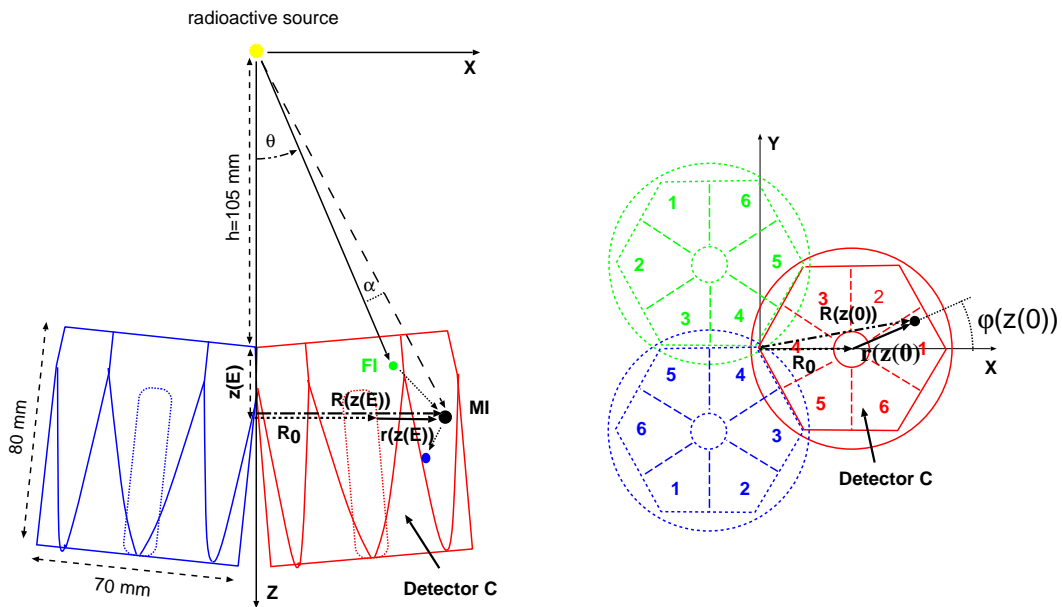


**Figure 3.2:** Geometry of the collimator measurement setup. The collimator is not shown, only the radioactive source 105 mm away from the detector. The definition of the segment radius  $r$  and the segment angle  $\varphi$  is shown in the XY plot. Capital letters denote the cluster coordinate system, while lower case letters denote the detector coordinate system.

### 3.3 Tests with measured waveforms

The response of segment 1 of detector C was measured in order to test the developed user DSP code and therefore also waveforms of  $1 \mu\text{s}$  length were recorded together with the on board PSA results, which allows an (even event-by-event) comparison of the PSA results obtained with the user DSP code with the results obtained with the offline analysis to confirm the functionality of the realtime PSA. Afterwards, the position resolution will be investigated.

#### 3.3.1 Comparison with offline analysis

A basic test of the functionality of the user DSP code is the comparison of the PSA information obtained by the DSP and the offline analysis.

The steepest slope  $t_{\text{ss}}$  and  $\log\left(\frac{|q_+|}{|q_-|}\right)$  spectra (including only full-energy events of 1.3 MeV as explained in section 2.1) are shown in figure 3.3 and 3.4 respectively. In figure 3.3 the drift time of the charge carriers is plotted for four radial ( $r(z(0)) = 5, 10, 15, 20$  mm) and three angular positions ( $\varphi(z(0)) = -20^\circ, 0^\circ, 20^\circ$ ) of the collimator (the collimator positions are referenced to the front face of segment 1). For the offline analysis the start time  $t_0$  was obtained with the NSR<sup>5</sup> algorithm [57] implemented previously [25] and the second derivative was obtained with a three point formula, whereas the user DSP code uses the L-EBC algorithm to determine the start time  $t_0$ . The difference between the drift times obtained with the user DSP code and the offline analysis is small and well below the variation coming from the interaction process itself. The position resolution is therefore not limited by the (fractional) fixed point computation of the DSP code, but the physics of the  $\gamma$  interaction process. It is important to note that the response of the detector is not symmetric with respect to the centerline of the segment, i.e. the  $\varphi(z(0)) = 0^\circ$  irradiation position.

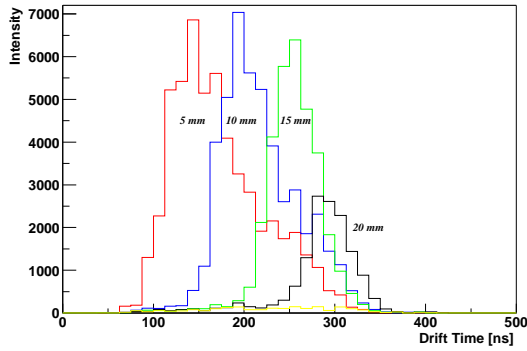
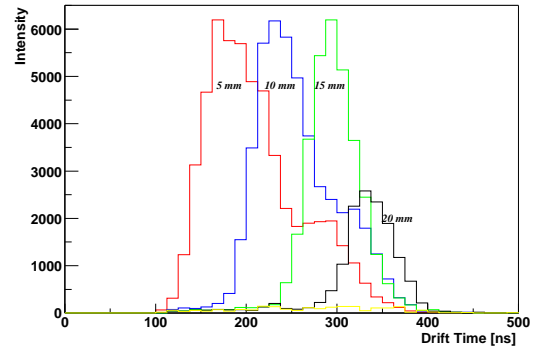
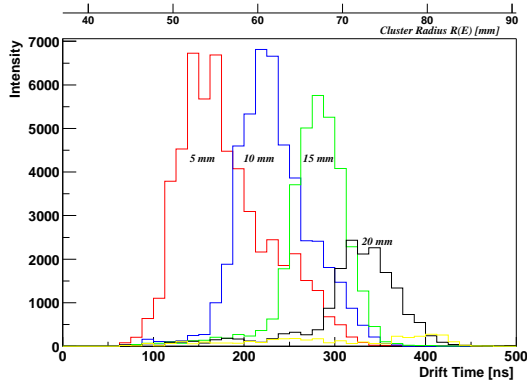
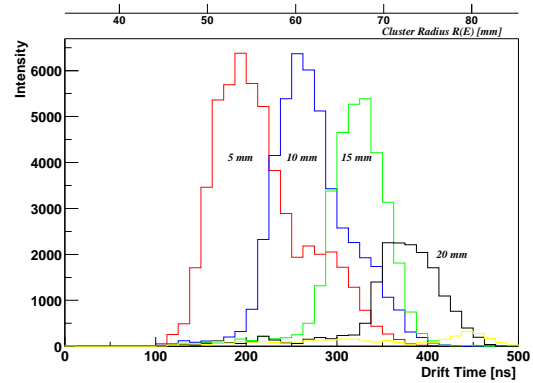
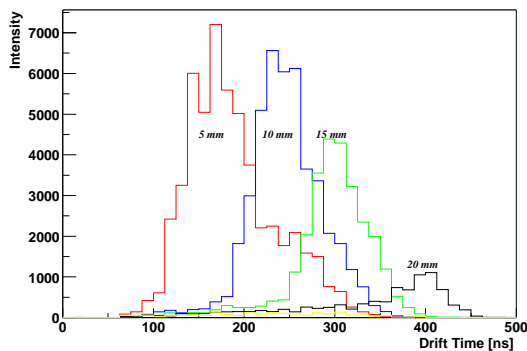
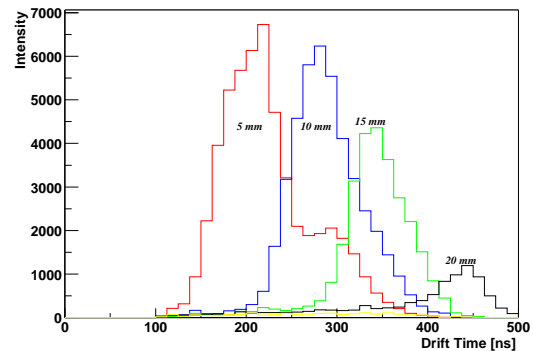
In figure 3.4 the  $\log\left(\frac{|q_+|}{|q_-|}\right)$  spectra are plotted for three different radial positions of the collimator ( $r(z(0)) = 5, 10$  and  $15$  mm). Again, the results of the user DSP code are shown in the left column whereas the offline analysis is shown in the right column. The angular resolution improves with increasing radius, which is due to two effects. Assuming that the position resolution is a (volume) pixel (voxel) of constant size (also determined by the spot size of the collimated  $\gamma$ -ray beam, i.e. the design of the collimator) it is obvious that the arc length resolution is (almost) constant [22]. In addition, the physical properties of the weighting field lead to a decrease in angular position resolution<sup>6</sup> in the middle between inner and outer contact due to variations in mirror charge amplitude as explained in figure 2.21. It can be concluded that any difference between the DSP and offline analysis is negligible compared to the position resolution that can be obtained, especially at small radii.

More insights can be gained by analyzing the implementation in detail. The main difference between offline and DSP pulse shape analysis comes from the fact that the DGF-4C module has only four channels and therefore a single MINIBALL detector has to be read out by two DGF modules with no possibility to exchange data. The algorithm to extract the mirror charge signal from segments featuring a superposition of mirror

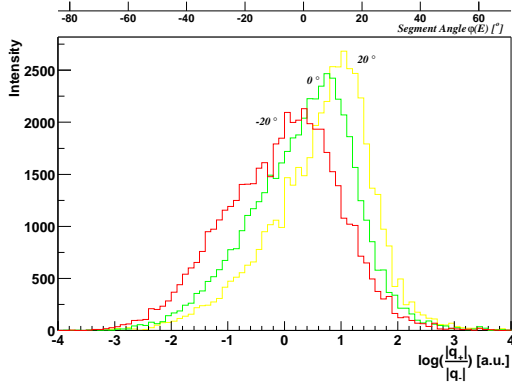
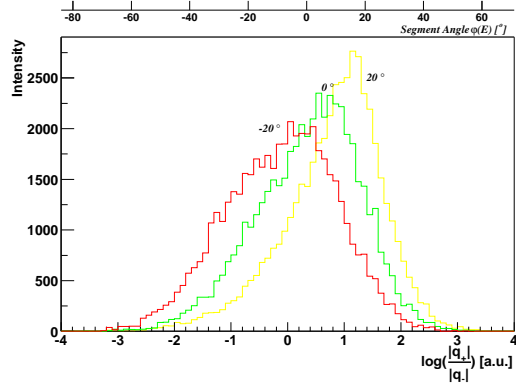
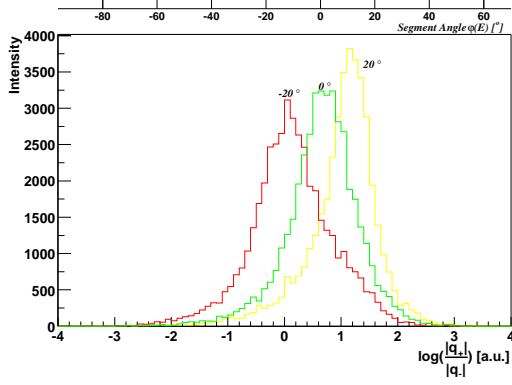
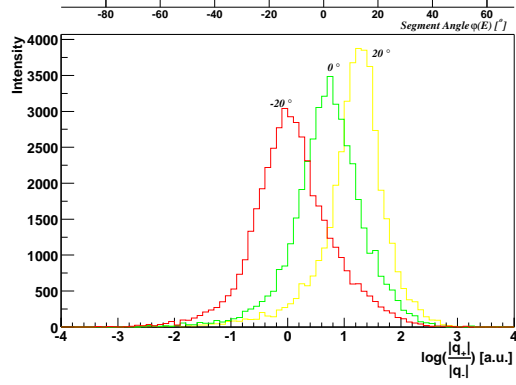
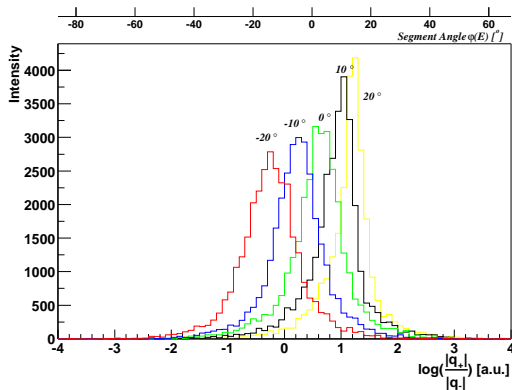
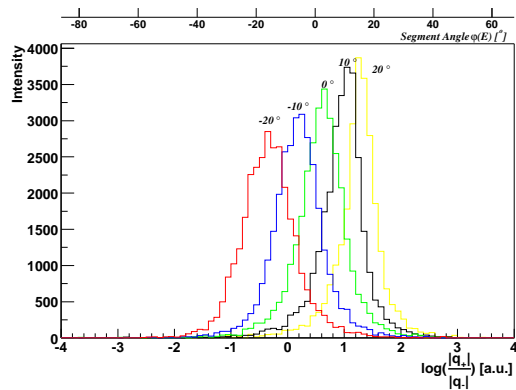
---

<sup>5</sup>Normalized Step Response

<sup>6</sup>In [54] an angular position resolution of  $4^\circ, 8^\circ$  and  $2^\circ$  was obtained for radial interaction positions between 4 and 16 mm, between 16 and 26 mm and between 26 and 32 mm in the coaxial part of the detector having an inner and outer diameter of 8 and 65 mm, respectively.

(a) Realtime analysis for  $\varphi(z(0)) = -20^\circ$  irradiation(b) Offline analysis for  $\varphi(z(0)) = -20^\circ$  irradiation(c) Realtime analysis for  $\varphi(z(0)) = 0^\circ$  irradiation(d) Offline analysis for  $\varphi(z(0)) = 0^\circ$  irradiation(e) Realtime analysis for  $\varphi(z(0)) = 20^\circ$  irradiation(f) Offline analysis for  $\varphi(z(0)) = 20^\circ$  irradiation

**Figure 3.3:** Steepest slope spectra for three different angular position of the collimator, irradiating segment 1 of detector. Only FEE of 1.3 MeV energy were considered for the analysis. Four different radial positions of the collimator are shown in each histogram. The left column shows the spectra obtained with the on board analysis using the user DSP code and the right column shows the spectra obtained by analyzing the waveform data offline with a PC. Contrary to the expectation, the response of the detector is not symmetric with respect to the middle of the segment, i.e the response for the  $\varphi(z(0)) = -20^\circ$  and the  $\varphi(z(0)) = 20^\circ$  positions are different.

(a) Realtime analysis for  $r(z(0)) = 5$  mm irradiation(b) Offline analysis for  $r(z(0)) = 5$  mm irradiation(c) Realtime analysis for  $r(z(0)) = 10$  mm irradiation(d) Offline analysis for  $r(z(0)) = 10$  mm irradiation(e) Realtime analysis for  $r(z(0)) = 15$  mm irradiation(f) Offline analysis for  $r(z(0)) = 15$  mm irradiation

**Figure 3.4:** Comparison of the realtime with the offline analysis for the  $\log\left(\frac{q+1}{|q-1|}\right)$  algorithm for FEE of 1.3 MeV at three different radial position  $r(z(0))$  in segment 1 of detector C. By comparing the left with the right row, it is obvious that the user DSP code achieves similar results to the offline analysis. By comparing the spectra in one column only, the conclusion is that the angular resolution improves with increasing radial position ( $r \cdot \Delta\varphi$  is almost constant [22]).

and a net charge signal uses the timing information ( $t_0$  and  $t_{90}$ ) of the central contact<sup>7</sup> (see figure 2.23). These parameters are not available to the user DSP code running on the second DGF. A possible solution is to split the core channel and connect it to channel zero of both DGFs.

The user DSP code can therefore be operated in different modes, controlled by DSP parameters. If the core channel is connected to channel zero of the DGF-4C the user DSP code can use the  $t_0$  and  $t_{90}$  parameters of this channel to extract the mirror charge signal. If the core channel is not connected to the DGF-4C, the user DSP code can use either average values of  $t_0$  and  $t_{90}$ , which have to be set by the user before taking data, or the user DSP code uses the `PSAOFFSET` parameter, which determines  $t_0$  and the `PSALENGTH` parameter, giving  $t_{90}$ . The average values can be obtained by histogramming the  $t_0$  and  $t_{90}$  parameters for the core channel.

The main differences between the DSP code and the offline analysis are therefore

- The realtime analysis distinguishes between segments signals showing induced signals only and segments showing a superpositions of mirror and net charge signals based on a user defined energy threshold parameter. The offline analysis applies the same algorithm in both cases.
- The amplitude of the net charge signal is determined from the DGF energy parameter in case of the realtime analysis and from the trace in case of the offline analysis.
- The timing parameters of the core are used for the extraction of the induced charge in case of the offline analysis. The realtime analysis uses average values for  $t_0$  and  $t_{90}$ .
- The start time  $t_0$  is determined using the L-EBC algorithm in case of the realtime analysis and the NSR algorithm in case of the offline analysis.
- The  $t_{90}$  time is determined by the position the signal reaches 95% of its final amplitude in case of the offline analysis and 93.75 % in case of the realtime analysis (The DSP code supports only fractions of 87.5 and 93.75% in close proximity to the 90 % fraction).
- In both cases the slope of the net charge signal is given by  $\frac{\text{ADC}(t_{90}) - \text{ADC}(t_0)}{t_{90} - t_0}$ .

In any case, it is mandatory to ensure that the core channel stops the FIFOs of all segment/slave channels since only in this case the core and segment waveforms are correlated.

For the actual measurement the user DSP code was setup differently.  $t_0$  was obtained from channel zero of the first and the second DGF-4C module, connected to the central contact and segment 1<sup>8</sup>, respectively. However, due to a bug in the DSP code, the  $t_{90}$  time was determined from the waveform of the corresponding channel.

In figure 3.5 the  $\log\left(\frac{|q+1|}{|q-1|}\right)$  spectra are shown for events where only one segment was hit, a **One Segment Event (OSE)**, in the left column and for events where more than one segment was hit, a **Neighboring Segment Event (NSE)**, in the right column. Again, the radial position of the collimator is  $r(z(0)) = 5, 10$  and  $15$  mm from the top to

<sup>7</sup>The reason is that the signals from the central contact are not affected by mirror charge signals.

<sup>8</sup>The segment the collimator was pointing to.

the bottom. As expected, there is no difference between the  $\log\left(\frac{|q_+|}{|q_-|}\right)$  spectra obtained by using the realtime and offline analysis in case of no net charge, i.e. mirror signals only (left column). However, in the presence of a net charge signal (right column), the spectra do differ. The separation between the peaks is decreased compared to the offline analysis, especially for a collimator position of  $r(z(0)) = 15$  mm, and one can expect that the angular position resolution is reduced too.

In order to find the reason for the decrease in position resolution in case of a NSE event, the PSA parameters  $t_0$  and  $t_{90}$  were investigated. Figure 3.6 shows that the determination of the rise time is more accurate by using the core signal than the segment signal. This is obvious since the actual energy deposition in a segment can be very small.

The consequences of this measurement for the position resolution of MINIBALL at REX-ISOLDE can only be estimated since the user DSP code of the second DGF module is configured to use constant average values for  $t_0$  and  $t_{90}$ , despite the rise time variations of large HPGe detectors, due to different radial interaction positions as obvious from figure 3.6.

However, in the overall spectra plotted in figure 3.4 the decrease in angular position resolution is not visible, i.e. most of the events are not affected by the DSP code approximations. Therefore, the further analysis does not distinguish between OSE and NSE events.

The PSA implementation uses various parameters that have to be adjusted for best performance. However, an instant feedback of the actual position resolution is impossible and therefore the parameters have to be adjusted without the knowledge of the actual position resolution. Furthermore, the position resolution might depend on environmental conditions and the detector setup, e.g. operating voltage and noise levels, which would make it difficult to identify small improvements. It is therefore recommended for future evaluations to download a benchmark data set onto the DGF-4C and run an in-situ simulation of the user DSP code with subsequent comparison to the expectations. The benchmark data allows to separate improvements due to a different implementation or a different parameter setting from accidental changes position resolution. The DGF-4C supports such an operation.

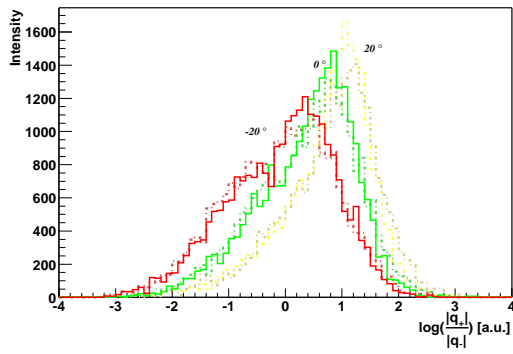
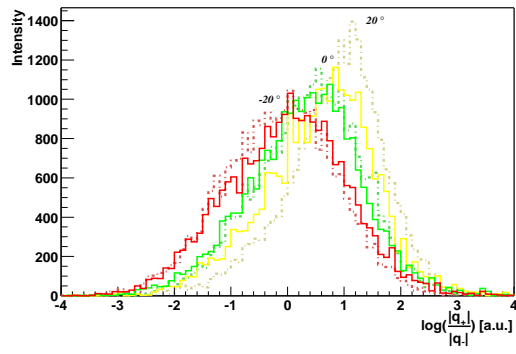
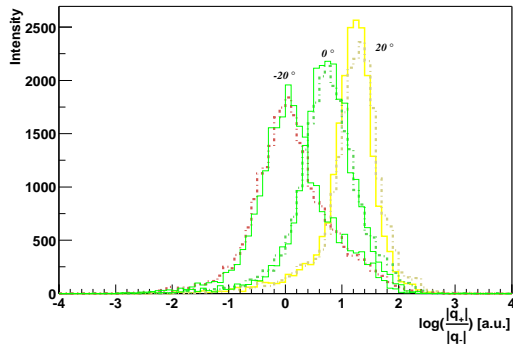
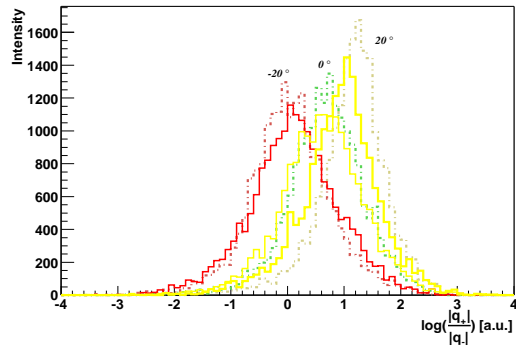
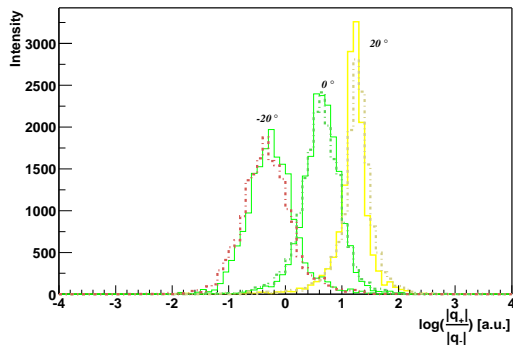
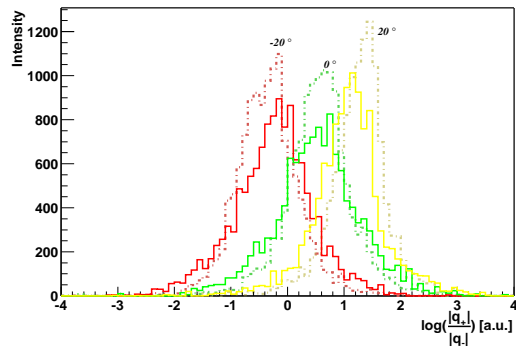
### 3.3.2 Investigation of the $r$ and $\varphi$ determination

The comparison of realtime and offline analysis was presented in the previous section. Additional properties of the detector response will be presented next.

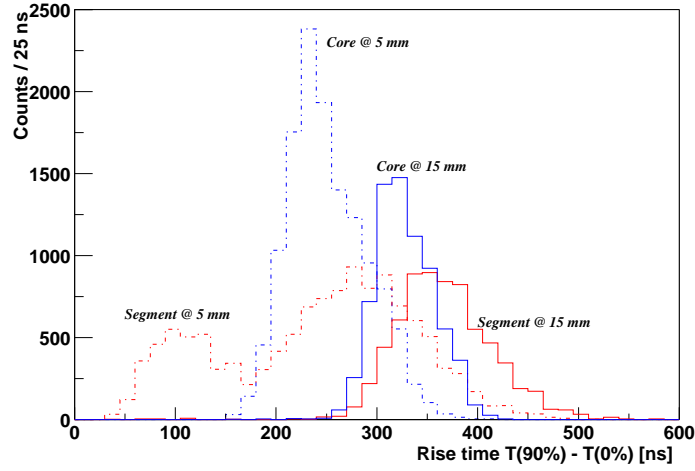
An unordinary feature of the spectra in figure 3.4 at  $r(z(0)) = 10$  and 15 mm is that the peak from the  $\varphi(z(0)) = 20^\circ$  irradiation is narrower compared to the  $\varphi(z(0)) = -20^\circ$  peak. The reason was an incorrect setup of the DGF-4C offset DAC parameter. The maximum negative amplitude that can be measured with the DGF-4C is limited by the ADC offset, which is controlled via the offset DAC of the DGF module.

Figure 3.7 shows the maximum amplitude of the induced charge in the neighboring segments for three different collimator positions of  $r(z(0)) = 5, 10$  and 15 mm (at the detector front face) from top to bottom and  $\varphi(z(0)) = -20^\circ, 0^\circ$  and  $20^\circ$  from left to right. The amplitudes of the mirror charge signals increase with increasing radial position apart from the relative change in amplitude which depends on the angular interaction position. For the  $r(z(0)) = 15$  mm,  $\varphi(z(0)) = 20^\circ$  position of the collimator the amplitude cannot be determined because the amplitude is outside the ADC range.

Figure 3.8 shows the distribution of the ADC offsets in front of the leading edge,

(a) OSEs for  $r(z(0)) = 5$  mm irradiation(b) NSEs for  $r(z(0)) = 5$  mm irradiation(c) OSEs for  $r(z(0)) = 10$  mm irradiation(d) NSEs for  $r(z(0)) = 10$  mm irradiation(e) OSEs for  $r(z(0)) = 15$  mm irradiation(f) NSEs for  $r(z(0)) = 15$  mm irradiation

**Figure 3.5:** Confirmation of the validity of the approximation made by the user DSP code if the timing information  $t_0$  of the core channel is not available. Only FEE events with an energy deposition of 1.3 MeV were analyzed and, in addition, separate spectra for One Segment Events (OSE) and Neighboring Segment Events (NSE) were generated. The approximation is used for segments which feature a superposition of a mirror and a net charge signal. The corresponding  $\log\left(\frac{|q_+|}{|q_-|}\right)$  spectra are shown in the right column, whereas the spectra for the neighboring segments which show induced signals only are shown in the left column. The results for the user DSP code are plotted with solid lines, whereas a dashed line is used for the offline analysis. The results for the user DSP code and the offline analysis differ in presence of a net charge signal, which shows that the approximation cannot achieve the performance of the offline analysis in this case. This is explained in figure 3.6 and a possible solution is mentioned in the main text.

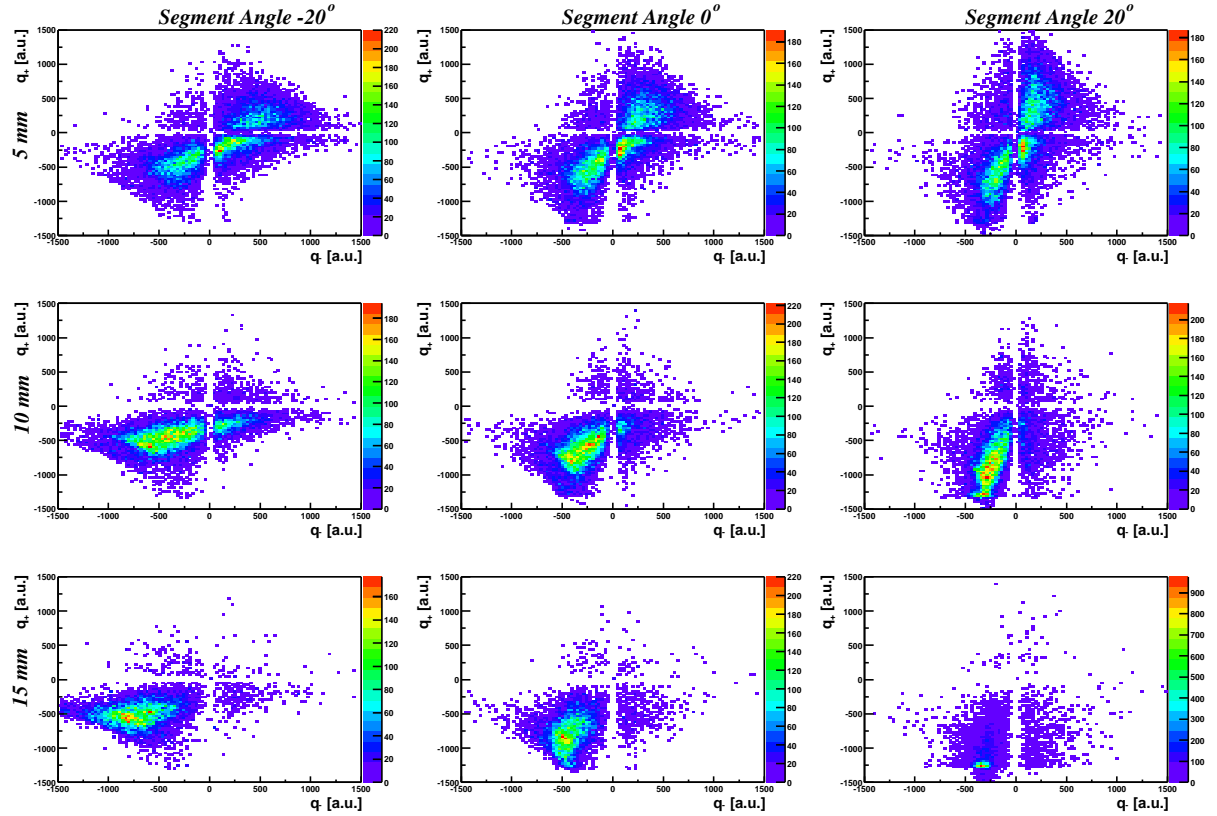


**Figure 3.6:** Risetime  $t_{90} - t_0$  of the detector determined by using the core signal and by using the segment signal for  $t_{90}$  parameter for FEE of 1.3 MeV. Two radial collimator positions of  $r(z(0)) = 5$  and 15 mm are plotted with dashed dotted and solid lines, respectively. In both cases the collimator was set to an angular position of  $\varphi(z(0)) = 20^\circ$ . It is obvious that the rise time of the detector signal can be determined more accurately from the core signal.

which have been determined offline since these values are only temporary stored in the user DSP code. The ADC offset is centered around an average value 1443 ADC units. The maximum negative mirror charge amplitude is 1430 ADC units, which nicely corresponds to the ADC offset of the corresponding channel. Therefore the ADC offsets, and also the gain, of the DGF-4C have to be setup such that the induced signal can be correctly measured. For the actual measurement the maximum energy range was set to about 3 MeV, i.e. the amplitude of the mirror charge exceeds 20 % of the net charge amplitude.

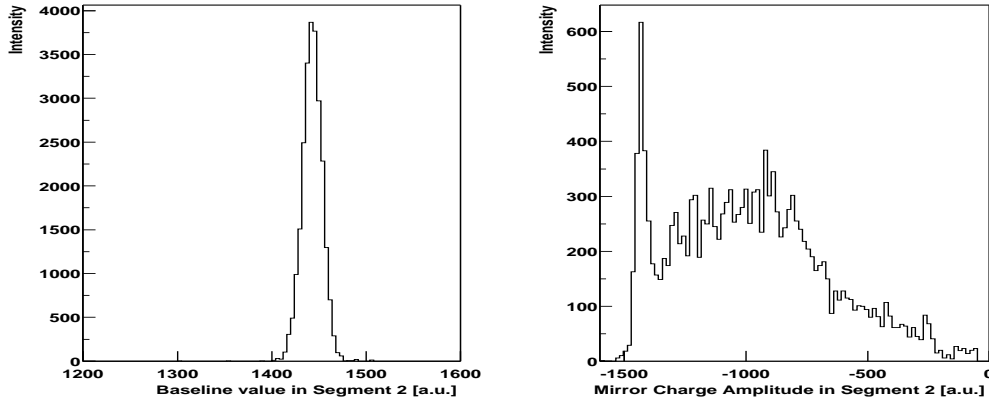
As visible from the calculated potentials in figure 2.1, the weighting field of a segment contact extends over the whole volume of the MINIBALL detector. Therefore, the mirror charge signals are also present in the segments next to the direct neighbor (trajectory 3), the **N**ext to **N**earest **N**eighbor **S**egments (NNNS). However, the capacitive coupling to the sensing electrode is weaker and consequently the amplitude of the induced charge signal is smaller by about a factor of 10 compared to the nearest neighbor segment. In figure 3.9 the negative amplitudes of the mirror charge signals are shown in panel (a) for the NNNS, i.e segment number 3 and 5 since segment 1 is under investigation. The change in relative signal amplitude with changing angular position is obvious and an increase in signal amplitude with increasing radius can be observed. The spectra for the logarithmic ratio  $\log\left(\frac{|q_{++}|}{|q_{--}|}\right)$  are shown below, demonstrating that an angular position resolution can be achieved. However, the angular resolution using the NNNS cannot match that of the  $\log\left(\frac{|q_{+}|}{|q_{-}|}\right)$  algorithm and therefore this method is especially useful if the nearest neighbor signal is not available due to problems with the detector or the electronics. In these cases, an angular resolution can be obtained by using the mirror charge amplitudes from the NNNS, e.g.  $\log\left(\frac{|q_{+}|}{|q_{--}|}\right)$ ,  $\log\left(\frac{|q_{++}|}{|q_{-}|}\right)$  or  $\log\left(\frac{|q_{++}|}{|q_{--}|}\right)$ .

Another feature of the MINIBALL detector signal is the polarity of the mirror charge

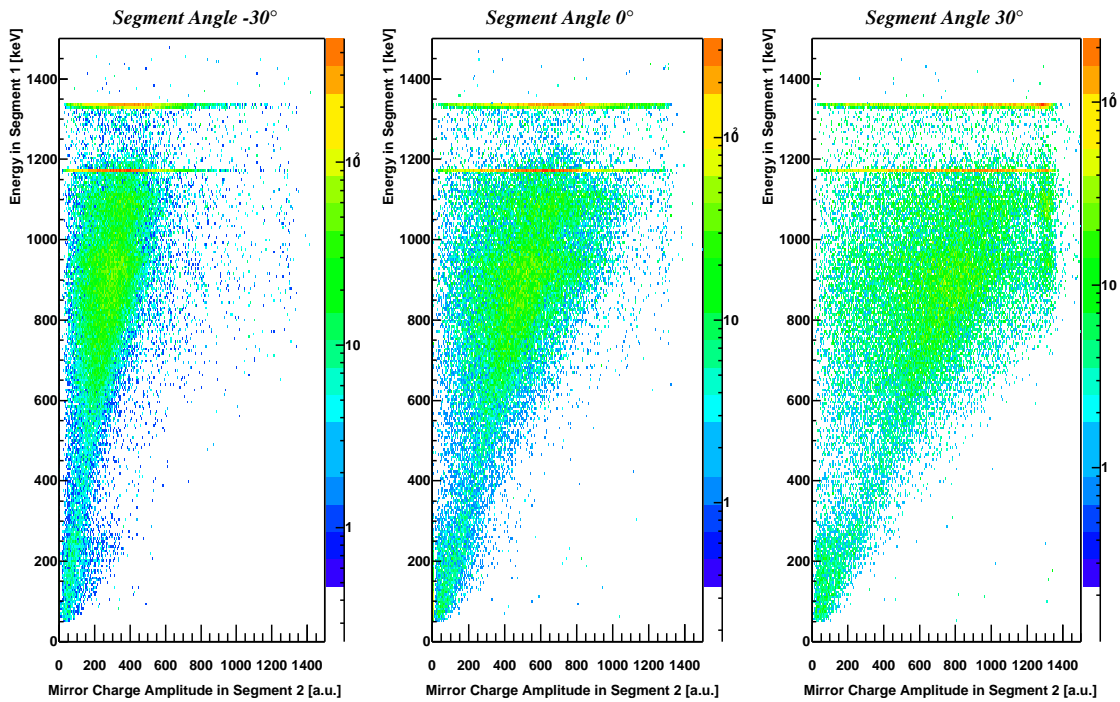


(a) Evolution of the amplitude of the induced charge determined with the offline analysis

**Figure 3.7:** Panel (a) shows the correlation of the amplitude of the induced charge  $q$  for both neighboring segments (6 and 2) of the hit segment (1) on the x and y axis respectively. Three different radial position of  $r(z(0)) = 5, 10,$  and  $15$  mm, as well as three different angular positions of  $\varphi(z(0)) = -20^\circ, 0^\circ$  and  $20^\circ$  are shown. The amplitude of the mirror charge increases with increasing radial position and the relative height of the induced charge changes with the angular position. There is a remarkable difference between the  $\varphi(z(0)) = 20^\circ$  and  $-20^\circ$  irradiation and it seems that the mirror charge amplitude  $q_+$  in segment 2 reaches a limiting value.



(a) ADC offset limits the negative mirror charge amplitude.



(b) Energy dependence of the mirror charge amplitude.

**Figure 3.8:** Influence of the ADC offset on the dynamic range of the induced charge. The distribution of the ADC offset determined offline is shown on the left in (a) and the corresponding maximum negative amplitude of the induced charge is shown on the right. The maximum value equals the ADC offset which proves the assumption that the ADC offset limits the determination of the induced charge amplitude. The evolution of the charge amplitude with deposited charge is shown below in (b), where the energy deposition in the segment 1 is plotted versus the mirror charge amplitude in segment 2 for three different angular collimator positions ( $\varphi(z(0)) = -30^\circ, 0^\circ$  and  $30^\circ$ ) and a radial position of  $r(z(0)) = 10$  mm. Similar to the charge signal, the temporary mirror charge signal amplitude is proportional to the energy deposition, in addition to the dependence on the angular (and radial) interaction position.

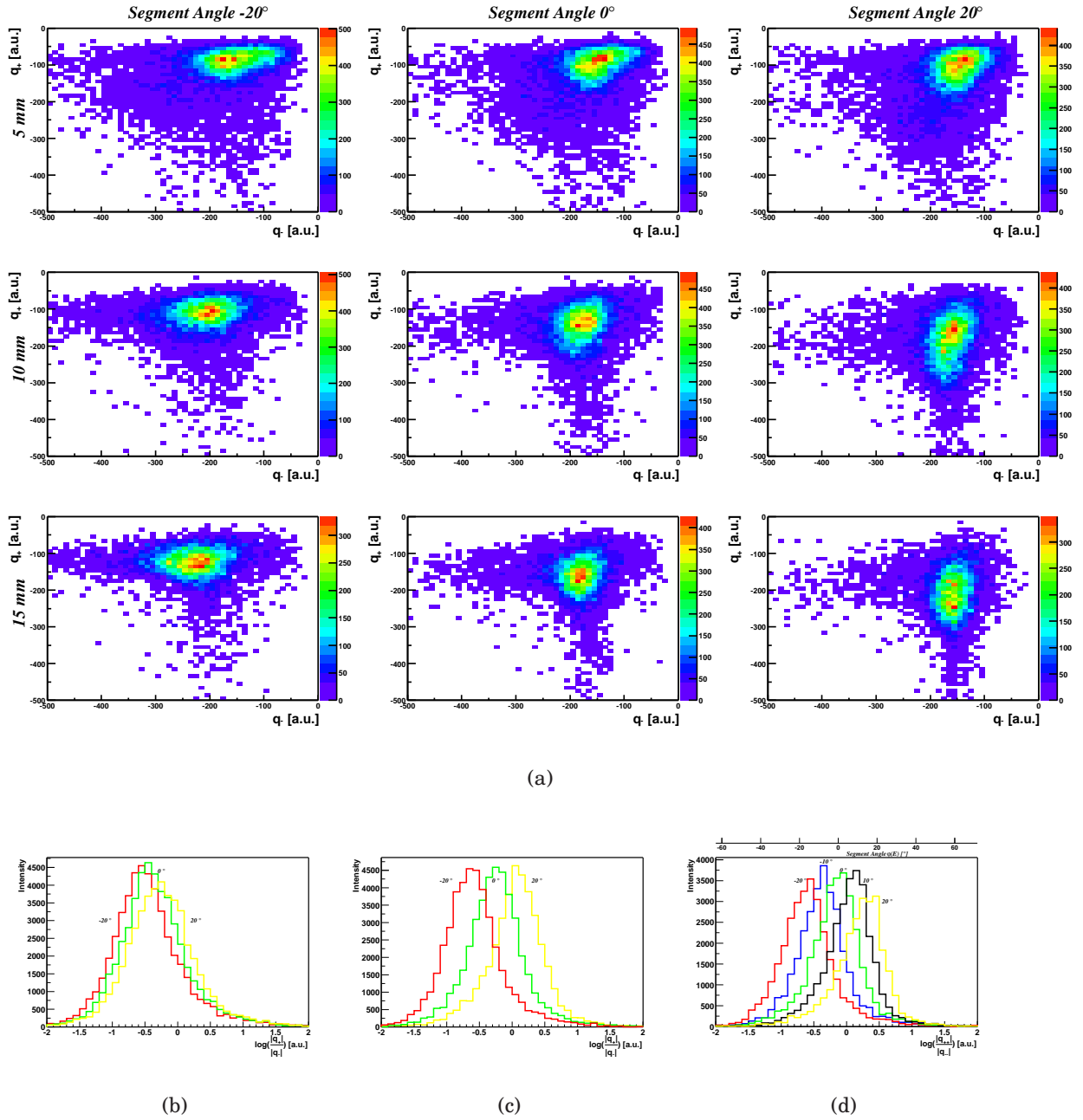


**Figure 3.9:** The evolution of the induced charge amplitudes for different radial and angular positions of the collimator is shown in panel (a), while panels (b), (c) and (d) show the  $\log\left(\frac{|q_x + |q_y||}{|q_x - |q_y||}\right)$  spectra using NNNS. Only the negative amplitudes are shown. The capacitive coupling is smaller compared to the nearest neighbor segments leading to a decrease in amplitude of about a factor of 10, but the amplitudes of the mirror charges are still correlated with the angular position. The radial positions of the collimator are  $r(z(0)) = 5, 10$  and  $15$  mm from top to bottom. Three angular positions of  $\varphi(z(0)) = -20^\circ, 0^\circ, 20^\circ$  are shown from left to right. The decrease in signal amplitude might limit the application to low energy events.

signal. The polarity of the mirror charge signal depends on whether the electron current or the hole current dominates the detector current. This in turn depends mainly on the radial interaction position. The mirror charge amplitude depends only on the amount of charge  $q$  created in the interaction process and the strength of the weighting field  $\Phi_w$   $q_{\text{ind}}(t) = -q \Phi_w(r(t))$  and the corresponding current is given by  $i_{\text{ind}} = -q \vec{E}_w(r(t)) \vec{v}(t)$ .

The origin for the different polarities of the mirror charge is explained in figure 2.21. The positive mirror charges happen close to the central contact, i.e. a small radii, while the negative amplitudes happen at large radii far away from the core contact. Therefore the discrimination between positive and negative amplitudes works as a radial cut as can be seen in the lower part of figure 3.10, where the steepest slope spectrum (shown on the left) is separated into two contributions. More important, the  $\log\left(\frac{|q_+|}{|q_-|}\right)$  spectra differ completely for positive and negative amplitudes, suggesting a separate calibration for the  $\log\left(\frac{|q_+|}{|q_-|}\right)$  spectra in case of positive and negative amplitudes. The reason for this ambiguity is explained in figure 3.11. The user DSP code returns signed numbers which allows the incorporation of this information into the analysis.

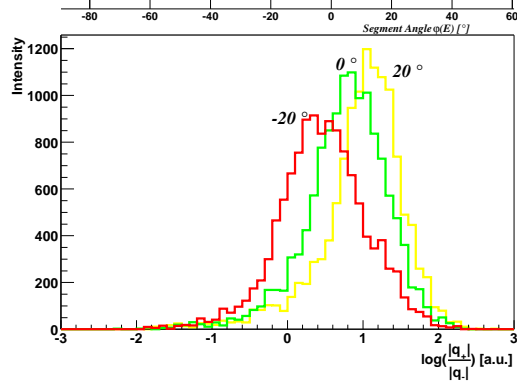
It is important to note the position resolution for a radial collimator position of  $r(z(0)) = 5$  mm is mainly determined by the interaction process and the decrease in the mirror charge amplitude. Despite the large variations in the steepest slope and the  $\log\left(\frac{|q_+|}{|q_-|}\right)$  spectra, all interaction positions are assigned the *same* average interaction depth  $z(E)$ , due the fixed  $\gamma$  energy<sup>9</sup>.

Two additional methods to extract the mirror charge amplitudes from segments showing a superposition of a mirror and net charge signal are presented in figure 3.12 together with the linear approximation which is shown in the leftmost column. In order to compare the validity of the different approximations only NSE events are shown. The  $\log\left(\frac{|q_+|}{|q_-|}\right)$  histograms are plotted for angular collimator positions of  $\varphi(z(0)) = -20^\circ, 0^\circ, 20^\circ$  and the radial positions of  $r(z(0)) = 5, 10$  and 15 mm. In the center column, the mirror charge signal was obtained by subtracting a scaled (segment energy  $E_s$ /core energy  $E_c$ ) core signal from the segment signals. In the rightmost column, the mirror charge signal was obtained by subtracting a scaled (segment energy  $E_s$ /MI segment energy  $E_s^{MI}$ ) MI segment signal from the segment signals, which automatically ensures a zero mirror charge amplitude for the MI segment. From figure 3.12 it can already be concluded that a core signal is not a good approximation for a segment signal. This is due to the fact that the weighting fields of the core and segment contact differ, e.g. the weighting field of the core is strong close to the core contact and weak close to the segment contact, while the inverse is true for a segment contact. The advantage of using the segment signal is the independence of any timing information, i.e. only the waveform and the energy information is needed. However, this method can only be performed offline, due to the fact that pulse shapes cannot be shared between different DGF-4C modules.

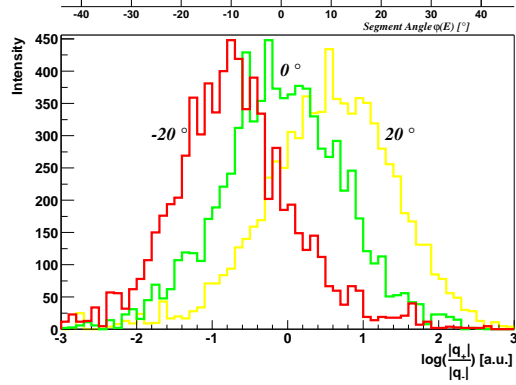
Finally, the sensitivity of segment 1 of detector C to  $\gamma$ -rays of 1.3 MeV is shown in figure 3.13. The sensitivity is not symmetric with respect to the centerline of the detector segment, i.e. the  $\varphi = 0^\circ$  line. The reason for this asymmetry could not unambiguously be identified (possibly a misalignment of the detector-collimator setup or a failure in the

---

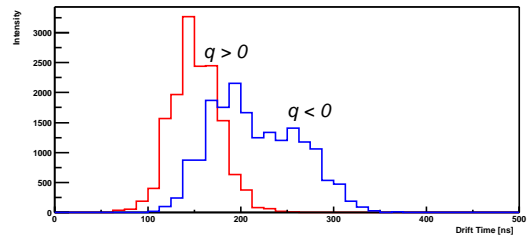
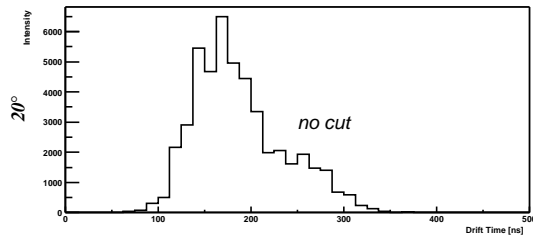
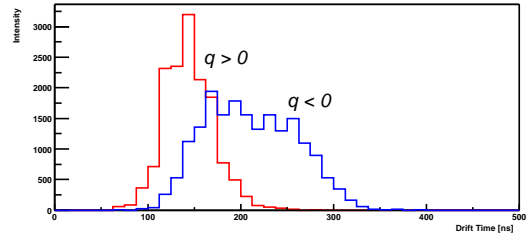
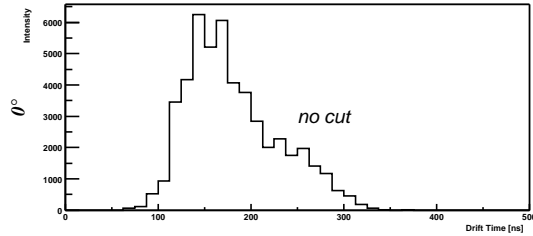
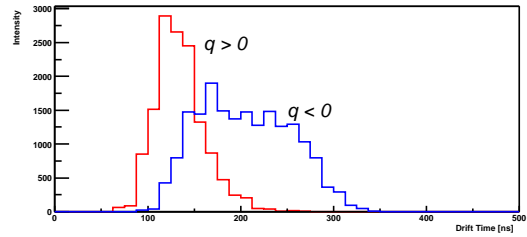
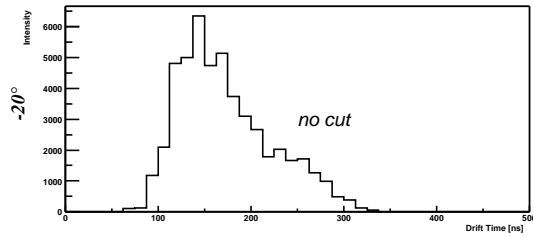
<sup>9</sup>If the depth of the interaction is determined from the energy deposition in the MI segment, the angular position resolution improves, probably due to fact that inter-segment scattering is more likely to happen close to the segment boundaries. The  $t_{ss}$  and  $\log\left(\frac{|q_+|}{|q_-|}\right)$  parameter are not correlated with the energy deposition in segment 1.



(a) Negative mirror charge amplitudes for the  $r(z(0)) = 5$  mm irradiation.



(b) Positive mirror charge amplitudes for the  $r(z(0)) = 5$  mm irradiation.



(c) Steepest slope spectra for angular position of  $\varphi(z(0)) = -20^\circ, 0^\circ$  and  $20^\circ$  for a radial position of  $r(z(0)) = 5$  mm.

**Figure 3.10:** Separation of the steepest slope and  $\log\left(\frac{q+1}{|q-1|}\right)$  spectra using the polarity of the mirror charge amplitude for an irradiation at  $r(z(0)) = 5$  mm. The spectra for the  $\log\left(\frac{q+1}{|q-1|}\right)$  algorithm differ strongly for positive and negative mirror charge amplitudes (other combinations were neglected), suggesting a separate calibration. In the steepest slope spectra a similar separation is obtained, showing two components, one with a high radial confinement for positive amplitudes and one with a large variation of the steepest slope time for negative amplitudes. This is explained in figure 3.11 and therefore the decrease on (radial) position resolution is caused by the irradiation geometry.

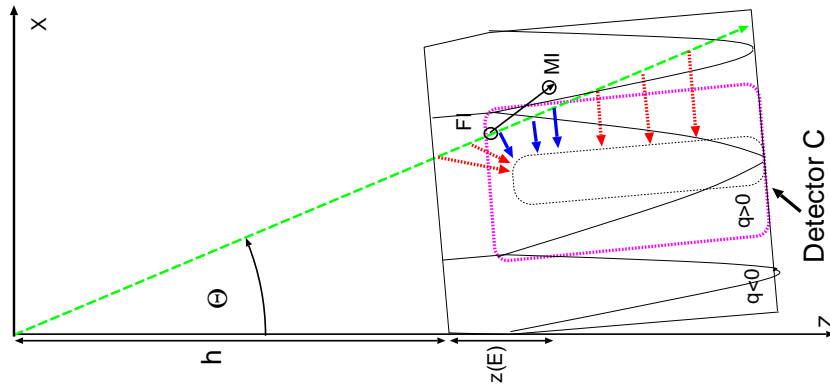


**Figure 3.11:** Explanation how the irradiation causes ambiguities in the steepest slope spectrum. A single MINIBALL detector module is shown together with the irradiation geometry for a radial collimator position of 5 mm. The first interaction FI happens along the initial emission direction of the collimator indicated by the dashed line, whereas the position of the main interaction MI depends on the interaction process. The dotted line highlights separation of the regions, showing mirror charge signals with either positive or negative amplitude. For the given irradiation geometry, the positive polarity signals happen in a very restricted region of the detector, with an almost constant distance to the core contact (indicated by the solid arrows) leading to a sharp steepest slope spectrum, on contrary to the negative mirror charge signals (dotted arrows).

control software responsible for the collimator movement) and in the following it will be assumed that the detector-collimator setup is perfectly aligned.

### 3.3.3 Calibration

Despite the problems in the setup of the digital electronics and the collimator, the calibration factors for the PSA algorithms will be obtained neglecting any non-idealities. As explained before, the segment containing the main interaction (MI) has to be determined by searching for the segment with the highest energy deposition for the reconstruction of the emission angle  $\Theta$ . The radial position information  $r$  is obtained from the signal of the central contact using the steepest slope algorithm, assuming that the MINIBALL detector is a true coaxial detector (assuming only drift paths similar to trajectory 3 in figure 2.1 and neglecting the possibility for drift paths like trajectories 5 and 6 in figure 2.1). The angular position information  $\varphi$  is obtained using the mirror charge amplitudes from the two neighboring segments of the MI segment. The AID depth  $z(E)$  has to be determined for the energy deposited in the detector using the data from the look-up table [22]. Since the position of the source is known it is possible to compare the reconstructed entry position with the entry position determined by the irradiation position of the collimator. The deviation  $\alpha$  can be used to judge the position resolution of the MINIBALL detector. Before the interaction position can be determined, the PSA parameters have to be translated into a position information using the known collimator position. The AID has to be taken into account, since the (first)  $\gamma$ -ray interaction takes place along the direction of the collimator but somewhere inside the detector. If the AID is not taken into account, the calibration information will depend on the  $\gamma$ -ray energy. Therefore, the AID, obtained from detailed simulations, was verified with real data by

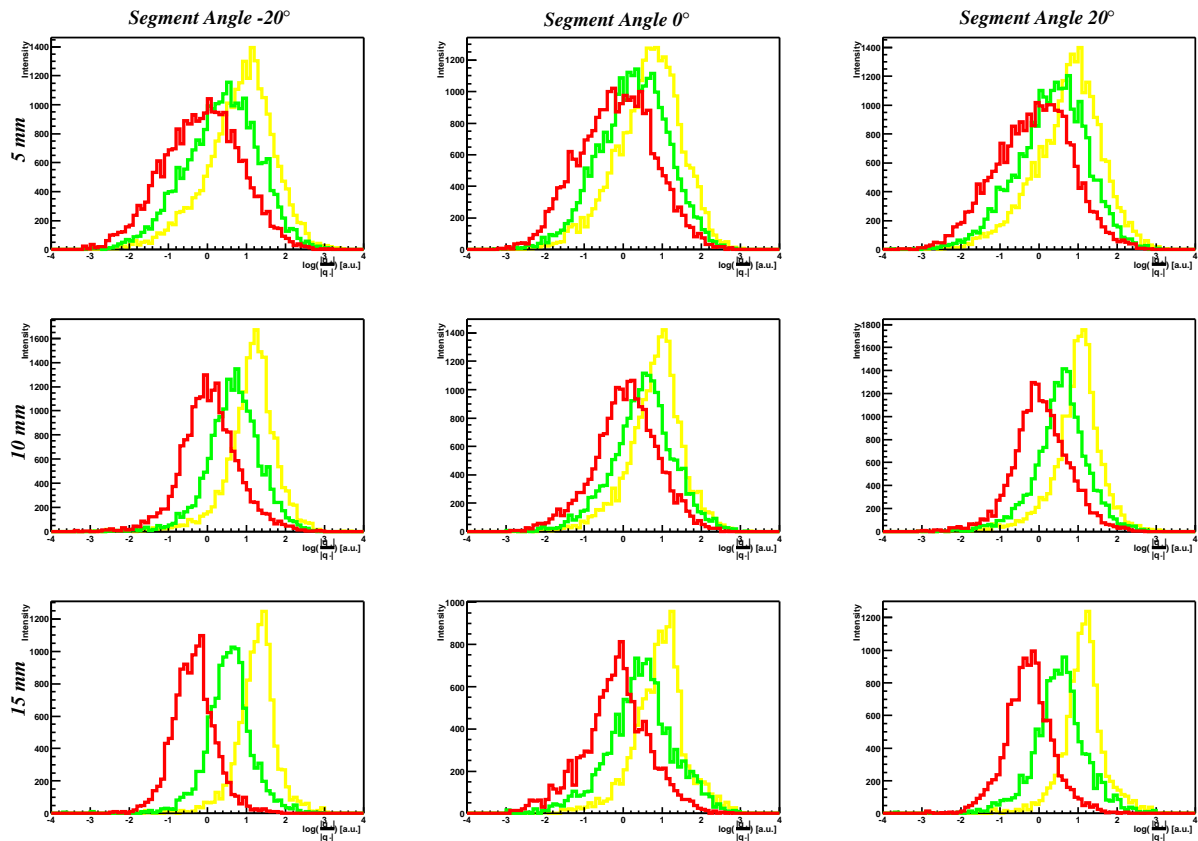


**Figure 3.12:** Spectra of the  $\log\left(\frac{|q_+|}{|q_-|}\right)$  algorithm obtained for three different methods to extract the induced charge from segment signals featuring also a net charge signal. The radial collimator position increases from  $r(z(0)) = 5$  to 10 and 15 mm from the top to the bottom. The spectra for the realtime algorithm are shown in the leftmost column. The central and the rightmost column show the spectra if a scaled core or MI segment signal is subtracted from the segment waveforms.

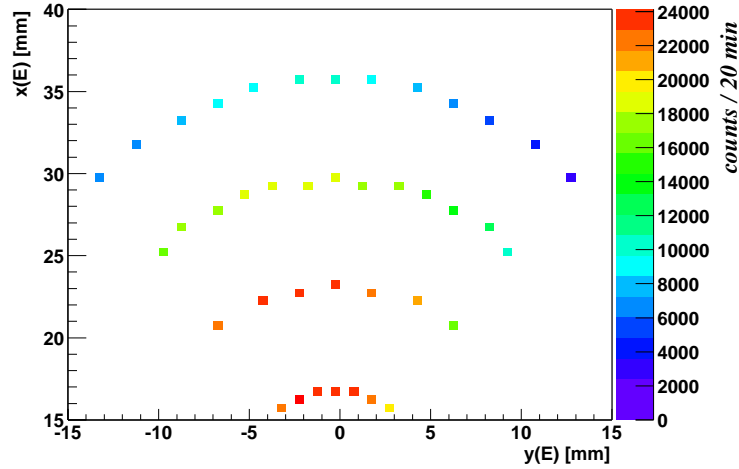


**Figure 3.13:** Sensitivity of segment 1 of detector C obtained by requiring a full energy deposition in the segment. If the detector is correctly centered with respect to the collimator position, then the sensitivity should be symmetric with respect to the centerline of the segment. However, this is not the case and sensitivity differs strongly at the borders of the segment. This could be explained by a misalignment of the detector with respect to the collimator. On the other hand, variations in sensitivity have been observed [54] for the front part of a segmented HPGe detector, which were explained by inferior charge collection properties, depending also on the orientation of the crystallographic axes.

using the radial information obtained from the pulse shape analysis and determining the height of collimator above the interaction position using the following relation between the difference in radial position ( $t_{ss}(r_2) - t_{ss}(r_1)$ ) and the difference in collimator position ( $\tan(\Theta_2) - \tan(\Theta_1)$ )

$$t_{ss}(r_2) - t_{ss}(r_1) = h(E) (\tan(\Theta_2) - \tan(\Theta_1)), \quad (3.1)$$

with  $h(E) = h + z(E)$  and  $\varphi_2 = \varphi_1 = 0$ . The resulting AID is shown in the last column of table 3.1. The estimate shows that the simulated AID is correct, but also that the estimated AID does strongly depend on the steepest slope time. In the following the simulated AID of 27.4 mm will therefore be used to determine the proper calibration factors.

It should be noted that due to the non-perpendicular irradiation, the position resolution of segment 1 will be worse compared to segment 4, where an almost perpendicular irradiation can be achieved. The missing knowledge of the interaction depth cannot be fully compensated, but the usage of the AID minimizes the deviation. As a result, the ambiguity of the steepest slope spectra, as shown in figure 3.10, cannot be removed since only FEE are investigated and the radial interaction position is not correlated with energy deposition in segment 1.

The calibration parameters for the steepest slope algorithm can be obtained from the fact that the radial interaction position in the cluster coordinate system is given by  $R(z(E)) = h(E) \tan(\Theta)$  in case of  $\varphi = 0$ . Using the corresponding data of the collimator measurement, the following linear calibration<sup>10</sup> was obtained for segment 1 of detector

<sup>10</sup>For the offline analysis a calibration of  $R(z(E))$  [mm] =  $0.103 \frac{\text{mm}}{\text{ns}} t_{ss}$  [ns] + 33.8 mm was obtained.

$r(z(0))$ [mm]	$\Theta$ [°]	$t_{ss}$ [ns]	$\Delta t_{ss}$ [ns]	$h(E)$ [ns]	$z(E)$ [mm]
5	22.3	159	-	-	
10	24.6	222	63	1321	$\approx 27$
15	26.8	283	61	1290	$\approx 24$
20	28.9	334	51	1088	$\approx 4$
25	31.0	398	64	1311	$\approx 26$

**Table 3.1:** Estimate of the average interaction depth from the steepest slope time  $t_{ss}$ , using only FEE of  $E_\gamma = 1332.5$  keV in segment 1 of detector C. The first column shows the radial position at the detector front face and the second column shows the corresponding angle  $\Theta$  of the collimator ( $\varphi \equiv 0$ ). The drift velocity was assumed to be 0.1 mm/ns in order to translate ns in mm and the height  $h$  of the collimator above the detector front face was assumed to be 105 mm [25]. The simulated AID is  $z(1332.5\text{keV}) = 27.4$  mm [22], the precise value is not important.

$r(z(0))$ [mm]	$\varphi(z(0))$ [°]	$r(z(E))$ [mm]
5	-20	16.4
5	0	17.2
20	-20	32.7
20	0	36.1

**Table 3.2:** Influence of the AID  $z(E)$  on the true radial interaction position  $r(z(E))$  compared to the radial position at the detector front face  $r(z(0))$  using equation 3.3. The interaction leads to interaction radii that are located about 10 mm further away from the core contact compared to the front face radii. In addition, the angular position of the collimator leads to an increasing difference in radial interaction position with increasing radius. At  $r(z(0)) = 5$  mm the difference between the  $\varphi(z(0)) = 0^\circ$  and the  $\varphi(z(0)) = -20^\circ$  position is only 0.8 mm, while at  $r(z(0)) = 20$  mm the difference is already 3.4 mm.

C

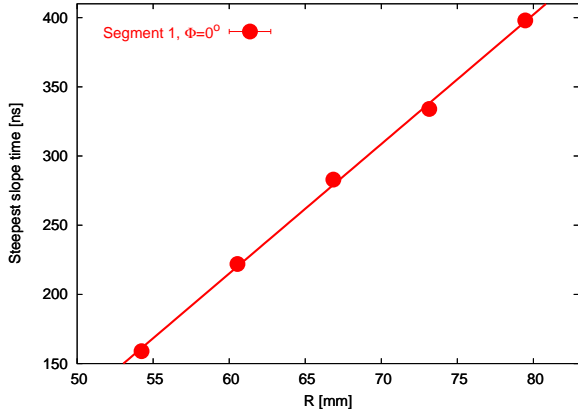
$$R(z(E)) \text{ [mm]} = 0.107 \frac{\text{mm}}{\text{ns}} t_{ss} \text{ [ns]} + 37.0 \text{ mm} = r(z(E)) + R_0. \quad (3.2)$$

In the case of a non-zero segment angle,  $\varphi(z(0)) \neq 0$ , the following equation gives the true radius of the interaction at a depth of  $z(E)$

$$R(z(E)) = \tan(\Theta) \cos(\varphi(z(0))) h(E) - R_0 \quad (3.3)$$

with  $h(E) = 132.4$  mm the effective target-detector distance and  $R_0=37$  mm the (effective) segment offset. Examples of the influence of the interaction depth on the true radial interaction position are given in table 3.2. The worse angular resolution for radial collimator positions of  $r(z(0)) = 5$  mm can now be understood, since the true radial interaction position is about  $r(z(E)) = 17$  mm, i.e. approximately in the center between the inner and outer electrode. In this region, the transition region between positive and negative mirror charge amplitudes, the absolute amplitudes are small compared to the amplitudes at large radii, enhancing the decrease in angular resolution.

In order to obtain the calibration factors for the  $\log\left(\frac{|q_+|}{|q_-|}\right)$  algorithm, a more compli-



(a)

**Figure 3.14:** Linear calibration of the steepest slope algorithm for segment 1 of detector C at the centerline of the segment, i.e.  $\varphi = \Phi = 0$ .

$r(z(0))$ [mm]	$\varphi(z(0))$ [°]	$\varphi(z(E))$ [°]	$r(z(0))$ [mm]	$\varphi(z(0))$ [°]	$\varphi(z(E))$ [°]
5	-30	-11.1	20	-30	-23.0
5	-20	-7.4	20	-20	-14.5
5	-10	-3.7	20	-10	-7.1
5	0	0.	20	0	0

**Table 3.3:** Influence of the interaction depth  $z(E)$  on the true angular interaction position  $\varphi(z(E))$  compared to the angular interaction position  $\varphi(z(0))$  determined by the collimator using equation 3.4.

cated relationship can be used

$$\sin(\varphi(z(E))) = \frac{\tan(\Phi)}{\cos(\Phi) - \frac{R_0}{D}} \quad (3.4)$$

with  $\Phi$  the angle in the XY plane of the collimator and

$$\frac{R_0}{D} = \frac{R_0}{(h + z(E)) \tan(\Theta)}. \quad (3.5)$$

It should be noted that the angular calibration depends on the *offset*  $R_0$  of the radial calibration. With these equations the true angular interaction position  $\varphi(z(E))$  at the AID can be determined. Examples for various segment angles at the detector front face  $\varphi(z(0))$ , which are determined by the collimator, and the resulting true segment angles  $\varphi(z(E))$  at the AID are given in table 3.3. The true angular position of the main interaction  $\varphi(z(E))$  is smaller than that at the detector front face  $\varphi(z(0))$  and approaches the front face position for increasing radius  $r(z(0))$ .

Using the true segment angles  $\varphi(z(E))$  leads to a linear calibration that is almost *independent* of the radial interaction position  $r$  as shown in table 3.4, comparing the calibration for the uncorrected ( $z(0)=0$ ) and for the corrected case ( $z(1332.5\text{keV})$ ). The

$r(z(0))$ [mm]	$\varphi(z(0))$ [°] realtime	$\varphi(z(E))$ [°] realtime	$\varphi(z(E))$ [°] offline
5	$52.7 \cdot \log\left(\frac{ q_+ }{ q_- }\right) - 17.9$	$19.4 \cdot \log\left(\frac{ q_+ }{ q_- }\right) - 6.6$	$16.28 \cdot \log\left(\frac{ q_+ }{ q_- }\right) - 5.54$
10	$37.3 \cdot \log\left(\frac{ q_+ }{ q_- }\right) - 23.7$	$20.8 \cdot \log\left(\frac{ q_+ }{ q_- }\right) - 13.2$	$18.12 \cdot \log\left(\frac{ q_+ }{ q_- }\right) - 11.53$
15	$28.6 \cdot \log\left(\frac{ q_+ }{ q_- }\right) - 13.9$	$19.2 \cdot \log\left(\frac{ q_+ }{ q_- }\right) - 9.3$	$17.17 \cdot \log\left(\frac{ q_+ }{ q_- }\right) - 8.34$
20	$24.6 \cdot \log\left(\frac{ q_+ }{ q_- }\right) - 10.6$	$18.5 \cdot \log\left(\frac{ q_+ }{ q_- }\right) - 7.9$	$16.85 \cdot \log\left(\frac{ q_+ }{ q_- }\right) - 7.22$
5 (-)	-	$25.0 \cdot \log\left(\frac{ q_+ }{ q_- }\right) - 19.3$	-
5 (+)	-	$15.1 \cdot \log\left(\frac{ q_+ }{ q_- }\right) + 1.7$	-
15 NNNS	-	$30.2 \cdot \log\left(\frac{ q_{++} }{ q_{--} }\right) + 5.7$	-
20 NNNS	-	$29.7 \cdot \log\left(\frac{ q_{++} }{ q_{--} }\right) + 3.5$	-

**Table 3.4:** Calibration of the angular position information for segment 1 of detector C, obtained by analyzing FEE of  $E_\gamma = 1.3$  MeV. Different calibration functions were obtained for the realtime and the offline analysis due to the different radial calibration. The segment offset  $R_0$  influences the angular calibration as can be seen from equation 3.4. An efficiency weighted average should be used to calibrate the PSA for the whole segment.

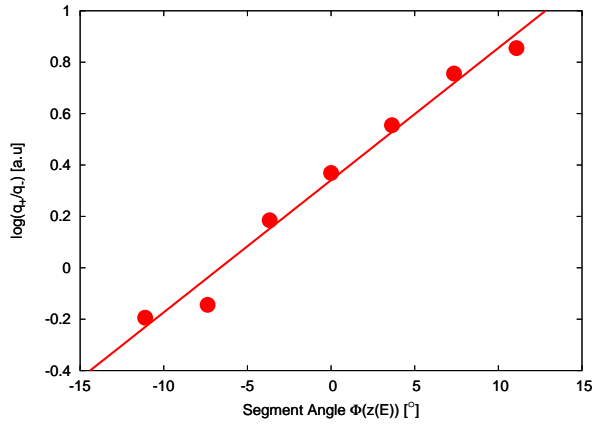
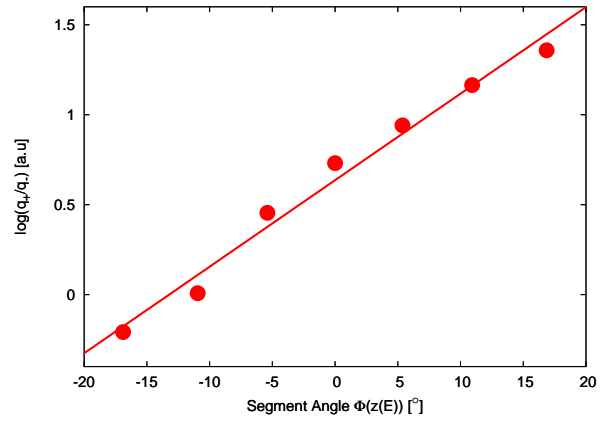
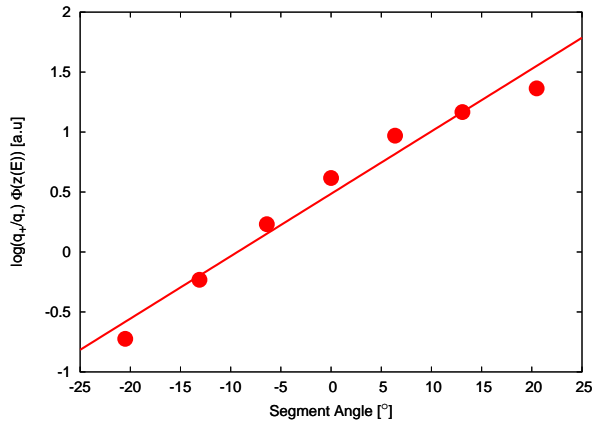
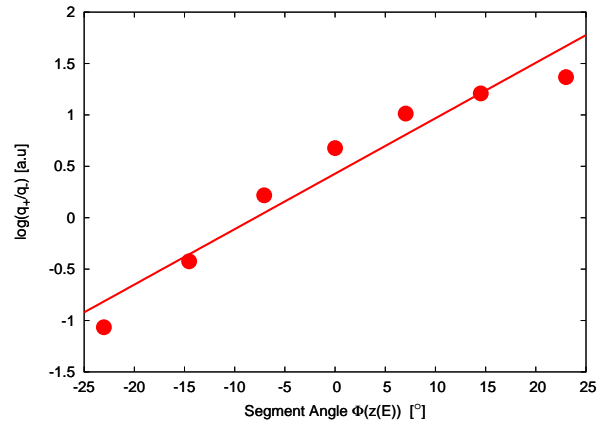
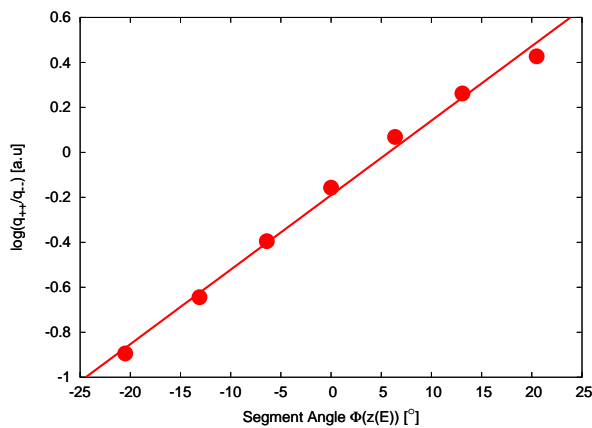
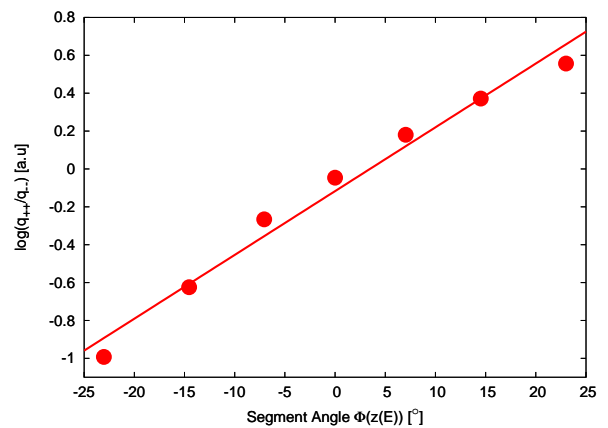
calibration  $\varphi(z(E))$  based on the average interaction depth is nicely independent of the radial interaction position, except for the  $r(z(0)) = 10$  mm irradiation where the offset differs by almost a factor of two from the average.

Furthermore, two additional sets of calibration factors were obtained for the  $r(z(0)) = 5$  mm irradiation, distinguishing positive (+) and negative (-) mirror charge signal polarities. The resulting coefficients are shown in the second part of table 3.4.

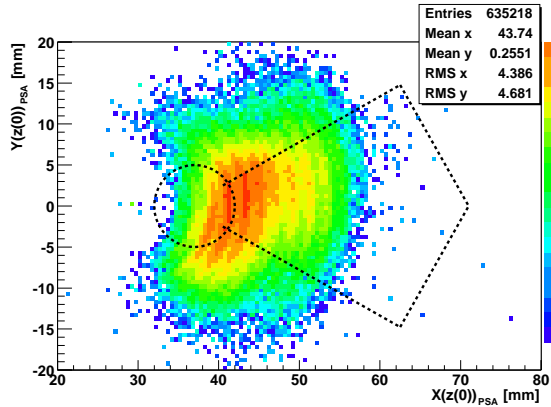
The fits for the angular position information calibration are shown in figure 3.15.

Using the obtained calibration factors, the entry positions at the detector front face can be reconstructed using the known position of the  $^{60}\text{Co}$  source. Figure 3.16 shows the reconstructed interaction positions at the detector front face. For the  $r(z(0)) = 15$  and 20 mm irradiation the cut off of the mirror charge amplitude leads to an incorrect angular position determination, being most prominent for the  $r(z(0)) = 20$  mm irradiation. For this irradiation position, also the reconstructed radial interaction position deviated strongly from the expected position for large segment angles  $\varphi$ . This is an indication that the collimator did not irradiated the expected position at the detector surface. However, improving the position resolution by using a radial calibration depending on the angular interaction position was not considered.

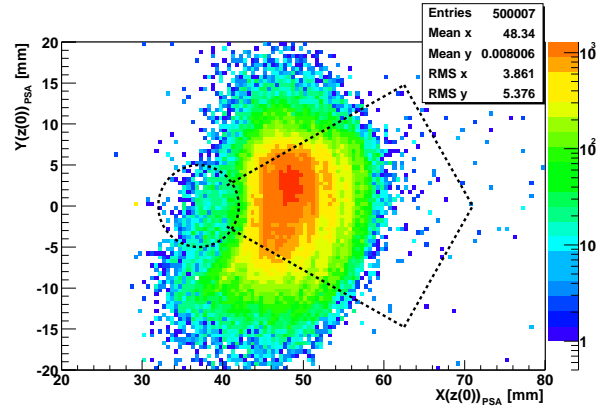
In order to improve the reconstruction of the entry position, the  $\log\left(\frac{|q_{++}|}{|q_{--}|}\right)$  algorithm was evaluated and this is shown in figure 3.17. Since the mirror charge amplitudes ( $q_{++}$ ,  $q_{--}$ ) in the NNNS are smaller by about a factor of 10 compared to the nearest neighbor segment, the true amplitudes can be determined. This leads to the expected "banana"-like shape of the reconstructed interaction positions for the  $r(z(0)) = 15$  mm irradiation. However, the reconstructed interaction positions for the  $r(z(0)) = 20$  mm irradiation are still distorted, due to the asymmetry in the steepest slope spectra, which could be removed by a radial calibration that is dependent on the angular interaction position.

(a)  $r(z(0)) = 5$  mm irradiation(b)  $r(z(0)) = 10$  mm irradiation(c)  $r(z(0)) = 15$  mm irradiation(d)  $r(z(0)) = 20$  mm irradiation(e) NNNS for  $r(z(0)) = 15$  mm irradiation(f) NNNS for  $r(z(0)) = 20$  mm irradiation

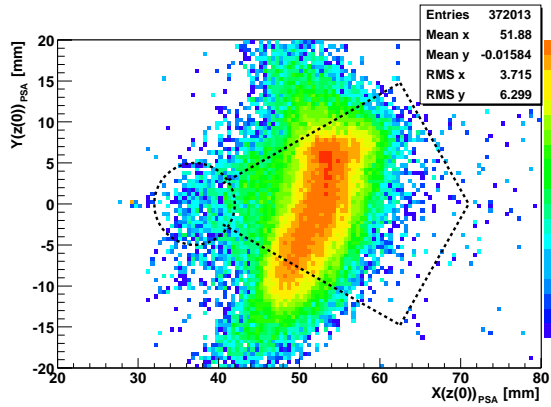
**Figure 3.15:** Angular calibration of the  $\log\left(\frac{q_{+}}{q_{-}}\right)$  algorithm for radii of  $r(z(0)) = 5, 10, 15$  and  $20$  mm. The last two panels show the calibration for the  $\log\left(\frac{q_{++}}{q_{--}}\right)$  algorithm, using the segments next to the nearest neighbor.



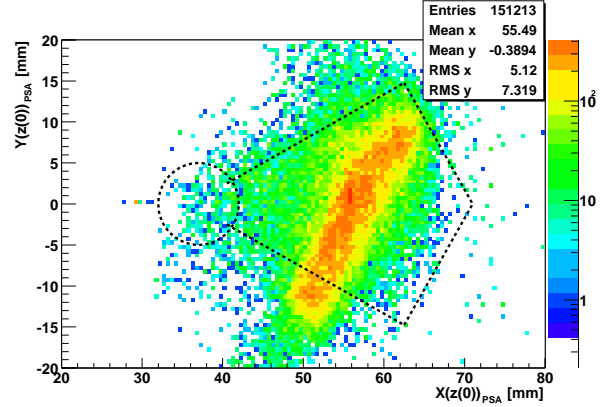
(a) Reconstructed positions for  $r(z(0)) = 5$  mm irradiation



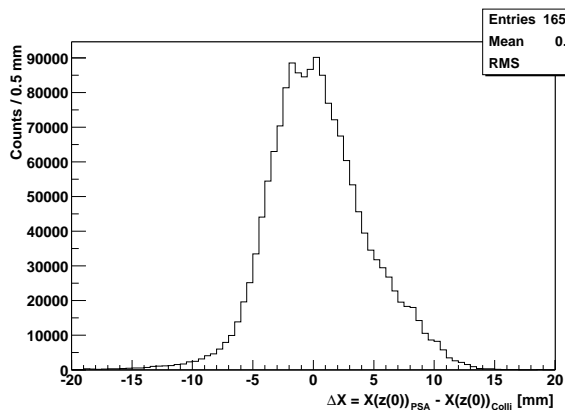
(b) Reconstructed positions for  $r(z(0)) = 10$  mm irradiation



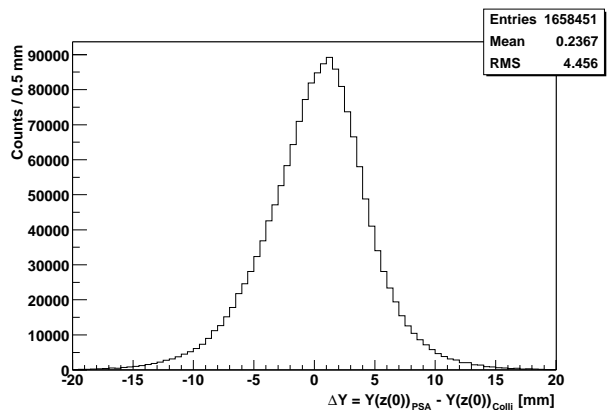
(c) Reconstructed positions for  $r(z(0)) = 15$  mm irradiation



(d) Reconstructed positions for  $r(z(0)) = 20$  mm irradiation



(e) Resolution in X direction



(f) Resolution in Y direction

**Figure 3.16:** Reconstructed interaction positions at the detector front face  $z(0)$  using the user DSP code. The position of the interactions is plotted for radial collimator positions of  $r(z(0)) = 5, 10, 15$  and  $20$  mm. The boundaries of the segment are indicated with dashed lines. The position resolution in x and y direction is shown panel (e) and (f) respectively.

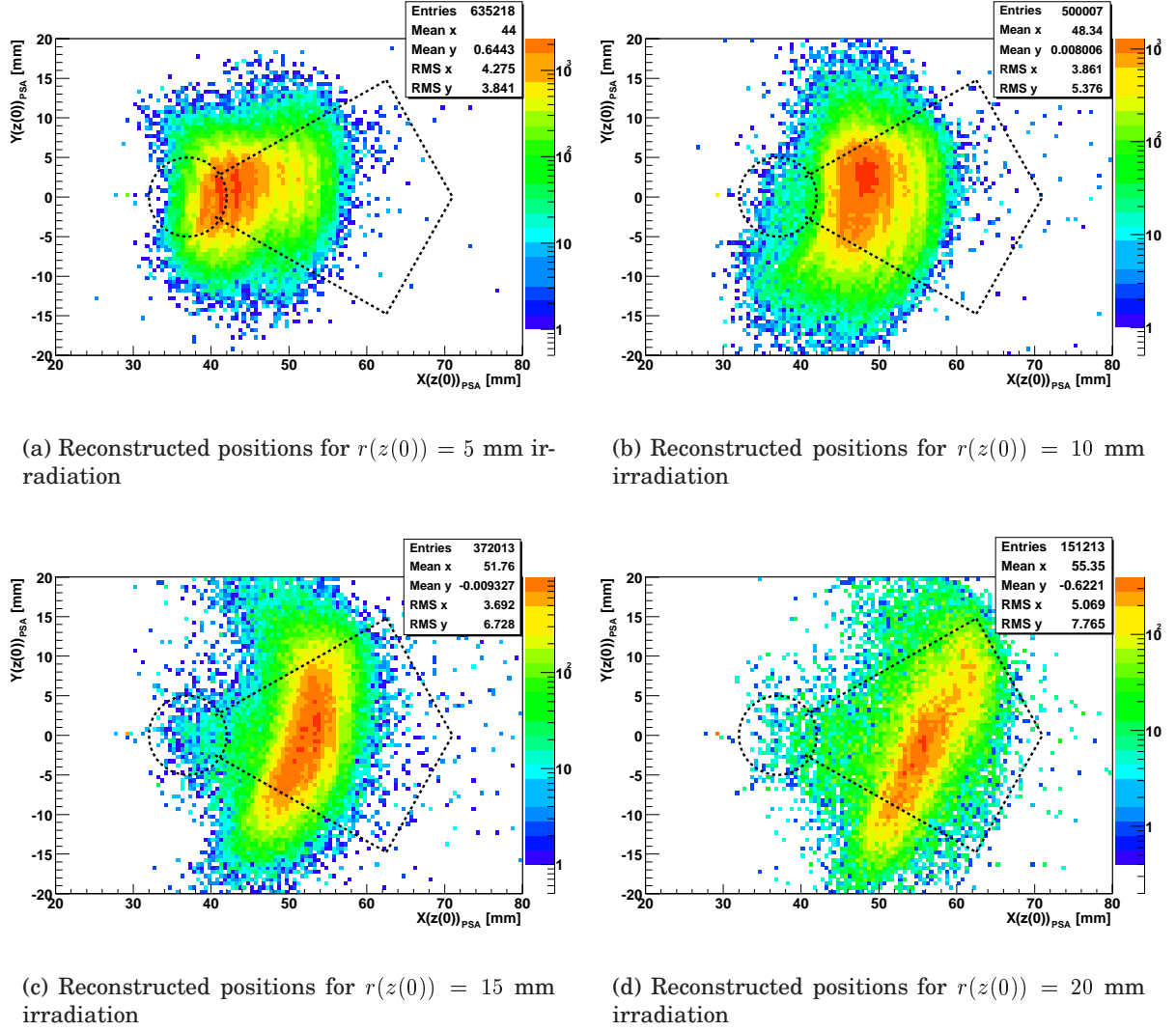


**Figure 3.17:** Panel (a) shows the reconstructed interaction positions at  $z(0)$  for the  $r(z(0)) = 5$  mm irradiation if the polarity of the mirror charge is taken into account. The resolution in x direction improves by 1 mm and the resolution in y direction improves by 2 mm. Panel (b) shows the reconstructed position for normal event processing as in figure 3.16. Panel (c) and (d) show the reconstructed interaction positions at  $z(0)$  using the  $\log\left(\frac{|q_{++}|}{|q_{--}|}\right)$  algorithm. The position resolution in y direction reduces by about 30 %, while the resolution in x direction remains unchanged.

### 3.3.4 Position Resolution

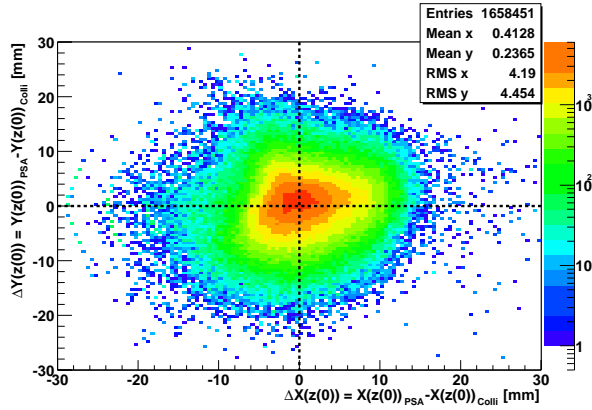
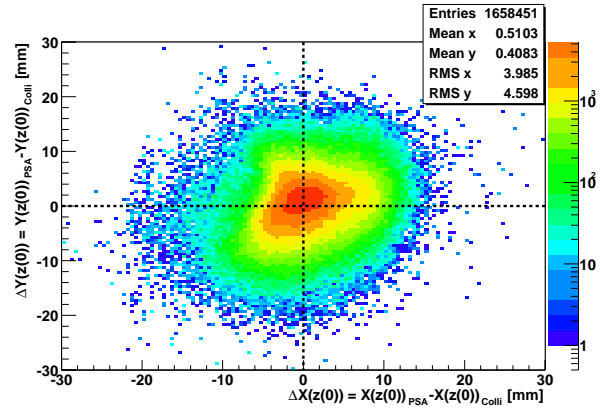
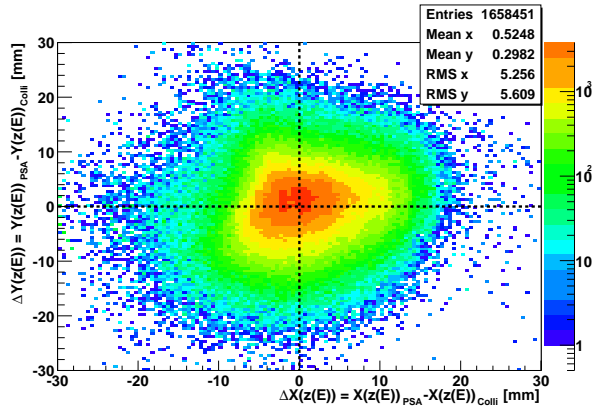
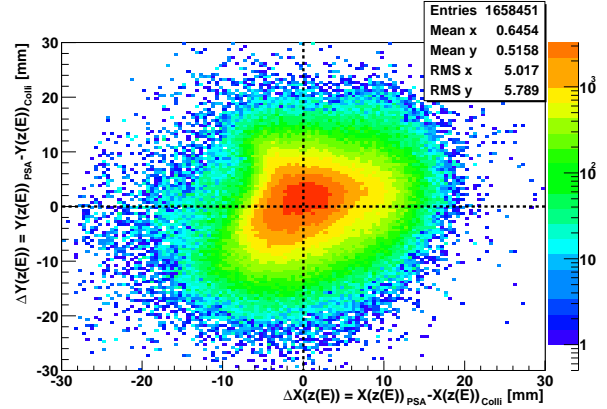
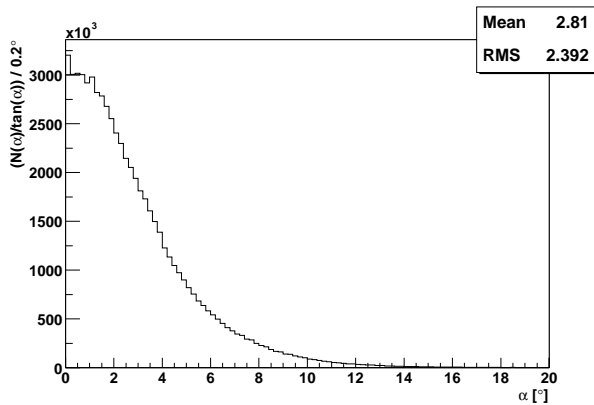
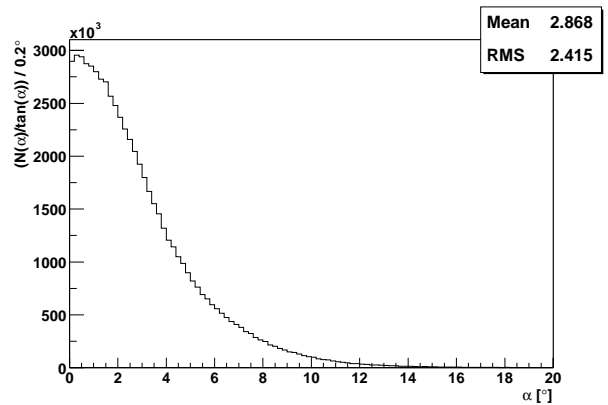
With the obtained calibration information, the position resolution of the MINIBALL detector using the user DSP code can be studied. The exact geometry of the setup was not taken into account, namely the tilt of the detector due to the tapering for dense packaging. This simplification, the unknown interaction depth and the unknown trajectory of the charge carriers (remember figure 2.1) contribute to the position resolution. In addition the following previously observed properties of the detector response contribute also to the position resolution.

- The decrease in the mirror charge amplitude in the center of the detector enhances the decrease in angular position resolution.
- Separate calibration factors for the  $\log\left(\frac{|q_+|}{|q_-|}\right)$  algorithm for positive and negative mirror charge amplitudes lead to an increase in angular resolution.
- The cut off of the mirror charge amplitude due to the ADC offset prevents a proper determination of the  $\frac{|q_+|}{|q_-|}$  ratio.
- The radial resolution is limited by the calibration, which does not take into account the asymmetry in the steepest slope spectra.
- For the 5 mm irradiation, the radial resolution is limited by the unknown interaction depth, which is important for non-perpendicular irradiation.

Therefore, the position resolution depends on the PSA implementation and configuration, the setup of the DGF modules and the calibration. Due to the different irradiation geometries and the lack of an information about the interaction depth the resolution depends also on the investigated detector segment (the AID minimizes the latter effect).

The overall position resolution of segment 1 of detector C is shown in figure 3.18, comparing the resolution in X and Y direction obtained with the realtime and the offline analysis. Panel (e) and (f) show the counting rate  $\frac{N(\alpha)}{\tan(\alpha)}$  as a function of the angle  $\alpha$  between the collimator direction and the interaction position. The position resolution obtained with the realtime analysis is *equivalent* to that of the offline analysis, being about 9 mm in x and 10 mm in y direction at the detector front face. Due to the non-perpendicular irradiation, which is most prominent for segment 1, the position resolution is worse than previously reported [25] for the whole detector but still satisfies the specification [22].

Table 3.5 summarizes the position resolutions obtained with the user DSP code, being 9 mm and 10 mm in X and Y direction, respectively. The improvement in position resolution if the polarity of the mirror charge is taken into account is presented in table 3.5. It is important to note that only for the *positive* amplitudes a different calibration was used, whereas for the negative amplitudes the usual calibration factors were retained. Due to different (radial) interaction positions for positive and negative mirror charges, as visible from the steepest slope spectra in figure 3.10, a different angular calibration was obtained for the negative polarities which turned out to be not correct. An improvement in angular position resolution of 1 mm FWHM for the whole segment and 2 mm for the  $r(z(0)) = 5$  mm (the radial resolution improves by 1 mm) was obtained as reported in table 3.5.

(a) Position resolution of the realtime analysis at the detector front face  $z(0)$ (b) Position resolution of the offline analysis at the detector front face  $z(0)$ (c) Position resolution of the realtime analysis inside the detector medium at  $z(E)$ (d) Position resolution of the offline analysis inside the detector medium at  $z(E)$ (e)  $\alpha$  distribution obtained with the realtime analysis(f)  $\alpha$  distribution obtained with the offline analysis

**Figure 3.18:** Position resolution of segment 1 of detector C obtained with the realtime and the offline analysis. The realtime and the offline analysis are shown in the left and right column, respectively. In the first row the position resolution referenced to the front face ( $z(0)$ ) of the detector is shown, while in the second row the resolution inside the detector at the main interaction depth is shown. Panel (e) and (f) show the distribution of the angle  $\alpha$  between the collimator direction and the reconstructed interaction position, normalized to  $\tan(\alpha)$ .

$r(z(0))$ [mm]	$\Delta X(z(0))$ [mm]	$\delta\Delta X(z(0))$ [mm]	$\Delta Y(z(0))$ [mm]	$\delta\Delta Y(z(0))$ [mm]
all	0.4	9.1	0.3	9.7
5	0.7	9.0	0.3	10.4
10	1.0	8.5	0.1	9.8
15	-0.2	7.4	0.4	7.9
20	-1.4	10.2	0.9	8.7
all (+)	0.5	8.9	0.5	8.8
5 (+)	0.8	8.1	0.7	8.3
15 NNNS	-0.3	7.3	0.3	10.5
20 NNNS	-1.5	10.1	0.5	10.7

**Table 3.5:** Position resolution of the user DSP code. The second part of the table shows the improvement in resolution if the sign of the induced charge is taken into account for the 5 mm irradiation. The overall position resolution improves mainly in y direction by 1 mm, while for the  $r(z(0)) = 5$  mm irradiation also the resolution improves from 9.0 to 8.1 and from 9.7 to 8.3 in x and y direction, respectively. The last part of the table shows the position resolution of the  $\log\left(\frac{|q_{++}|}{|q_{--}|}\right)$  algorithm for the  $r(z(0)) = 15$  and 20 mm irradiation. The position resolution in X direction is unaffected, but the position resolution in Y direction decreases by about 30 %, demonstrating that despite the smaller signal amplitude a good position resolution can be obtained.

The position resolution of segment 1 of detector C is shown in detail in table 3.6 for the standard offline analysis. The results in table 3.7 were obtained by subtracting a scaled MI segment signal instead of a linear function, which improves the angular position resolution by about 10%.

The shortcomings of the realtime analysis code, identified during analysis of the data from the collimated source, were used to create the user DSP code for the use with the MINIBALL spectrometer at REX-ISOLDE.

$r(z(0))$ [mm]	$\Delta X(z(0))$ [mm]	$\delta\Delta X(z(0))$ [mm]	$\Delta Y(z(0))$ [mm]	$\delta\Delta Y(z(0))$ [mm]
all	0.5	8.8	0.5	10.4
5	0.5	8.6	0.5	12.2
10	1.1	8.5	0.4	9.5
15	0.0	7.1	0.4	7.9
20	-1.2	9.4	0.5	9.4

**Table 3.6:** Position resolution of the offline analysis for all data points that have been scanned and for the individual radial positions. For the  $r(z(0)) = 15$  mm irradiation the best position resolution is achieved, being equivalent to previous results [25]. However, the overall resolution in segment 1 of detector C is worse by 10 % in x and 30 % in Y direction compared to previous results, not only due to the unfavorable irradiation but also due to the setup of the electronics.

$r(z(0))$ [mm]	$\Delta X(z(0))$ [mm]	$\delta\Delta X(z(0))$ [mm]	$\Delta Y$ [mm]	$\delta\Delta Y(z(0))$ [mm]
all	0.6	8.8	0.1	9.4
5	0.7	8.8	0.2	10.9
10	1.3	8.5	-0.3	8.5
15	0.1	7.1	0.0	7.1
20	-1.0	9.4	0.0	8.4

**Table 3.7:** Position resolution of the offline analysis if a scaled MI segment signal is subtracted instead of a linear signal. The position resolution in segment 1 of detector C in Y direction, which is mainly determined by the angular position resolution, is improved compared to that obtained with the linear approximation method presented in table 3.6.

# Chapter 4

## GRT4 VME module

”Not everything that can be counted counts, and not everything that counts can be counted.” - Albert Einstein

Initially, pulse shape analysis was performed by digital signal processors because FPGAs were not powerful enough for this task, involving multiplications and divisions. In the mid 1990s, digital spectroscopy systems consisted of several DSPs and a flash ADC typically running at 20 MHz [39], in order to accomplish the various tasks of a spectroscopy system. FPGAs are well suited for this application, since it is possible to implement various modules in a single FPGA device, that run in parallel without disturbing each other.

This chapter presents the implementation and test of preprocessing algorithms on the digital electronics GRT4, a VME module that features only FPGAs for event processing. It will be shown that nowadays, a single low-cost FPGA is powerful enough to implement a digital spectrometer, i.e. fast and slow channel for trigger and energy determination, as well as waveform capturing for subsequent pulse shape analysis<sup>1</sup>.

The GRT4 card (Gamma-Ray Tracking 4 channel) [58] was designed for the UK Gamma-Ray Tracking and Digital Pulse Processing project, a joint research project between the CCLRC<sup>2</sup> Daresbury Laboratory (DL), University of Liverpool and University of Surrey. The MWD algorithm, giving the  $\gamma$  energy, and a digital trigger algorithm, generating the event trigger, were added to the GRT4 VME module in the framework of this thesis [59]. The details of the developed VHDL code are compiled in chapter B.

### 4.1 Overview of the hardware

The GRT4, shown in figure 4.1, is a VME module featuring four acquisition channels operating in parallel. Each channel consists of one AD6645 14 bit 80 MHz flash ADC<sup>3</sup> from Analog Devices [60] and two XILINX Spartan XC2S200 Field Programmable Gate Arrays (FPGA) [61] for data processing and buffering. The first FPGA after the ADC, the ADC FPGA, is responsible for the preprocessing, i.e. applies event and energy filters, while the second FPGA, the DPP<sup>4</sup> FPGA, stores the event data and will perform the

---

<sup>1</sup>The possibility to perform pulse shape analysis with a FPGA device still has to be demonstrated. However, current high-performance FPGAs exceed the processing capabilities of an DGF-4C by far.

<sup>2</sup>Central Laboratory of the Research Councils

<sup>3</sup>The advantage of *oversampling* is explained in section A.5.

<sup>4</sup>Digital Pulse Processing

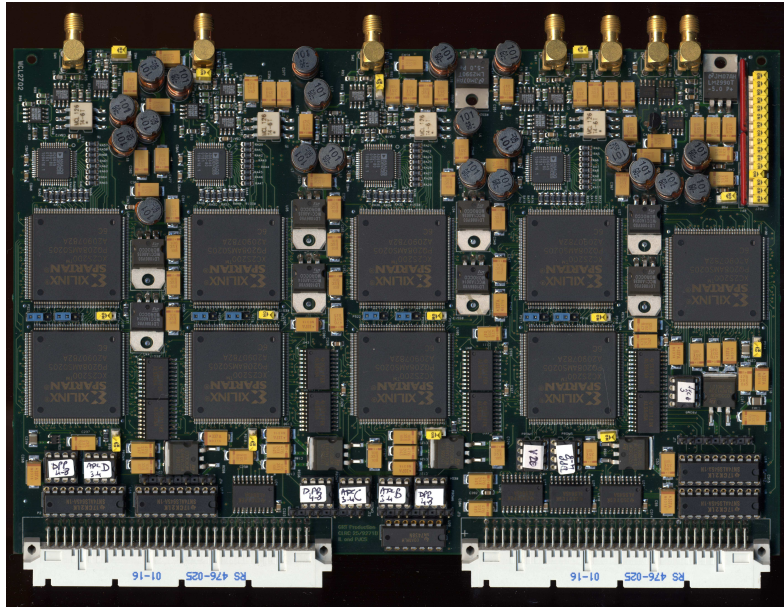


**Figure 4.1:** Picture of the GRT4 VME module. The front panel was removed. At the bottom are the connectors for the VME bus. At the top are the (analog) inputs. Each channel features two FPGAs and one ADC. The VME FPGA is the single FPGA on the right side.

PSA algorithms. The analog inputs have to fall into the range from  $-550$  to  $550$  mV. For a typical MINIBALL preamplifier with a sensitivity of  $150$  mV/MeV this translates into an energy range of about  $6.7$  MeV. The analogue input signals are filtered by a Nyquist filter before being passed to the ADC.

The VME board includes three SMA connectors that are used for NIM logic signals. The connector labeled *Trigger In* can be used to feed an external trigger signal into the GRT4 and the trigger logic can be configured to listen to the external trigger instead of the internal trigger. The connector labeled *Trigger Out* can be used if a coincidence between different detectors is required. It can also be programmed to function as a Busy Out. Together with the *Gate In* connector one can assure a common start and stop if the setup consists of multiple GRT4 modules [59].

The program of the SRAM<sup>5</sup> based FPGAs is volatile and is therefore loaded after power up from a configuration PROM<sup>6</sup>. The reprogrammability was used to add new features to the FPGA.

On the GRT4 board, the A/D conversion result, the over-range and data ready signal are routed to the ADC FPGA, which continuously applies the digital filters for energy determination and event trigger generation. The interesting part of the detector pulse is stored after a valid event trigger.

#### 4.1.1 XILINX Spartan 2

Each channel of the GRT4 module is equipped with two XILINX XC2S200 -6 PQ208C FPGAs, where the -6 label indicates a higher performance FPGA (Speed Grade) and

<sup>5</sup>Static Random Access Memory

<sup>6</sup>Programmable Read Only Memory

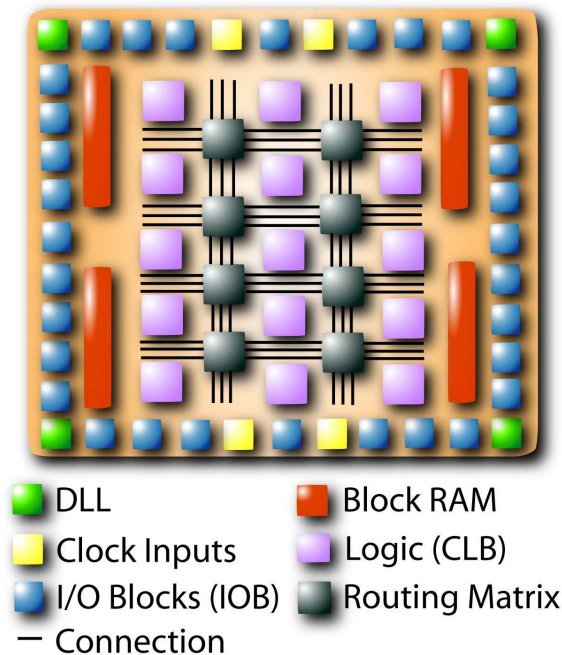


**Figure 4.2:** Strongly simplified layout of a Spartan 2 chip. The I/O blocks are located along the edges of the chip. According to the data sheet the DLL units are located at the edges of the chip. The block RAM is placed along the left and right edges and the logic block form an array in the center of the chip. Between the logic block, there's a vast amount of routing resources, i.e. connections of different length and switching matrices.

PQ208 label indicates that the 208-pin Plastic QFP<sup>7</sup> package type is used, allowing for a total of 140 User I/O connections.

The Spartan 2 FPGA consists of an 28 x 42 array of **C**onfigurable **L**ogic **B**locks (CLB). Each of the 1176 CLBs contains four **L**ogic **C**ells (LC) organized in two identical slices. Each slice consists of two 4-input function generators, implemented using a 4-input **L**ook **U**p **T**able (LUT), carry logic (allowing the implementation of fast adders) and storage elements (registers).

The chip also includes 56K of Block RAM memory consisting of 14 blocks of dual ported 4096 bit RAM. The Block RAM is located on the left and right side of the chip. Data transfers with 100 MHz are possible with the Block RAMs.

Four **D**elay **L**ocked **L**oop (DLL) units, providing zero clock delay with respect to an user source clock, are located at the edges of the FPGA. The DLL can also provide multiple phases of the source clock, e.g. 90°, 180°, 270°. The DLL can further act as a clock multiplier or divider by up to a factor of 16. The corresponding four global clock buffers are located at the top and bottom center. The clock distribution network has a tree like structure with a horizontal global clock line connected to global clock rows in vertical direction. The global clock rows then distribute the clock further to horizontal clock networks. A schematical drawing of the Spartan 2 FPGA is shown in figure 4.2.

The configuration information for the Spartan 2 is stored in a XC17S200APDBC

<sup>7</sup>Quad Flat Package

PROM<sup>8</sup> from XILINX. The XC17S200 can be programmed only once (One Time Programmable (OTP) PROM). The configuration of the DPP FPGA can be changed by using either the corresponding PROM or the Boundary-Scan configuration mode together with the JTAG<sup>9</sup> connector next to the device.

The Spartan 2 is not very well suited for digital signal processing, because the multipliers needed for the implementation of digital filters, occupy many logic resources (CLBs). The successor of the Spartan 2 FPGA, the Spartan 3, will therefore include embedded 18x18 multipliers to satisfy the need for fast multiplications with FPGA devices<sup>10</sup>.

With the availability of FPGAs with large amount of on-chip memory and also dedicated multipliers, DSPs are no longer necessary and more important the parallel processing capabilities of FPGAs enables a higher throughput and further reduces the event processing time which is of importance for high-rate  $\gamma$ -ray spectroscopy.

#### 4.1.2 Existing GRT4 Firmware

Initially, the ADC FPGA contained a circular buffer 512 samples<sup>11</sup> deep with programmable pre-trigger delay. A digital trigger algorithm looking for a rising or falling tendency in the ADC data (non-differentiated) was also part of the existing firmware. Each trace in this buffer is tagged with a 16 bit header, of which 8 bits are programmable, e.g. with a unique module number, and the remaining 8 bits contain the trigger counter. In addition, each trace is tagged with a 48 bit timestamp (LSB = 12.5 ns).

The DPP FPGA is used for event buffering of up to 4 events [59] and allows the addition of further modules in the future. The FPGA is large enough to implement a simple micro controller or DSP which are (freely) available from various suppliers [61, 63]. In the future, further pulse processing, e.g. PSA, can be implemented. If PSA is implemented, only the rising portion of the detector signal needs be send to the DPP FPGA ( $\approx 80$  samples = 1  $\mu$ s).

The readout takes place over the VME bus using single word or block transfer protocol. The VME interface is implemented in another Spartan 2 S200 FPGA, leaving most of the FPGA resources empty. Unfortunately, the VME interface is limited to 16 bit data transfers, limiting the maximum data transfer. Since the GRT4 was build as a test module for the readout of HPGe detectors irradiated by collimated sources a high data transfer rate is not necessary.

Segmented HPGe detectors are usually triggered by the central contact which sees a sum signal of all individual interactions. The GRT4 allows the implementation of such a trigger scheme by using an external analog Constant Fraction Discriminator (CFD) to generate a common trigger signal from the central contact and put this signal onto the Trigger inputs of all the GRT4 modules needed to read out this detector [59]. With the Busy output signal, a GRT4 card indicates that the buffers are full and that no more triggers should be generated until all the data has been read from the module. The gate input allows the simultaneous en-/disabling of the data acquisition in multiple

---

<sup>8</sup>Programmable Read-Only Memory

<sup>9</sup>Joint Test Action Group

<sup>10</sup>It should also be mentioned that there are more FPGA manufacturers apart from XILINX. Altera [62] offers the Stratix device with embedded memory blocks of three different sizes and embedded DSP blocks including four 18x18 multipliers, adders/subtractors, pipeline registers and a 52 bit accumulator.

<sup>11</sup>The size of the waveform buffer was increased to 2048 samples in order to perform the MWD algorithm offline.

GRT4 cards. The gate input can also be used to synchronize all time stamp counters by resetting them to zero simultaneously if the corresponding parameters are set.

## 4.2 Implementation of the VME interface

The existing VME interface, delivered as a schematic, was converted into a VHDL description. As shown in figure 4.3 the VME FPGA decodes the VME address and issues the corresponding action using the control signals routed to the ADC and DPP FPGA. The most important part of the VME FPGA is therefore the decoding of the VME address. After tests showed that the VME interface was working, the VHDL code was extended to support the MWD implementation in the ADC FPGA. The chip has access to the VME system clock, which is currently not used. This clock, or a multiple of it, could be used as a common clock for the time stamp generation.

A part of the unused VME address space was reserved to access the MWD registers, which contain the parameters for the algorithm. To prevent any interference and ensure backward compatibility, it was decided to switch between the *Standard* and *MWD* address decoding schemes by using the VME address signal A(11). If A(11) is set to one then all the standard encoders are disabled, setting their outputs to zero. At the same time eight address lines A(7:0) are put onto the common spare bus CS(18:11) and A(11) is connected with CS(10). Since the common spare bus is shared by the ADC and DPP FPGA, the ADC FPGA can detect a A(11)=1 condition and subsequently enable the decoders for the Common Spare (18:11) signals. Currently, only 4 address lines, A(7:4) = CS(18:15), are decoded in the ADC FPGA and therefore the total amount of registers for the MWD is limited to 16.

The SN74ALS645A chip is used as a transceiver between the VME bus and the GRT4 data bus. The VME FPGA controls the enable signal for the transceiver and the direction of the connection. If the transceiver chip is disabled, the VME and GRT4 bus are isolated. If the direction signal is one and the chip is enabled, data can be read from the GRT4 module.

## 4.3 Implementation of the MWD algorithm

The implementation of the MWD algorithm for the XILINX Spartan 2 FPGA is subdivided into various modules as shown in figure 4.4. The ADC data is internally routed to three locations: the waveform memory consisting mainly of Block RAM modules, the trigger module and the MWD module.

Before the ADC data reaches the MWD module, two corrections are applied: the ADC DNL correction and the conversion of the signed ADC data into an unsigned data word. Inside the MWD module, the signal processing consists of a decimation unit, i.e. a moving average and a resampler, the deconvolution operation and the subsequent MA for the generation of the trapezoidal shape.

A fundamental component of the MWD algorithm is the **Moving Average (MA)** module (see figure 4.5) which consists of a **Delay Subtract (DS)** unit and an **Accumulator (ACC)**. The DS unit subtracts a delayed ADC data word from the current ADC data word. The variable delay is implemented using the dual-ported block RAM. The read and write addresses are generated by two counters, the write address counter advances the read counter by  $M$  samples. The subtracter calculates the difference between the two

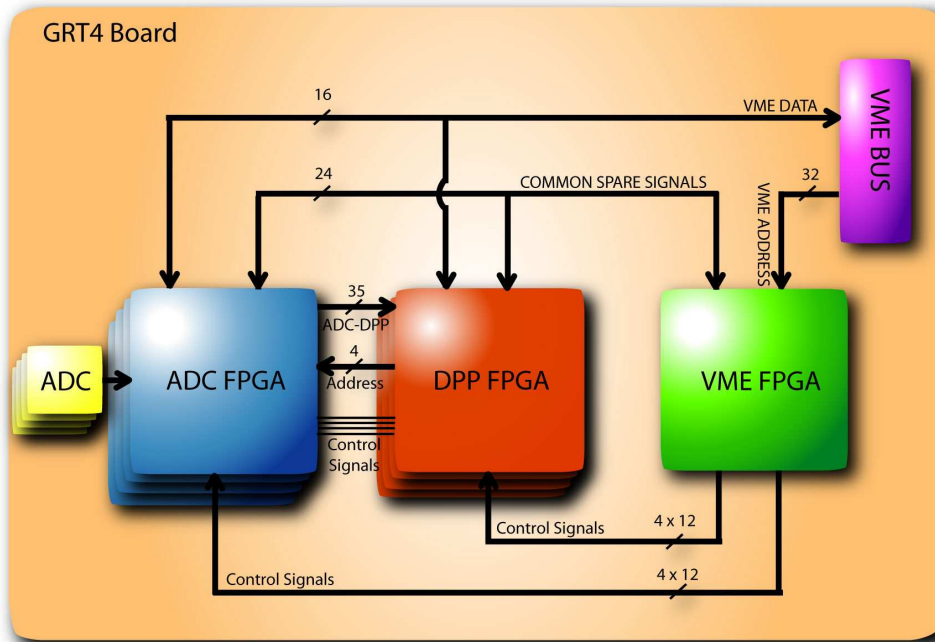


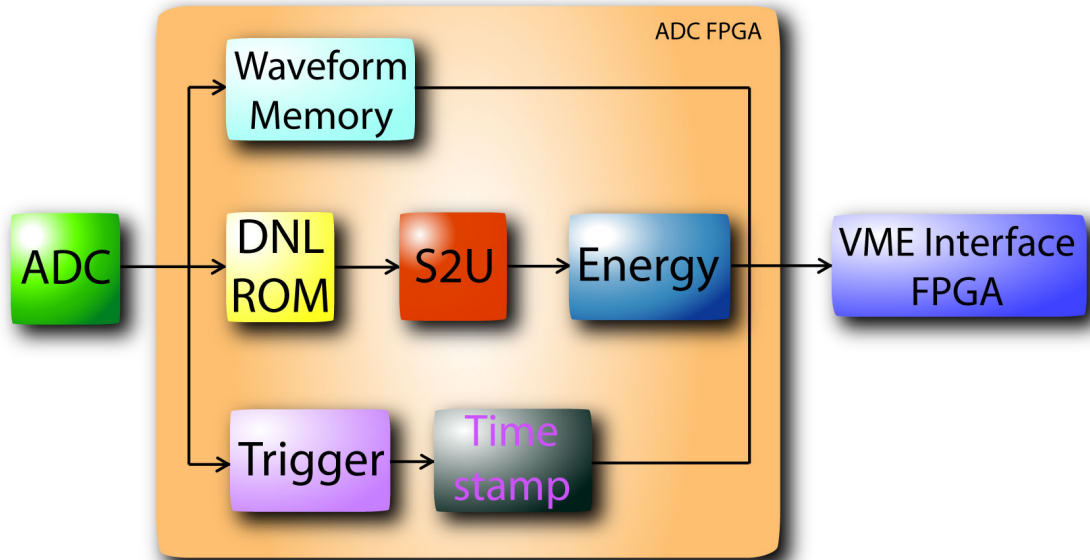
**Figure 4.3:** Schematic view of the VME interface showing the interconnection between VME FPGA, ADC/DPP FPGA and VME bus.

output ports of the memory. The result of the subtractor is connected with an accumulator. The configuration yields a moving average operation  $MA(n) = \sum_{k=n-M+1}^n x[k] = x[n] - x[n - M] + MA(n - 1)$  as illustrated in figure 4.5.

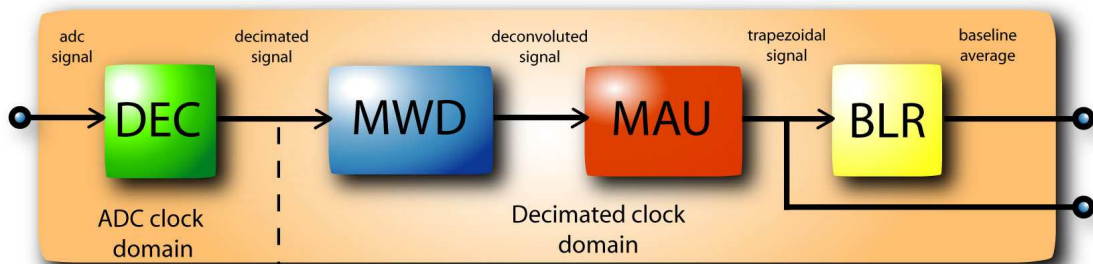
Important for the proper operation of the filters is the initialization phase which is started after each (software) reset of the MWD module. During the initialization phase all memories are presented with a zero input value, setting all memory locations to zero. During the memory clearing period the computational units (subtractor and accumulator) are disabled, to prevent the accumulation of invalid data. The subtractor is enabled first, before the accumulator is enabled. Finally, the MA module leaves the initialization phase by enabling the processing of the ADC data.

## DNL ROM

The need for an ADC DNL correction will be explained in section 4.7.1. The algorithm removes the two least significant bits (LSBs) from the ADC data word. A certain part of the ADC data word, ADC(8:5), is used to address the 16x4 ROM. The output of the ROM is a 4 bit data word (Nibble) which replaces the two removed LSBs and adds 2 fractional bits. The data format of the ROM entries is therefore 2.2, i.e. a fractional fixed point number. The obtained DNL correction coefficients are compiled in table B.2. This module was added *after* the MWD code development was finished and is therefore neglected in the following discussion, especially the increase of the ADC data width from 14 to 16 bits.



(a) Overview of the implementation featuring three branches: waveform capture, fast trigger generation and energy filtering.



(b) More detailed view of the energy module, including the trapezoidal shaper, consisting of the moving window deconvolution (MWD) unit followed by a moving average (MAU) module, and the baseline restorer (BLR) module.

**Figure 4.4:** Overview of the MWD implementation. The ADC data is routed through two modules that prepare the data for pulse processing first, before reaching the energy module, featuring the MWD implementation.

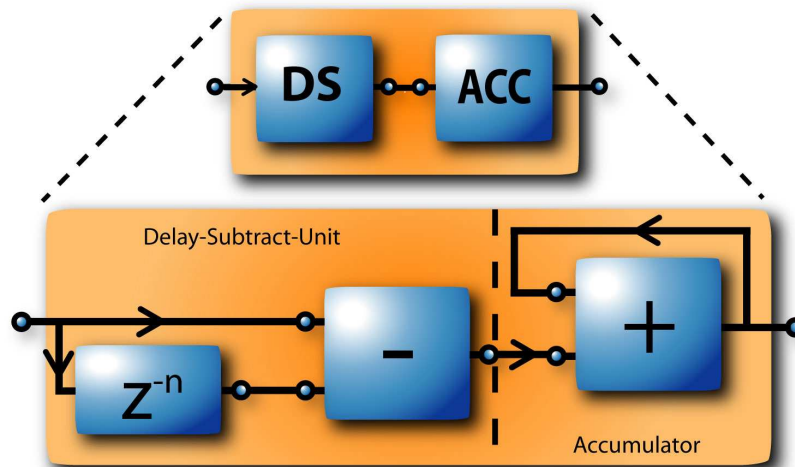


**Figure 4.5:** Schematic of the moving average unit (MAU) consisting of a delay subtract unit and an accumulator.

### Unsigned ADC data

Following the DNL correction the signed ADC data (two's complement) is converted into an unsigned data word. However, taking the absolute value would map the negative onto the positive ADC range reducing the dynamic range of the ADC from 14 to 13 bits. What's actually needed is the conversion of the 14 bit signed data into a 14 bit unsigned data word.

For this, one has to distinguish two cases, depending on the actual polarity of the input signal. For a positive polarity<sup>12</sup>, the signed ADC word simply has to be shifted fully into the positive range. For a 14 bit ADC this is equal to the addition of  $2^{13}$ , such that the ADC range  $[-2^{13}, 2^{13}]$  is shifted to  $[0, 2^{14}]$ . The actual implementation can be achieved more easily by recognizing that the addition of  $2^{13}$  leads to a simple inversion of the MSB.

In order to understand the method it is best to consider a simple example, e.g. a signed 4 bit ADC and a step signal with an initial amplitude of  $-5 (=1011_2)$  rising to a final amplitude of  $+5 (=0101_2)$ . The conversion into an unsigned number can be done either by adding  $2^3 = 8 = 1000_2$  leading to  $+3 (00011_2)$  and  $+13 (=1101_2)$  or by simply inverting the MSB such that  $-5 = 1011_2 \rightarrow 0011_2$  and  $+5 = 0101_2 \rightarrow 1101_2$ . The latter method can easily be implemented in VHDL with two statements

```
adc_u(width-2 downto 0) <= adc(width-2 downto 0);
adc_u(width-1) <= NOT(adc(width-1));
```

Similarly, if the ADC data shows a negative polarity the same operation can be applied preceded by an inversion of the ADC data word. The inversion transforms the negative slope into a positive slope and then the same operations as before can be applied. For the previous example of a 4 bit ADC, this means that the step signal has an initial amplitude of  $+5 (=0101_2)$  decreasing to a final amplitude of  $-5(=1011_2)$ . The inversion (ones complement) leads to  $-6 (=1010_2)$  and  $+4 (=0100_2)$ . The ones complement of a signed number leads to the unexpected result  $+5 \rightarrow -6$  and  $-5 \rightarrow +4$ . The expected result is obtained by adding one after the ones complement operation, implementing the twos

<sup>12</sup>The polarity of the input signal is defined as the direction in which the ADC values changes during the charge collection. If the ADC value increases the signal is defined to have a positive polarity.

MWD CSR (5:4)	Operation
00 <sub>2</sub>	$ADC_u = ADC + 2^{13}$
01 <sub>2</sub>	$ADC_u = \overline{ADC} + 2^{13}$
10 <sub>2</sub>	$ADC_u = ADC$
11 <sub>2</sub>	$ADC_u = ADC$

**Table 4.1:** Settings of the MWD CSR register controlling the behavior of the S2U unit.

Decimation	Decimated Clock	Minimum Shaping	Maximum Shaping
1	80 MHz	12.5 ns	3.2 $\mu$ s
2	40 MHz	25 ns	6.4 $\mu$ s
4	20 MHz	50 ns	12.8 $\mu$ s
8	10 MHz	100 ns	25.6 $\mu$ s
16	5 MHz	200 ns	51.2 $\mu$ s

**Table 4.2:** Possible shaping times with the various clock reduction factors and MA implementation using a single block RAM (256 memory locations).

complement operation. However, a twos complement operation is not needed since the absolute offset of the signal contains no information. The whole process, inversion and addition of  $2^{13}$ , is modeled in VHDL with two statements

```
adc_u(width-2 downto 0) <= NOT (adc(width-2 downto 0));
adc_u(width-1) <= adc(width-1);
```

The VHDL code (S2U module) allows to switch between these two behaviors and furthermore allows to bypass the ADC data word without any manipulations. The results of the operation of the S2U onto the ADC data was observed with real data by connecting the output of the S2U unit with the debug output of the MWD code and reading the waveform with single word VME accesses from the GRT4 module. The waveforms for different S2U settings (MWD CSR bit 4 and 5), summarized in table 4.1, are shown in figure 4.6.

### Decimation

The decimation unit consists of a MA unit and a resampler and is plotted in figure 4.7. The MA unit can average up to 32 samples, which allows a reduction of the clock rate by up to a factor of 32. However, the decimated clock is generated by the DLL<sup>13</sup>, which allows a maximum reduction by a factor of 16 only. Nevertheless, this allows a wide range of possible shaping times as shown in table 4.2. The DLL component is instantiated from the XILINX library (it is impossible to synthesize a DLL unit) with the following VHDL code inside the definition part of the architecture description of the VHDL top level code

```
dll: CLKDLL
port map (CLKIN => drdy,           -- data ready clock from ADC
          CLKFB => dav2fb,        -- feedback for "delay lock"
          RST   => dllreset,
```

<sup>13</sup>Delay Locked Loop

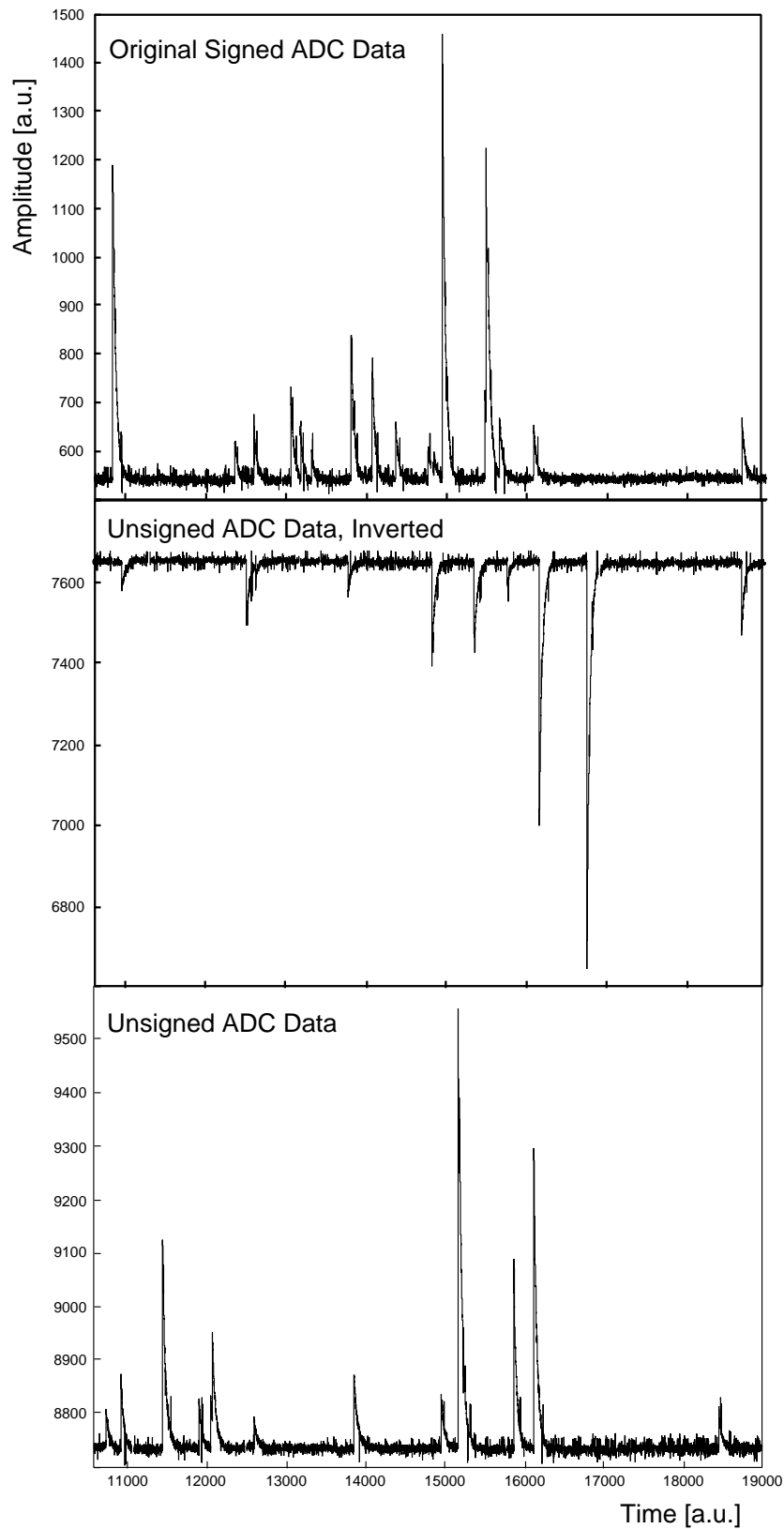


**Figure 4.6:** Three different waveforms that have been acquired with different settings for the S2U unit. The three panels show the effect of the S2U unit onto the ADC waveform. The MWD implementation requires positive signals with positive polarity.

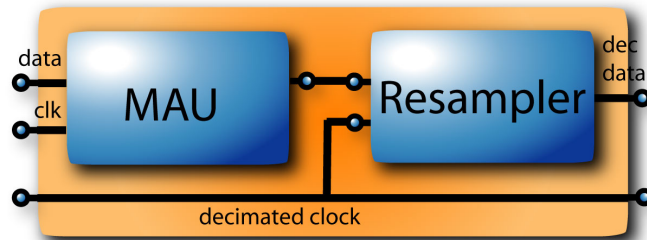


**Figure 4.7:** Schematic of the decimation unit.

```

CLK0  => dav_fb,          -- data clock
CLK90  => open,
CLK180 => pre_dav180,    -- inverted clock
CLK270 => open,
CLK2X  => open,
CLKDV  => pre_davdec,    -- decimated clock
LOCKED => open);

```

The signal *drdy* is the ADC **D**ata **R**eady (DR) clock signal, which is in phase with the A/D conversion result. The DLL output signal *dav\_fb* is used to latch the ADC data into the FPGA. The inverted clock signal (and the other two phases) are not used. The clock divider output is used to latch the MA output of the decimation unit. The clock reduction factor is determined by a timing constraints, which is not entered in the UCF, but entered as a VHDL attribute, which is an equivalent way of specifying this constraints:

```

attribute clkdv_divide of dll: label is "4.0";          -- divide by 4
attribute duty_cycle_correction of dll: label is "true";

```

Since the DLL is used to generate the divided clock signal, there is no way to change the reduction factor without changing the FPGA configuration. The length of the MA has to match the clock reduction factor. If four samples are averaged, the clock frequency can be reduced by factor of four. The decimation by a factor of  $2^n$  leads to  $n$  additional data bits, leading to an increase of the width of the ADC data word from 14 to 16 bits for clock division by four. Since the block RAMs are used in the 256x16 configuration, a width of 16 bit is desirable and therefore the clock reduction factor of four is the preferred implementation. If a higher decimation factor is used, as it was the case in the beginning,  $n - 2$  LSBs have to be removed.

If a variable decimation factor is desired, the DLL cannot be used to generate the divided clock and a clock divider module has to be designed. Furthermore, a multiplexer has to be added to select the proper range of the MA output, preventing the following stages from overflowing. With such a configuration, the decimation factor could be changed by setting a few parameters, e.g. clock reduction factor, MA length and multiplexer setting.

The effect of the decimation onto the waveforms is shown in figure 4.8.

## Deconvolution

The MWD module consists of two parts: a special MA unit and a fixed point multiplier. The implementation of the deconvolution operation is shown in figure 4.9. The output

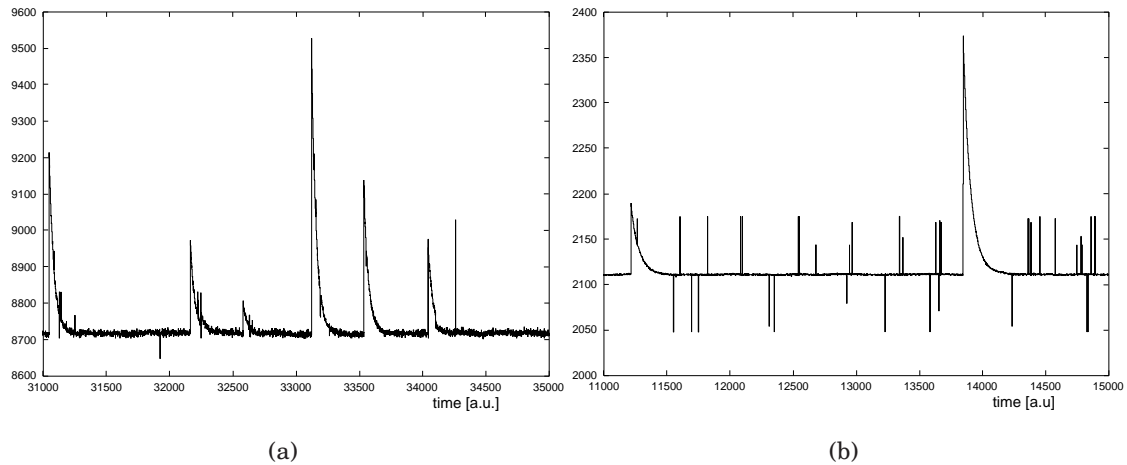


**Figure 4.8:** Waveforms that have been acquired with different settings of the decimation unit. It can be seen that the details of the signal are smoothed out by the decimation operation. The spikes in the waveforms are due to the fact that the VME read accesses are not synchronized with the ADC clock.

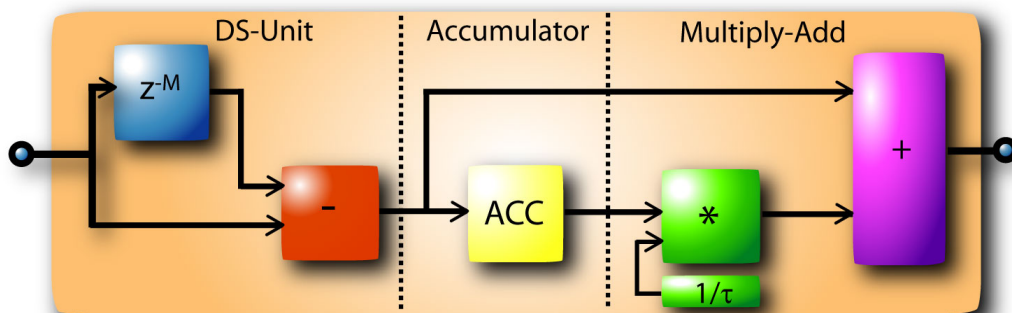


**Figure 4.9:** The structure of the MWD unit. The first part is the delay subtract unit followed by an accumulator whose output is multiplied by the decay time constant and added to the initial result of the DS unit.

of the decimation unit is connected to the input of a MA module. The MA module implements the  $MA_m[n] = \sum_{k=n-M-1}^n x[k]$  operation. The outputs of the dual ported block RAM can directly be used for the differentiation operation  $D_M[n] = x[n] - x[n - M]$ .

Before the two results can be added to form the final MWD result  $MWD_M[n] = D_M[n] + \frac{1}{\tau} MA_M[n]$ , the output of the MA unit has to be multiplied with the decay time coefficient  $\frac{1}{\tau}$ . For this the multiplication module is needed.

In VHDL a multiplier is described with the statement `mul <= b * a;`. A  $24 \times 24$  non-pipelined multiplier, implemented using the LUTs of the Spartan 2 -6 FPGA, can run with a clock frequency of about 50 MHz and occupies about 363 Slices (15 %). A  $16 \times 16$  pipelined multiplier (latency is four clock cycles) runs with about 135 MHz and needs 194 Slices (8 %) and additional pipeline registers. The output of the MA module with 16 bit input data is a 24 bit word, because the length of the block RAM is  $256 = 2^8$  leading to a gain of 8 bits. Therefore a  $24 \times 24$  multiplier was implemented even though only 23 bits (15.8 fractional number) of the resulting 48 bit number (24.24 fractional) are used.

The results of the multiplication and the differentiation have to be combined. In order to prevent rounding errors seven fractional bits and the sign bit are included. The corresponding VHDL code is

```
Mult_select(22 downto 0) <= Mult(38 downto 16); -- select proper range
Mult_select(23) <= '0'; -- ALU always positive
Sub_select(23 downto 7) <= Sub(16 downto 0); -- including SIGN bit !
Sub_select(6 downto 0) <= (others => '0'); -- add 7 LSBs
```

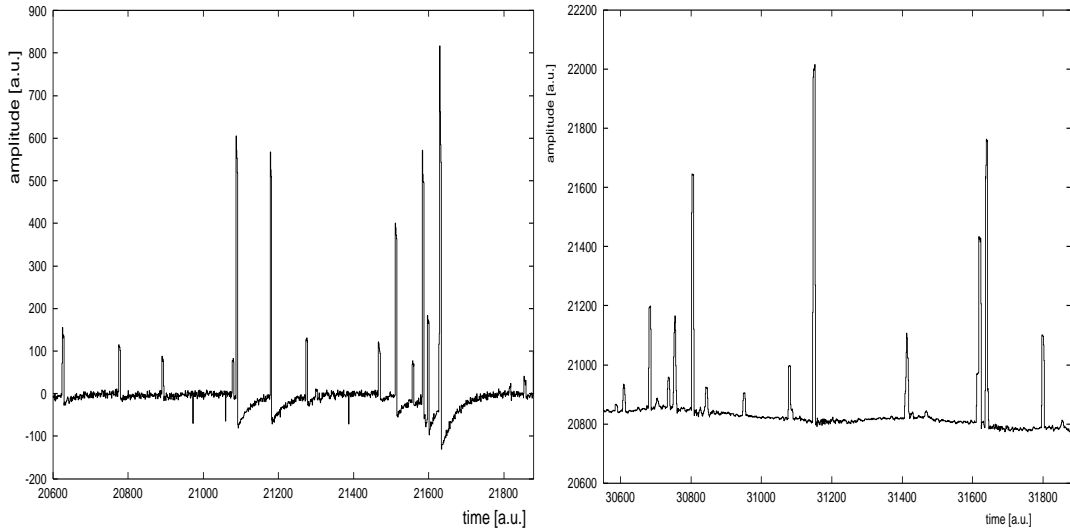
As can be seen from the VHDL code, the result of this operation is a 17.7 signed fractional fixed point number. `Sub_select` and `Mult_select` are added to obtain the deconvoluted and differentiated signal  $MWD[n]$ . The MA unit generates the final trapezoidal signal. The output of the MA unit is fed onto the baseline restorer module, which in turn determines the average baseline of the energy filter signal. The trapezoidal filter value and the current value of the baseline filter are latched at a fixed time after a trigger.

In figure 4.10 the operation of the deconvolution module is shown for two different settings of the decay time constant  $\tau$ . In panel (a) the decay time constant does not match the preamplifier decay time and therefore the signal shows undershoots, which are removed if the proper decay time constant is used as demonstrated in panel (b).

## Software

In order to correctly setup the MWD module for data acquisition a few parameters have to be calculated and transferred to the GRT4 module. The MWD parameters are

- DEC: the length of the MA for the decimation unit
- M: the differentiation time of the MWD algorithm
- L: the length of the MA for the trapezoidal shaping
- PS: the peak capture delay
- PU: the pile up rejection interval
- BU: the clock period for the baseline sampling

(a) MWD signal with bad  $\tau$  adjustment.(b) MWD waveform with good  $\tau$  adjustment.

**Figure 4.10:** Waveforms that have been acquired after deconvolution with different settings for the decay time correction coefficient. If the decay time  $\tau$  is not set correctly the MWD signal will show under- or overshoots which are visible in Panel (a). If  $\tau$  is set correctly, these effects are removed.

- BC: the threshold for baseline acceptance
- Alpha  $\alpha$ /BA: the filter parameters for the baseline restorers

The shaping times for the filter have to be inverted for proper operation. The following piece of code illustrates the proper calculation of the parameters:

```
decimation = 32 - DEC + 1;      /* decimation 4: 32 - 4 + 1 = 29 */
mwd_shaping = 256 - M/dt -1;   /* 8.8 us -> 256 - 8.8/0.05 = 80 */
trapez_shaping = 256 - L/dt -1; /* 6.8 us -> 256 - 6.8/0.05 = 120 */
trapez_norm = L/dt;           /* L = 136 */
peaksampling = PS/dt_80;      /* 7 us -> 560 */
peakdistance = PU/dt_80;      /* 9 us -> 720 */

baseline_upddate = BU/dt;     /* 2 us -> 40 */
baseline_cutoff = BC;        /* signed/twos complement */
averaging = Alpha;           /* EA BLR */
averaging = 256 - BA + 1;    /* MA BLR */
```

with  $dt$  the decimated clock period and  $dt_{80}$  the 80 MHz clock period (12.5 ns). The additional +1 and -1 for all filter modules were added because the actual filter length is different from the parameter due to a pipeline register in the filter implementation.

The decay time parameter is calculated using an expression taken from [38], which is equivalent to the expression that has been previously derived, as can be seen from the following approximation

$$(1 - \exp(-\frac{M}{\tau}))(\frac{\Delta t}{M}) \approx \frac{M}{\tau} \frac{\Delta t}{M} = \frac{\Delta t}{\tau}. \quad (4.1)$$

The result of the MA has to be normalized with respect to the length of the MA, which introduces the factor  $\frac{\Delta t}{M}$ . Since the output of the MA is a 24 bit number and a symmetric  $24 \times 24$  bits multiplier was implemented, the decay time coefficient has to be expressed as a fractional fixed point 24 bit number. The conversion is achieved by multiplying the decay time with  $2^{24}$ . The following piece of code illustrates the correct conversion of the decay time parameter into a fractional fixed point number

```
decay = (1. - exp(-M/tau))/(M/dt)*16777216.; /* decay = 0.161382 / 176 * 2^24 */
decay_high = decay/65536; /* decay_h = 0 */
decay_low = decay-decay_high*65536.; /* decay_l = 15383 */
```

The calculated parameters can now be downloaded onto the GRT4 module with a few VME accesses

```
VME_Write_A32D16(GRT4 Base Address+Channel Offset+0x1810, (mwd_shaping+trapez_shaping*256));
VME_Write_A32D16(GRT4 Base Address+Channel Offset+0x1830, peaksampling);
VME_Write_A32D16(GRT4 Base Address+Channel Offset+0x1840, peakdistance);
VME_Write_A32D16(GRT4 Base Address+Channel Offset+0x1850, (averaging+baseline_update*256));
VME_Write_A32D16(GRT4 Base Address+Channel Offset+0x1870, baseline_cutoff);
VME_Write_A32D16(GRT4 Base Address+Channel Offset+0x1880, decay_low);
VME_Write_A32D16(GRT4 Base Address+Channel Offset+0x1890, (decay_high+decimation*256));

#define RES_MWD (1<<2)
#define ENA_MWD (1<<3)
csr = VME_Read_A32D16(GRT4 Base Address + Channel Offset + 0x18b0); /* READ MWD CSR */
csr = csr & ~ENA_MWD;
VME_Write_A32D16(GRT4 Base Address + Channel Offset + 0x18b0, csr); /* DISABLE MWD */
csr = csr | RES_MWD;
VME_Write_A32D16(GRT4 Base Address + Channel Offset + 0x18b0, csr); /* SOFTWARE RESET */
csr = csr & ~RES_MWD;
VME_Write_A32D16(GRT4 Base Address + Channel Offset + 0x18b0, csr); /* STOP RESET */
csr = csr | ENA_MWD;
VME_Write_A32D16(GRT4 Base Address + Channel Offset + 0x18b0, csr); /* ENABLE MWD */
```

After successful configuration of the GRT4, a run can be started with the following commands

```
/* start acquisition in GRT4 */
VME_Write_A32D16(GRT4 Base Address + Channel Offset + 0x0000, 0x0f);
VME_Write_A32D16(GRT4 Base Address + Channel Offset + 0x1000, 0x02);
/* wait for DATA READY from MWD CSR */
while((csr&0x80)!=(0x80))
    csr = VME_Read_A32D16(GRT4 Base Address + Channel Offset + 0x18b0);
```

The following code illustrates how the final 16 bit energy word is obtained from the 32 bit energy filter and baseline restorer (BLR) words for each event

```
filter_low = VME_Read_A32D16(GRT4 Base Address + Channel Offset + 0x18e0);
filter_high = VME_Read_A32D16(GRT4 Base Address + Channel Offset + 0x18f0);
baseline_low = VME_Read_A32D16(GRT4 Base Address + Channel Offset + 0x18c0);
baseline_high = VME_Read_A32D16(GRT4 Base Address + Channel Offset + 0x18d0);

filter = filter_low + filter_high*65536;
baseline = baseline_low + baseline_high*65536;
filter = filter/(128.*trapez_norm);
baseline = baseline/(128.*trapez_norm); /* EA BLR */
baseline = baseline/(128.*trapez_norm) * (256./baseline_average); /* MA BLR */
energy = filter - baseline;
```

## 4.4 Implementation of the Baseline Restorer

Two **BaseLine Restorers** (BLR) have been developed based on the EA and the MA filters<sup>14</sup> shown in figure 4.11. The BLR module further comprises a sampler and a comparator. The trapezoidal filter output is sampled if the following conditions are fulfilled

1. The BLR is enabled
2. The sampler reaches the predefined value.
3. The energy filter is below the user-defined threshold

The MWD state machine controls the global enable signal for the BLR module. The MWD state machine therefore includes a counter that is loaded with twice the pile up inspection period ( $2 \times \text{PU}$ ) and starts counting after each trigger. The BLR module is disabled during this period, because the trapezoidal filter can show an under- or overshoot after returning to the baseline value. The trapezoidal filter lasts  $M + L$  cycles, e.g.  $15.6 \mu\text{s} = M + L = 8.8 \mu\text{s} + 6.8 \mu\text{s}$ . If the pile up period is set to  $10 \mu\text{s}$ , then the baseline module is disabled for  $20 \mu\text{s}$ , exceeding the trapezoidal filter by  $4.4 \mu\text{s}$ .

The sampler is implemented as a counter, that generates an overflow signal each time the counter reaches a predefined counter value. With each overflow signal a new filter value is latched. In case of the MA BLR, the overflow signal of the counter is used to clock the new data into the MA module.

If the energy filter is below a positive or above a negative threshold, a new baseline sample is accepted and subsequently a new baseline average is calculated.

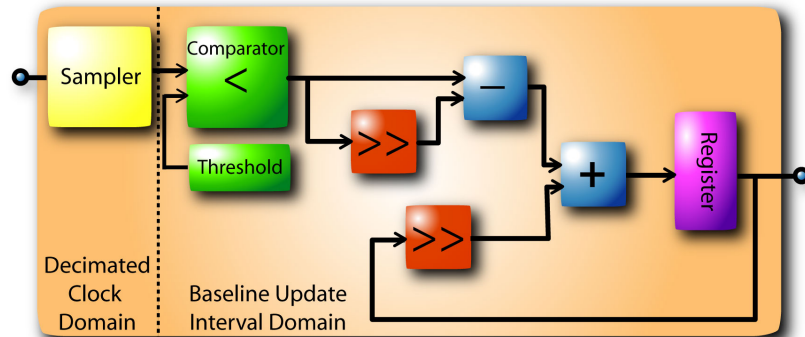
The response of the baseline restorer is determined in case of the exponential averaging by the parameter  $\alpha$  and in case of the moving average by the length of the filter. To simplify the implementation of the EA and to prevent the usage of another multiplier, the parameter  $\alpha$  is restricted to powers of two, i.e.  $2^{-n}$ . The multiplication is replaced by a simple bit shift operation.

## 4.5 Implementation of the Trigger Algorithm

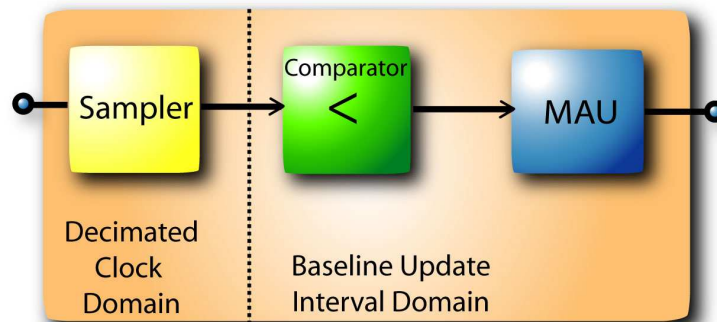
The implementation of a trigger algorithm, accepting signed data, was kept as simple as possible in order not to delay the MWD implementation. Therefore a **Leading Edge** (LE) trigger was chosen. The design is shown in figure 4.12. The first submodule is a delay-subtract unit (DS), which differentiates the digitized preamplifier signal with a time constant that can be adjusted between 12.5 and 800 ns. The resulting signal is then fed onto an MA unit (DS + accumulator (ACC)), to remove noise from the signal. The length of the moving average can be varied between 12.5 and 800 ns, too. Finally, the signal is compared to a threshold value, which can be positive or negative because of the signed ADC data. In order to debounce the trigger signal and prevent false trigger from signal glitches, the output of the comparator is delayed by up to 200 ns and combined with the original comparator signal using a logical and. With this configuration, the trigger signal has to achieve a minimum width and therefore this configuration ensures that a valid trigger is generated only for events that cause the trigger filter to exceed the threshold for a minimum time. The parameters of the trigger module are

---

<sup>14</sup>The filter are explained in section A.3.



(a) The baseline restorer based on the exponential averaging module.



(b) The baseline restorer based on the moving average module.

**Figure 4.11:** Layout of the EA and MA baseline restorer.

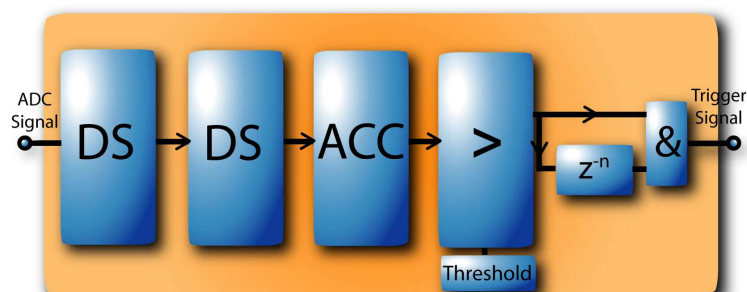


**Figure 4.12:** Layout of the FIR leading edge trigger module.

- D1: delay for the DS unit of the differentiator module,
- D2: delay for the DS unit of the integrator (MA) module,
- TOT: minimum time over threshold (deglitch of trigger signal), and
- Trigger\_Threshold: reference value for the comparator (signed).

The parameters D1, D2 and TOT have to be written into the ADC Header H(15:0) register of the GRT4. D1 has to be written to H(5:0), D2 into H(11:6) and the time-over-threshold into H(15:12) range of the ADC Header register. The trigger threshold has to be stored in the spare register four of the GRT4. The following code illustrates the configuration of the FIR trigger

```
VME_Write_A32D16(Base Address + Channel Offset + 0x1004, D1 + D2*64 + TOT*4096);
VME_Write_A32D16(Base Address + Channel Offset + 0x100a, Trigger_Threshold);
```

The response of the trigger to a step and a detector signal was simulated with the ModelSim VHDL simulator and is shown in figure 4.13.

## 4.6 Simulation of VHDL code

The ModelSim XE Starter software was used to simulate the design at various stages of the implementation, before and after synthesis and after place and route. The simulation after place and route was done using the worst case timing parameters, which is the default setting, meaning that the actual design could run a higher clock frequency as reported by the XILINX software but probably not under all operating conditions. The worst case timing values are obtained by operating the FPGA at the maximum operating temperature<sup>15</sup> and with the minimum supply voltage<sup>16</sup>. Additionally, also variations in the production process are taken into account. The timing specifications are compiled in the SDF<sup>17</sup> file, which is used by the simulator.

For the timing simulation the design is translated into a special netlist that is entirely build from instantiated components from the XILINX simulation libraries, the UNISIM<sup>18</sup> and the SIMPRIM<sup>19</sup> library. The UNISIM library is used for functional simulations at the RTL level or after synthesis. The SIMPRIM library is used for timing simulations after MAP and after PAR. Simulations after PAR include the full timing information (logic and routing delays) and therefore model the actual behavior of the circuit.

In order to perform a (V)HDL simulation a testbench code has to be generated including the Design Under Test (DUT) and the test vectors that are used to stimulate the DUT. In order to simulate the submodules of the MWD, simple testbenches were generated using the testbench generation wizard of the XILINX WebPACK software. For the MWD module and the top level module itself, testbenches were generated that first set up the DUT for simulation and second apply recorded waveform data to the ADC input such that the output of the filter can be observed in the waveform display of the simulator. The following code stores the amount of pre-trigger data, which is needed for the waveform capture in the FIFO, into a GRT4 register and reads it back afterwards.

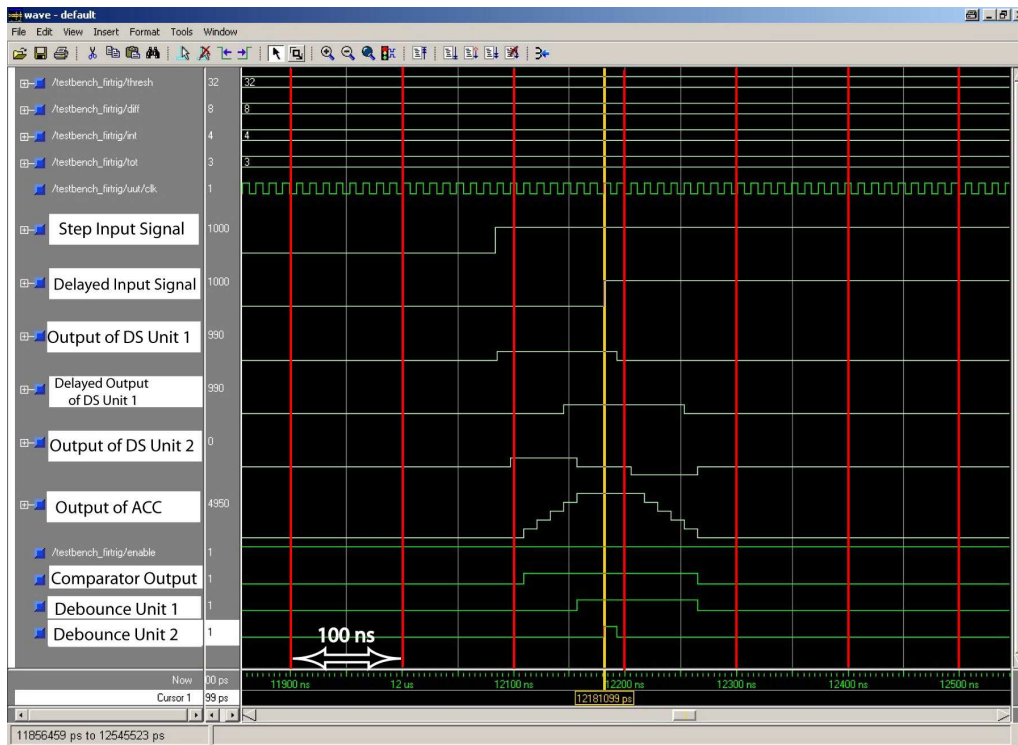
<sup>15</sup>In the SDF file this is expressed with the statement (TEMPERATURE 85:85:85).

<sup>16</sup>In the SDF file this is expressed with the statement (VOLTAGE 1.7:1.7:1.7).

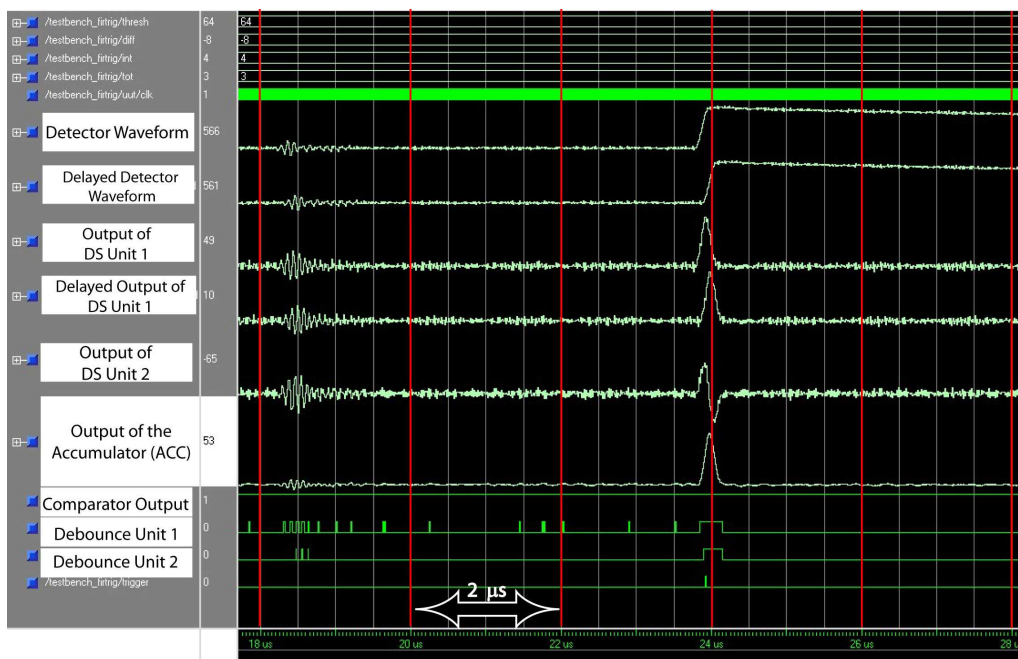
<sup>17</sup>Standard Delay Format

<sup>18</sup>Unified Library components that represents the logical view of the design

<sup>19</sup>SIMPRIM components represent the physical view of the design



(a) Step response of the LE trigger, giving the latency (FPGA internal) of the implementation.



(b) Response of the LE trigger to a (noisy) detector waveform

**Figure 4.13:** Response of the FIR trigger module to a step input is shown in panel (a). The latency of the trigger is 8 clock cycles, i.e. 100 ns at 80 MHz sampling frequency. The response to a detector waveform is shown in panel (b). The debounce circuit ensures that only a single trigger signal is generated (Output of Debounce Unit 2 in Panel (b)), at the same time preventing noise triggers if very low thresholds are used.

```

VWRITE_L <= '0'; -- VME write access
WAIT FOR 50 ns;
VD <= transport std_logic_vector("0000000000011000"); -- 24 pre-trigger samples
WAIT FOR 50 ns;
WR_PRETRG_IN <= transport '1';
WAIT FOR 50 ns;
COMMON_SP(8) <= transport '1'; -- VME data strobe
WAIT FOR 100 ns;
COMMON_SP(8) <= transport '0'; -- VME data strobe
WAIT FOR 50 ns;
VWRITE_L <= '1'; -- VME read access
WR_PRETRG_IN <= transport '0';
VD <= transport std_logic_vector("ZZZZZZZZZZZZZZZZ"); -- buffers off
WAIT FOR 50 ns;

```

The recorded waveforms are read from a file and applied to the ADC input as illustrated in the following code, which loops over the file and converts each entry into a 14 bit vector that is connected to the ADC input. Then the VHDL code waits for 10 ns, before the loop starts again from the beginning.

```

while(endfile(in_file)=false) loop
  readline(in_file, line_in);
  read(line_in, trace);
  ADC <= to_stdlogicvector(trace, 14);
  WAIT for 10 ns;
end loop;

```

The interaction with the DPP FPGA is modeled as a process, that reacts onto the TRIGGERED\_OUT signal from the ADC FPGA: `process(TRIGGERED_OUT, DRDY_IN)`. When the process is triggered, it starts with the readout of the time stamp and event header information. Then this process triggers another process that reads out the waveform memory of the GRT4.

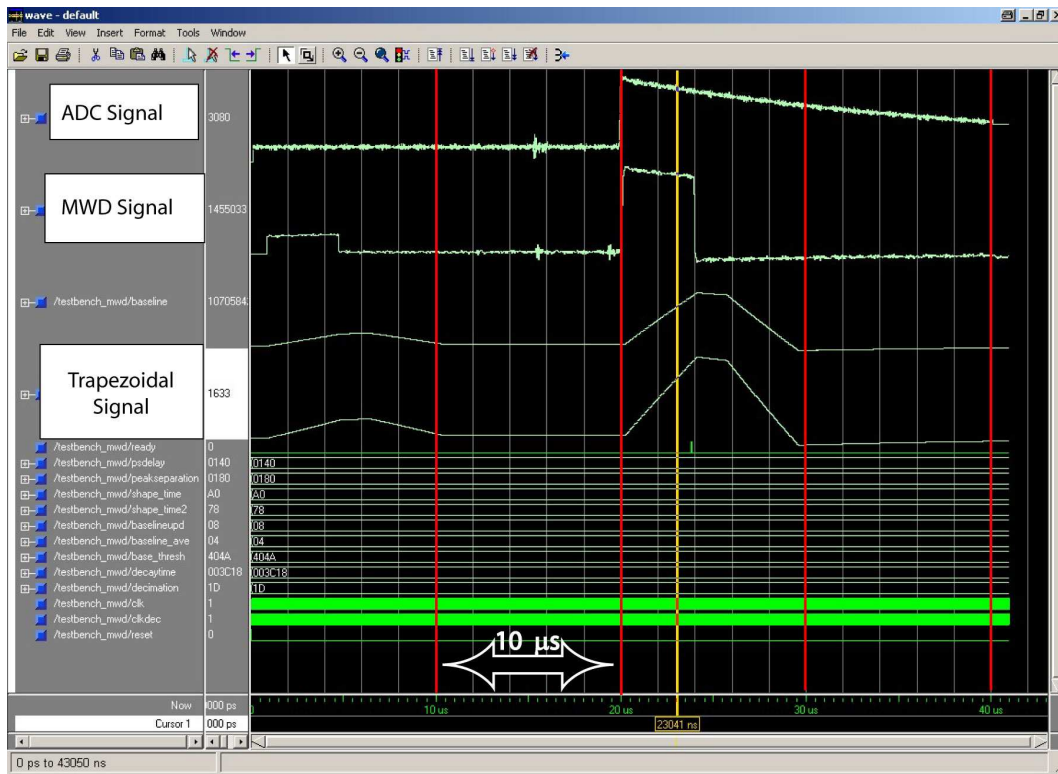
With the developed testbench it was possible to test the functionality of the MWD implementation before testing the algorithm in hardware, which was mandatory due to the limited amount of configuration PROMS.

## 4.7 Measurements

The MWD implementation on the GRT4 module was tested with three different detectors and a pulser. If possible the results were compared to that obtained with an analog spectroscopy amplifier or the XIA DGF-4C.

### 4.7.1 Measurement of the DNL

The **Differential NonLinearity** (DNL) is defined [64] as the difference between the actual width of an ADC channel and the ideal width of one channel (1 LSB). The differential nonlinearity of the AD6645 was measured with a setup [65] that was used to test the performance of the MPI made 13 bit peak sensing ADCs. It consisted of the HAMEG [66] function generator HM 8030-3 to generate a ramp signal that was fed onto the GRT4. A noise/random time pulser was fed onto the external trigger input of the GRT4. The external trigger stopped the internal waveform memory and an ADC value at a fixed position in the memory was used to address the histogram memory and the corresponding channel was incremented. The number of entries per channel was around 28000, the



(a) Energy Filter Response

**Figure 4.14:** Waveform window of the ModelSim XE Starter software showing the trapezoidal filter output after running real detector data through the module. Note that the first step response is due to the initialization of the filters (zero data input gets non-zero).

statistical error is about 0.5 %. The differential non-linearity is determined by dividing each channel by the average number of entries in the histogram, excluding entries at the beginning and end of the spectrum, and subtracting one.

The resulting histogram is shown in figure 4.15. Because of the large number of channels, an additional histogram was generated by averaging over 16 ADC channels leading to histograms for 10 ADC bits. The small scale structure visible in panel (a) is removed in panel (b) by the averaging process, only the large deviations remain in the histogram. The repetitive structure is a feature of a pipelined flash ADC.

The DNL measurement was performed because of the observation of a degradation in energy resolution of about 30 % when spectra were acquired at high event rates. The IEEE standard 301 [67] summarizes the testing procedure for amplifiers for radiation detection. However, as explained in [68], the baseline restorer performance is of great importance and therefore the energy resolution should be measured with varying signal offset. A superposition of a staircase (from a function generator) and the preamplifier signal was proposed. Measuring at high event rates leads to a similar configuration since the average distance between events decreases with increasing event rate and more events sit on the exponential tail of the previous event. Similarly to the addition of a staircase signal, the detector signal offset differs for each event and this is illustrated

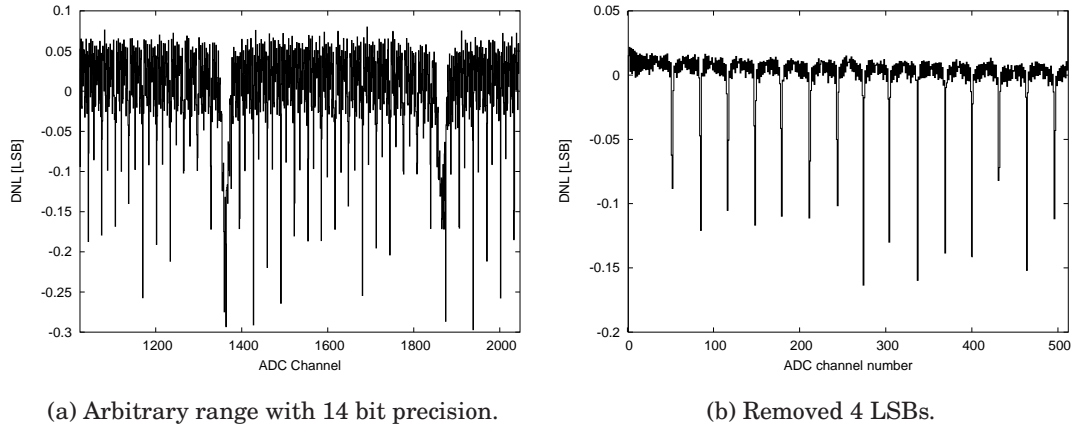


**Figure 4.15:** Measured differential non-linearity of the AD6645. Panel (a) shows an arbitrary range of the measured DNL for the full 14 bit ADC precision, whereas four least significant bits have been removed in Panel (b) through averaging.

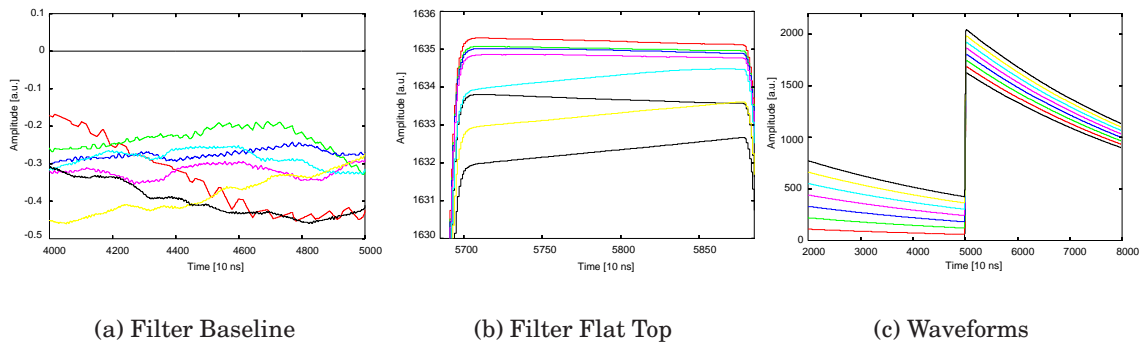


**Figure 4.16:** Simulation of the effect of the DNL of the ADC. The response of the trapezoidal filter to signals of the same height generated for different amplitudes of the preceding event is plotted in panels (a) and (b) for the filter baseline and flat top, respectively. The corresponding detector signals are shown in panel (c).

in figure 4.16.

Since it is not directly obvious how the DNL of the ADC affects the energy resolution in a digital spectroscopy system<sup>20</sup>, the simulation of the true coaxial detector was extended to include an additional event, using the same simulated detector current pulse. The time difference between the two events and the relative charge produced in both events can be adjusted. In figure 4.16 only the charge, i.e amplitude, of the first event was changed. The simulated preamplifier signal was subjected to the measured DNL of the AD6645 ADC. This was done by remapping the actual ADC channels onto the channels of a virtual ADC, comprising the DNL of the AD6645. The channels of the DNL ADC were obtained by accumulating the measured channel width, again excluding the beginning and end of the spectrum by setting the channel width to one LSB. The resulting look up table is accessed with the ADC code and returns the DNL ADC code.

<sup>20</sup>It is obvious that imperfect A/D conversion modifies the signal shape and prevents proper deconvolution.

An ADC code of 128 gives the DNL ADC code 127.91 and 129 gives the DNL ADC code 129.02. After remapping of the ADC, the signal was processed with the MWD algorithm. The effect onto the trapezoidal baseline and flat top is shown in 4.16 for signals with different ADC offsets due to a previous event. Whereas for the baseline the effect is below 0.5 channels <sup>21</sup>, the ADC DNL leads to a variation of the flat top of the trapezoidal filter of about 2.5 channels, i.e.  $\approx 0.15\%$  of the filter height which is of the order of the typical energy resolution of a HPGe detector, degrading the resolution by a factor of about  $\sqrt{2}$ .

The effect of DNL onto energy resolution was previously reported by [69] for a system using an 8 bit flash ADC and the method of remapping the ADC was used to correct the ADC DNL. However, the direct application of this method, which was successfully applied to the 8 bit ADC, did not improve the energy resolution due to the limited statistics of the DNL measurement. The usual approach to ADC DNL correction is dithering [70], i.e. the addition of a random signal (noise), which spreads the incoming signal over multiple channels<sup>22</sup>. Unfortunately, this method could not be used because of the pipelined structure of the ADC, which on the other hand allowed to simplify and improve the method of [69], as will be explained next. In figure 4.17 the effect of the ADC DNL is plotted versus the ADC offset, i.e. the baseline of the preamplifier signal, directly in front of the leading edge of the detector signal, i.e. the ADC offset. As derived in figure 4.16, the ADC DNL leads to different filter heights, i.e. different energies, if the ADC offsets changes. In figure 4.17 this effect is shown for measured detector signals, leading to a shift in peak position, which is plotted on the x-axis. The peak shift is only visible in panel (b), where the peak position is plotted versus the ADC range (8:5) and not for the 5 LSBs (4:0) shown in panel (a). This effect is caused by the pipelined structure of the AD6645, which converts the analog input in three steps into a digital word as explained in section A.2.3. Figure 4.17 suggests that the second stage of the conversion process is responsible for the peak shift. This explains why dithering would not improve the ADC performance. The noise that has to be added to the detector signal has to be large enough to affect the second ADC stage, i.e. the noise amplitude should be larger than 32 ADC units. The addition of such a noise signal would definitely decrease the energy resolution for low energy signals and in order to decrease the step noise contribution for the energy measurement the peaking time of the trapezoidal filter would have to be increased.

The DNL measurement and subsequent correction of individual stages of pipelined ADCs is a standard technique [71, 72, 73]. Since such a self-calibration is not mentioned in the AD6645 data sheet, it is likely to assume that the AD6645 architecture does not include a self-calibration. Therefore, the DNL of the AD6645 was corrected after A/D conversion. It is advantageous to calibrate each ADC stage individually, since this reduces the amount of memory needed for the storage of the calibration coefficient. Instead of  $2^{14} = 16384$  only  $2^4 + 2^5 + 2^5 = 80$  coefficients need to be stored. Since the correction coefficients cannot be obtained directly from the DNL histogram, a new method was applied, using a two dimensional plot of the ADC offset versus the peak position, i.e. energy. As can be seen from figure 4.18, the peak position changes with the ADC offset if the decay time  $\tau$  is not correctly adjusted. In order to obtain the best energy resolution, the peak position should be *independent* of the ADC offset since any shift in peak position broadens the energy peak. However, a perfect adjustment of the  $\tau$  parameter, i.e. the pole-zero cancellation, is impossible since the effect can only be seen at high

<sup>21</sup>The moving average process leads to sub-channel precision.

<sup>22</sup>The step noise contribution of the detector/preamplifier can be regarded as an intrinsic dithering.

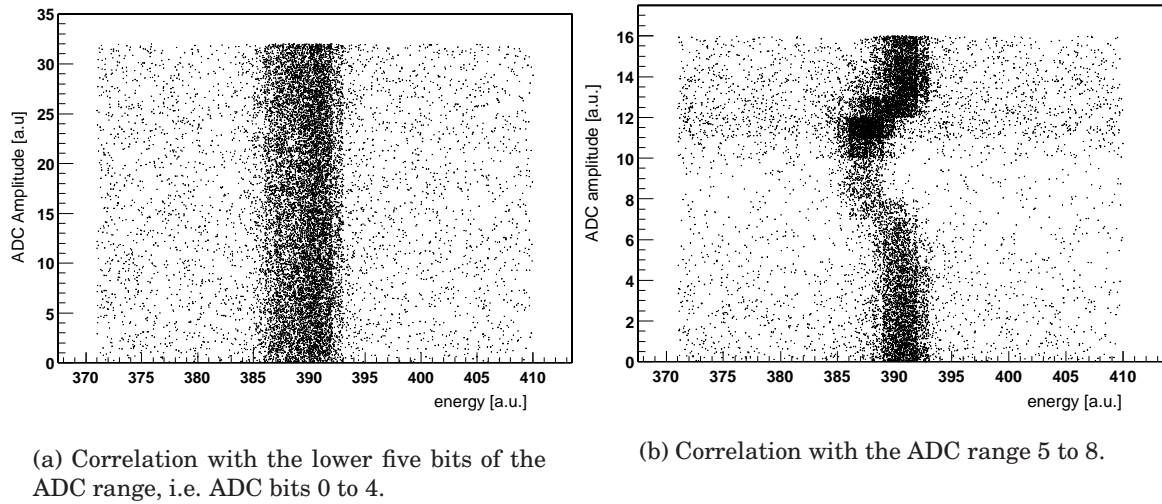


**Figure 4.17:** Correlation of the energy peak shift with the ADC offset. The ADC offset is defined as the ADC code directly in front of the leading edge of the detector signal. In panel (a) only the lower five bits of the ADC offset are shown and in panel (b) the bits 5 up to 8 are plotted versus the peak position. (b) demonstrates that only a certain part of the ADC, probably the second stage of the pipelined ADC, is responsible for the peak shift.

event rates, i.e. when the DNL effect is large. The distortion of the energy spectra due to the ADC DNL prevents any precise  $\tau$  determination. In order to be independent of the decay time  $\tau$ , the algorithm uses a linear regression and simply minimizes the width of the correlation in figure 4.18, neglecting the slope, by adjusting the 16 ADC correction coefficients. Since the lower five bits of the ADC range are ignored, i.e. averaged, the absolute DNL error increases to about three channels, which eases the determination of the correction coefficients and explains the removal of the 2 LSBs. The DNL correction coefficients replace the lower two bits of the ADC range and add two fractional bits, converting the 14 bit ADC word into a 16 bit word. The ADC calibration therefore works as follows. The ADC data word is extended by two fractional bits. The 4 LSB (including the fractional bits) are given by a LUT which is addressed using the ADC range (8:5). The 4 LSB are initially set to a certain value, e.g.  $1.5_{10} = 01.10_2$ . The algorithm tries to optimized the energy resolution by increasing (e.g.  $01.11_2$ ) or decreasing (e.g.  $01.01_2$ ) the channel width in dependence of the ADC range (8:5) until no further improvement can be achieved. The resulting table is shown in B.2 and the improvement in energy resolution is demonstrated in figure 4.19.

Once the ADC correction coefficients have been determined, the linear regression can be used to determine the decay time parameter  $\tau$ , by simply changing the  $\tau$  value until the slope of the linear regression is infinite (maximized). This is the definition of a perfect  $\tau$  adjustment, i.e. the position of the peak is then independent of the ADC offset as compared to the  $\tau$  settings in figure 4.18. The best value for  $\tau$  was determined to  $48.7 \mu\text{s}$ <sup>23</sup>. The result of the ADC DNL and  $\tau$  calibration process is shown in figure 4.19. The double-peak structure, originating from the dependence of the energy on the ADC offset,

<sup>23</sup>The algorithm was started with different step sizes, leading to best values for  $\tau$  of 48.5, 48.7 and 48.69  $\mu\text{s}$  for a steps size 0.5, 0.1 and 0.01  $\mu\text{s}$  respectively

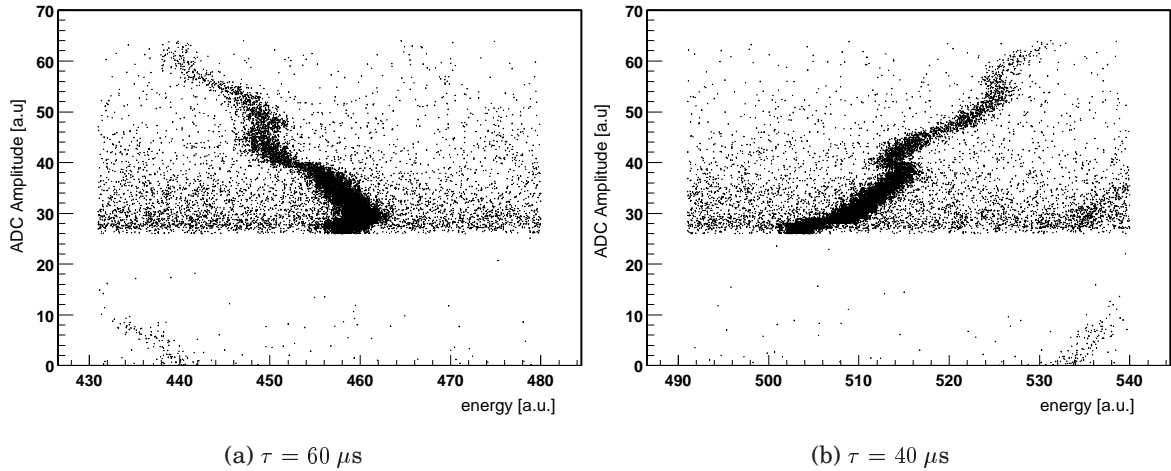


**Figure 4.18:** The effect of the decay time onto the energy resolution. If the decay time is not correctly adjusted, then the energy will depend on the offset of the ADC signal and consequently the energy peak will broaden as can be imagined by projecting the plot onto the x-axis.

$\gamma$ energy	Resolution before (FWHM)	Resolution after (FWHM)
121.8 keV	1.9 keV	1.7 keV
344.3 keV	3.5 keV	1.8 keV
1408.0 keV	2.7 keV	2.3 keV

**Table 4.3:** Energy resolution before and after ADC DNL correction using an  $^{152}\text{Eu}$  source. At 344 keV the peak distortion due to the ADC DNL is most prominent and therefore the effect of the ADC calibration is most obvious. It should be noted that the peaking and gap time were set to  $L = 5$  and  $M - L = 1 \mu\text{s}$  only, due to the limited amount of waveform data, leading to a decrease in energy resolution especially at low  $\gamma$  energies.

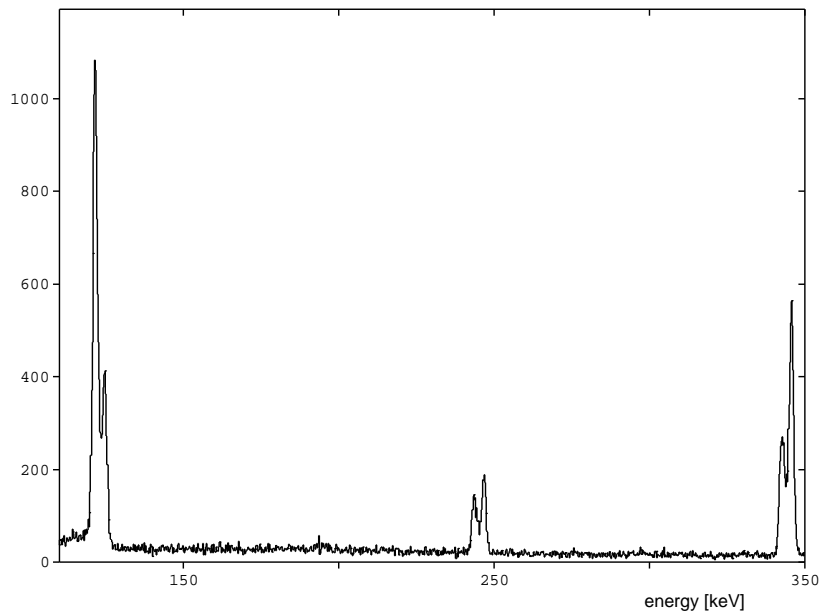
can successfully be removed and the energy resolution improves even for the low energy line of 121 keV, demonstrating that the method improves the energy resolution over the whole range of the spectrum as shown in table 4.3.

#### 4.7.2 Measurement with a NaI detector

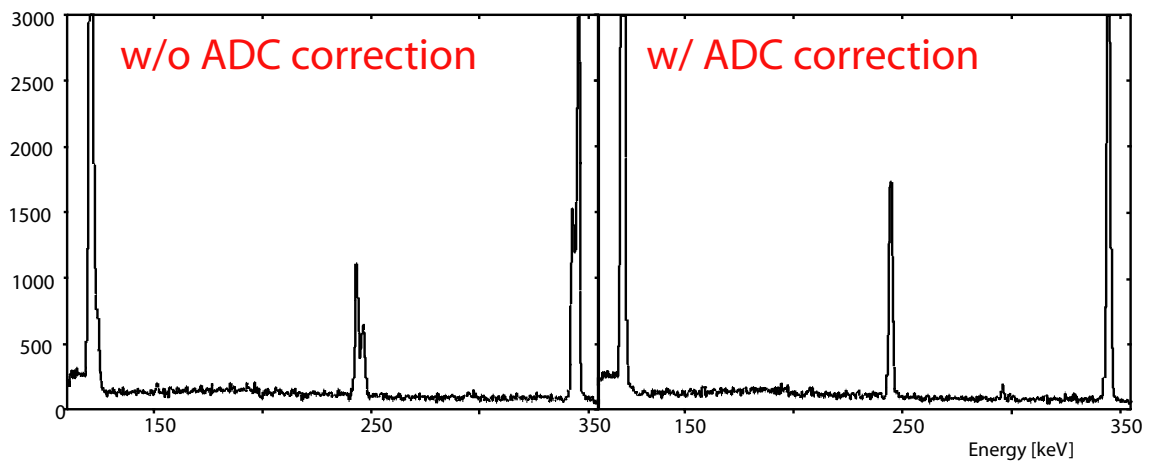
Since the energy resolution of a typical NaI detector is of the order of about 7-9 %, the readout of such a detector is less demanding with respect to energy resolution but, since the duration of the signal is less than  $1 \mu\text{s}$ , a fast ADC is necessary.

The firmware was not modified for this measurement but the MWD algorithm was operated to work as a charge integrator. By looking at the equation for the deconvolution  $\text{MWD}_m[n] = D_m[n] + \frac{1}{\tau} \text{MA}_m[n]$  it is obvious that if  $\tau$  decreases the contribution from the moving average increases, which can therefore be used to integrate the output of the NaI scintillator. A spectrum, acquired with such a configuration, is shown in figure 4.20, demonstrating that the approach is feasible.

However, if the GRT4 is used with NaI detector only, the firmware can be simplified, especially the wide range of shaping times and the multiplier are not necessary.



(a) Low energy part of a  $^{152}\text{Eu}$  energy spectrum acquired with the GRT4.



(b) Simulated spectra before and after DNL correction using 2k waveforms acquired with the GRT4.

**Figure 4.19:** Effect of the DNL correction onto the  $\gamma$  energy spectra. Panel (a) shows an example of a measured spectrum using an  $^{152}\text{Eu}$  source that was put close to the detector in order to achieve an event rate of about 10 kHz. In (b) the effect was reproduced using the MWD algorithm applied to stored waveforms of  $25.6 \mu\text{s}$ . Then the DNL correction coefficients were included in the offline analysis leading to the spectrum on the right side, which shows no indications of DNL effect, especially the double-peak structure has been removed. The offline spectrum shows less details especially at the 121 keV line, which is due to the shorter peaking time that was used compared to the online spectrum because the acquired waveforms of  $25.6 \mu\text{s}$  did not allow to use the same filter parameters for online and offline analysis.

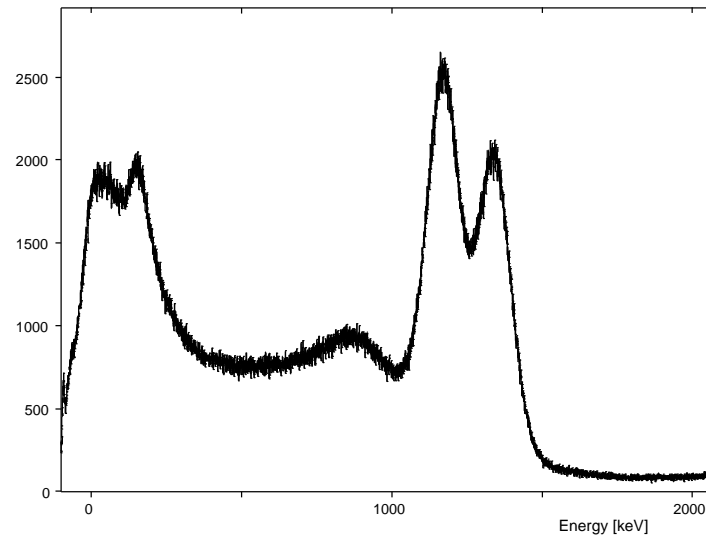


**Figure 4.20:**  $^{60}\text{Co}$  spectrum acquired with a GRT4 and a NaI detector. Note that the spectrum extends to negative energy values indicating that the baseline restorer was not working as expected and that the trigger algorithm produces many noise triggers. Nevertheless, the readout of such a detector seems feasible but the firmware of the ADC FPGA has to be modified for this type of detector.

Apart from the trapezoidal filter, different digital filters have been successfully applied to NaI signals [74]. The baseline restorer of the MWD implementation was not working as expected and therefore the baseline peak is visible at about zero energy in the NaI spectrum in figure 4.20. This measurement shows that the GRT4 module is capable of processing pulses from a NaI detector, but the resolution is only about 14 % which needs to be investigated further. More work is necessary to implement a simple firmware for NaI detectors and add pulse shape discrimination techniques, to distinguish and identify different particles interacting in the scintillation detector [29, 74].

### 4.7.3 Measurements with an ORTEC HPGe detector

The first measurements were performed with an unsegmented HPGe detector from ORTEC. Ballistic deficit effects limit the energy resolution in large Germanium detector with remarkable rise time variations. Nevertheless, a smaller HPGe detector can also be used to test the functionality of the MWD implementation and therefore the ORTEC detector was used whenever the MINIBALL detector was not accessible. Table 4.4 summarizes the results obtained and the corresponding energy spectra obtained with  $^{60}\text{Co}$  and  $^{152}\text{Eu}$  sources are shown in 4.21.

In figure 4.22 the most important parameters of the MWD algorithm, the peaking ( $L$ ) and the flat top time ( $M - L$ ), were investigated, showing that the minimum peaking time to obtain a good energy resolution is about  $L = 5 \mu\text{s}$  and the minimum flat top time is  $M - L = 1 \mu\text{s}$ . In order to achieve a high throughput and a high energy resolution, the flat top time need not to be increased further and, since the next event can happen directly after the flat top, the dead time of the trapezoidal filter time is then in the order of  $6 \mu\text{s}$ . The exact value depends on the setting of the pileup inspection period parameter.

Compared to the peaking times of an analog shaping amplifier shown in figure 4.23,

$E_\gamma$	Resolution (FWHM)
121.8 keV	1.3 keV
344.3 keV	1.4 keV
778.9 keV	1.7 keV
1332.5 keV	2.1 keV
1408.0 keV	2.0 keV

**Table 4.4:** Energy resolution achieved with the ORTEC detector and the GRT4 VME module at different energies  $E_\gamma$  combining measurements made with  $^{60}\text{Co}$  and  $^{152}\text{Eu}$  sources. The peaking and flat top time of the trapezoidal filter were set to  $L = 7.2$  and  $M - L = 2 \mu\text{s}$  respectively.

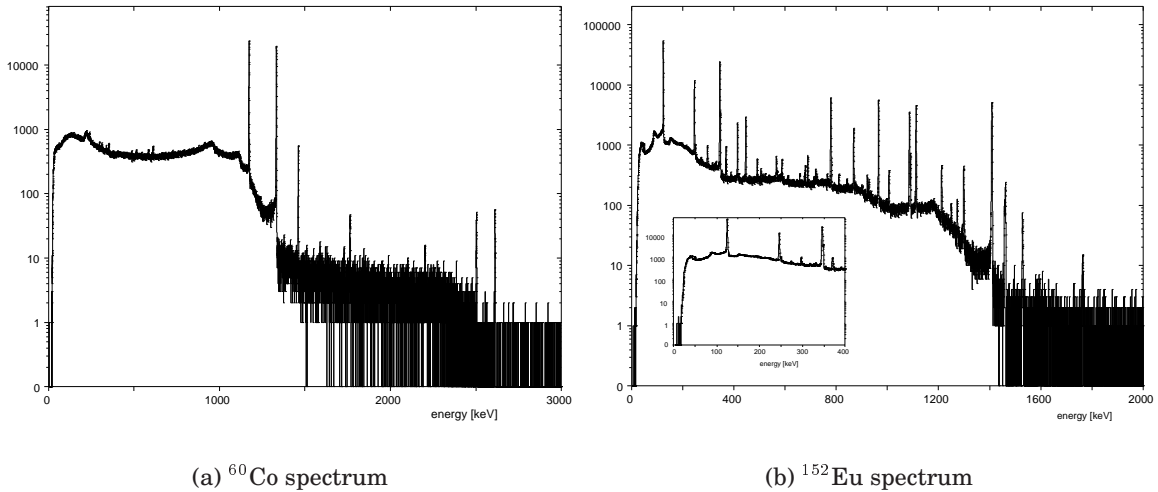


**Figure 4.21:** Spectra acquired with the GRT4 and the ORTEC detector using two different sources, a  $^{60}\text{Co}$  and a  $^{152}\text{Eu}$  source. In the  $^{60}\text{Co}$  spectrum the pile up events are visible at the sum of the fundamental  $\gamma$  energies. The inset in the  $^{152}\text{Eu}$  spectrum shows the low energy range.

the digital shaper is best compared to the  $3 \mu\text{s}$  shaping time setting which shows a peaking time of  $6.6 \mu\text{s}$  and achieved an energy resolution of  $2.4 \text{ keV}$ , whereas with the  $6 \mu\text{s}$  shaping time an energy resolution of  $2 \text{ keV}$  at  $1332.5 \text{ keV}$  was reached. Comparing this result to that compiled in table 4.4 leads to the conclusion that the trapezoidal shaper yields a higher energy resolution at the same peaking time.

The XIA DGF-4C module delivers an energy resolution of  $2 \text{ keV}$  at an energy of  $1.3 \text{ MeV}$  using a peaking time of  $7.2 \mu\text{s}$  and a gap time of  $2 \mu\text{s}$ , which is comparable to the energy resolution measured with the GRT4 module and the MWD algorithm.

A measurement with an  $^{152}\text{Eu}$  source was used to determine the (integral) linearity of the energy spectrum as shown in panel (a) of 4.24. The lowest and the highest energy line in the spectrum, the  $121$  and the  $1408 \text{ keV}$  lines, were used for the calibration and the position of the  $\gamma$  lines in between can be compared to that obtained from the fitted function. Since the deviation exceeds almost the energy resolution at some positions, an ADC calibration (which was not implemented at that time) is needed for high resolution spectroscopy. Panel (b) of figure 4.24 demonstrates that the energy resolution increases

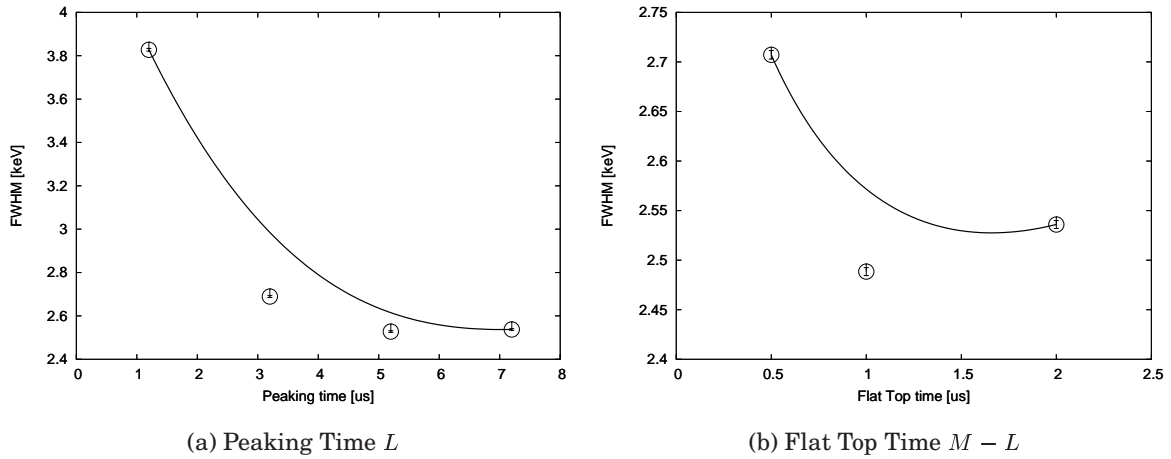


**Figure 4.22:** Dependence of the energy resolution measured with  $^{60}\text{Co}$  and the filter parameter peaking and gap time. The energy resolution improves with increasing peaking time up to a peaking time of  $L = 5.2 \mu\text{s}$ , above which no improvement can be achieved (at the investigated energy of 1332.5 keV) by increasing the peaking time. The minimum flat top time is  $M - L = 1 \mu\text{s}$  as can be seen from panel (b), increasing the flat top time further does not improve the energy resolution.

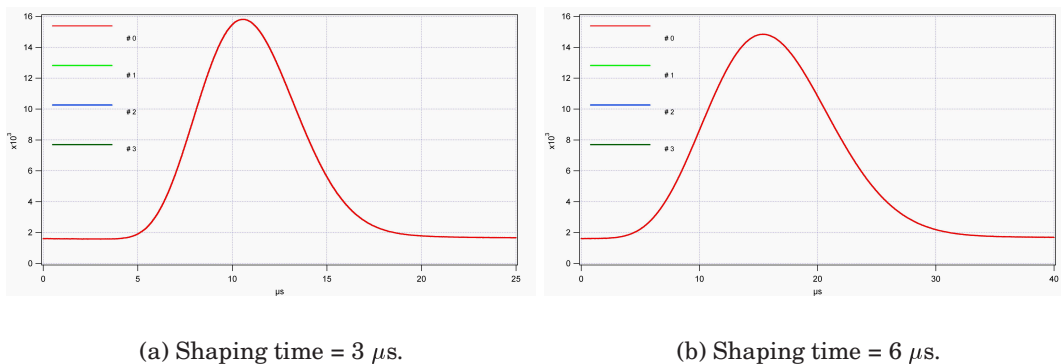
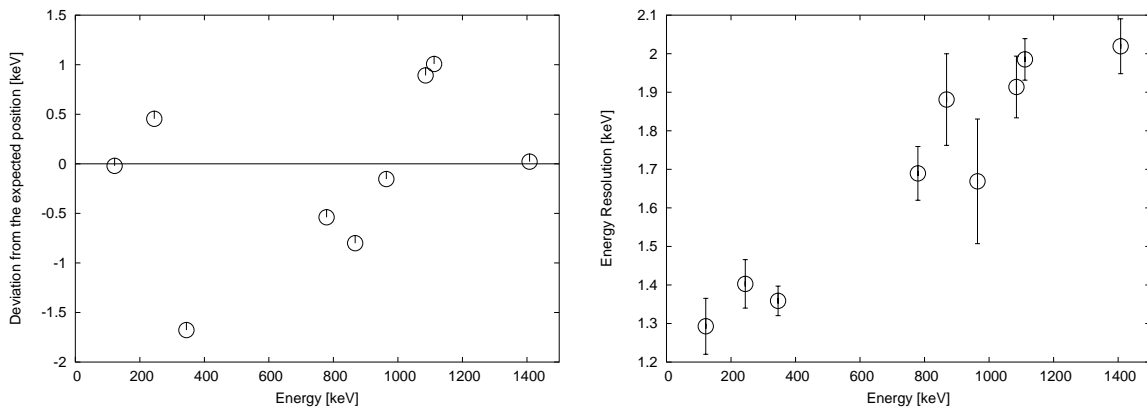
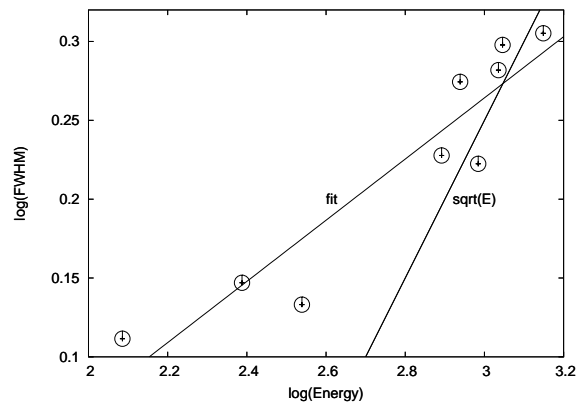


**Figure 4.23:** Signal shape of an analog spectroscopy amplifier ORTEC 671 for shaping times of 3 and 6 μs. This semi-gaussian shaper has to be compared to the trapezoidal shape of the digital filter. Note that the actual peaking time of the signal is 2.2 times the shaping time [68], which causes a large dead time. This clearly demonstrates the advantage of the trapezoidal shaper which yields a better energy resolution at the same peak time, resulting in a higher throughput due to the reduced dead time of the energy filter. The 3 μs setting achieved an energy resolution of 2.4 keV, while the 6 μs setting achieved a FWHM of 2 keV at 1.3 MeV.



(a) Deviation of the peak position from a linear function (Integral non-linearity).

(b) Energy dependence of the resolution.



(c)  $\log(\text{FWHM})$  versus  $\log(E_\gamma)$

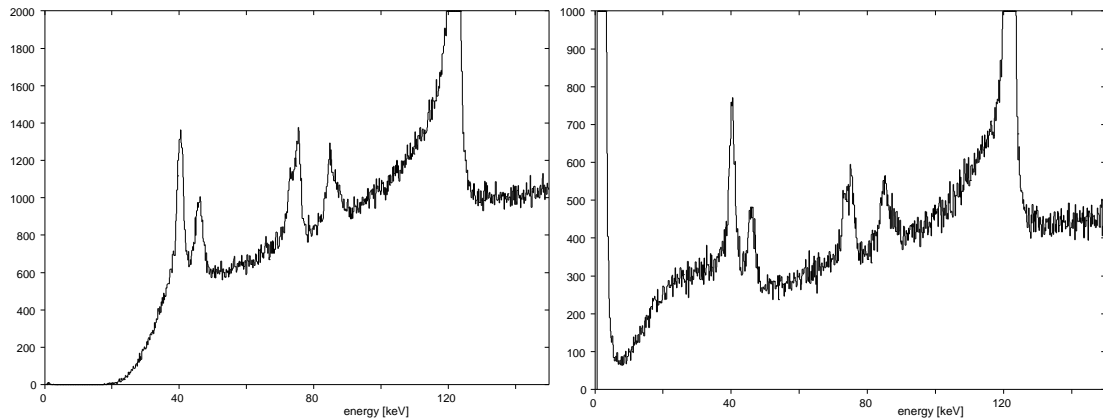
**Figure 4.24:** Energy dependence and linearity of the energy resolution measured with an  $^{152}\text{Eu}$  source. The detector was operated at 2000 V only, which is rather low compared to the recommended high voltage of 3500 V.

from 1.3 keV at 121 keV to 2 keV at 1408 keV. Below the *transition energy* [75] the energy resolution is dominated by the electronics noise and this should be visible as a constant from the plot in panel (c) of figure 4.24. Above the transition energy, the energy resolution is dominated by the statistics of the charge carrier production and the energy resolution should be proportional to  $\sqrt{E_\gamma}$ . However, the transition energy could not be determined.

#### 4.7.4 Measurements with a MINIBALL HPGe detector

A set of measurements was performed with a single crystal from one of the MPI owned MINIBALL triple cluster detectors.

The setting of the trigger threshold can be judged by observing the appearance of the pedestal in the energy spectrum as shown in figure 4.25. The difference between the two spectra is the additional peak at zero energy, the pedestal, due to noise triggers



(a) The trigger threshold is high enough to avoid noise triggers.

(b) The trigger threshold is too low, causing many noise triggers. The pedestal, zero energy peak, is visible.

**Figure 4.25:** Adjusting the trigger threshold for the measurements with an  $^{152}\text{Eu}$  source. It is important to configure the trigger such that noise triggers are prevented, since otherwise the baseline restorer will not get enough baseline samples and the energy resolution will decrease. The pedestal is clearly visible in the spectrum if the threshold is set too low, as it is the case in panel (b), where the baseline peak starts below 7 keV.

leading to baseline samples that appear in the energy spectrum after subtraction of the baseline average. Clearly, the subtraction of the baseline average from the baseline event could result in a negative energy value, but these values are suppressed in the spectrum. From figure 4.25 and the estimate of the dynamic range of about 6 MeV, it can be concluded that a trigger threshold of 1 % of the dynamic range can be easily achieved, which is reported for other digital spectrometers, e.g. [13], and that with further tuning a reduction by a factor of two seems feasible.

The energy resolution determined with the DGF-4C was 2.58 keV for the 1332.5 keV line of  $^{60}\text{Co}$ . Using the MWD implementation on the GRT4 module with the EA BLR the energy resolution is 2.54 keV and with the MA BLR the energy resolution is 2.56 keV, i.e. the energy resolutions are equal. For the large MINIBALL detector, the energy resolution was mainly determined by the performance of the baseline restorer.

### Exponential Averaging Baseline Module

The dependence of the energy resolution on the filter parameters was measured with  $^{152}\text{Eu}$  and  $^{60}\text{Co}$  sources. The GRT4 firmware for these measurements featured the MWD trapezoidal filter followed by a baseline restorer based on the exponential averaging. The ADC data was decimated by a factor of four.

The dependence of the energy resolution on the decay time parameter  $\tau$  could not be derived, because the spectra were acquired at an event rate of about 1 kHz, i.e. baseline shifts are expected to happen very seldom. If the deconvolution is disabled by setting the decay time coefficient  $\tau$  to infinity, then the resolution degrades by only 0.3 keV at an event rate of 1 kHz. Therefore,  $\tau$  was set to 46  $\mu\text{s}$  for all measurements.

The results for the  $^{152}\text{Eu}$  measurements are compiled in figure 4.26. The results for the dependence of the energy resolution on the flat top time  $M - L$  are ambiguous. For an energy of 121 keV the resolution decreases above  $1 \mu\text{s}$ , whereas for an energy of 1408 keV, the best energy resolution was obtained for a flat top time of  $2 \mu\text{s}$ . However, in both cases the gap time should be set to the minimum value that allows a good energy resolution, since the energy resolution decreases with increasing flat top time as can be seen from the  $4 \mu\text{s}$  setting.

The energy resolution improves with increasing peaking time  $L$ , as shown in panel (c) and (d) in figure 4.26. For the high energy line of 1408 keV energy, the optimal energy resolution is obtained with peaking times of  $5.2$  to  $7.2 \mu\text{s}$ , suggesting the usage of the shorter peaking to increase the throughput. However, for the low energy line of 121 keV, the energy resolution improves up to an peaking time of  $L = 7.2 \mu\text{s}$ , indicating that the noise from the detector and electronics influences the energy resolution at low energies, i.e. small signal amplitudes. For high energy signals the best resolution is achieved at shorter shaping times compared to the low energy signals, where a further increase in peaking time yields a better energy resolution.

For the scan of the peak sample delay PS the flat top time  $M - L$  was set to  $2 \mu\text{s}$  and the peaking time  $L$  was set to  $7.2 \mu\text{s}$ . It is obvious from the panels (e) and (f) in figure 4.26 that the energy resolution is almost independent of the peak sample delay PS as long as the sampling happens during the flat top period. If the delay is increased further, the resolution decreases strongly. Care has to be taken, when using the GRT4 with external or different internal trigger signals, since then the peak sample delay PS has to be adjusted differently. Nevertheless, energy spectra were acquired using an analog CFD and this method will be used for the scanning of the highly segmented AGATA detector [76], since a common trigger signal is needed to acquire signal from contacts that see no or an induced signal only.

The performance of the GRT4 was also tested using a  $^{60}\text{Co}$  source at an event rate of about 800 Hz. Panel (a), (b) and (c) of figure 4.27 confirm the previous results, i.e. the flat top time should not exceed  $2 \mu\text{s}$ , the optimum the peaking time is  $L = 7.2 \mu\text{s}$  and the peak capture delay can be adjusted over a wide range, but should not exceed a maximum value leading to a strong degradation in energy resolution. The best value for the coefficient  $\alpha$  of the exponential averaging was determined by fixing the update frequency BU of the baseline restorer to  $2 \mu\text{s}$  and varying the baseline parameter  $\alpha$ . The best energy resolution was obtained with a setting of 6 which is equivalent to  $\alpha = 2^{-7}$  due to the implementation, i.e. the actual baseline sample contribute only  $\frac{1}{128}$  to the baseline average.

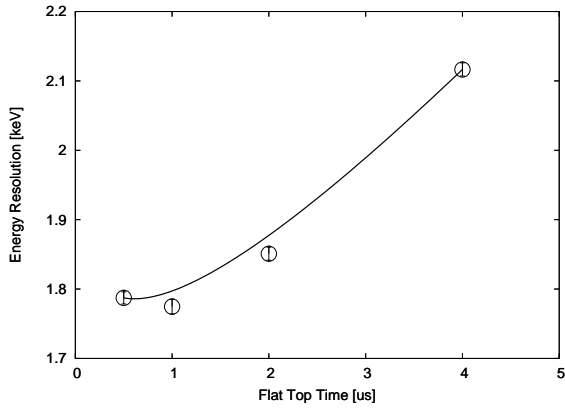
Panel (e) of figure 4.27 shows the number of acquired baseline samples during the acquisition of  $10^3$  events<sup>24</sup>. As expected, the number of acquired baseline samples decreases with increasing update period BU, showing the baseline sampling process is working as expected.

The relaxation time of the exponential averaging filter can be obtained by determining the time when the filter signal reaches  $\frac{1}{e}$  of the initial amplitude after a delta input signal

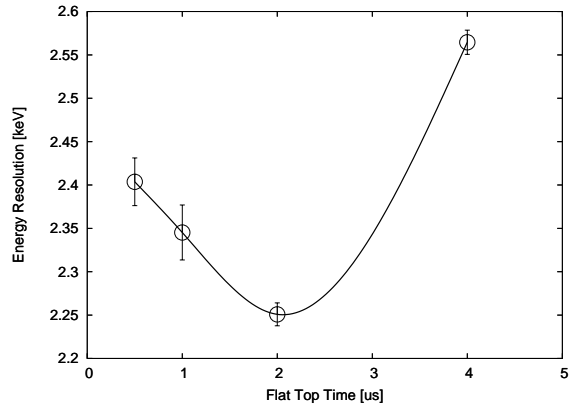
$$A[n] = (1 - \alpha)^n A[0] = \frac{A[0]}{e} \quad (4.2)$$

---

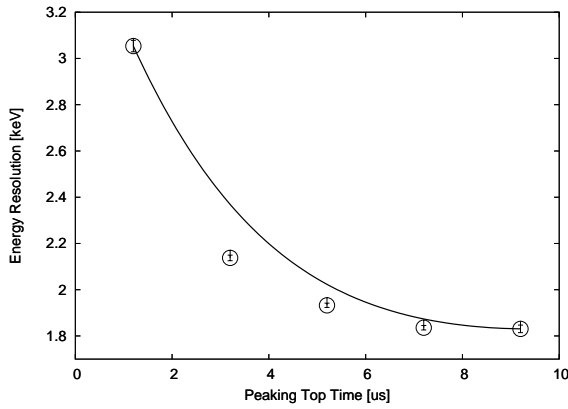
<sup>24</sup>Acquisition of data for a preset live time are not yet supported by the GRT4 firmware.



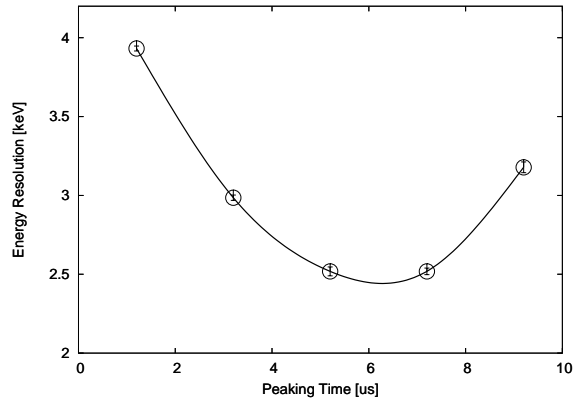
(a) Flat top time  $M - L$  for 121 keV.



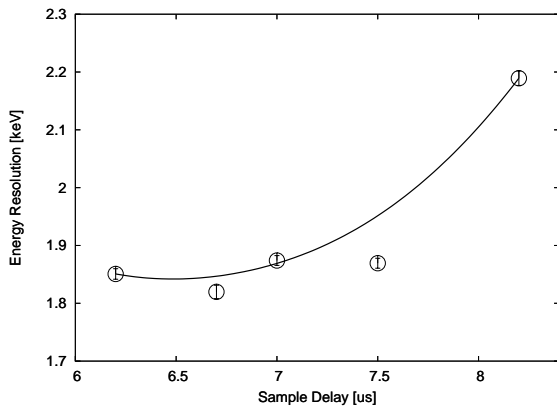
(b) Flat top time  $M - L$  for 1408 keV.



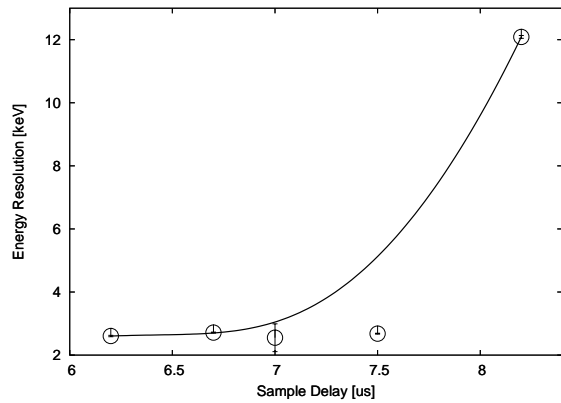
(c) Peaking time  $L$  for 121 keV.



(d) Peaking time  $L$  for 1408 keV.

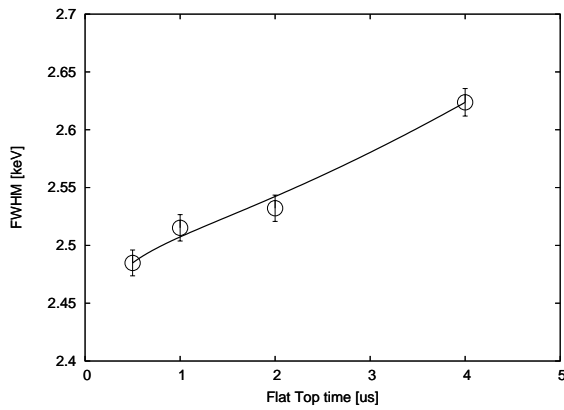


(e) Peak sample time PS for 121 keV.

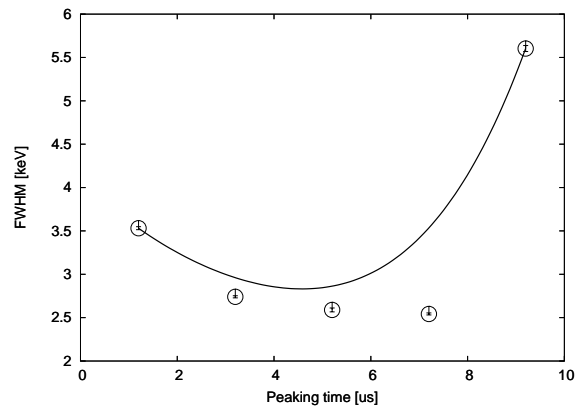


(f) Peak sample time PS for 1408 keV.

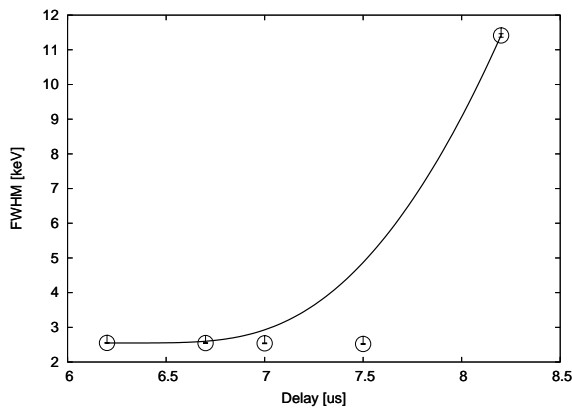
**Figure 4.26:** Dependence of the energy resolution on the MWD filter parameters for two  $^{152}\text{Eu}$  lines of 121 and 1408 keV.



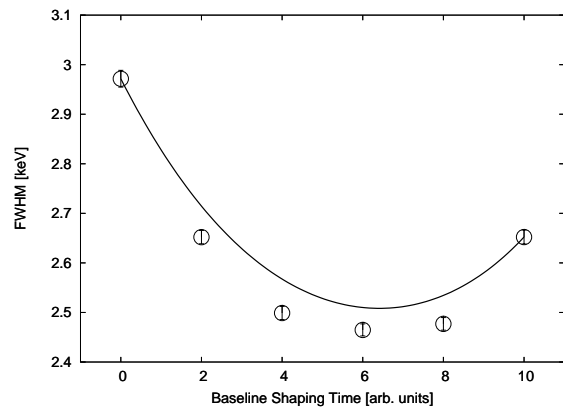
(a) Flat top time  $M - L$  for 1332.5 keV.



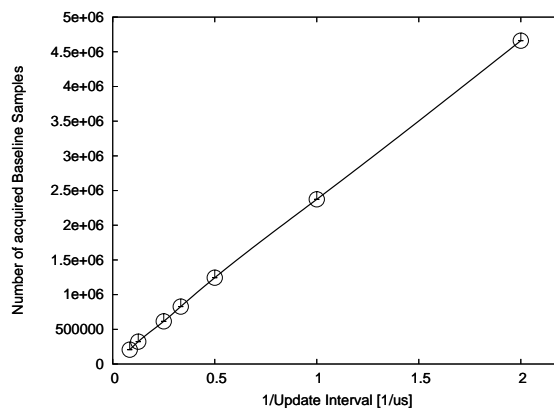
(b) Peaking time  $L$  for 1332.5 keV.



(c) Peak sample time PS for 1332.5 keV.



(d) Baseline parameter  $\alpha$  for 1332.5 keV.



(e) Number of accepted baseline sample during acquisition of  $10^3$  event versus  $1/BU$ .

**Figure 4.27:** Dependence of the energy resolution on the MWD filter parameters measured with a  $^{60}\text{Co}$  source. The baseline update period has to be larger than  $1 \mu\text{s}$  to obtain a good energy resolution.

$\alpha$	n [samples]	n [ $\mu$ s]
$2^{-1}$	1.4	2.9
$2^{-2}$	3.5	7
$2^{-3}$	7.5	15
$2^{-4}$	15.5	31
$2^{-5}$	31.5	63
$2^{-6}$	63.5	127
$2^{-7}$	127.5	255

**Table 4.5:** Relaxation time of the exponential averaging filter for different  $\alpha$ . The second column shows the relaxation time in sample ticks which are translated into time units using the typical baseline update period of 2  $\mu$ s.

$$n = -\frac{1}{\ln(1 - \alpha)}. \quad (4.3)$$

The typical relaxation times are compiled in table 4.5 for a baseline sampling period of 2  $\mu$ s, which is the typical value used in the measurements. The optimal energy resolution is obtained for a setting of  $\alpha = 2^{-7}$ , equals a MWD setting of 6, i.e. the optimal relaxation time is about 250  $\mu$ s.

### Moving Average Baseline Module

In addition to the BLR based on the exponential averaging, also a BLR based on a moving average (MA) filter was implemented, since the previous tests in section 2.5.4 were very promising. However, unlike the EA BLR which functions perfectly, the alternative MA BLR was found to have some shortcomings. It was unable to reach a stable operating condition over a longer period. Especially, if the update period BU was set below 1  $\mu$ s, the spectra were strongly distorted. However, a few tests could be performed which indicate that the MA baseline restorer could yield an equivalent performance as the baseline restorer based on the exponential averaging, which was used all the time. Table 4.6 summarizes the results of the measurements. If the baseline update period was set to 1  $\mu$ s or less, the spectra were distorted and therefore no energy resolution could be determined. The energy resolution without baseline restorer is about 4.8 keV and with baseline restorer the energy resolution improves to 2.6 keV. Furthermore, the baseline interval, i.e. the total amount of pre-event data averaged by the BLR, is a useful parameter for evaluating the performance of the MA baseline restorer. The baseline interval is calculated by multiplying the update period with the length of the moving average, i.e. baseline interval = MA length  $\times$  update period BU. From table 4.6, the minimum baseline interval is estimated to be 256  $\mu$ s. If the baseline interval is shorter, e.g. for the first two entries, then the resolution decreases up to the value without baseline restorer in the case of an update interval of 32  $\mu$ s, which is definitely too short.

The optimal baseline interval of 256  $\mu$ s corresponds nicely to the optimal relaxation time of 255  $\mu$ s for the exponential averaging, showing the equivalence of these parameters and that the performance of the baseline restorer depends mainly on these two parameters.

Length	BU	Interval	FWHM @ 1172 keV	FWHM @ 1332.5 keV
16	2 $\mu$ s	32 $\mu$ s	4.00(7) keV	4.14(6) keV
32	4 $\mu$ s	128 $\mu$ s	3.02(6) keV	2.92(6) keV
32	8 $\mu$ s	256 $\mu$ s	2.56(6) keV	2.61(6) keV
128	0.5 $\mu$ s	64 $\mu$ s	-	-
128	1 $\mu$ s	128 $\mu$ s	-	-
128	1.2 $\mu$ s	154 $\mu$ s	2.88(5) keV	2.86(9) keV
128	1.5 $\mu$ s	188 $\mu$ s	2.74(6) keV	2.72(5) keV
128	2 $\mu$ s	256 $\mu$ s	2.41(6) keV	2.56(5) keV
128	4 $\mu$ s	512 $\mu$ s	2.46(2) keV	2.70(4) keV
128	8 $\mu$ s	1024 $\mu$ s	2.39(6) keV	2.58(5) keV
128	8 $\mu$ s	1024 $\mu$ s	4.6(1) keV	4.75(7) keV

**Table 4.6:** Energy resolution achieved with the baseline restorer based on moving average. The last row displays the typical energy resolution *without* baseline restorer, using the trapezoidal filter only. Again, using the baseline restorer improves the energy resolution by almost a factor of two. If the baseline restorer averages at least the previous 256  $\mu$ s (Baseline Interval = MA Length  $\times$  Update Period) of data, a good energy resolution is achieved. The DGF-4C module achieves an energy resolution of 2.58 keV at 1.3 MeV.

In order to further separate the exponential averaging from the moving average baseline restorer, more measurements have to be performed, especially at high event rates, which again requires the ADC DNL correction. In addition the longterm stability of the baseline average and the reason why the MA BLR fails at update periods below 1  $\mu$ s have to be investigated.

### Test of the pile up rejection

In order to test the functionality of the pile up rejection circuitry, which is part of the state machine, energy spectra were acquired at a high event rate and with varying settings for the pile up rejection period PU.

The pileup rejection period is measured using a counter that starts counting after a trigger signal. If another event trigger happens during the pileup rejection period then no event is acquired and the counter is restarted and the pileup inspection period starts again. The dead time of such a system is described with the extendable dead time model [32]. Such a system can be *paralyzed* by increasing the event rate such that no event is acquired because of continuous pile up<sup>25</sup>.

The energy filter was set to 7.2 and 2  $\mu$ s peaking and flat top time, respectively. If the energy value is latched at the end of the flat top period then a pile up rejection period of 9.2  $\mu$ s should be sufficient. Indeed, the distortion of the spectra plotted in figure 4.28 caused by event pile up are removed as soon as the pile up rejection period exceeds 10  $\mu$ s. For a pile up rejection period of 1 and 5  $\mu$ s, the peaks show strong tailing effects in addition to an increased background and a decreased energy resolution which smooths

<sup>25</sup>This can be easily verified with a pulser.

out the double-peak structure caused by the ADC DNL.

The tests confirm the proper operation of the pile up rejection operation. The pileup rejection performance is limited by the dead time of the trigger filter, i.e. if two events happen so close that the trigger filter cannot separate the two hits, then these pileup events will not be detected by the state machine.

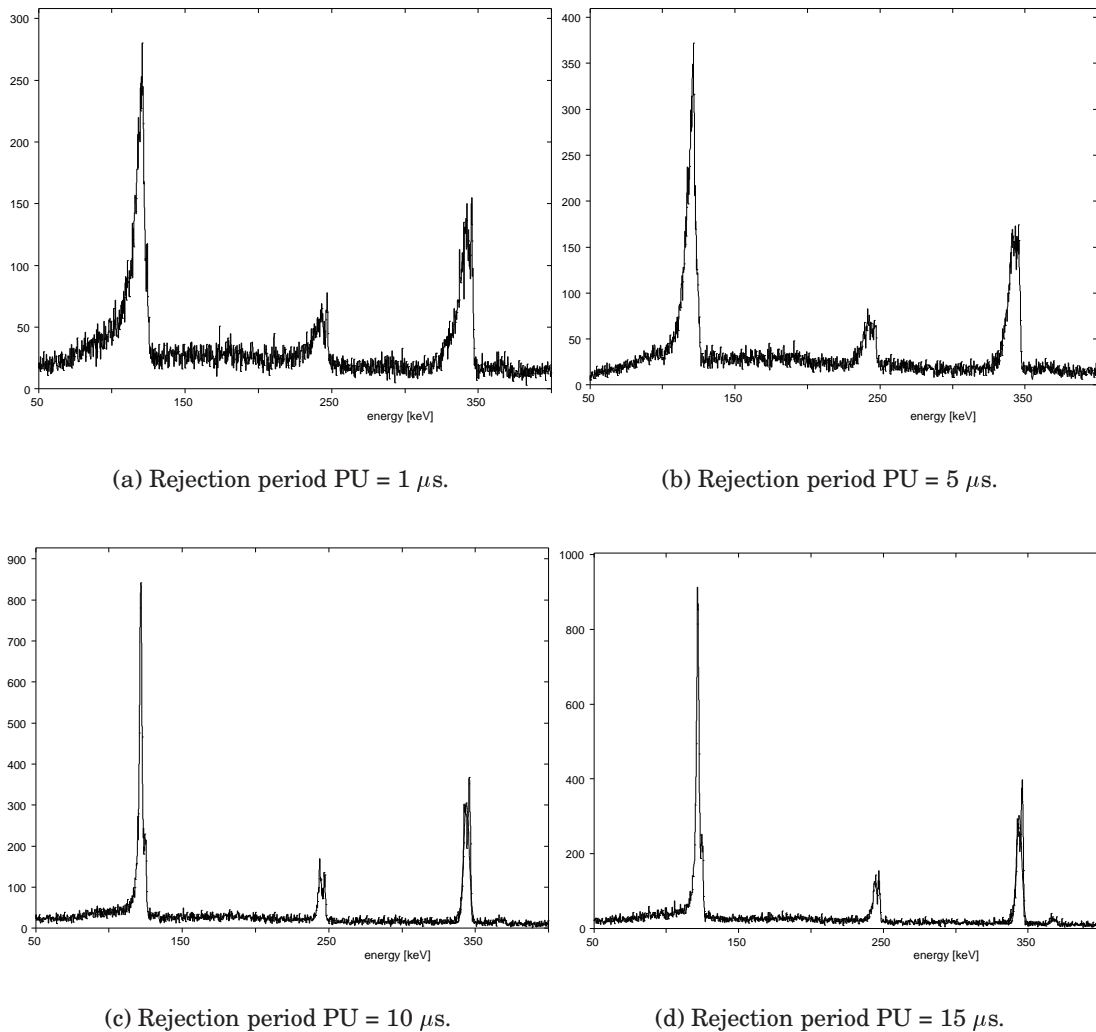


**Figure 4.28:** The influence of the pileup rejection period parameter  $PU$  on the energy spectra. The peaking time of the energy filter was set to  $L = 7.2 \mu s$  and the flat top time was set to  $M - L = 2 \mu s$ . A pile up rejection period of  $PU = 10 \mu s$  is therefore sufficient for this filter setting, increasing the rejection period further does not improve the energy spectrum but decreases the throughput. The double-peak structure in the spectra is caused by the DNL of the ADC, which was not corrected at that time.

## Chapter 5

# Conclusions and Outlook

”Being right too soon is socially unacceptable.” - Robert A. Heinlein

### 5.1 Realtime Pulse Shape Analysis

The pulse shape analysis algorithms for the MINIBALL HPGe detector array have been implemented for the digital signal processor, which is part of the XIA DGF-4C modules, and the developed user PSA code delivers the same position resolution as the offline analysis despite the differences in the implementations. A position resolution of about 1 cm was achieved, which is in accordance with the MINIBALL specifications [22].

Two digital timing algorithms have been implemented, the L-EBC and the Q-EBC algorithm. The shortcoming of the L-EBC, the sensitivity to sampling artifacts and insufficient approximation of the detector pulse shape, lead to the development of the Q-EBC algorithm, achieving the best time resolution, while retaining the same computational effort. The performance of the L-EBC algorithm was improved by introducing an additional factor (the ML-EBC algorithm), removing the additional side peaks in the coincidence spectra. The current implementation of the Q-EBC algorithm does not support the usage of the position of the steepest rise (SR) as a starting point for the algorithm, which was shown to be mandatory for a high efficiency. The time resolution was determined using two different data sets. While for the high  $\gamma$  energy data set a time resolution of about half of the sampling rate, i.e. 12.5 ns, could be achieved, the time resolution of the low energy data set was just below the sampling rate, i.e. about 20 ns. In addition, the time resolution was found to depend on the time stamp information TS, i.e. the triggering of the DGF-4C, varying between 17 and 23 ns.

The drift time of the electrons is determined using the steepest slope algorithm. The implementation supports an additional interpolation of the steepest slope position. The interpolation is not necessary since the steepest slope time is distributed over 2-3 sample intervals and can thus be disabled. The subtraction of the start time  $t_0$  is mandatory to be independent of the DGF trigger timing.

The best method to extract the mirror charge amplitudes from segments with energy deposition is the subtraction of an energy weighted MI segment signal, due to the similar pulse shape. This algorithm cannot be performed in realtime. The user DSP code therefore implements a linear approximation of the leading edge of the detector signal. The amplitude information is taken from the waveform while the timing information, i.e the signal rise time, can be supplied in different ways depending on the actual configuration.

In order to minimize the influence of the unknown depth of the (main) interaction on the position resolution the simulated average interaction depth is used in the analysis process, ensuring a calibration independent of irradiation geometry and  $\gamma$ -ray energy. The effect of the AID is most prominent for the aligned 3-cluster configuration, since the effect differs for each segment due to the different irradiation angles. The validity of the simulated AID  $z(E)$  was confirmed for the 1.3 MeV  $\gamma$  line of the  $^{60}\text{Co}$  source.

The position resolution in segment 1 of detector C at an energy of 1.3 MeV varies between 7 and 10 mm depending on the position of the interaction inside the detector volume with an overall position resolution of about 9 mm. In the center between core and segment contact, the angular resolution decreases due to the decrease in mirror charge amplitude. In addition, due to the non-perpendicular irradiation, positive and negative mirror charge amplitudes occur for the same collimator position. Using separate calibration parameters for the positive and negative polarities leads to an improvement in position resolution of about 25 %.

In order to ease the process of testing the user DSP code, a data base of reference signals, obtained with a collimated source, should be generated. The response of the user DSP code to the reference data set can be judge by comparing the results with that obtained using an offline analysis code without the need for a calibration in order to test the basic functionality of the implementation.

With the developed user DSP code the MINIBALL PSA can be performed on the onboard DSP of the DGF-4C modules after proper configuration of DGF-C and user DSP code. The granularity of the MINIBALL detector array will increase from 6 to about 60-100, depending on the electronics setup and the irradiation geometry.

## 5.2 Preprocessing Algorithms: MWD and GRT4

The current FPGA technology enabled the integration of a digital spectroscopy channel, including trigger and energy filters together with a long waveform buffer, into a single low-cost FPGA device. The energy resolution of the moving window deconvolution implementation for the GRT4 VME module exceeded the expectations, which is also due to the low noise of the GRT4 analog stage.

The supplementary modules generated for the energy filter, i.e. trigger filter and waveform buffer, performed as expected. For small systems the internal digital trigger allows a quick and remote setup of the GRT4, while for larger system, e.g. highly segmented HPGe detector, an external common trigger signal has to be fed onto the GRT4. The extended waveform buffer allowed for the investigation of the ADC non-linearities with slightly suboptimal filter parameters. For pulse shape analysis applications a single Block RAM, storing up to 3.2  $\mu\text{s}$  of data, is sufficient and is therefore foreseen for the final implementation [76].

The state machine allowed for an adjustment of the peak capture delay and the pile up rejection period, the proper operation was verified in various measurements. However, the waveform memory was not integrated into the MWD state machine. If waveform and energy are to be read in coincidence, then the pile up signal should be used to flag the events only, since the waveform buffer is stopped with each trigger. In order to enable the usage of the GRT4 in nuclear physics experiments, live and real time clocks have to be added to enable dead time correction if the implemented internal digital trigger algorithm is used.

The energy resolution at high  $\gamma$  energies is mainly limited by the detector. The trapezoidal shaping eliminates the risetime effects due to the adjustable flat top period and the BLR allows a proper suppression of the pedestal of the energy filter and improves the energy resolution considerably. The dependence of the energy resolution on the trapezoidal filter parameters was measured and the best energy resolution was obtained if the BLR averages the previous 256  $\mu\text{s}$  of energy filter data. At small  $\gamma$  energies the contribution of noise from the electronics becomes more important, which can be compensated by using longer peaking times  $L$ . The resolution at low energies is also very sensitive to ADC non-linearities and an initial DNL correction showed promising results. Further tests have to be performed after the non-linearity correction has been fully implemented and tested.

The non-linearities of the AD6645 ADC were corrected using a small look-up table and the energy resolution improved significantly over the whole energy range. The ADC non-linearity has to be investigated further using a pileup pulser to determine the correction coefficients for the full ADC range. First tests have already been performed with a different ADC confirming the observations [76]. If the observed non-linearities would be device dependent, each channel of the system would have to be calibrated individually and the obtained coefficients would have to be downloaded to the corresponding GRT4. In this case it would be advisable to evaluate ADCs from different manufacturers<sup>1</sup>.

The developed VHDL code enables the realization of a digital spectroscopy system at low cost and furthermore the conversion of commercially available waveform digitizers into a spectroscopy system. Since the VHDL code is largely independent of the FPGA architecture, the code can be synthesized for other XILINX FPGAs allowing the setup of a digital DAQ system based on commercially available digitizer modules with user FPGAs<sup>2</sup>. A more resource saving variant of the MWD code has been developed and simulated including 8 spectroscopic channels into a single Spartan 2 FPGA. Based on the existing code, the MWD algorithm can be tailored quickly to new detectors and applications.

For the characterization of the AGATA detector at the University of Liverpool, the GRT4 cards will be used. First tests were already performed with a highly segmented detector [76]. Based on the experience gained with the MWD and the GRT4, new electronics are currently in the planning or design phase, a dedicated electronics for the  $\gamma$ -ray tracking array AGATA [16] and a dedicated electronics for the smartPET detector [78], a planar HPGe detector for medical imaging applications. Furthermore, it is envisaged to build a low cost digital electronics for the DSSSD [79] detector of the MINIBALL experiment.

The developed VHDL implementation of the moving window deconvolution proved the advantage of trapezoidal shaping for HPGe detectors and - since the energy is the most important information of a  $\gamma$ -ray - enables creation of custom digital spectrometers at a low cost in the future. This is of great importance for the AGATA array, further increasing the number of channels by a factor of 40 compared to the MINIBALL array.

---

<sup>1</sup>ADCs including calibration circuits are available for low sampling rates (1 MHz) only.

<sup>2</sup>Nallatech [77] offers the BenADIC, a 20 channel ADC CompactPCI module with 6 user FPGAs and external clock input.



# Appendix A

## Introduction to Digital Signal Processing

”The secret to creativity is knowing how to hide your sources.” - Albert Einstein

In this chapter, the fundamentals of digital signal processing necessary for the understanding of the following chapters will be reviewed and the properties of various digital filters will be discussed. For further details the reader is referred to the literature [80, 51, 81, 82, 83, 84, 85].

In the following a one-dimensional problem is assumed. The incoming analog signal is represented as a function of a single variable, usually the time  $t$ ,  $f(t)$ .

The most important system for digital signal processing is the linear time-invariant system (LTI), which is characterized by its impulse response. The output of such a system for any input signal can be derived from the knowledge of the impulse response.

The LTI system is defined in section A.1 and is followed by a description of the analog-to-digital conversion process in section A.2. Two important types of digital filters are presented, the IIR and the FIR filter. Afterwards, the numerical differentiation and the resampling process are presented, because of their importance for pulse shape analysis.

### A.1 Discrete Linear Time-Invariant Systems

A discrete system is represented by the transformation of the input sequence  $x[n]$  into the output sequence  $y[n]$

$$\begin{aligned}x[n] &\rightarrow y[n] \\ \delta[n] &\rightarrow h[n],\end{aligned}$$

where the last equation defines the response of the system to a single impulse  $\delta[n]$ , the impulse response  $h[n]$ , of the system.

The superposition property defines the linear system. If  $y_1[n]$  is the response of a system to an input  $x_1[n]$  and  $y_2[n]$  is the response to  $x_2[n]$

$$\begin{aligned}x_1[n] &\rightarrow y_1[n], \\ x_2[n] &\rightarrow y_2[n],\end{aligned}$$

then a system is called linear if the response of the system to a superposition of two signals is given by

$$c_1 x_1[n] + c_2 x_2[n] \rightarrow c_1 y_1[n] + c_2 y_2[n].$$

The time-invariant system is defined by the property that the output is delayed by the same amount of time as the input signal:

$$x[n + d] \rightarrow y[n + d],$$

which means, that the system is invariant under translation operations.

If the input sequence can be expressed as

$$x[n] = \sum_k x[k] \delta[n - k]$$

the response of the LTI system is determined by the convolution [80] of the input sequence with the impulse response

$$\begin{aligned} y[n] &= \sum_k x[k] h[n - k] \\ &= x[k] * h[n - k]. \end{aligned}$$

If two systems are connected in series then the overall impulse response is the convolution of the individual impulse responses  $h_s[n] = h_1[n] * h_2[n] = h_2[n] * h_1[n]$ . The *inverse* system  $h_i$  is defined by  $\delta[n] = h[n] * h_i[n] = h_i[n] * h[n]$  meaning that the overall response to an input sequence  $x[n]$  is the input sequence itself.

## A.2 Analog-Digital (A/D) Conversion (ADC)

The first step of digital signal processing is the conversion of the analog data  $f(t)$  into the digital domain, where the continuous signal  $f(t)$  is represented by a finite set of discrete values  $f[n]$ . The function will be represented by a grid of finite time increments  $\Delta t$  and finite amplitude<sup>1</sup> steps  $\Delta A = 2^{-n}$  with  $\Delta t = T = \frac{1}{f_s}$  the inverse of the sampling frequency and  $n$  the number of bits of the ADC

$$f(t) \rightarrow f(m\Delta t) = f(mT) =: f_m \quad (\text{A.1})$$

with  $t \in R$  and  $m \in Z$ . Thus the sampling process consists of two parts: the quantization of the signal amplitude and the discretization of the time increments.

### A.2.1 Quantization

The *quantization* process introduces an error because of the limited number of amplitudes available for the representation of the input signal. For an ideal ADC with a constant and fixed step size  $\Delta A$  the variance  $\sigma$  of the rounding error  $(A - a)$ , with  $A$  the true amplitude and  $a$  the measured ADC value, due to the quantization process is

$$\sigma^2 = \frac{1}{\Delta A} \int_{A-\Delta A/2}^{A+\Delta A/2} (A - a)^2 da = \frac{1}{3} \left( \frac{\Delta A}{2} \right)^2 = \frac{\Delta A^2}{12}, \quad (\text{A.2})$$

---

<sup>1</sup>The amplitude is normalized to 1.

and thus the average deviation from the true amplitude is only  $1/\sqrt{3}$  of the maximal rounding error. In order to reduce the error introduced by the quantization process a technique called *dithering* [70, 85] can be employed. To increase the accuracy of a measured quantity (e.g. the pulse height of a detector signal) the results of multiple measurements of the same quantity are averaged to obtain the final result. The output of a digitizer, however, will always be the same digital value if the analog input signal is noiseless and prevent any gain in information. In the presence of noise adding to the analog signal the output of the digitizer will span more than one channel, in which case averaging the results of multiple conversions results in a determination of the analog input value with an accuracy *higher* than that given by the quantization step size. By averaging  $N$  measurements the standard deviation of the mean value is given by:

$$\sigma_{\langle a \rangle} \approx \frac{1}{\sqrt{N}} \sigma_a, \quad (\text{A.3})$$

which shows that  $N$  has to be chosen large enough to (over-)compensate the additional noise added by the dithering process. This property (also called *bit gain*) and its importance for  $\gamma$  energy determination will be discussed again in section A.3.3 when the noise reduction capabilities of pulse shaping networks will be discussed in presence of two noise sources.

A more advance technique is the *subtractive dithering*, where a DAC in front of the ADC is used to add a noise pattern to the signal which is subsequently subtracted from the ADC output. A similar technique is the *sliding scale* method for Wilkinson-type ADCs, which is used in standard nuclear spectroscopy setups.

A real ADC usually does not satisfy the condition of a fixed step size, leading to a variable width for each ADC channel. The importance of this effect will be explained in chapter 4.7.1, showing that an ADC for nuclear spectroscopy has to be chosen with great care to fulfill the requirements for proper digitization.

## A.2.2 Discretization: Periodic Sampling

The sampling process is represented by the multiplication of the analog signal  $f(t)$  with the sampling function  $s(t) = \sum_n \delta(t - t_n)$ , the Shah function, which is a sum of delta functions  $\delta(t - t_n)$ , where  $t_n = n\Delta t$

$$f_s(t) = f(t) s(t) = f(t) \sum_n \delta(t - t_n). \quad (\text{A.4})$$

The discrete representation  $f_s$  of the input signal  $f(t)$  is achieved through an integration

$$f_s = \sum_n \int f(t) \delta(t - t_n) dt = \sum_n f(t_n) = \sum_n f(n\Delta t), \quad (\text{A.5})$$

with  $f(t_n) = \int f(t) \delta(t - t_n) dt$  the sample of  $f(t)$  at  $t_n$ . Since the Fourier transformation of a multiplication yields a folding operation and the transformation of the Shah function is also a Shah function<sup>2</sup>, the corresponding equation for the Fourier transformation of  $f_s$ ,  $F(\omega)$ , is

$$F_s(\omega) = \frac{1}{2\pi} (F(\omega) * \omega_s \sum_{m=-\infty}^{\infty} \delta(\omega - \frac{2\pi m}{\Delta t})) \quad (\text{A.6})$$

---

<sup>2</sup> $s(t) = \sum_n \delta(t - nT) \rightarrow S(\omega) = \omega_s \sum_k \delta(\omega - k\omega_s)$

$$= \frac{\omega_s}{2\pi} \int F(\omega') \sum_{m=-\infty}^{\infty} \delta(\omega - m\omega_s - \omega') d\omega' \quad (\text{A.7})$$

$$= \frac{\omega_s}{2\pi} \sum_{m=-\infty}^{\infty} F(\omega - m\omega_s), \quad (\text{A.8})$$

with  $\omega_s = \frac{2\pi}{\Delta t} = 2\pi f_s$  and  $F(\omega)$  the Fourier transformation of  $f(t)$ .  $F_s(\omega)$  is a superposition of periodic repeating copies of the original frequency spectrum  $F(\omega)$  shifted by multiples of  $\omega_s$ . The frequency ambiguity, if  $F(\omega)$  covers a wide (infinite) frequency range, is called *aliasing*. Aliasing can only be prevented if the frequency range of  $F(\omega)$  is restricted to  $< \frac{\omega_s}{2}$ , i.e.  $F(\omega) = 0$  if  $|\omega| \geq \frac{\omega_s}{2}$ . This expression is called *Nyquist criterion*, the corresponding frequency  $\omega_n = \frac{\pi}{\Delta t}$  the *Nyquist frequency*. For the sampling of low-pass signals<sup>3</sup> the sampling theorem states that the frequency of the conversion process must be twice as high as the highest frequency in the analog data. In order to fulfill the Nyquist criterion, typical ADC systems use an analog low-pass *anti-aliasing* filter prior to the A/D conversion, such that  $F'(\omega) = F(\omega) LP(\omega)$  where  $LP(\omega)$  is the low-pass filter employed to fulfill the Nyquist criterion:  $LP(\omega) = 0$  for  $\omega \geq \frac{\omega_s}{2}$ . Such a signal can be perfectly reconstructed from the sampled data points because there is no ambiguity. This is called the *sampling theorem*. The process of reconstructing the continuous signal from the sampled data points, called Whittaker reconstruction, is presented in section A.5.2.

### Finite Duration of the Sampling Process

The finite duration of the sampling process can be described by replacing the sum of delta functions in equation A.5 with a sum of rectangular impulses of finite width  $W$  and height  $\frac{T_s}{W}$ :

$$s(t) = \begin{cases} T_s/W & , nT_s - \frac{W}{2} \leq t \leq nT_s + \frac{W}{2}, n \in Z \\ 0 & , \text{otherwise} \end{cases} \quad (\text{A.9})$$

The frequency response is that of the perfect sampling with an additional envelope of the form  $\frac{\sin(x)}{x}$ . To show this the sampling function  $s(t)$  is expanded into a Fourier series

$$s(t) = \sum_{m=-\infty}^{\infty} c_m \exp(i\omega_s m t). \quad (\text{A.10})$$

The coefficients  $c_m$  are given by

$$c_m = \frac{1}{T_s} \int_{T_s/2}^{T_s/2} s(t) \exp(-i\omega_s m t) dt \quad (\text{A.11})$$

$$= \frac{1}{T_s} \int_{W/2}^{W/2} \frac{T_s}{W} \exp(-i\omega_s m t) dt \quad (\text{A.12})$$

$$= \frac{2}{\omega_s m W} \sin\left(\frac{\omega_s m W}{2}\right). \quad (\text{A.13})$$

<sup>3</sup>In IF or bandpass sampling a bandwidth limited signal centered around non-zero base frequency is sampled by taking advantage of spectral replications at multiples of the sampling frequency. The advantage is that the ADC has to cover the bandwidth of the signal only, since the carrier frequency is not of interest.

The sampling process is described, as before, by

$$f_s(t) = f(t) s(t) \quad (\text{A.14})$$

$$= \sum_{m=-\infty}^{\infty} \frac{2}{\omega_s m W} \sin\left(\frac{\omega_s m W}{2}\right) f(t) \exp(i\omega_s m t). \quad (\text{A.15})$$

With the translation property<sup>4</sup> of the fourier transformation the frequency response is given by

$$F_s(\omega) = \sum_{m=-\infty}^{\infty} \frac{2}{\omega_s m W} \sin\left(\frac{\omega_s m W}{2}\right) F(\omega - m\omega_s). \quad (\text{A.16})$$

For  $W = T_s$  this leads to  $F_s(\omega) = F(\omega)$ , only the term for  $m = 0$  remains and any aliasing is automatically prevented. A similar sampling scheme will be used for the implementation of the decimation unit (section 4.3) in order to avoid any aliasing effects.

### A.2.3 The Flash ADC Architecture

A typical DSP system consists of a sensor/detector connected to an Analog to Digital Converter (ADC or A/D Converter), whose output is connected to a Digital Signal Processor (DSP). There exist a vast amount of different ADC architectures, as an example the architecture of a typical flash ADC is shown in the figure A.1.

The reference voltage is divided down to ground potential using a series of resistors. A comparator compares the input voltage with the corresponding fraction of the reference voltage. If the input voltage is above this threshold of the comparator, the comparator sets its output and the subsequent encoder converts this into the digital ADC word. The output code is a result of the parallel comparison. For an  $n$ -bit ADC,  $2^n - 1$  comparators are necessary. The precision and stability of the comparator thresholds and the reference voltage determine the quality of the A/D conversion result.

For fast high resolution converters a pipelined scheme is preferred. This converter type consists of several ADCs with less accuracy, i.e. less bits, that are arranged such that the following stage achieves a further refinement of the previous conversion result. Therefore a single ADC stage consists of an ADC and a DAC as shown in figure A.1. An ADC is used for A/D conversion and the DAC translates the ADC result into analog data again. The difference between the input voltage and the DAC voltage, the *residual* voltage, is transferred to the following stage which in turn performs the same operations but with the residual voltage only. In order to use identical stages, usually an amplification stage is added in between the pipeline stages. The digital outputs of the individual ADC stages are combined to form the final ADC word as shown in figure A.1.

An advantage of the pipelined flash ADC is the reduced amount of comparators needed. For example a two stage pipelined 12 bit ADC needs only  $2^6 - 1 + 2^6 - 1 = 2^7 - 2$  comparators compared to  $2^{12} - 1$  of the non-pipelined version. However, the first ADC stage still has to have the full precision. For a two stage ADC with 6 bits per stage this means that if the threshold of a comparator of the first ADC deviates by  $\frac{1}{64}$  LSB<sup>5</sup> from the proper value then the ADC will show a missing code, i.e. the corresponding ADC

<sup>4</sup>Also called shift theorem, see section A.3.1.

<sup>5</sup>Least Significant Bit

result cannot be achieved. This happens because the residual voltage exceeds the input range of the following stage, which will therefore have a constant conversion result. Therefore pipelined flash ADCs implement a scheme called *error correction* to prevent missing ADC codes. Typically this works by increasing the input range of the following stage, e.g. by 1 bit, such that the residuum of the preceding stage never exceeds the input range. The additional codes of the ADC can be used to detect and subsequently correct the errors of the previous stages.

### A.3 Digital Filter

Two types of digital filters will be presented in the following: the infinite impulse response (IIR) and the finite impulse response (FIR) filter. The difference between both filters is the use of feedback for the IIR filters, which can cause an infinite impulse response. Both types of filters were used and are therefore described in more detail.

#### A.3.1 Transfer Function

The properties of digital filters are usually displayed by plotting the magnitude  $M(\omega) = |H(\omega)|$  and phase response  $\Phi(\omega) = \tan^{-1}\left(\frac{\Im(H(\omega))}{\Re(H(\omega))}\right)$  of the, usually complex, transfer function  $H(\omega) = \frac{Y(\omega)}{X(\omega)}$ , which is defined as the ratio between output and input spectrum. With the *shift* theorem of the Fourier transformation<sup>6</sup>, it is apparent that any transfer function  $H(\omega)$  that can be expressed as  $H(\omega) = \hat{H}(\omega) \exp(i\omega t_d) = \hat{H}(\omega) \exp(i\Phi(\omega))$  with  $\hat{H}(\omega)$  a real function of the frequency  $\omega$  has a linear phase ( $\Phi(\omega) = \omega t_d$ ) and acts as a constant delay in the time domain. The magnitude response  $|H(\omega)|$  is not affected by the linear phase term. A zero delay is achieved for real transfer functions only. The *group delay*  $D(\omega)$  is defined as  $D(\omega) = \frac{\partial}{\partial \omega} \Phi(\omega)$  and for the above example a group delay of  $D(\omega) = t_d$  is obtained. The *phase delay*  $P(\omega) = \frac{\Phi(\omega)}{\omega} = t_d$  is equal to the group delay in case of a linear phase. Since pulse shape analysis is about the extraction of timing information from the digitized detector signals, linear phase filters are preferred, because otherwise the pulse shapes are distorted.

#### A.3.2 IIR filter

Infinite impulse response (IIR) filters are defined by the use of feedback, meaning that the output not only depends on the previous inputs but also on the previous filter outputs. Due to this remembrance of past outputs it is possible that the output of an IIR filter stays non-zero even if all the following input samples are zero, resulting in an infinite impulse response. The equation describing a general IIR filter is

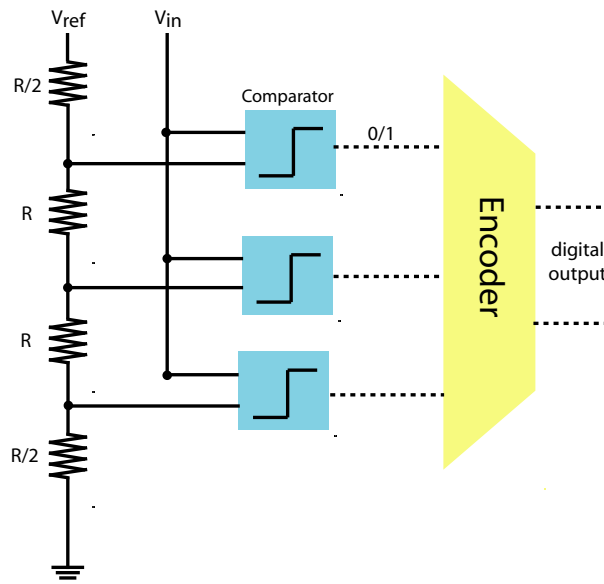
$$y[n] = \sum_{m=0}^N a_m x[n-m] + \sum_{m=1}^M b_m y[n-m]. \quad (\text{A.17})$$

The general expression for the transfer function  $H(\omega)$  of IIR filters is

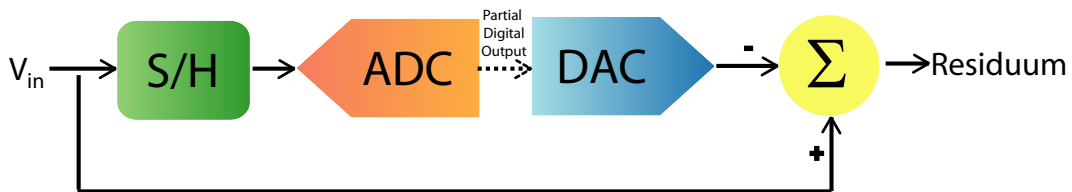
$$H(\omega) = \frac{\sum_{k=0}^N a_k z^{-k}}{1 - \sum_{k=1}^M b_k z^{-k}} \quad (\text{A.18})$$

---

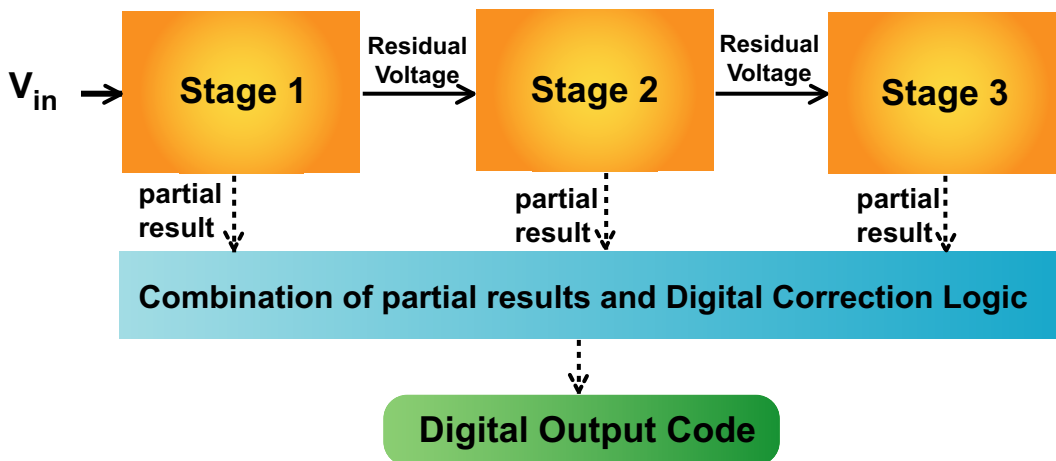
<sup>6</sup> $f(t - t_d) \rightarrow F(\omega) \exp(i\omega t_d)$



(a) Structure of a flash ADC.



(b) Single ADC stage of a pipeline flash ADC.



(c) Pipelined flash ADC with error correction.

**Figure A.1:** The pipelined flash ADC. The upper panel shows the structure of a 2 bit flash ADC consisting of  $2^2 - 1 = 3$  comparators and an encoder, which forms the final digital data word. Panel (b) shows a single stage of a pipelined flash ADC consisting of a sample and hold (S/H) circuit, an ADC and a DAC. The output of the DAC is subtracted from the input signal and the residuum is transferred to the following stage. This is shown in (c), where the individual conversion results of three ADC stages are combined to one digital data word. The digital error correction logic ensures that the ADC shows no missing bits.

$$= \frac{\sum_{k=0}^N a_k \exp(-ik\omega)}{1 - \sum_{k=1}^M b_k \exp(-ik\omega)} \quad (\text{A.19})$$

$$= \frac{\sum_{k=0}^N a_k \cos(k\omega) - i \sum_{k=0}^N a_k \sin(k\omega)}{1 - \sum_{k=1}^M b_k \cos(k\omega) - i \sum_{k=1}^M b_k \sin(k\omega)}, \quad (\text{A.20})$$

where the first equation corresponds to the z-transform, which is usually preferred over the Fourier transform. A zero phase response can be achieved with IIR filter by filtering the data twice, first in forward direction and then in backward direction. This time-reversal causes a zero phase as can directly be seen from the shift property of the Fourier transformation

$$f(t-d) \rightarrow H_1(\omega) = \hat{H}_1 \exp(-i\omega d) \quad (\text{A.21})$$

$$f(t+d) \rightarrow H_2(\omega) = \hat{H}_2 \exp(i\omega d) \quad (\text{A.22})$$

$$f(t) = f(f(t+d)-d) \rightarrow H(\omega) = H_1(\omega)H_2(\omega) = \hat{H}_1\hat{H}_2 \quad (\text{A.23})$$

### Exponential Averaging

An example for an IIR filter is the exponential averaging (EA) filter. The EA filter is a simple IIR filter with a low-pass behavior, used e.g. for noise reduction in the following applications. The mathematical equation for this IIR filter is

$$y[n] = \alpha x[n] + (1-\alpha)y[n-1] \quad (\text{A.24})$$

$$= \alpha \sum_{k=0}^{\infty} (1-\alpha)^k x[n-k], \quad (\text{A.25})$$

with  $\alpha$  the relaxation constant, a constant weighting factor that controls the amount of feedback. It can be seen from the filter equation A.25 that only one storage element is needed to hold the previous filter output sample. Furthermore the algorithm requires only one multiplication if arranged such that  $y[n] = \alpha(x[n] - y[n-1]) + y[n-1]$ .

If  $\alpha$  is one then the input is not attenuated and the previous filter output is ignored. With decreasing  $\alpha$  the input gets more and more attenuated and the influence of the previous filter output increases, resulting in an increased smoothing and slower step response. The effect of different  $\alpha$  on the impulse and step response is plotted in figure A.3.

The reduction of the noise variance by exponential averaging is given by [82]

$$\frac{\text{output noise variance}}{\text{input noise variance}} = \frac{\alpha}{2-\alpha}, \quad (\text{A.26})$$

which shows that the output noise variance decreases with decreasing  $\alpha$  and therefore this filter acts as a low-pass filter.

From equation A.18 the transfer function of the exponential averaging is obtained by setting  $N = 0$ ,  $M = 1$ ,  $a_0 = \alpha$  and  $b_1 = 1 - \alpha$

$$H(\omega)_{\text{exp}} = \frac{\alpha}{1 - (1-\alpha)\cos(\omega) + i(1-\alpha)\sin(\omega)}. \quad (\text{A.27})$$

The magnitude response as well as the phase response are plotted in figure A.2.

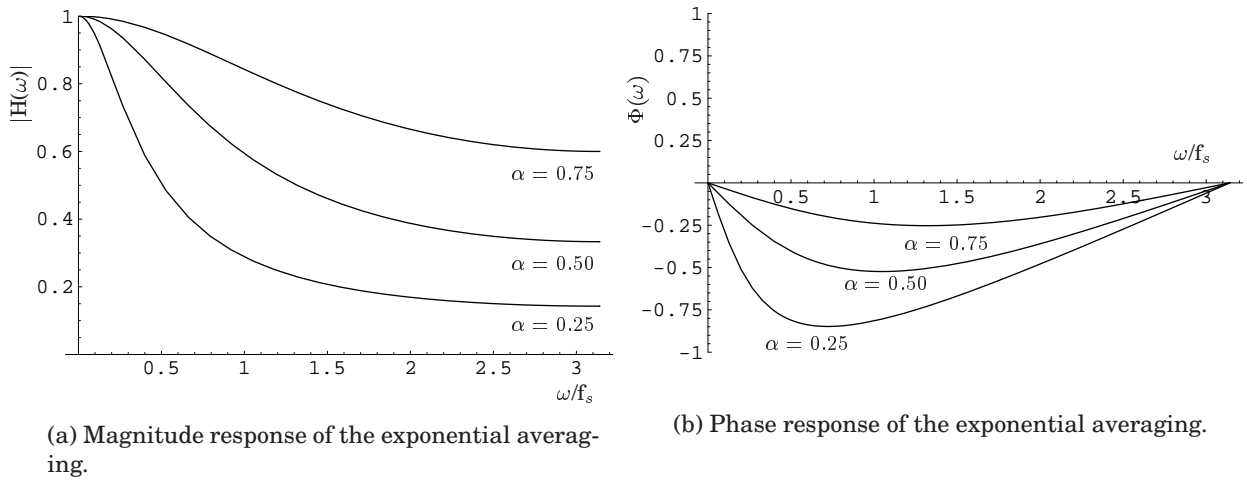


**Figure A.2:** Magnitude and phase response of the exponential averaging. With decreasing  $\alpha$  the EA filter acts more and more as low-pass filter, suppressing the high-frequency components of the input signal. The phase response is highly non-linear and therefore the shape of the input signal will be distorted.

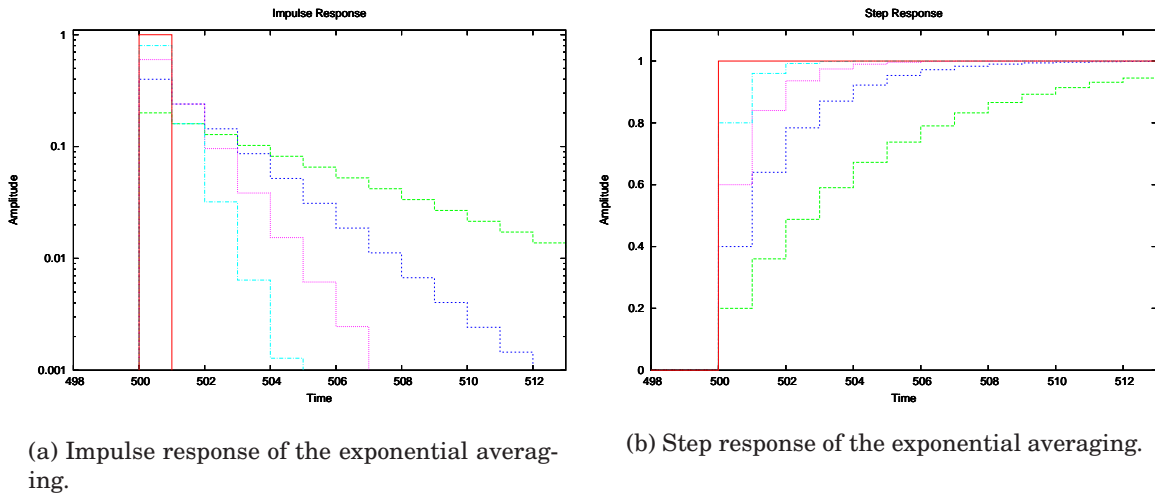


**Figure A.3:** Impulse and steps response of the exponential averaging for  $\alpha$ s of 1., 0.8, 0.6, 0.4 and 0.2. From the semi-logarithmic plot of the impulse response it is clearly visible why the filter is called exponential averaging. With decreasing  $\alpha$  the step and the impulse response get slower. In both plots the data was offset by 500 units.

### A.3.3 FIR filter

On contrary to the IIR filter, Finite Impulse Response (FIR) filters are always stable<sup>7</sup> due to the lack of any feedback. The general expression for FIR filters is

$$y[n] = \sum_{k=0}^N c_k x[n-k]. \quad (\text{A.28})$$

The output sequence  $y[n]$  of a FIR filter is equal to the convolution of the input sequence with the filter's impulse response, which is given by the filter coefficients  $c_k$ , and therefore the frequency response of the FIR filter is given by the Discrete Fourier Transform (DFT) of the impulse response (coefficients):

$$H(\omega) = \sum_{k=0}^N c_k \exp(-ik\omega) = \sum_{k=0}^N c_k \cos(k\omega) - i \sum_{k=1}^N c_k \sin(k\omega). \quad (\text{A.29})$$

A linear phase response of FIR filters can easily be achieved, by writing equation A.28 in a symmetrical way  $y[n] = \sum_{k=-\frac{N}{2}}^{\frac{N}{2}} c_k x[n+k]$  and choosing  $c_k = c_{-k}$ .

#### The Ideal Low Pass Filter

The ideal low-pass filter is an example for a FIR filter with zero phase shift. It has a rectangular transfer function

$$H(\omega) = \begin{cases} 1 & , |\omega| < \omega_c \\ 0 & , |\omega| \geq \omega_c \end{cases} \quad (\text{A.30})$$

and the coefficients  $c_n$  (impulse response  $h[n]$ ) of the FIR filter are given by the Fourier transformation of the transfer function

$$c_n = h[n] = \frac{1}{2\pi} \int_{-\infty}^{\infty} H(\omega) \exp(i\omega n) d\omega \quad (\text{A.31})$$

$$= \frac{1}{2\pi} \int_{-\omega_c}^{\omega_c} \exp(i\omega n) d\omega \quad (\text{A.32})$$

$$= \frac{\sin(\omega_c n)}{\pi n}, \quad (\text{A.33})$$

with  $\omega_c$  being the cut-off frequency. In case the ideal low-pass filter is implemented as a digital filter the cut-off frequency is defined relative to the sampling frequency  $\omega_c = 2\pi \frac{f_c}{f_s}$ . For a digital filter, only a finite number of  $2N + 1$  coefficients can be used for the implementation. Therefore the transfer function is only an approximation of the ideal low-pass transfer function as can be seen from the discrete Fourier transformation of the FIR implementation of the low-pass filter  $H_N(\omega)$  with  $2N + 1$  coefficients

$$H_N(\omega) = \sum_{n=-N}^N \frac{\sin(\omega_c n)}{\pi n} \exp(-i\omega n), \quad (\text{A.34})$$

which is plotted in figure A.4 for  $N = 9$  and  $N = 19$ , both with  $\omega_c = \frac{\pi}{2}$ .

<sup>7</sup>If the response to a bound input sequence  $|x[n]| \leq B_x$  is also bound for all  $n$ , i.e.  $|y[n]| \leq B_y$ , the system is called stable.

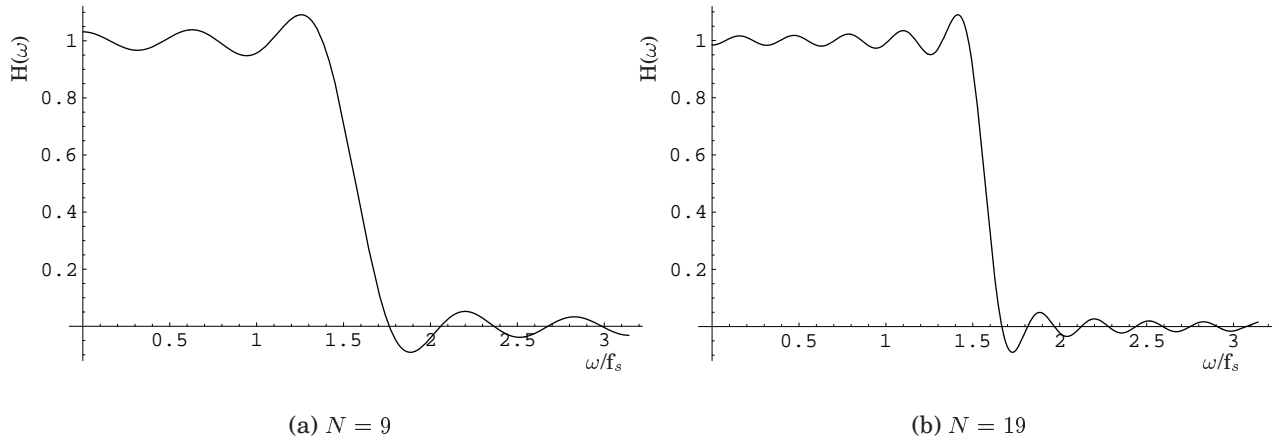


**Figure A.4:** Transfer functions of the ideal low-pass filter for different filter lengths  $N$ .

### Moving Average

A moving average (MA) filter is very simple to realize in hardware after digitization and at the same time an effective low-pass filter. Therefore this filter is presented as a second example of a FIR filter. The MA filter adds  $L = 2N + 1$  samples with a constant weight

$$c_n = \begin{cases} \frac{1}{2N+1} & , |n| \leq N \\ 0 & , |n| > N \end{cases} \quad (\text{A.35})$$

$$y[n] = \sum_{i=-\infty}^{\infty} c_i x[n+i] \quad (\text{A.36})$$

$$= \frac{1}{2N+1} \sum_{i=-N}^N x[n+i]. \quad (\text{A.37})$$

The transfer function can be determined from the Fourier transformation of the filter coefficients

$$H(\omega) = \int_{-\infty}^{\infty} c(t) \exp(-i\omega t) dt \quad (\text{A.38})$$

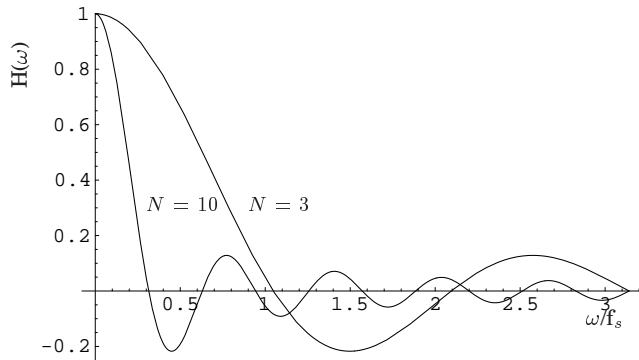
$$= \frac{1}{2N\Delta t} \int_{-N\Delta t}^{N\Delta t} \exp(-i\omega t) dt \quad (\text{A.39})$$

$$= \frac{1}{2T_N} \int_{-T_N}^{T_N} \exp(-i\omega t) dt \quad (\text{A.40})$$

$$= \frac{\sin(\omega T_N)}{\omega T_N}, \quad (\text{A.41})$$

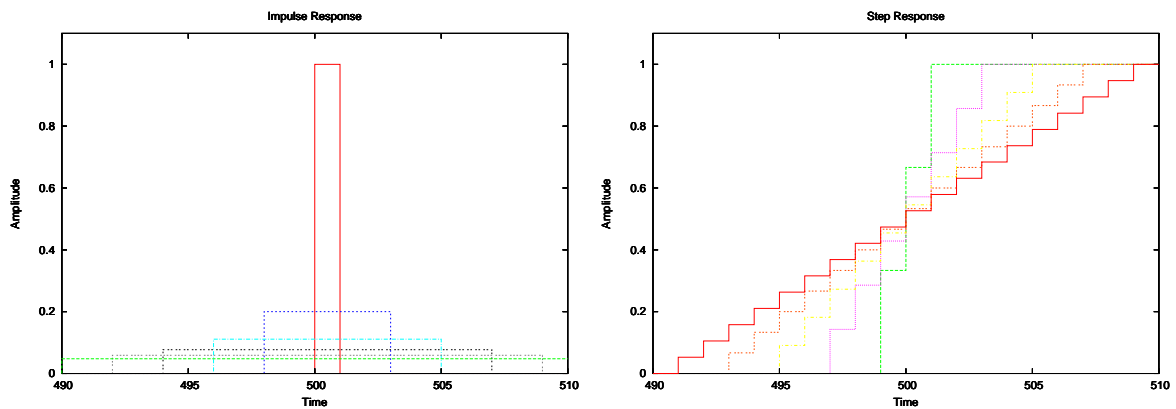
with  $T_N = N\Delta t$ . The transfer function is plotted in figure A.5<sup>8</sup> for  $N = 3$  and  $N = 10$ . Whereas the ideal low-pass has a step-like transfer function, the MA has a step-like behavior in the time-domain. The transfer function of the MA shows an oscillating behavior, i.e. the attenuation does not constantly increase with frequency. However, if

<sup>8</sup>With the DFT the transfer function is  $H(\omega) = \frac{1}{2N+1} \sum_{-N}^N \exp(-i\omega t) = \frac{1}{2N+1} \frac{\exp(i\omega N) - \exp(-i\omega(N+1))}{1 - \exp(-i\omega)} = \frac{1}{2N+1} \frac{\sin(\omega(2N+1)/2)}{\sin(\omega/2)}$



(a)

**Figure A.5:** Transfer function of the moving averaging filter for two different lengths  $N = 3$  and  $N = 10$ . For increasing filter length  $N$  the higher frequency components of the signal are stronger suppressed demonstrating the low-pass behavior of the filter.



(a) Impulse response.

(b) Step response.

**Figure A.6:** Step and impulse response of the moving averaging filter plotted for  $N = 1, 3, 5, 7, 9$  and  $N = 0, 2, 4, 6, 8, 10$  respectively.

the signal power is concentrated mainly in the lower frequency range or the signal was oversampled, then the MA filter is the preferred low-pass filter because of its simple structure. The MA operation can also be expressed as a recursive filter  $y[n] = y[n - 1] + \frac{1}{m}(x[n] - x[n - m])$ , which is the preferred equation for real-time applications and consequently can use the actual and previous data samples only. The length of the MA filter can be adjusted by changing the parameter  $m$ .

### Binomial Filter

As a third example of a low-pass FIR filter, the binomial filter will be discussed. The binomial filter can be constructed from a two point  $MA_2$  filter

$$y[n] = \frac{1}{2}(x[n] + x[n - 1]). \quad (\text{A.42})$$

The repeated convolution of the  $MA_2$  with itself leads to the desired binomial filter coefficients  $BF = MA_2 * MA_2 * \dots * MA_2$ . The convolution of a step function with itself leads to a triangular shape and the resulting binomial filter is  $y[n] = MA_2 * MA_2 = \frac{1}{4}(x[n+1] + 2x[n] + x[n-1])$ .

Generally, if this process is repeated  $n$  times then the transfer function is that of the *two point*  $MA_2$  to the  $n$ -th power, i.e.  $H(\omega) = \left(\frac{\cos(\omega/2)}{2}\right)^n$ .

Contrary to the MA filter, the binomial filter shows no oscillating behavior and is therefore a better low-pass filter than the MA filter. However, the filter coefficients have to be stored and the filter requires multiplications with fractional precision, whereas in case of the MA filter the multiplication can be replaced by a simple shift operation of the filter length  $L$  is chosen in powers of two, i.e.  $L = 2^m$ .

### Least-Squares Smoothing - Trend Analysis

The performance of the previous FIR filters was judged using the transfer function. Now, a FIR filter will be derived on the basis of the principle of least-squares<sup>9</sup>, stating that the best approximation  $\hat{x}[n]$  of the data sequence  $x[n]$  is that one minimizing the squares of the deviations of the data sequence from their estimate  $\sum_{n=0}^M (x[n] - \hat{x}[n])^2$ . The detector signal can be modeled as the sum of two contributions, the detector current signal and the noise. The noise dominates the signal at high frequencies and in order to extract the signal trend the filter should remove the high-frequency noise. The smoothing of the data based on the principle of least squares is therefore also regarded as trend analysis [86].

The detector signal  $x[k]$  is modeled as the sum of the detector and noise contribution  $x[k] = t[k] + n[k]$ , with  $t[k]$  the signal trend and  $n[k]$  the noise. The assumption is that the trend  $t[k]$  can be extracted from the signal  $y[n]$  using a FIR filter of the following form

$$t[k] = \sum_{r=-M}^M a_r y[k+r]. \quad (\text{A.43})$$

The filter should be symmetric and have a gain of one

$$\sum_{r=-M}^M a_r = 1 \quad (\text{A.44})$$

$$a_r = a_{-r}. \quad (\text{A.45})$$

The filter coefficients can be determine by assuming that the signal trend  $t[k]$  is of polynomial form  $p[k]: t[k] \approx p[k]$ . The signal  $y[k] = t[k] + n[k] \approx p[k] + n[k]$  is represented as the sum of a polynomial  $p[k]$ , which is used to approximated the signal trend, and the noise  $n[k]$ . The input data sequence is represented in the form of a (transposed) vector  $\mathbf{x}^T = (x[-M], x[-M+1], \dots, x[0], x[M])$ , i.e.  $\mathbf{x}$  is the data vector for the desired FIR filter of length  $2M+1$ . The polynomial  $\mathbf{p}$  of degree  $n$  is represented as

$$p[k] = b_0 + b_1 k + b_2 k^2 + \dots b_n k^n \quad (\text{A.46})$$

<sup>9</sup>Mathematicians believe it is a physical principle while physicists believe it is a mathematical principle.

with  $\mathbf{b}^T = (b_0, b_1, \dots, b_n)$  the coefficients of the polynomial. This leads to  $2M + 1$  equations for  $\mathbf{p}$

$$p[-M] = b_0 + b_1(-M) + b_2(-M)^2 + \dots + b_n(-M)^n \quad (\text{A.47})$$

$$\vdots \quad (\text{A.48})$$

$$p[0] = b_0 + b_1 \cdot 0 + b_2 \cdot 0^2 + \dots + b_n \cdot 0^n \quad (\text{A.49})$$

$$\vdots \quad (\text{A.50})$$

$$p[M] = b_0 + b_1 M + b_2 M^2 + \dots + b_n M^n \quad (\text{A.51})$$

which can be expressed as  $\mathbf{p} = \mathbf{F}\mathbf{b}$  with

$$\mathbf{F} = \begin{pmatrix} 1 & -M & (-M)^2 & \dots & (-M)^n \\ \vdots & \vdots & \vdots & \vdots & \vdots \\ 1 & 0 & 0 & 0 & 0 \\ \vdots & \vdots & \vdots & \vdots & \vdots \\ 1 & M & M^2 & \dots & M^n \end{pmatrix}, \quad (\text{A.52})$$

a  $(2M + 1) \times (n + 1)$  matrix.

The unknown coefficients  $\mathbf{b}$  can be determined from the least-squares condition, requiring that the desired coefficients  $\hat{\mathbf{b}}$  minimize the squares of the deviation of the polynomial from the data points

$$(\mathbf{y} - \mathbf{p})^T (\mathbf{y} - \mathbf{p}) = (\mathbf{y} - \mathbf{F}\hat{\mathbf{b}})^T (\mathbf{y} - \mathbf{F}\hat{\mathbf{b}}), \quad (\text{A.53})$$

which gives the result [86]  $\hat{\mathbf{b}} = (\mathbf{F}^T \mathbf{F})^{-1} \mathbf{F}^T \mathbf{y}$ .

The coefficients  $a_r$  of the filter can be obtained from  $p[0]$ , which describes the signal  $y[0]$  at  $t = 0$ . Using  $p[0] = \mathbf{e}_1^T \hat{\mathbf{b}} = \hat{b}[0]$  with  $\mathbf{e}_1^T = \begin{pmatrix} 1 & 0 & \dots & 0 \end{pmatrix}$ ,  $p[0]$  can be expressed as

$$p[0] = \mathbf{e}_1^T \hat{\mathbf{b}} = \mathbf{e}_1^T (\mathbf{F}^T \mathbf{F})^{-1} \mathbf{F}^T \mathbf{y}. \quad (\text{A.54})$$

If the order of the polynomial and the window size is constant, then the Matrix  $\mathbf{F}$  is constant, thus allowing the replacement  $p[0] = \mathbf{a}^T \mathbf{y}$  with  $\mathbf{a}^T$  the filter coefficients

$$\mathbf{a}^T = \mathbf{e}_1^T (\mathbf{F}^T \mathbf{F})^{-1} \mathbf{F}^T = \begin{pmatrix} a_{-M} & \dots & a_0 & \dots & a_M \end{pmatrix}. \quad (\text{A.55})$$

For a linear signal trend the FIR filter obtained with the principle of least squares equals a MA filter. This means that the MA filter is the best filter to approximate a noisy data sequence that features either a constant or a linear rising or falling signal trend.

### Trapezoidal Shaping

The properties of the trapezoidal shaping, derived in [87, 88], are summarized in the following. An extensive overview over the field of signal processing with semiconductor detectors is given in [33].

The noise analysis will be carried out in the time domain [89] and only two sources of noise were considered: current<sup>10</sup> and voltage<sup>11</sup> noise.

<sup>10</sup>Current noise is often referred to as step noise or parallel noise.

<sup>11</sup>Voltage noise is often referred to as delta or series noise.

The former noise source consists of one current sources in parallel to the detector, the signal source. The sum of these two contributions is integrated on the input capacity, i.e. detector and preamplifier capacity. In this setup the signal to noise ratio is independent of the input capacity ( $\frac{q_s}{q_n} = \frac{i_s/C}{i_n/C}$ ).

The latter noise source is connected in series to the signal after the input capacity and is therefore modeled as voltage noise generator with (constant) amplitudes independent of  $C$  which leads to a signal-to-noise (SNR) ratio proportional to  $\frac{1}{C}$ .

Another assumption is that the measurement takes place at a fixed time  $T_{ps}$  on the signal. In order to determine the cumulative effect of all noise steps prior to the time when the peak value is sampled the so-called step-noise residual function  $R(t)$ <sup>12</sup>, which represents the effect of a single noise step that has happened  $-t$  before peak capture, is used. The total mean square step and delta noise indices are defined as [88]

$$\langle N_s^2 \rangle = \frac{1}{S^2} \int_{-\infty}^{T_{ps}} (R(t))^2 dt \quad (\text{A.56})$$

$$\langle N_{\Delta}^2 \rangle = \frac{1}{S^2} \int_{-\infty}^{T_{ps}} (\dot{R}(t))^2 dt, \quad (\text{A.57})$$

with  $S$  being the signal amplitude.

For the example of a trapezoidal shaper<sup>13</sup> with a rise and fall time of  $T_p$  and  $T_f$ , a gap time of  $T_g$  and amplitude of  $S = 1$  the corresponding noise indices are given by [88]

$$\langle N_s^2 \rangle = \int_0^{T_f} \left(\frac{t}{T_f}\right)^2 dt + \int_0^{T_g} (1)^2 dt + \int_0^{T_p} \left(\frac{t}{T_p}\right)^2 dt \quad (\text{A.58})$$

$$= T_g + \frac{T_p + T_f}{3} \quad (\text{A.59})$$

$$\langle N_{\Delta}^2 \rangle = \int_0^{T_f} \left(\frac{1}{T_f}\right)^2 dt + \int_0^{T_p} \left(\frac{1}{T_p}\right)^2 dt \quad (\text{A.60})$$

$$= \frac{1}{T_p} + \frac{1}{T_f} \quad (\text{A.61})$$

The previous equations show that the step noise contribution increases with the length of the filter rise and gap time whereas the delta noise index is inverse proportional to the filter rise time. Therefore the delta noise contribution can be reduced by increasing  $T_p$  and  $T_f$  of the trapezoidal shaper and  $T_g$  should be set to a minimum value. Furthermore, it can be derived from equation A.61 that symmetrical pulse shapes yield better noise indices for a fixed total filter length.

Another important feature of the trapezoidal shaping is the insensitivity to rise time variations of the detector signal due to the flat top, eliminating the so-called ballistic deficit [90] which is limiting the energy resolution for high energy  $\gamma$ -rays. This is explained in section 2.5.3 in more detail.

Furthermore the trapezoidal shaper is ideally suited for high rate applications because of the finite width of the pulse shape, which is  $T_p + T_g + T_f$ . The gaussian shaper

<sup>12</sup>The step noise residual function  $R(t)$  is a measure of the contribution of a step noise happening  $-t$  before peak capture to the shaper output at time  $T_{ps}$  and is therefore also called the *weighting function*. The step noise residual function is given by the time derivative of the step noise residual function  $\dot{R}(t)$  [88].

<sup>13</sup>An example of a trapezoidal shaper is the Moving Window Deconvolution presented in chapter 2.5.

used in standard analog electronics shows a slow return to the baseline after an event which disturbs the baseline determination and limits the performance at high event rates.

## A.4 Numerical Differentiation

Numerical differentiation is an important FIR filter for PSA because not only the charge signal contains information about the interaction position, but also the current signal and even the derivative of the current signal. For example, the radial interaction position information for the MINIBALL detector is extracted from the second derivative of the digitized charge pulse.

The transfer function is obtained by applying the differentiation to a single frequency signal  $\exp(i\omega t)$  and dividing the result by the input signal

$$H(\omega) = \frac{\frac{d}{dt} \exp(i\omega t)}{\exp(i\omega t)} = i\omega \quad (\text{A.62})$$

The transfer function is proportional to the frequency, resulting in a high-pass behavior of the differentiation operation. Therefore differentiation leads to an decreased signal to noise ration (SNR), since the high-frequency components are amplified and the signal amplitude decreases.

### A.4.1 Differentiability of bandwidth limited Signals

A bandwidth limited signal can be represented in the time domain by [91]

$$x(t) = \frac{1}{2\pi} \int_{-\omega_c}^{\omega_c} X(\omega) \exp(i\omega t) d\omega, \quad (\text{A.63})$$

with  $X(\omega)$  the Fourier transformation of the input signal  $x(t)$  and  $\omega_c$  the cut-off frequency. The  $n$ -th differentiation of  $x(t)$

$$\frac{d^n}{dt^n} x(t) = \frac{1}{2\pi} \int_{-\omega_c}^{\omega_c} X(\omega) (i\omega)^n \exp(i\omega t) d\omega. \quad (\text{A.64})$$

features an additional term  $(i\omega)^n$  which could prevent the integral from convergence without the bandwidth limitation. Therefore differentiation of bandwidth limited signals is always possible.

### A.4.2 Differentiation Equations

The most simple approach to numerical differentiation leads to differences of the forward, backward or central type

$$d[n]_b = x[n] - x[n-1] \quad (\text{A.65})$$

$$d[n]_f = x[n+1] - x[n] \quad (\text{A.66})$$

$$d[n]_c = \frac{1}{2}(x[n+1] - x[n-1]) \quad (\text{A.67})$$

$$= \frac{1}{2}(d[n]_f + d[n]_b). \quad (\text{A.68})$$

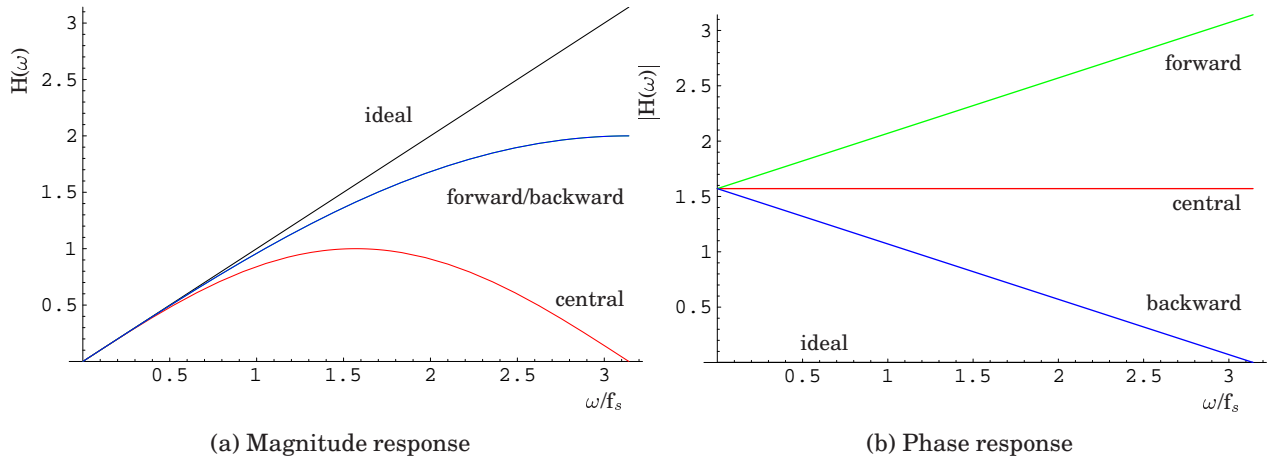


**Figure A.7:** Magnitude and phase response of the numerical differentiation of forward, backward and central type together with that of the ideal differentiation. The higher frequency components of the signal are strongly suppressed for the central type, whereas in the case of forward and backward differentiation the transfer functions approximate the ideal transfer function up to about half of the bandwidth. For the ideal and central differentiation no phase shift is observed on contrary to the forward and backward types.

The advantage of the differentiation of central type, is that the filter is symmetric and therefore has a linear phase. The differentiation of forward and central type are non-causal, in the sense that the output of the differentiation filter depends on future samples. The corresponding transfer functions can be determined by applying the differentiation equations onto a single frequency signal  $\exp(i\omega n)$

$$H_b[\omega] = 2i \sin\left(\frac{\omega}{2}\right) \exp\left(-i\frac{\omega}{2}\right) \quad (\text{A.69})$$

$$H_f[\omega] = 2i \sin\left(\frac{\omega}{2}\right) \exp\left(i\frac{\omega}{2}\right) \quad (\text{A.70})$$

$$H_c[\omega] = i \sin(\omega) . \quad (\text{A.71})$$

The transfer functions are complex and magnitude and phase response are plotted in figure A.7. The differentiation is a good approximation for the true transfer function for low frequencies  $\omega$ , but high frequencies are attenuated compared to the transfer function of the ideal differentiation (equation A.62).

Similarly the transfer function for the second derivative

$$sd[n] = x[n + 1] - 2x[n] + x[n - 1] \quad (\text{A.72})$$

is

$$H_{sd}[\omega] = 2(1 - \cos(\omega)) , \quad (\text{A.73})$$

which is also a good approximation only at low frequencies<sup>14</sup>, while high frequencies are also attenuated compared to the ideal transfer function  $H(\omega) = -\omega^2$  which can be seen from figure A.8.

An alternative approach to numerical differentiation [81] is to start from the desired transfer function of the differentiation  $H(\omega) = i\omega$  and design a matching FIR filter.

<sup>14</sup> $H_{sd}[\omega] \approx 2(1 - (1 - \omega^2/2 + \dots))$

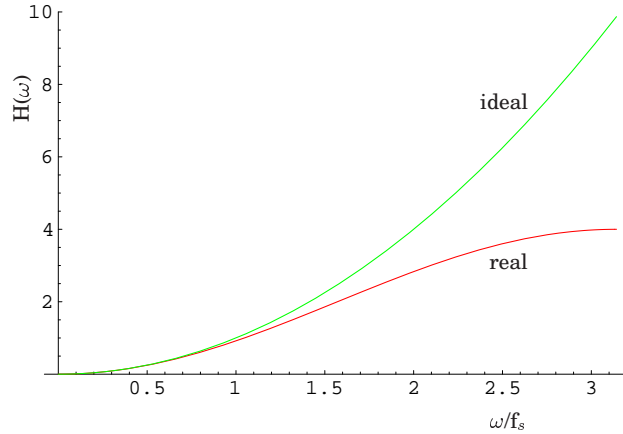


**Figure A.8:** Transfer function of the numerical second derivative compared to that of the ideal second derivative. The numerical second derivative is a good approximation for the ideal second derivative up to about half of the bandwidth.

Assuming a symmetrical FIR filter of the form

$$y[m] = \sum_{n=-N}^N c_n x[m-n] \quad (\text{A.74})$$

with  $c_n$  the coefficients that have to be determined for the desired transfer function from the coefficient equation

$$c_n = \frac{1}{2\pi} \int_{-\infty}^{\infty} H[\omega] \exp(in\omega) d\omega. \quad (\text{A.75})$$

For the transfer function of the differentiation this leads to the following expression for the coefficients:

$$c[n] = \frac{1}{2\pi} \int_{-\omega_s/2}^{\omega_s/2} (i\omega) \exp(in\omega) d\omega \quad (\text{A.76})$$

$$= \frac{1}{2\pi} \left( \omega_s \frac{\cos(n\omega_s/2)}{n} - 2 \frac{\sin(n\omega_s/2)}{n^2} \right) \quad (\text{A.77})$$

$$= \frac{\cos(n\pi)}{n} - \frac{\sin(n\pi)}{\pi n^2}, \quad (\text{A.78})$$

where  $\omega_s = 2\pi$  was used. This leads to the following coefficients

$$c_0 = 0 \quad (\text{A.79})$$

$$c_n = \frac{(-1)^n}{n} \text{ for } n \neq 0. \quad (\text{A.80})$$

The corresponding filter equations are:

$$\begin{aligned} c_3[n] &= x[n+1] - x[n-1] \\ c_7[n] &= \left( \frac{1}{3}x[n+3] - \frac{1}{2}x[n+2] \right) \\ &+ x[n+1] - x[n-1] \\ &+ \left( \frac{1}{2}x[n-2] - \frac{1}{3}x[n-3] \right) \end{aligned}$$

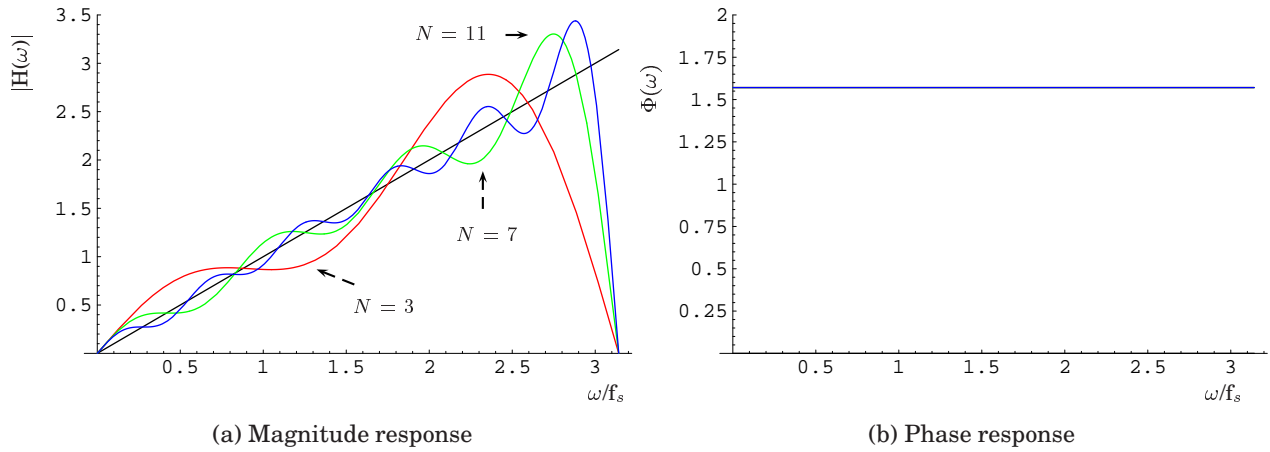


**Figure A.9:** Transfer function of the differentiation filter for different  $N$ ,  $N = 3$ ,  $N = 7$  and  $N = 11$ , compared to that of the ideal differentiation (black).

$$\begin{aligned}
 c_{11}[n] &= \left( \frac{1}{5}x[n+5] - \frac{1}{4}x[n+4] \right) + \left( \frac{1}{3}x[n+3] - \frac{1}{2}x[n+2] \right) \\
 &+ x[n+1] - x[n-1] \\
 &+ \left( \frac{1}{2}x[n-2] - \frac{1}{3}x[n-3] \right) + \left( \frac{1}{4}x[n-4] - \frac{1}{5}x[n-5] \right).
 \end{aligned}$$

As an example, the transfer function of the differentiation filter with  $N = 11$  is plotted in figure A.9 together with the ideal transfer function of the differentiation to demonstrate the approximation of the true transfer function.

More complex differentiation formulas are obtained by differentiating Lagrangian interpolation formulas [84]

$$\begin{aligned}
 d_{l5}[n] &= \frac{1}{12}(-x[n+2] + 8x[n+1] - 8x[n-1] + x[n-2]) + \frac{h^4}{30}f^4(\lambda) \\
 d_{l7}[n] &= \frac{1}{60}(x[n+3] - 9x[n+2] + 45x[n+1] \\
 &- 45x[n-1] + 9x[n-2] - x[n-3]) + \frac{h^6}{160}f^7(\lambda),
 \end{aligned}$$

where  $d_{l5}[n]$  and  $d_{l7}[n]$  are obtained from five and seven point interpolation formulas respectively. The last term is the error, which decreases with decreasing step size  $h$ , i.e. with increasing sampling frequency<sup>15</sup>. The transfer functions are

$$\begin{aligned}
 H_{l5}(\omega) &= \frac{1}{12}(16i \sin(\omega) - 2i \sin(2\omega)) \text{ and} \\
 H_{l7}(\omega) &= \frac{1}{30}(45i \sin(\omega) - 9i \sin(2\omega) + i \sin(3\omega)),
 \end{aligned}$$

which are plotted in figure A.10.

A better differentiation formula for bandwidth limited signals should be obtained by a smooth interpolation, i.e. an interpolation without discontinuities<sup>16</sup>. This should

<sup>15</sup>The error for the differentiation formula of central type  $d_c[n]$  is  $\frac{h^2}{6}f'''(\lambda)$ .

<sup>16</sup>The smoothness of the spline interpolation is shown in [83] in comparison to a polynomial interpolation.

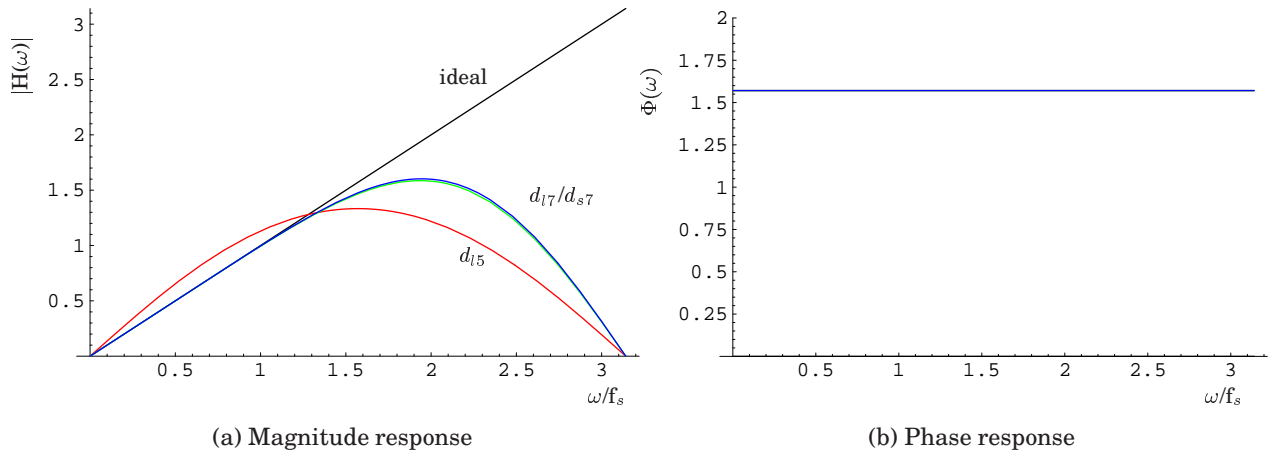


**Figure A.10:** Transfer function of numerical differentiation formulas based on lagrangian,  $d_{l5}[n]$  and  $d_{l7}[n]$ , and spline,  $d_{s7}[n]$ , interpolation in comparison to the ideal differentiation. The seven point formula approximates the ideal magnitude response very well up to half of the bandwidth, whereas the five point formula suppresses higher frequency components strongly and emphasizes the low frequencies.

especially be true if the derivatives of the interpolated data sequences are of importance. Therefore a differentiation formula  $d_s$  based on a spline interpolation [84] of fourth order using 7 data points

$$d_{s7}[n] = \frac{1}{168} (3x[n+3] - 26x[n+2] + 127x[n+1] - 127x[n-1] + 26x[n-2] - 3x[n-3]),$$

and the corresponding transfer function

$$H_{s7}(\omega) = \frac{1}{84} (127i \sin(\omega) - 26i \sin(2\omega) + 3i \sin(3\omega)), \quad (\text{A.81})$$

are mentioned here.

## A.5 Digital Resampling: Decimation and Interpolation

Digital resampling [80, 82, 91, 92, 93] is the process of changing the sampling rate after A/D conversion. The process of decreasing the sampling rate is called *decimation* and the process of increasing the sampling rate is called *interpolation*. The need for a resampling of the ADC data for nuclear spectroscopy application comes from the different conversion frequency requirements for energy filtering and PSA. Typical large high-purity germanium (HPGe) detectors like the MINIBALL detectors require shaping times on the order of a few  $\mu\text{s}$  (e.g.  $\sim 7 \mu\text{s}$ ) whereas the rise time of such a detector is only a few hundred ns (e.g.  $\sim 350 \text{ ns}$ ). Thus, for the energy (slow) branch of the digital spectroscopy system a sampling rate of about 10 MHz is sufficient, whereas for PSA a sampling rate of 100 MHz or more is desirable. If the ADC conversion rate is somewhere between these two cases, the ADC data can be resampled for the two applications.

In order to understand the effect of a digital increase of the sampling rate, it is best to consider a two channel DSP system with 40 MHz ADCs fed by a common clock. Single

frequency sine waves are assumed to be used as input signals. The purpose of the experiment is the determination of the phase shift or delay between the two sine waves. If 30 MHz sine waves are used the experiments will fail because the signal will be removed by the Nyquist filter. If 5 MHz sines waves are used the sine wave will be sampled with an oversampling ratio of 4. The phase shift will be determine by measuring the time difference when the signal crosses a certain threshold (or use the detection of the zero crossing) between the two channels. If the signal is resampled to 160 MHz, i.e. the signal is oversampled by a factor of 16, then the phase difference between the two channels can be determined with a four times higher precision, because the time difference between the samples decreased by a factor of four.

The main purpose of digital resampling is the simplification of the further digital filtering. The decimation unit reduces the amount of memory needed for the energy filter by a large factor. Similarly, a digital upsampling unit could be used in front of a PSA unit to increase the time resolution of the PSA algorithms.

### A.5.1 Decimation

The process of *downsampling* an ADC output sequence  $x[n] = x(n T_s)$  works by simply sampling the original output sequence at a new rate  $M T_s$ :

$$x_d[n] = x[nM]. \quad (\text{A.82})$$

However, if the bandwidth of the original data exploits the full range allowed by the Nyquist theorem, then the new data sequence will be subjected to aliasing, because now the original frequency band will overlap with the mirror signals at multiples of the new sampling frequency  $\omega_s^d = \frac{\omega_s}{M}$ . Therefore a system is needed that consists not only of a resampler but also of a low-pass filter applied to the original data sequence that ensures that aliasing is prevented for the new data sequence, i.e  $H(\omega) = 0$  for  $\omega > \omega_d$  with  $\omega_c^d = \frac{\omega_c}{M}$  the Nyquist frequency of the decimated signal. Such a system, a low-pass filter followed by a downsampler, is called *decimator*. The reason for aliasing can be seen from the Fourier transformation of the downsampling processes by replacing the frequencies  $\omega_s$  in equation A.8 with the down sampled frequencies  $\frac{\omega_s}{M}$

$$F_k(\omega) = \frac{\omega_s}{2M\pi} \sum_{k=-\infty}^{\infty} F\left(\left(\frac{\omega}{M}\right) - k\left(\frac{\omega_s}{M}\right)\right) \quad (\text{A.83})$$

$$= \frac{\omega_c^d}{\pi} \sum_{k=-\infty}^{\infty} F\left(\frac{\omega}{M} - k\omega_s^d\right). \quad (\text{A.84})$$

The resulting spectrum features copies of the original signal, which is scaled in frequency by the factor M, with a period of  $\omega_s^d = \frac{\omega_s}{M}$ . A decimation unit will be presented a section 4.3.

### A.5.2 Upsampling

Similarly to the decimation process which is used for data rate reduction, a process for increasing the data rate of the ADC can be developed. The process of upsampling should yield a sequence  $x_i[n]$  of data points  $x_i[n] = x(n T_i)$  with the new sampling interval  $T_i = \frac{T_s}{L}$  from the original data sequence  $x_o[n] = x(n T_s)$  with  $T_s$  the original sampling

interval. The implementation consists of a *sample rate expander* which implements the zero-padding operation

$$x_e[n] = \sum_{k=-\infty}^{\infty} x[k] \delta_{n,kL}. \quad (\text{A.85})$$

As before, the resampling process produces copies of the original signal at multiples of the new sampling frequency while at the same time the frequency is scaled by the factor  $L$  as can be seen by replacing the original sampling frequency  $\omega_s$  with the new sampling frequency  $\omega_s^i = L\omega_s$  in equation A.8

$$F^i(\omega) = \frac{L\omega_s}{2\pi} \sum_{k=-\infty}^{\infty} F(L\omega - kL\omega_s) \quad (\text{A.86})$$

$$= \frac{\omega_c^i}{\pi} \sum_{k=-\infty}^{\infty} F(L\omega - k\omega_s^i), \quad (\text{A.87})$$

with  $\omega_c^i = \omega_s^i/2$  the corresponding Nyquist frequency.

Therefore the expander is followed by an (ideal) low-pass filter<sup>17</sup> set to the original Nyquist frequency  $\omega_c = \frac{\omega_s^i}{2L}$  to remove the additional copies from the frequency spectrum. In the time-domain the low-pass filter works as an interpolator, i.e. the zeros that were added in between the original data points will be modified such that the Nyquist condition is fulfilled. However, an ideal low-pass filter cannot be realized and therefore an ideal interpolation cannot be achieved. With the impulse response of the ideal low-pass (equation A.33 and A.85) it can be seen that the interpolation condition is fulfilled

$$x_i[n] = \sum_{k=-\infty}^{\infty} x[k] \frac{\sin(\pi(n-kL)/L)}{\pi(n-kL)/L} \quad (\text{A.88})$$

$$= \begin{cases} x[\frac{n}{L}] & , \text{ for } n = 0, \pm L, \pm 2L, \dots \\ \sum_{k=-\infty}^{\infty} x[k] \frac{\sin(\pi(n-kL)/L)}{\pi(n-kL)/L} & , \text{ otherwise.} \end{cases} \quad (\text{A.89})$$

Equation A.88 is also called the *cardinal interpolation function* or *Whittaker reconstruction formula* and it is the most general form of recovering a function from a sequence of data points.

In order to understand the concept of upsampling, i.e. zero-padding and low-pass filtering, it is best to consider a modification of equation A.85

$$x_e[n] = \begin{cases} x[k] & , n \leq kL < n+1, \end{cases} \quad (\text{A.90})$$

i.e. instead of inserting zeros the original sample values are repeated until a new sample is available. This process is called zero-order or nearest neighbor interpolation. The nearest neighbor interpolation can also be expressed as a combination of a zero-padding operation plus a moving average of gain  $L$ , i.e.  $x[n] = \sum_{k=0}^{L-1} x[k]$ . Similarly, any interpolation operation can be split into zero-padding plus subsequent application of filter with the same transfer function as the interpolation.

The ideal interpolation process can also be understood as zero-padding in the frequency domain. Here, the pass band of the transfer function is increased to match the

<sup>17</sup>The low-pass filter needs a gain of  $L$ .

new sampling frequency. The content of the transfer function for frequencies in between the original cut-off frequency  $\omega_c^o$  and the new cut-off frequency  $\omega_c^i = L\omega_c^o$  is set to zero, which is equivalent to the application of the ideal low-pass filter with the cut-off frequency of the original data set.

### Linear Interpolation

Linear interpolation is the second simplest form of interpolation after nearest neighbor interpolation. It can be expressed as

$$y(x) = y[n] + x(y[n+1] - y[n]) \quad (\text{A.91})$$

$$= y[n](1-x) + y[n+1]x \quad (\text{A.92})$$

with  $0 < x < 1$ .

The transfer function can be derived by applying the symmetrical form of the linear interpolation

$$y(x) = \frac{y[n - \frac{1}{2}] + y[n + \frac{1}{2}]}{2} + x \left( y[n + \frac{1}{2}] - y[n - \frac{1}{2}] \right), \quad (\text{A.93})$$

with  $\frac{1}{2} < x < \frac{1}{2}$  onto a single frequency signal  $f(\omega, n) = \exp(i\omega n)$ :

$$H(\omega) = \frac{\exp(i\omega(n - \frac{1}{2})) - \exp(i\omega(n + \frac{1}{2}))}{2 \exp(i\omega n)} \quad (\text{A.94})$$

$$+ x \frac{\exp(i\omega(n - \frac{1}{2})) + \exp(i\omega(n + \frac{1}{2}))}{\exp(i\omega n)} \quad (\text{A.95})$$

$$= \frac{\exp(-\frac{i\omega}{2}) - \exp(\frac{i\omega}{2})}{2} + x \left( \exp(-\frac{i\omega}{2}) + \exp(\frac{i\omega}{2}) \right) \quad (\text{A.96})$$

$$= \cos\left(\frac{\omega}{2}\right) + 2xi \sin\left(\frac{\omega}{2}\right). \quad (\text{A.97})$$

The magnitude and phase response of the linear interpolation are plotted for different  $x$  in figure A.11. The imaginary part of the transfer function causes a phase shift. At  $x = 0$ , i.e. in the middle between the sample points, the transfer function is real (phase response is zero), but compared to the transfer function of the ideal low-pass the higher frequencies are suppressed leading to an incorrect interpolation result. Furthermore the transfer function is not zero above the cut-off frequency, causing aliasing if the resulting data sequence is not filtered with a low-pass.

However, if the data is oversampled, i.e. the sampling rate is well above the highest frequency of the signal, then the damping at higher frequencies is less severe and the linear interpolation is more useful.

Linear interpolation can also be understood as a convolution of the input signal  $x(n)$  with a triangular pulse  $L(t) = 1 - \frac{t}{T}$ , which is itself a convolution of two rectangular functions (compare with the trapezoidal shaping in section A.3.3). Therefore the overall transfer function for the linear interpolation is the quadratic *sinc* function  $\left(\frac{\sin(\omega)}{\omega}\right)^2$ .

## A.6 Useful IIR Filters

$$y[n] = \sum_{m=0}^M a_m x[n-m] + b_m y[n-m]$$

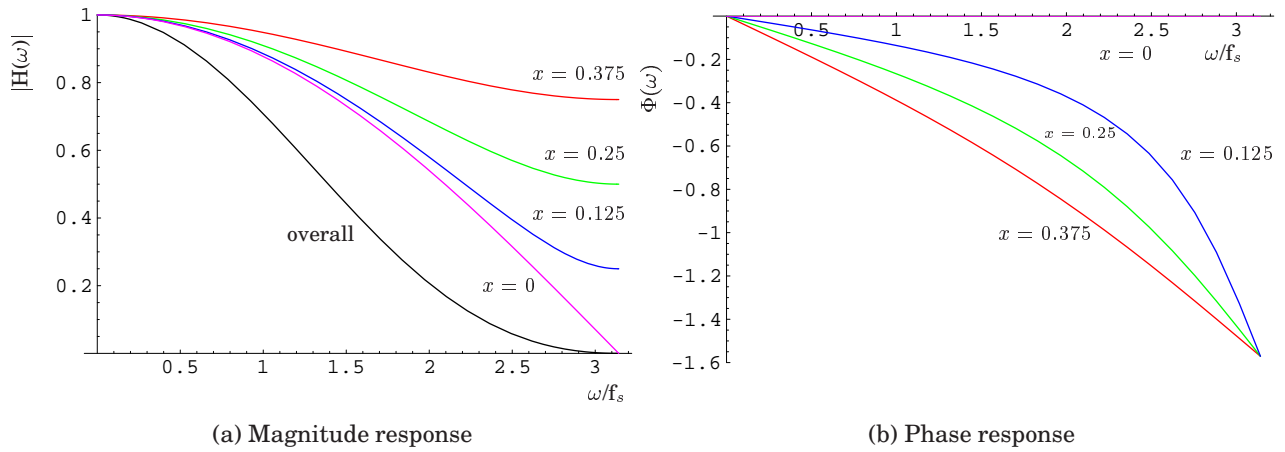


**Figure A.11:** Magnitude and phase response of the linear interpolation. The overall transfer function is plotted in black together with the transfer function for four different  $x$  settings:  $x = 0.375$ ,  $x = 0.25$ ,  $x = 0.125$  and  $x = 0$ .

### 1. Single Pole High Pass Filter

$$\begin{aligned} a_0 &= \frac{1+x}{2} \\ a_1 &= -\frac{1+x}{2} \\ b_1 &= x \end{aligned}$$

with  $x = \exp(-2\pi f_c)$  and all other coefficients are zero such that  $y[n] = a_0x[n] + a_1x[n-1] + b_1y[n-1]$ .

### 2. Single Pole Low Pass Filter

$$\begin{aligned} a_0 &= (1-x) \\ b_1 &= x \end{aligned}$$

with  $x = \exp(-2\pi f_c)$  and all other coefficients are zero such that  $y[n] = a_0x[n] + b_1y[n-1]$ .

### 3. 4 Stage Single Pole Low Pass Filter

$$\begin{aligned} a_0 &= (1-x)^4 \\ b_1 &= 4x \\ b_2 &= -6x^2 \\ b_3 &= 4x \\ b_4 &= -x^4 \end{aligned}$$

with  $x = \exp(-2\pi f_c)$  and all other coefficients are zero such that  $y[n] = a_0x[n] + b_1y[n-1] + b_2y[n-2] + b_3y[n-3] + b_4y[n-4]$ .

4. Bessel Filter with  $f_c = \frac{1}{2}f_s$ 

- 1st Order Bessel Filter:

$$y[n] = x[n] + x[n - 1] - y[n - 1]$$

- 2nd Order Bessel Filter:

$$\begin{aligned} y[n] = x[n] &+ 2x[n - 1] + x[n - 2] \\ &- 2y[n - 1] - y[n - 2] \end{aligned}$$

- 3rd Order Bessel Filter:

$$\begin{aligned} y[n] = x[n] &+ 3x[n - 1] + 3x[n - 2] + x[n - 3] \\ &- 3y[n - 1] - 3y[n - 2] - y[n - 3] \end{aligned}$$

- 4th Order Bessel Filter:

$$\begin{aligned} y[n] = x[n] &+ 4x[n - 1] + 6x[n - 2] + 4x[n - 3] + x[n - 4] \\ &- 4y[n - 1] - 6y[n - 2] - 4y[n - 3] - y[n - 4] \end{aligned}$$



## Appendix B

# Details of the MWD implementation

”I no longer wish to belong to the kind of club that accepts people like me as members” - Groucho Marx

### B.1 FPGA Design Flow

Before starting with the implementation of the MWD algorithm, the proper design environment has to be chosen. Formerly, FPGA designs were generated using schematic entry where the design was created by adding modules to a design sheet and connecting by wires. Nowadays, the usual way of creating a FPGA design is to use a **Hardware Description Language (HDL)** which allows a behavioral description of the logic.

However, it is not necessary to learn a HDL before creating a FPGA design, because the generation of FPGA designs using a language similar to the well-known C language (Handel-C [94]) is possible.

XILINX offers two tools that simplify the generation of FPGA models by adding modules from libraries. Such a digital module is called a *core* and the software *Core Generator* [95], supporting the generation of various configurable modules, for example a PCI interface and a Fast Fourier Transformation (FFT).

A software targeted to digital signal processing applications is also available and the FPGA code is generated from a MatLab model, generated using the Matlab SimuLink environment [96]. The XILINX *System Generator for DSP* [97] translates the MatLab model into VHDL code including the necessary LogiCOREs (cores generated with Core Generator).

The graphical programming of an FPGA device is also supported by the LabView software [98]. However, the design can only run on hardware supplied by National Instruments.

HDL languages like VHDL and Verilog are standardized and can therefore be used with various software packages, which greatly simplifies the interchange of the HDL design. Since the MWD implementation was a collaboration between MPI-K and CCLRC Daresbury a HDL was chosen to develop the MWD implementation.

### B.1.1 Development Environment

A free version of the XILINX ISE<sup>1</sup> software package, the WebPack 5.2 [99], was used to develop the MWD implementation for the GRT4 card. The simulations of the VHDL codes were done with a free version of Mentor Graphics ModelSim XE<sup>2</sup>, the MXE II Starter, software. The advantage of using the XILINX edition is that the software comes with precompiled versions of the XILINX simulation libraries containing models for each component. However, the free VHDL simulator is aimed for small designs only and if the design exceeds a certain size, determined by the so called critical design size, the simulation slows down strongly especially for simulations after place and route. However, this limitation can partly be circumvented by simulating only certain modules of the design.

### B.1.2 VHDL

VHDL<sup>3</sup> stands for VHSIC<sup>4</sup> **H**ardware **D**escription **L**anguage. The advantage of a HDL are that the system can be simulated on a high level of abstraction, that the documentation can be included in the code and that the HDL code itself serves as documentation (in case of an algorithmic description).

VHDL supports the modeling of a circuit at various levels of abstraction. The algorithmic level describes the behavior of a circuit with the help of variables, functions and parallel processes. The register transfer level (RTL) replaces variables with storage elements and functions with logic elements. Furthermore, the circuits now reacts onto clock and reset signals. However, the proper timing information like delay through logic elements is added at the logic level or gate level, where the design components are replaced by basic elements of the technology library.

A typical VHDL file consists of an interface definition (*entity*) and the actual implementation (*architecture*). It should be noted that a VHDL entity can have multiple implementations. Two types of implementation are distinguished: behavioral and structural implementations. The former type models the behavior of a circuit by using state machine descriptions and Boolean logic equations. The latter type is used mainly the combine various components of a system to the final design.

The final design can be simulated with a VHDL simulator. For this purpose, a *test-bench* including the design under test (DUT) and a circuit that feeds the DUT with test vectors have to be created. The response of the DUT to the test vector can be viewed with a waveform display and compared with the expected response.

As the existing firmware for the GRT4 was supplied as schematics for the Viewdraw software [100], the first step of the development was the creation of a corresponding VHDL [101] description of the GRT4 firmware without any changes. The firmware for the VME FPGA and the ADC FPGA was translated, because the energy and trigger module were added to the ADC FPGA in order to being directly applied to the continuous ADC data. Otherwise a very long waveform would have to be transferred to the DPP FPGA for further analysis. Therefore, it was decided [76] to put the realtime filters into the ADC FPGA and use the DPP FPGA for event buffering only. Since the ADC FPGA

---

<sup>1</sup>Integrated Software Environment

<sup>2</sup>XILINX Editon

<sup>3</sup>Very **H**ard and **D**ifficult to **L**earn

<sup>4</sup>Very High Speed Integrated Circuits

can be accessed via the VME bus directly, there was no need to buffer any data in the DPP FPGA, in order to test the MWD implementation.

### B.1.3 Synthesis

The Xilinx Synthesis Technology (XST) software takes the (V)HDL code to generate a netlist, the NGC file. The formal VHDL description of the hardware gets translated into a hardware that realizes the described behavior. First the syntax of the VHDL is checked. Then the code gets translated into a set of components or macros recognized by the synthesis tool. Examples for macros are "Dual-Port Block RAM with Different Clocks" or "Unsigned  $8 \times 4$ -bit Multiplier". In order to ease the process of macro recognition one should follow the recommendations in the XST User guide (VHDL coding styles). The synthesis process determines if signals should be stored and the conditions for the data storage. From this information the appropriate component is chosen, for example a D Flip Flop or a register or just a connection in case the signal needs no storage.

This process is followed by an optimization process. Typical (global) optimization goals are the area (logic resources) taken by the design and the speed of the design (maximize clock frequency, minimize delay times, less logic levels).

The last step of the synthesis process is the mapping of the design components onto XILINX primitive components like for example the FDCE component, a D Flip-Flop with Clock Enable and Asynchronous Clear. More examples can be found in the XILINX Libraries Guide [102].

### B.1.4 Translate

NGDBuild reads all the netlist files in EDIF<sup>5</sup>, or NGC<sup>6</sup> format of the modules of the design and creates a merged NGD<sup>7</sup> netlist file describing the logical design (a logical design is in terms of logic elements such as AND gates, OR gates, decoders, flip-flops, and RAMs). The NGD file resulting from an NGDBuild run contains a logical description of the design reduced to XILINX Native Generic Database (NGD) primitives and a description of the original design hierarchy. Furthermore the placement and timing constraints from the UCF<sup>8</sup> are included to enable the inspection of the timing specification and a check of the design rules. The output NGD file can be mapped to the desired device family.

### B.1.5 Mapping

The MAP program maps a logical design to the XILINX FPGA resources, the CLBs<sup>9</sup> and IOBs<sup>10</sup>. The input to MAP is the NGD file generated by the translate process, which contains a logical description of the design in terms of both the hierarchical components used to develop the design and the lower level XILINX primitives. The NGD file also contains the macro library files, each of which contains the definition of a physical macro.

---

<sup>5</sup>Electronic Data Interchange Format

<sup>6</sup>Binary file containing the implementation of a module.

<sup>7</sup>Native Generic Database. Describes the logical design reduced to XILINX primitives.

<sup>8</sup>User Constraints File

<sup>9</sup>Configurable Logic Block

<sup>10</sup>Input/Output Blocks

MAP first performs a logical DRC (Design Rule Check) on the design in the NGD file. MAP then maps the logic to the components (logic cells, I/O cells, and other components) in the target XILINX FPGA. The output design is an NCD<sup>11</sup> file, which is a representation of the design mapped to the components in the XILINX FPGA. The NCD file can afterwards be placed and routed.

### B.1.6 Place and Route (PAR)

PAR uses an NCD file as input, places and routes the design, and outputs an NCD file to be used by the bitstream generator (BitGen). The placer determines the best locations for mapped blocks based on their interconnections and the desired performance. Finally, the router interconnects the blocks. The *Timing-Driven* PAR allows to place and route a design based on the timing constraints defined by the user in the UCF file. PAR also runs a physical DRC on nets during routing of the design in order to detect any design errors.

### B.1.7 Timing Constraints

The implementation constraint file for the place and route software consists of timing and placement constraints only. The placement constraints are necessary to associate a top level interface signal to a certain pin location of the FPGA device. The timing constraints are used to ensure that the timing requirements (clock frequency and delay of signal path) are met. All constraints are specified in a single **User Constraints File (UCF)**. The UCF contains the logical constraints, because these constraints are associated with elements in the initial design, i.e. before mapping onto a certain FPGA device. The physical constraints are located in the **Physical Constraints File (PCF)** and are automatically generated during the mapping process.

The timing constraints for the GRT4 schematic design were specified by defining the delay of every important data path by using the MAXDELAY constraints. The timing constraints for the VHDL design are very simple compared to that. Only the clock frequencies of the incoming clocks from the on-board oscillator, the data ready signal of the ADC and the frequency of the VME data strobe signal were specified .

Typical location constraints for pin assignment and placement of a DLL and clock buffer for the GRT4 are:

```
NET "in_adc_clk" LOC = "P80";
NST dllhf LOC = DLL0;
INST ob1dllhf LOC = GCLKBUF0;
```

Typical timing constraints for the clock period are expressed as:

```
NET "drdy_in" TNM_NET = "drdy_in";
TIMESPEC "TS_drdy_in" = PERIOD "drdy_in" 10 ns HIGH 50 %;
```

XILINX recommends to use the exact timing requirements for the constraints. However, for the GRT4 design the clock frequency constraints was slightly over constraint to 100 MHz instead of 80 MHz. Nevertheless, the compiler could fulfill the timing constraints and a typical PAR output shows also that the constraints for the decimated clock (davdec) were automatically generated relative to the ADC clock (drdy\_in \* 4).

---

<sup>11</sup>Native Circuit Description

\*\*\*\*\*  
 Generating Clock Report  
 \*\*\*\*\*

Clock Net	Resource	Fanout	Max Skew(ns)	Max Delay(ns)
pre_dav	Global	428	0.358	0.570
davdec	Global	393	0.356	0.564
incr_rdptr	Local	9	1.332	5.402

The Number of signals not completely routed for this design is: 0

Constraint	Requested	Actual	Logic Levels
TS_increment_rp = PERIOD TIMEGRP "increme nt_rp" 10 nS HIGH 50.000000 %	10.000ns	4.590ns	5
TS_adcbuffer_a_speicher_rpclk = PERIOD TI MEGRP "adcbuffer_a_speicher_rpclk" 10 nS HIGH 50.000000 %	10.000ns	4.611ns	5
TS_dav_fb = PERIOD TIMEGRP "dav_fb" TS_dr dy_in * 1.000000 HIGH 50.000 %	10.000ns	9.662ns	5
TS_pre_davdec = PERIOD TIMEGRP "pre_davde c" TS_dr dy_in * 4.000000 HIGH 50.000 %	40.000ns	35.820ns	2

All constraints were met.

All signals are completely routed.

Total REAL time to par completion: 1 mins 24 secs  
 Total CPU time to par completion: 1 mins 20 secs

Placement: Completed - No errors found.  
 Routing: Completed - No errors found.  
 Timing: Completed - No errors found.

Writing design to file adcbufa\_top.ncd.

### B.1.8 Configuration

The advantage of a SRAM based FPGA is the possibility to change the configuration by downloading the *bit stream* into the device, configuring the CLBs and the interconnections. The bitstream for XILINX device configuration is produced by the program BitGen, which configures the device so that it can execute the desired function. BitGen takes a fully routed NCDfile as input and produces a configuration bitstream, a binary file with the .bit extension. The most important configuration options for BitGen are summarized in table B.1. The BIT file contains all of the configuration information from the NCD file that defines the internal logic and interconnections of the FPGA. The bi-

Bitgen Option	Setting
ConfigRate	4
StartupClk	Cclk
M0/1/2 Pin	Pullup
DonePin	PullNone
DriveDone	Yes
UnusedPin	PullUp

**Table B.1:** Bitgen options for the generation of bitstream for the ADC FPGA. All other settings are equal to the default settings. The ADC FPGA is configured in Master/Serial Mode, for this the M0, M1 and M2 pins are tied to ground level.

nary data in the BIT file can be downloaded into the FPGAs memory cells directly or it can be used to create a PROM file.

PROMGen converts a configuration bitstream (BIT) file into the PROM format file, e.g. the MCS-86 (Intel) format. This file was afterwards used to program the PROM device using the JetProg programmer from Elneec [103]. After power-up of the GRT4 module, the FPGA are configured by the configuration information from the installed PROM.

The physical Design Rule Check (DRC) that is performed after running MAP. PAR and BitGen run some tests to discover physical errors and logic errors in the design. The *net check* examines the interconnections of the design and reports unconnected signals or problems with the pin count. The *block check* examines the components of the design and reports problems with logic, physical pin connections or programming. The *chip check* performs a DRC at the chip level, e.g. placement rules.

## B.2 ADC DNL correction

### B.2.1 Analog Signal Conditioning

Following the SMA connector for the preamplifier signal, there is first an optional differentiation stage. If this feature is used, the ADC sees a differentiated input representing the detector current pulse. Afterwards the analogue inputs are filtered with a second order 40 MHz low-pass Bessel filter. The circuit is the so-called Sallen-Key configuration [104], implemented using the AD811 operational amplifier. The Bessel filter is chosen because of the appropriate properties in the time domain, which is important for PSA. The step response of the Bessel filter has a linear phase<sup>12</sup> and shows no overshoot or ringing. The low-pass filter ensures that the Nyquist condition for proper sampling is fulfilled (section A.2.2). The last stage before the ADC is a differential ADC driver chip, the AD8138, because the ADC (AD6645) accepts only differential data inputs. The connection of the ADC  $V_{REF}$  pin with the  $V_{OCM}$  pin of the AD8138 ensures a proper common mode voltage.

<sup>12</sup>A nonlinear phase filter leads to a distortion of the signal. As for the digital filters, a nonlinear phase is caused by an asymmetric impulse response, which causes an asymmetric step response.

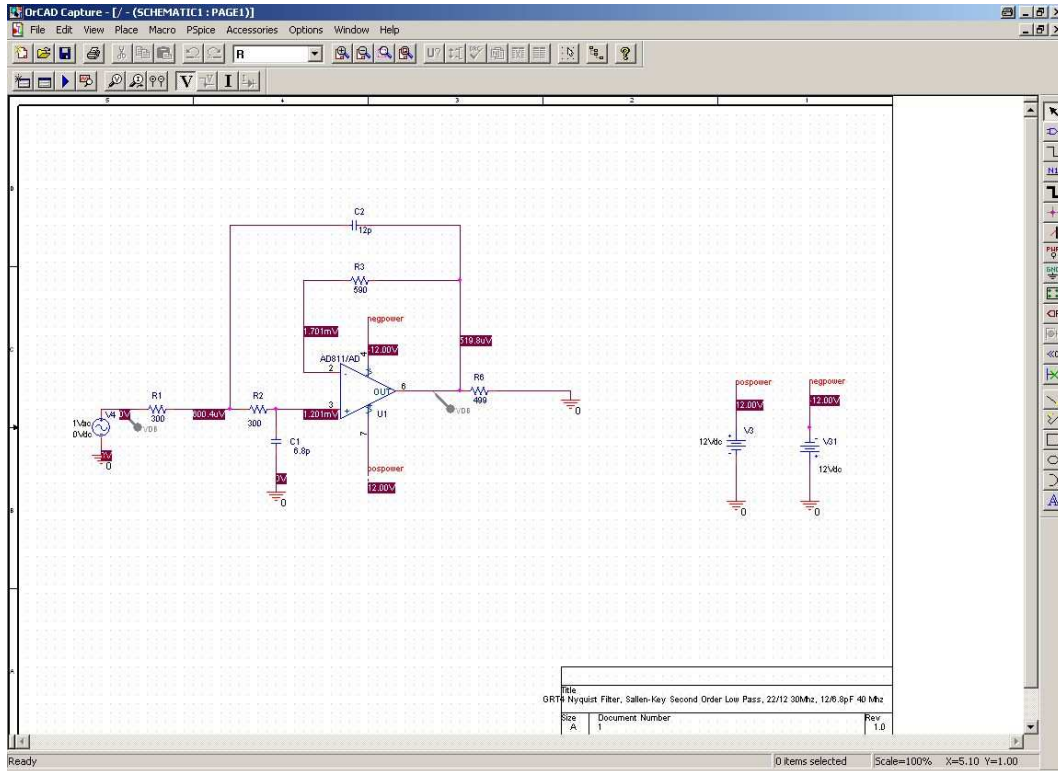


**Figure B.1:** The Sallen-Key circuit. After cut-off frequency  $f_c$ ,  $R_1$  and  $C$  are determined,  $R$  and  $R_f$  are determined with the proper values for the coefficients  $k_1 = 0.1251$  and  $k_2 = 0.268$  for a Bessel filter. In fact, the component values match a Butterworth type filter with a cut-off frequency of about 35 MHz, which was validated using the online filter design software from Analog Devices [105].

## B.2.2 Analog to Digital Converter

The AD6645 from Analog Devices is used for the A/D conversion. The differential input signal is centered at 2.4 V and the signal amplitude is limited to  $\pm 0.55$  V. The maximum differential voltage amplitude is therefore 2.2 V peak to peak ( $-1.1 \text{ mV} < \Delta V < 1.1 \text{ mV}$ ). The AD6645 converts its analog input into 14 bits of two's complement data [106]. In addition an *Over-Range* (OR) bit is supplied, that is set if the analog input exceeds the full scale range of the ADC on either side of the polarity. The maximum conversion rate is 80 MHz and the minimum conversion rate is 30 MHz. Typical values for differential non-linearity (DNL) and integral non-linearity (INL) are  $\pm 0.25$  and  $\pm 0.5$ , respectively with no missing codes<sup>13</sup> due to the error correction. The ADC needs a 5 V power supply for its analog parts and a 3.3 V supply for the digital (output) part. A SMD resistor of 100  $\Omega$  per pin limits the current flow caused by transitions of the digital output.

The AD6645 is a three stage pipelined ADC. The first and second ADCs have 5 bit resolution and the last ADC has 6 bit resolution. The 14 bit result is obtained after adding the results of the three stages and applying digital error correction logic as explained in section A.2.3.

The AD6645 provides a Data Ready (DR) signal indicating the end of the conversion

<sup>13</sup>The ADC code is the twos complement result of the A/D conversion. A missing code is a code that cannot occur, due to large ADC non-linearities.

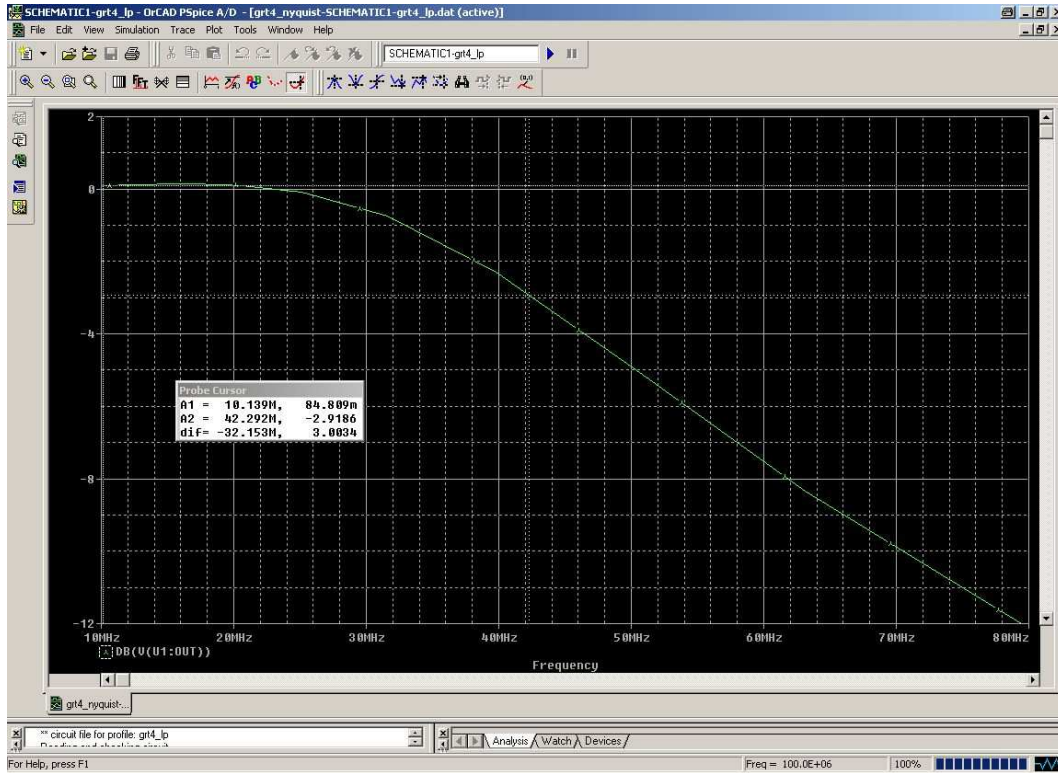


**Figure B.2:** Spice simulation of the analog low-pass filter of the GRT4. The cut-off frequency is 43 MHz.

process. The DR signal is the corresponding clock signal of the output data word and is derived by delaying and inverting the input clock (`Encode`).

### B.2.3 DNL correction coefficients

The correction coefficients, replacing the lower two bits of the 14 bit ADC word and adding 2 additional fractional bits, are compiled in table B.2. The coefficients are represented as floating point numbers, while the LUT entries are fixed point number of 2.2 format. The table is addressed using the bits 5 to 8 of the ADC word, i.e. `ADC(8:5)`.

## B.3 Addressing of the MWD code

The VME base address is set using 16 switches on the address lines `A(31:16)`. The GRT4 decoding of the `A(15:1)` address can be found in the GRT4 manual [107]: `A(15:14)` select the channel of the GRT4, `A(13)` selects the FIFO and `A(12)` selects DPP or ADC FPGA. Finally `A(3:1)` are used to target a certain register. The VME data strobe signal (`DS`) is shared with ADC and DPP FPGA and is used to clock the data into the register together with the VME write signal line.

The interface to the MWD module inside the ADC FPGA is implemented using spare signals routed between the VME and ADC FPGA. The added code uses `A(11)` to switch between the old and new address decoding. `A(11)` disables the former decoding module and `A(11)` is send to the ADC LCA using the `Common Spare(10)` signal line. At the

ADC code (8:5)	ROM entry (2.2 format)	Coefficient [LSB]
0000 <sub>2</sub>	1.5 = 0110 <sub>2</sub>	1.47
0001 <sub>2</sub>	1.25 = 0101 <sub>2</sub>	1.14
0010 <sub>2</sub>	1.0 = 0100 <sub>2</sub>	0.99
0011 <sub>2</sub>	1.0 = 0100 <sub>2</sub>	0.96
0100 <sub>2</sub>	0.75 = 0011 <sub>2</sub>	0.68
0101 <sub>2</sub>	0.5 = 0010 <sub>2</sub>	0.5
0110 <sub>2</sub>	0.0 = 0000 <sub>2</sub>	0.1
0111 <sub>2</sub>	1.75 = 0111 <sub>2</sub>	1.24
1000 <sub>2</sub>	3.0 = 0110 <sub>2</sub>	2.89
1001 <sub>2</sub>	2.75 = 0101 <sub>2</sub>	2.82
1010 <sub>2</sub>	2.5 = 0100 <sub>2</sub>	2.49
1011 <sub>2</sub>	2.5 = 0100 <sub>2</sub>	2.41
1100 <sub>2</sub>	2.0 = 0010 <sub>2</sub>	2.04
1101 <sub>2</sub>	2.0 = 0010 <sub>2</sub>	2.09
1110 <sub>2</sub>	2.0 = 0010 <sub>2</sub>	1.99
1111 <sub>2</sub>	1.75 = 0001 <sub>2</sub>	1.8

**Table B.2:** Entries of the ROM that were used for the ADC DNL correction.

same time Common Spare(18:11) are used to send A(7:0) to the ADC LCA. The decoding of A(7:0) happens then in the ADC LCA. The MWD address space was mapped onto unused address space of the GRT4 A(7:4) or Common Spare(18:15), which allowed a total of 16 register (16 bit) for the MWD module.

## B.4 MWD and double-exponential decaying signals

In order to study the response of the MWD to double-exponential decaying signals, the input signal was modified to  $f_{2e}(t) = \frac{A_1}{\tau_1} \exp\left(-\frac{t}{\tau_1}\right) + \frac{A_2}{\tau_2} \exp\left(-\frac{t}{\tau_2}\right)$ . Now, the input signal to the MWD algorithm is the sum of two exponential signals. The two decay times were chosen to differ by a factor of 25 ( $\tau_1 = 50 \mu\text{s}$  and  $\tau_2 = 2 \mu\text{s}$ ) and the amplitude  $A_2$  was set to 10 % of the  $A_1$  amplitude.

First, each contribution was simulated on its own in order to determine the proper shaping times and the correct decay time for each individual deconvolution. For the  $\tau_2$  contribution very short shaping times are necessary because this contribution decays very rapidly. The parameters were determined to  $M = 0.5 \mu\text{s}$ ,  $L = 0.4 \mu\text{s}$  and  $\tau_2 = 1.57 \mu\text{s}$ . If one applies MWD with these parameters to the double-exponential decaying signal the signal in panel (b) figure B.3 is achieved. Similarly, for the  $\tau_1$  contribution the derived parameters were  $M = 8.8 \mu\text{s}$ ,  $L = 6.8 \mu\text{s}$  and  $\tau_2 = 45.483 \mu\text{s}$ . The response of the MWD with these parameters is shown in panel (c) in figure B.3. Clearly, both algorithms were unable to fully deconvolute the double exponential decay and a step signal as in the previous examples could not be achieved.

VME address	Standard Firmware	MWD Firmware
A(0)		mapped onto Common Spare(0)
A(3:1)	register in ADC and DPP FPGA	mapped onto Common Spare(3:1)
A(7:4)	unused	MWD registers, mapped onto Common Spare(7:4)
A(10:8)	unused	unused
A(11)	unused	disables Standard Firmware, mapped onto Common Spare(10)
A(12)	select DPP or ADC FPGA	same
A(13)	select FIFO	same
A(15:14)	select Channel	same
A(31:16)	VME Base address (switches)	same

**Table B.3:** Usage of VME Address Lines

However, by investigating panel (b) in figure B.3 in more detail, one can see that the signal has two features: a sharp step like signal in the beginning, where the  $\tau_2$  contribution is highest and the removal of the  $\tau_2$  component dominates the signal shape, followed by an exponential decay from the remaining  $\tau_1$  contribution. This can be understood by imaging the operation of the short  $MWD_{\tau_2}$  filter. At a time scale of 400 ns the contribution from the slow  $\tau_1$  decay can be neglected and assumed to cause a constant offset. Any difference in signal amplitude is therefore caused by the fast  $\tau_2$  decay which can be correctly removed with the MWD algorithm. The  $MWD_{\tau_2}$  algorithm assumes that the signal decays with a slope of  $-\frac{A_1(t)+A_2(t)}{\tau_2}$ , but the actual slope is only  $-\left(\frac{A_1(t)}{\tau_1} + \frac{A_2(t)}{\tau_2}\right)$ . The  $MWD_{\tau_2}$  tries to restore the initial amplitude by adding  $f' \cdot \Delta t$  to the signal. The difference between the correct slope and the  $MWD_{\tau_2}$  slope and is

$$\Delta f' = -\frac{A_1(t)}{\tau_1} - \frac{A_2(t)}{\tau_2} + \frac{A_1(t)}{\tau_2} + \frac{A_2(t)}{\tau_2} \quad (\text{B.1})$$

$$= -\frac{A_1(t)}{\tau_1 - \tau_2} \quad (\text{B.2})$$

$$\approx -\frac{A_1(t)}{\tau_1}. \quad (\text{B.3})$$

This is exactly the slope of the remaining single exponential decay signal after the first deconvolution operation.

In order to remove the remaining decay, a second deconvolution is applied to this signal with a decay time constant of  $\tau_1 - \tau_2 \approx \tau_1$ . The resulting, now fully deconvoluted, signal is shown in panel (d) in figure B.3. Compared to the deconvolution of a single exponential decay the MWD signal features a shorter but higher step at the beginning of the MWD step signal caused by the first deconvolution with the  $\tau_2$  time constant. This effect appears again, but inverted, at the end of the step because of the differentiation operation with  $\Delta t = 8.8 \mu\text{s}$ . The two-fold deconvoluted signal still features a flat top, only the beginning and end of the signal gets modified. The following MA operation does not yield a trapezoidal shape anymore, instead a bipolar signal is obtained. This can be understood as over- and undershoot of the trapezoidal signal, caused by the additional

MWD Addresses	Function	Description	Direction
0x18f0	Energy High Word	-	r
0x18e0	Energy Low Word	-	r
0x18d0	Baseline High Word	-	r
0x18c0	Baseline Low Word	-	r
0x18b0	MWD CSR	Control and Status Register (CSR), see CSR table	rw
0x18a0	Baseline Counter	counts accepted baselines divided by 256	r
0x1890	Decay Time High, Decimation	(7:0): Decay Time $\tau$ (23:16) (12:8): Decimation DEC(4:0)	rw
0x1880	Decay Time Low	Low Word of Decay Time $\tau$ (15:0)	rw
0x1870	Baseline Cut BC	Energy Threshold for Baseline Acceptance (signed)	rw
0x1860	Counter: Accepted Triggers	divided by 16, MWD Enabled	rw
0x1850	Baseline Update Frequency BU , Baseline Filter Parameter	(15:8): Baseline Update BU(7:0), (7:0): Shaping Time $\alpha$ (7:0)	rw
0x1840	Pile Up Rejection Interval PU	Minimal Distance between Triggers, 80 MHz clock	rw
0x1830	Peak Capture Delay PS	Distance between Trigger and Peak Capture, 80 MHz clock	rw
0x1820	Counter: All Triggers	divided by 16, MWD Enabled	r
0x1810	Shaping Times $M$ and $L$	(7:0) : MWD Differentiation $M$ (7:0), (15:8): Moving Average $L$ (7:0)	rw
0x1800	Debug Port	VME access to MWD or Trapezoidal Signal	r
0x1004	FIR Trigger CSR	(5:0): Differentiation, (11:6): Integration, (15:12): Time-Over-Threshold	rw
0x100a	FIR Trigger Threshold	Threshold (signed, 2s complement)	rw

**Table B.4:** Mapping of MWD Register into VME Address Range

CSR	Function	Description	Direction
(1:0)	MWD State Machine Mode	Changes Baseline Latching	rw
(2)	Soft Reset of MWD module	starts MWD Initialization procedure	rw
(3)	MWD Enable	enables MWD module	rw
(5:4)	ADC Polarity Selection	Converts signed to unsigned data and swaps polarity	rw
(6)	Debug Port Mode	Selects either MWD or Trapezoidal Signal	rw
(7)	Data Ready from MWD	latched, cleared after reading Low Word of Energy	r
(8)	MWD Running	equal to Enable Signal	r
(9)	Data Ready from MWD	raw signal, not latched	r
(10)	Trigger Status	Used for Debugging	r
(12:11)	ADC Polarity Selection	Used for Debugging	r
(13)	Event Trigger to DPP FPGA	Used for Debugging	r
(14)	All FIFO data send to DPP FPGA	Used for Debugging	r
(15)	Data Acknowledge from DPP FPGA	Used for Debugging	r

**Table B.5:** Description of the MWD CSR register

Common Spare	Function	Remark
(0)	VME SysReset	
(1)	External Trigger Input	Front Panel, Option: Time Stamping Clock
(2)	Gate Input	Front Panel
(3)	Trigger Out	Front Panel driven by channel D only, Option: Busy Out
(4)	Internal Trigger A	Channel 0
(5)	Internal Trigger B	Channel 1
(6)	Internal Trigger C	Channel 2
(7)	Internal Trigger D	Channel 3
(8)	VME data strobe	-
(9)	unused	-
(10)	MWD enable	-
(18:11)	VME address (7:0)	-
(23:19)	unused	-

**Table B.6:** Usage of Common Spare I/O Signals

ADC-DPP	Function	Description	Direction
(0)	Cycle	Clock for Data Transfer	w
(1)	Read Header	Read Non-ADC data including timestamp	r
(2)	Enable ADC Read	read ADC data buffer	r
(3)	Soft Reset		w
(4)	Trigger	Send all Trigger Signals to DPP	r
(8:5)	MWD Address	Selects MWD registers	w
(9)	DPP Read MWD	Enable Read Out	w
(10)	DPP Strobe MWD	Read Out Clock	w
(11)	My Ready	MWD data ready	r
(35:11)	unused	-	-

**Table B.7:** Usage of ADC-DPP Spare Signals as seen from ADC FPGA

features of the two-fold deconvoluted MWD signal. The part of the step signal with higher amplitude in the beginning leads to an increased slope. The slope reduces more and more as the moving average operation is applied mainly to the flat portion of the MWD signal and leads to a flat top when the MA operation is applied to the flat top of the MWD signal only. Similarly, when the MA operation moves on, the additional negative contribution to the MWD signal decreases the slope further, consequently leading to an undershoot in the MA result. The familiarity with the trapezoidal signal can still be recognized and the difference in signal shape can be understood as originating from the different amplitudes of the MWD signal.

It should be noted that for the implementation the time resolution of the energy branch has to be chosen such, that the short shaping time of 400 ns as well as the long shaping time of 8.8  $\mu$ s can be accomplished.

## B.5 Measurements with a Pulser

An ORTEC Research Pulser was used to measure the linearity of the energy algorithm, using two different implementations, and the electronics. The difference between the MWD implementations is the size of the multiplication unit, multiplying either 16 or 24 bit numbers. A  $16 \times 16$  multiplier would be desirable, since it needs only about half of the FPGA resources compared to the  $24 \times 24$  multiplier and fits also to the embedded  $18 \times 18$  multipliers in the Spartan 3 FPGA.

The pulser method is not perfect since the pulser signal usually has a constant offset. The problem with the linearity of the ADC indicates that the pulser should also be able to generate piled up signals to measure the linearity of the full ADC range. A similar method was proposed in [68] in order to take into account the count rate effects namely baseline shifts and pulse pile up. The detector or pulser signal should be mixed with a stair case like signal generating different baseline levels as mentioned in the previous section. However, such a setup was not available and a pulser which generates piled up pulses was bought after the GRT4 evaluation. Another advantage of actual pulsers is the possibility to fill the whole spectrum with peaks of different amplitudes [108], which

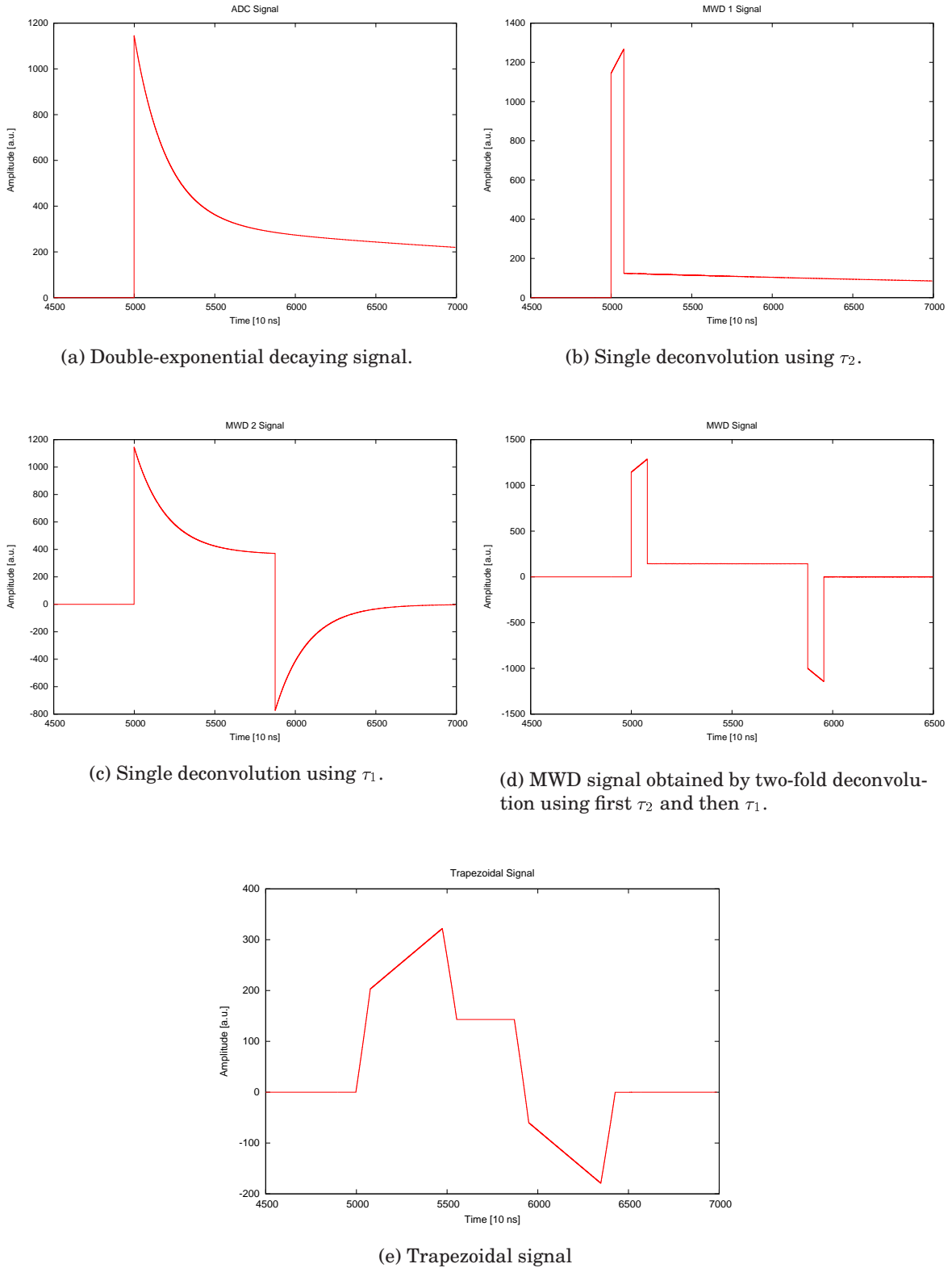


**Figure B.3:** The double-exponential decaying signal  $f_{2e}(t)$  is shown in (a). Panel (b) and (c) show the result of a single deconvolution, which cannot fully remove the exponential decay. Panel (c) shows the two-fold deconvolution, which removes the exponential decay and achieves a flat top. If a MA is applied to (c) then the shape in (d) is obtained. The trapezoidal shape has been transformed into a bipolar shape.

was also not available, but such a test was performed meanwhile [76]. Therefore, the amplitude of the pulser signal was increased by hand after about 10000 counts have been acquired.

The result is shown in figure B.4 for two different designs, the first one uses a  $16 \times 16$  multiplier and the second a  $24 \times 24$  multiplier. The design using the  $16 \times 16$  multiplier is clearly inferior compared to the one using the  $24 \times 24$  multiplier and this could be due to the implementation of the  $16 \times 16$  MWD, which has to be verified in further tests. The deviation of the pulser peak position from the function value is very large and even a quadratic fit does not improve the result. Therefore the design using the  $24 \times 24$  multiplier is the preferred implementation and was consequently used for the measurements with the detectors.

### B.5.1 Changing the ADC clock

The AD6645-80 ADC supports a minimum conversion rate of 30 MHz and a maximum conversion rate of 80 MHz. Since the ADC clock is generated by the FPGA a special VHDL code variant was written that reduces the ADC clock from 80 to 40 MHz. The result is shown in the figure B.6. One can clearly see that the decay time of the pulser seems to be different because the time difference between each sample is 12.5 and 25 ns in the upper and the lower panel, respectively.

Since the Nyquist filter is fixed to 40 MHz, the possibility to change the ADC clock is not very useful. Using a Nyquist filter set to 20 MHz, which is considered sufficient for current HPGe preamplifiers, would allow to switch between 40 and 80 MHz conversion frequency depending on the detector type connected to the GRT4. On the other hand, the preamplifiers for HPGe detectors already limit the bandwidth to about 20-30 MHz, i.e. a Nyquist filter might not be necessary since the signal power at high frequencies is very low<sup>14</sup>.

For slow detectors the 40 MHz conversion frequency also allows an increase of the shaping times by a factor of two without occupation of more block RAMs. For faster detectors like silicon strip detectors or inorganic scintillation detectors, the 80 MHz sampling frequency allows the analysis of the pulse shape<sup>15</sup>. However, since the GRT4 module was designed for the purpose of scanning highly segmented HPGe detectors, the operation at 80 MHz is mandatory and was used for the measurements in the following sections.

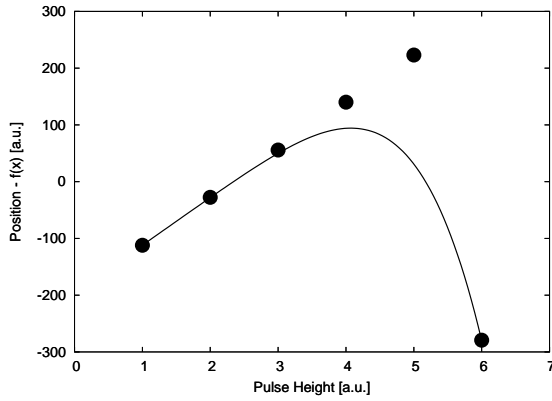
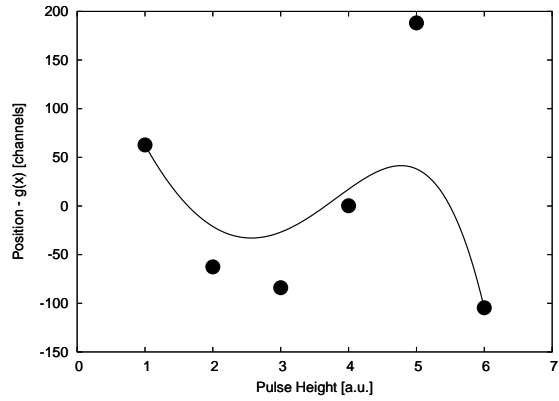
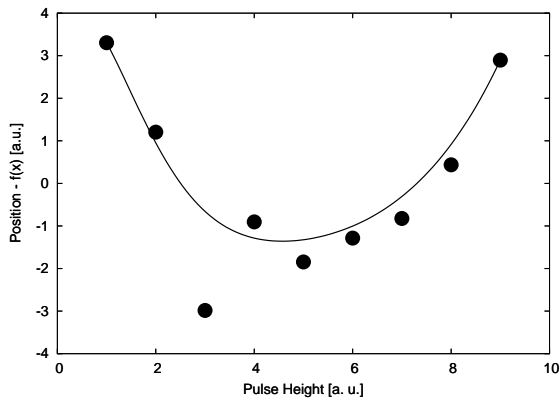
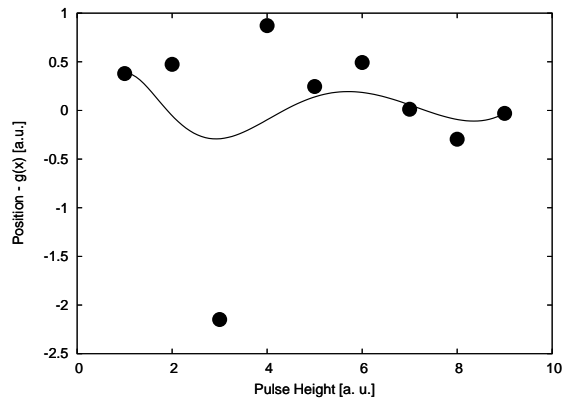
## B.6 MWD implementation for the DDC-8 module

The MWD implementation was tailored to the DDC-8 module [109], which can be used as a daughter card for the XLM-80 VME module and was considered as an electronics for the MINIBALL DSSSD detector. The DDC-8 features eight 10 bit 40 MHz ADC as well as one Spartan XC2S300E FPGA and can be read out using the USB connector.

In order to process all channels in parallel without disturbing interference, the trigger and state machine were generated eight times. However, for the energy branch a more efficient implementation was chosen. For this, the data from the ADC, coming

<sup>14</sup>If the response of the Nyquist filter is slow it allows the measurement of signal which are shorter than  $T_s$ , since the fast signal loads the capacitance of the filter which in turn discharges slowly.

<sup>15</sup>Very fast detectors, e.g. organic scintillator, are read out using analog electronics.

(a)  $16 \times 16$  multiplier with linear calibration(b)  $16 \times 16$  multiplier with quadratic calibration(c)  $24 \times 24$  multiplier with linear calibration(d)  $24 \times 24$  multiplier with quadratic calibration

**Figure B.4:** Linearity of the energy spectrum determined with a pulser. Two different MWD implementations were tested using either a  $16 \times 16$  or a  $24 \times 24$  multiplier. The pulser peak positions were fitted using a linear and a quadratic function and the residual, i.e. the difference between the peak position and the function value is plotted. The  $24 \times 24$  multiplier achieves the best results and the quadratic expression fits better than the linear function.

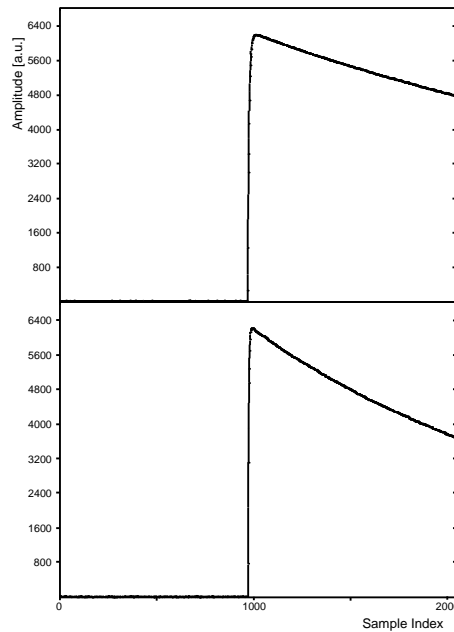


**Figure B.5:** The signal from a pulse generator was sampled with 80 and 40 MHz. This was possible with a modification to the VHDL code, because the ADC clock is generated by the DLL units in the Spartan 2 FPGA.

at a rate of 40 MHz, is first reduced by a decimation unit to a 10 MHz rate. Then all eight channels are consecutively processed at a 80 MHz rate by the energy filter (“octal pumped pipeline”) using a common peaking  $L$  and flat top time  $M - L$ , but separate decay time parameters  $\tau_{1...8}$ . In this configuration the peaking time can be adjusted between 100 ns and 3.2  $\mu$ s. The BLR update frequency is usually only 500 kHz and a processing of all eight channels can easily be achieved.

One of the most important components is the state machine, which allows an independent processing of all eight channels and is therefore present eight times. It does not feature any pile up rejection (non-extendable dead time model), but does detect a pile up condition. The state machine is connected to the associated fast trigger module (8 in total) and allows an independent latching of the corresponding energy and baseline filter values a fixed time after a trigger.

The code was simulated but the test with the hardware was deferred indefinitely.

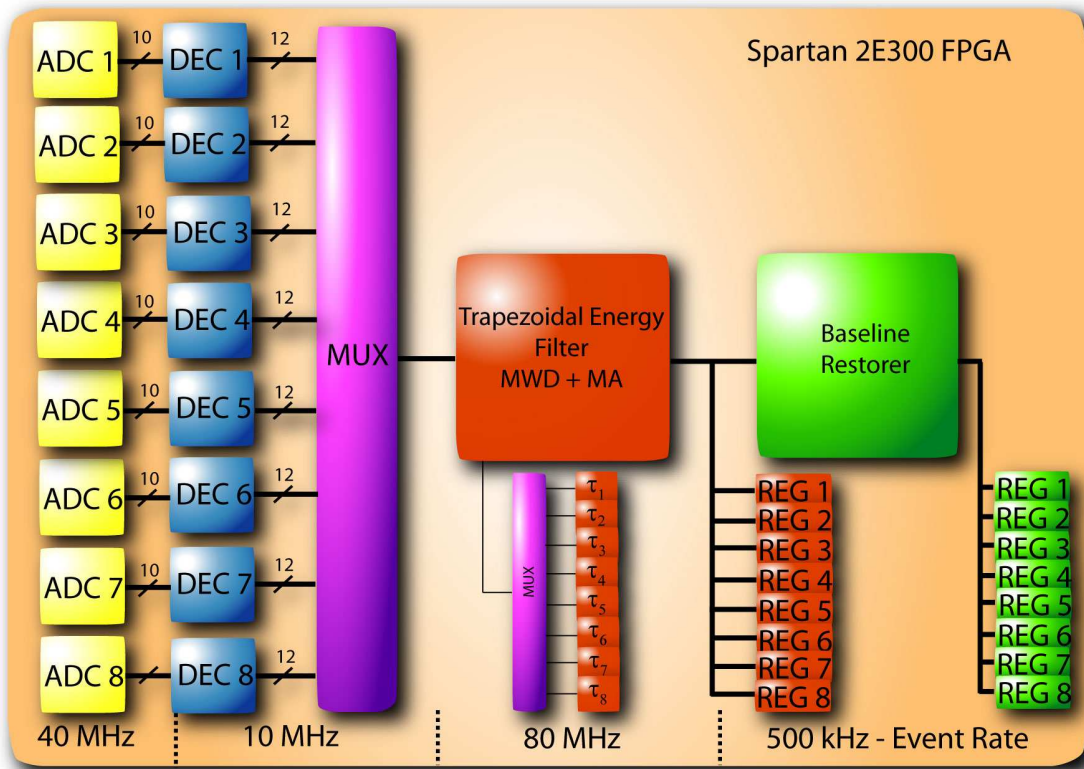


**Figure B.6:** MWD implementation for the DDC-8 module. Eight 10 bit 40 MHz ADC are processed by a single Spartan2 XC2S300E FPGA by combining the decimated data (DEC unit) into a single stream (MUX unit) for the single trapezoidal filter and baseline module.

# Appendix C

## The MINIBALL User Code

### C.1 Description of the User Code

The interface to the DGF-4C DSP code provided by XIA is explained in [24] and appendix A of the DGF programmer's manual [13]. The user code has to be added to a template file called `User.dsp` which consists of various subroutines that are called at certain stages of the DSP code. The user code can be comprised of up to 2048 instructions and 1000 words of data memory are reserved for variables and buffers. Interface to the XIA main code happens through global variables and data arrays. The user code writes the PSA results into an array comprising six data words (`URETVAL`)

```
ax0=0;
ar=ax0+1;
dm(UretVal) = ax0; /* chnhead[3]=0 */
dm(UretVal+1)= ar; /* chnhead[4]=1 */
ar=ar+1;          /* ar++ */
dm(UretVal+2)= ar; /* chnhead[5]=2 */
ax0=dm(PSA1);     /* get PSA result */
dm(UretVal+3)= ax0; /* chnhead[6]=PSA1 */
```

and the XIA main code writes this data into the list mode buffer. The User DSP code is executed only if bit zero of `MODCSR` and `CHANCSR` are set. If bit one of `CHANCSR` is set, the XIA code overwrites *all* channel header information after the energy word which allows between 2 and 6 return values depending on the list mode format (so called **compression**, which equals the value of the two LSBs of `RUNTASK`, i.e. `RUNTASK(1:0)`).

The user code will be linked with the XIA DSP code and has to be developed in the DSP assembly language that supports algebraic syntax which greatly enhances code readability as can be seen in the previous example. The Analog Devices Assembler Version 6.1 was used to compile the user code module with the supplied make file `dgf4cmake`. Executing `nmake -f dgf4cmake` in the `dsp` folder results in a `dgfcode.exe` and a `dgfcode.bin` file which can be downloaded to the DGF DSP using the `DGFViewer` software or the XIA C-code library.

The user code was debugged and tested with the `DGFViewer` software from XIA which is based on the data acquisition and analysis software `IGOR Pro` from WaveMetrics [110]. Since this software is also used by XIA to develop the DGF DSP code, the `DGFViewer` software comprises some XIA-made functions that ease the process of DSP code development but are not accessible through a GUI. Especially useful is the possibility to display the full DSP memory, by entering `memoryscan(n)` with `n` the module number and then `memoryview()` in the `IGOR` shell, and the parameter memory space,

by entering `dsppanel()`. With the knowledge of the DSP source code the contents of various variables, used by the DSP during event processing, give valuable information about the status of the DSP code. When debugging the DSP code, the debug output has to be written into reserved variables and arrays as illustrated in the next section and these variables can be read out together with the event data.

For pulse shape analysis the DSP reads the waveforms from the FIFO with each event trigger. The delay between trigger and the FIFO halt can be set by the user via the DSP variable `USERDELAY` after the threshold of the LE trigger has been set. Otherwise a change in the trigger threshold settings will change the trigger time with respect to the beginning of the signal and consequently change the trigger delay too.

All PSA algorithms need some pre-trigger data to determine the actual offset of the signal and the pre-trigger data should at least cover the length of any filter that is applied to the signal. Another constraint is the maximum length of the waveform buffer. The circular buffer is 2048 and the linear (list mode) buffer 8192 memory locations (16 bit words) deep. For on board pulse shape analysis, the waveforms are limited by the size of the circular buffer, because in this case the DGF-4C is operated such that the waveform output in the list mode buffer is suppressed (`COMPRESSION > 0` or `RUNTASK(1:0) ≠ 002`). In this case the data from the FIFOs and FPGAs, that is read by the event interrupt routine, is stored in the circular buffer and the final results (energy and PSA) are copied into the list mode buffer for read out.

It has also been observed - although unlikely - that the DGF has stopped data acquisition because the circular buffer was filled (write pointer crosses the read pointer). In this case either the event rate, the complexity of the XIA DSP code (including PSA) or the amount of intermediate data has to be reduced.

### C.1.1 Description of the User code subroutines

In the following section the various routines of the user code will be explained. The data array `merker` is used to call each module with up to 12 parameters and allow the function to return 12 parameters by overwriting the array contents. There was no specification for the user code with respect to complexity or computational effort, but the complexity is automatically limited by the available resources of DSP memory. The requirement to operate the MINIBALL array at high event rates was dropped and for the current operation at REX-ISOLDE with low beam intensities the current user code is considered to be fast enough (<0.1 ms). Nevertheless, it is possible to disable each individual PSA module. Furthermore interpolation operations, requiring a division, can be prevented, minimizing the processing time if a high throughput is more important than an improved accuracy.

It is important to note that the user code works only with the dedicated FPGA configuration files made for the MINIBALL collaboration, because with the MINIBALL firmware the ADC data is stored as a 14 bit word and not as a 16 bit data (as it is the case for the XIA firmware) in the FIFO. The reason is that computations with the 16 bit ADC word could lead to signed data, but for the 16 bit DSP this means that all computations have to be performed with multi-precision causing additional computations. Consequently, using the existing user code with the original XIA firmware will fail.

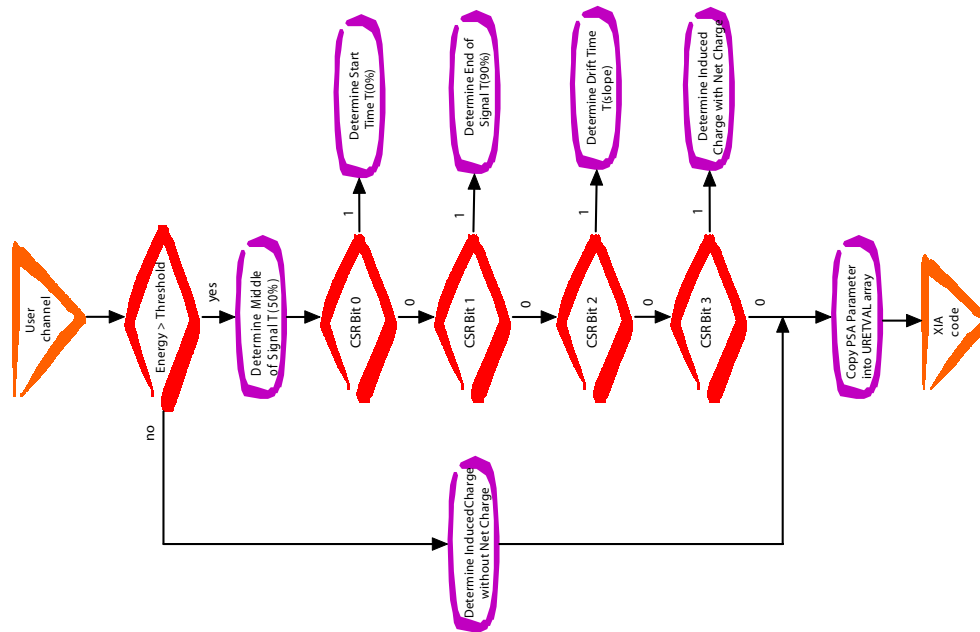


**Figure C.1:** The data flow of the channel processing. The channel code determines the value of the baseline in front of the leading edge of the signal first, before it checks if the energy is below a user defined threshold. In this case the induced charge is determined only, otherwise all timing algorithms are executed too if the corresponding bits in the PSA CSR are set. Before returning to the XIA code, the PSA results are copied into the URETVAL array.

## Overview

The main loop of the user code checks the actual channel number and then jumps to the corresponding subroutine. The channel processing code calls, depending on the settings, the various PSA modules and combines the data into the URETVAL array, which is later copied into the channel header by the main code. The channel code is shown in figure C.1.

The need to create a dedicated code for each channel comes from the requirement to check the intermediate results of each channel after event processing. Therefore the individual PSA results of each channel are stored in separate variables. In addition the XIA code is made such that the channels can be individually configured and this scheme was adopted for the user DSP code. Therefore the PSA modules interact with the channel module using the merker array. The channel routines write the configuration parameters into the merker array and call a certain PSA code module. The PSA module returns the results of the algorithm, possibly overwriting the previous contents of the merker array. On return to the channel code, the channel code copies the entries in the merker array into the proper variables reserved for this channel and PSA module.

But before the PSA algorithms can be called, the data structures have to be defined, which happens outside any function in the first part of the user DSP code, where all definitions of constants, variables and buffers can be found. The following excerpt illustrates

the process of defining data structures.

```

/* CONSTANTS SECTION*/
.CONST buflen=55; /* max. 1.375 us for PSA */
.CONST numchan=4;
.CONST fullbuffer=buflen*numchan;
/* VARIABLES SECTION */
.VAR/DM/SEG=UserData ShapeBuffer[fullbuffer]; /* Buffer: signal averaging */
.VAR/DM/SEG=UserData merker[12]; /* buffer: function */
.VAR/DM/SEG=UserData zaehler;
.VAR/DM/SEG=UserData nenner;

```

The constants are used to define the length of the data buffers and variables are used to store the results of the pulse shape analysis (e.g. Start0) or to store temporary results of a computation (e.g. zaehler). These are global variables with respect to the fact that they are accessible from all modules of the user code.

The user code added to the UserBegin section of the template computes various constant address offsets to data buffers. Since this part of the user code is only called once after startup of the ADSP-2181, it can only be used to define constant parameters.

```

UserBegin:
    ax0=666;
    dm(EvilError)=ax0; /* error code for "evil error" */

    i0=^SlopeBuffer; /* get address offset of slope buffer */
    m3=buflen; /* get length of slope buffer */
    dm(SlopeBuf0)=i0; /* store address of slope buffer 0 */
    modify(i0,m3);
    dm(SlopeBuf1)=i0; /* store address of slope buffer 1 */

JUMP UserBeginReturn; /* return to XIA code */

```

The UserRunInit section of the user code is responsible for the initialization of the data buffers and variables, since it is called during startup of every run. However, due to the large amount of data buffers it was decided to skip a large fraction of the initialization for resume runs, i.e. a series of data acquisition runs with the same parameter settings. The DGF-4C DSP code skips the initialization of the external memory for resume runs. In order to distinguish between new and resume runs the user code reads the contents of data memory at address **0x3fe5** and checks if bit 1 is set. If this is the case the current run is a new run, if not the current is a resume run and the code jumps directly to the location of the InitShortCut label. The process is illustrated in figure C.2. In case of a resume run, the user code clears only the variables that store the PSA results, but the new run code also has to clear all buffers and further zeros the variables that count the number of good and bad events, where a bad event is defined as an event which lead to an invalid PSA result.

### Determination of the Baseline

In order to determine the baseline value in front of the leading edge of the detector signal the user code averages a user-defined number of samples starting with the first data point of the waveform memory in the list mode buffer or a user-defined data buffer. The baseline routine shares three parameters with the main user code: the number of samples used for averaging (BASELEN), the number of digits to be shifted left (BASESHIFT) and the return value (BASELINE). During run initialization for a **new** run, the user

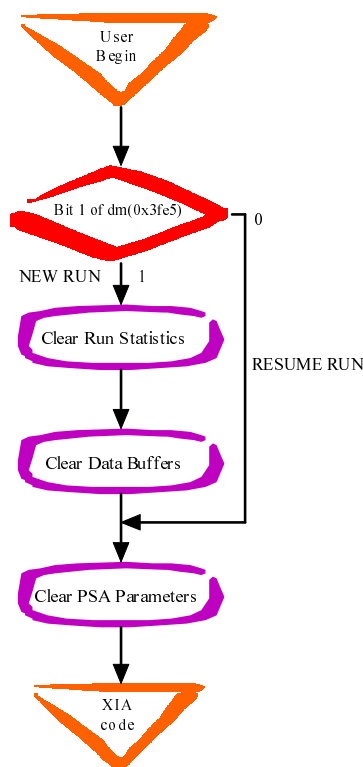


**Figure C.2:** The data flow of the run initialization routine. The initialization routine of the user DSP code checks if the current run is a new run or a resume run, i.e. no parameters were changed. In the latter case the code skips the initialization of the data buffers and run statistics and clears only the PSA results of the previous run.

code determines the number of samples (BASELEN) that should be added to the average and determines the exponent for the shifter operation (BASESHIFT) for normalization purpose. The process of determination the baseline is sketched in figure C.3.

The averaging starts with the first data word of the waveform buffer. It would be possible to define also an offset for the start of the MA operation or to use the existing PSAOFFSET parameter, however, the USERIN array is currently completely occupied and an additional user-defined array was not created.

### Determination of the Start Time $t_0$

The determination of the beginning of the detector signal, the start time  $t_0$ , consists of two parts. First a simple leading edge (LE) trigger algorithm searches for the beginning of the signal with a user-defined threshold and second a more accurate determination of the start time is obtained with an optional extrapolation from the position of the LE trigger to the baseline in front of the leading edge.

In order to be less sensitive to the noise of the baseline and to enable the usage of a low threshold, the leading edge trigger analyzes the waveform in backward direction. It does not start at the end of the waveform, because this would not work with a differen-

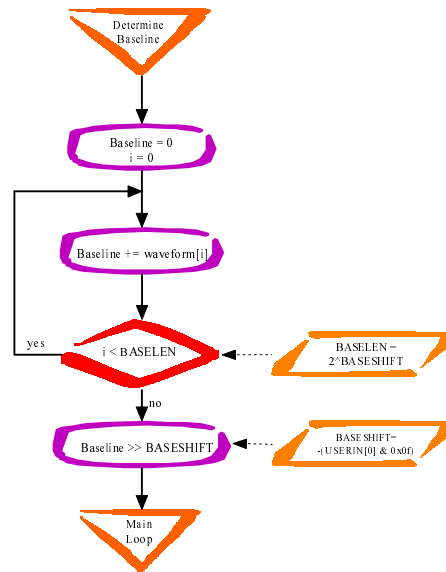


**Figure C.3:** The DSP code to determine the baseline needs two parameters, the length of the average and the shifter exponent. Both parameters are calculated during run initialization. The code then simply adds the required amount of samples, which can be adjusted in powers of two, before dividing the result by the filter length.

tiated signal, but from somewhere in the middle of the signal. In the previous release [24] the user code first performed the steepest slope algorithm and used the position of the steepest slope as a starting point for the LE trigger. With this release, the user code first determines the point where the signal reaches 50% of the final height ( $t_{50}$ ) and from this position the LE trigger is applied in backward direction. The threshold for the LE trigger is computed as the sum of the actual baseline value plus the trigger threshold that has been set by the user in the `USERIN[3]` or `USERIN[4]` parameter. By setting bit 13 of the PSA CSR (`PSA[13]`) the user indicates that an inter- or extrapolation operation is desired. For the determination of the start time it is possible to use two different methods for to achieve subsampling time resolution. The L-EBC algorithm is selected with `PSA[12]=0` and the Q-EBC algorithm can be chosen by setting `PSA[12]=1`. Both methods were previously described in section 2.6. Figure C.4 represents the process of the start time  $t_0$  determination.

### Risetime $t_{90}$

This module determines the position when the detector current signal ends. The current signal is integrated, i.e shaped, by the preamplifier<sup>1</sup>. In electronics engineering the step response of pulse shaping network is usually characterized by the rise time of the output signal, which is defined as the time difference between the position when the signal reaches 10% and 90% of its full height. The risetime of the detector signal contains also a radial position information as shown in [25, 54].

<sup>1</sup>Another approach to PSA is to model the response of the whole system, i.e. detector, preamplifier and electronics and create a data base of signals for various interaction positions. For the MINIBALL algorithms, it was verified in simulations and measurements [21, 22] that the preamplifier and electronics response does allow the usage of the developed algorithms.

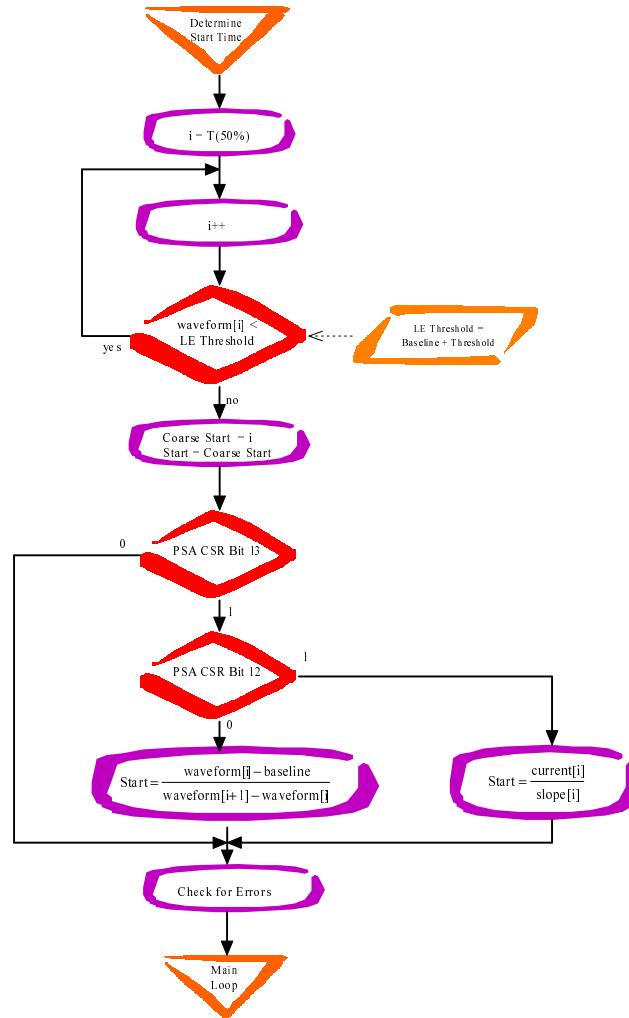


**Figure C.4:** The algorithm that determines the start time  $t_0$  consists of two parts, a leading edge trigger and an interpolation routine. The leading edge trigger starts from the  $t_{50}$  position and advances to the beginning of the buffer until the detector signal is below a user-defined threshold. Depending on the settings of the PSA CSR, the interpolation process can be skipped or two different methods of interpolation can be chosen. Before returning to the main loop, the code checks if the PSA results are outside of the waveform range.

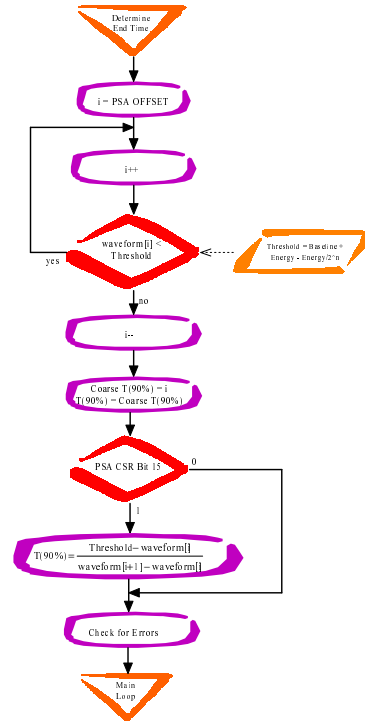


**Figure C.5:** The user DSP code that extracts the  $t_{90}$  time from the waveform starts from the position set with the PSA OFFSET parameter and advances to the end of the waveform until the signal crosses the user-defined threshold. If desired, an subsequent interpolation can be used to achieve a sub-sample accuracy. The algorithm checks if the determine PSA parameter is outside the signal boundaries after all processing is done.

In the user code the threshold can be adjusted in 16 steps and the fractional amplitude  $A$  is calculated by  $A = E - \frac{E}{2^n}$ , where  $E$  is the height of the signal<sup>2</sup> and  $n$  is the threshold parameter extracted from the USERIN[5] parameter. With  $n = 3$  the threshold is 87.5% and with  $n = 4$  the threshold is 93.75%. The  $t_{90}$  modules start from the coarse  $t_{50}$  position and advance to the end of the trace and compares at each position the actual value with the threshold value. A more accurate position of the  $t_{90}$  threshold position can be achieved by using a linear interpolation which is enabled with PSA[13]=1. The process is illustrated in figure C.5.

### Steepest Slope $t_{ss}$

In order to determine the steepest slope of the current signal, the derivative of the digitized charge signal has to be taken twice. The backward form of the two-point numerical derivative  $i[n] = c[n] - c[n - 1]$  was chosen for the implementation (being the only causal

<sup>2</sup>Which is currently derived from the energy information, which gives the best resolution. However, the height can also be extracted directly from the acquired waveform.

form) consequently leading to an asymmetric form of the second derivative

$$\begin{aligned} s[n] &= i[n] - i[n-1] = c[n] - c[n-1] - (c[n-1] - c[n-2]) \\ &= c[n] - 2c[n-1] + c[n-2] \end{aligned}$$

Clearly, the asymmetric form leads to an additional delay of the steepest slope position. However, since also the preamplifier transfer function has a non-zero phase response [21], both contributions can simply be taken into account with proper calibration constants. The derivative of the current signal is delayed with respect to the original charge signal, which is used to determine the beginning of the detector signal and therefore both effects lead to an additional offset of the steepest slope spectra. Previously, the second derivative was applied starting from the data point indicated by the `PSAOFFSET` parameter and for a length of `PSALENGTH` samples. Currently, the code uses the information from previous PSA modules, namely the start time  $t_0$  and the end of the rising edge, the  $t_{90}$  position, and applies the second derivative only to the data in between these two positions. However, an additional safety interval was added, such that the PSA starts from  $t_0 - 1$  and ends at  $t_{90} + 3$ . Once the coarse position of the steepest slope has been found by searching for the minimum in the second derivative, a sub-sampling position can be obtained using a quadratic interpolation if required by the user (`PSA[13]=1`).

The code includes a simple error check routine, that verifies that the resulting position is inside the boundaries of the acquired waveform and if not sets an error code. If only the interpolated position is outside the waveform interval and the coarse position is inside the valid range, the code sets the interpolated value to the coarse value, but still indicates the problem with an error code. If both values are invalid, the user code sets the `EVILERROR` code and stops further event processing. The assembler program is represented in figure C.6.

### Induced Charge $q^{max}$

The determination of the height of the induced charge  $q^{max}$  is split in two modules, depending if energy was deposited in the current segment or not. In case there was an energy deposition in the segment, which is assumed if the energy value determined by the DGF-4C exceeds a user defined threshold (`USERIN[1]` & `USERIN[2]`), the charge signal of a segment is a superposition of a net charge signal originating from the charge carriers drifting towards the segment and core contacts and a mirror charge signal coming from the charge collection processes in neighboring segments. In this case, the mirror charge signal has to be extracted from the detector signal first before the same algorithm as in case of a zero net charge can be applied. If the segment signal features only the temporary mirror charge signal, the algorithm first determines the absolute value of each sample (`waveform[i]=abs(waveform[i])`) and then searches for the maximum amplitude of the charge signal. Of course the signal offset is subtracted in advance. The maximum amplitude  $q^{max}$  of the induced charge will be used as input to the  $\log\left(\frac{|q_+|}{|q_-|}\right)$  algorithm and the algorithm is shown in figure C.8.

The presence of a net charge signal requires further processing. It was found out [23] that the leading edge of the net charge signal can be approximated with a linear rising signal. However, the rise time and the start position of the signal are not known, since the segment signal is distorted by the additional component coming from the temporary mirror charge. Therefore, the begin and end of the segment signal is not extracted from the segment itself but from the core signal, which is not influenced by mirror charges.

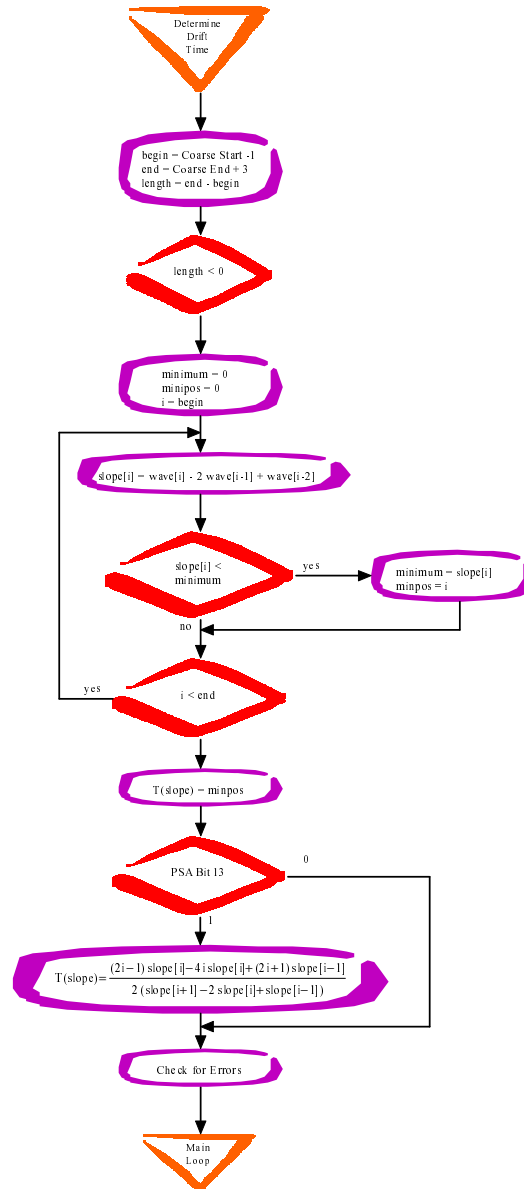


**Figure C.6:** The position of the steepest slope  $t_{ss}$  of the current signal is derived from the second derivative of the charge signal. During calculation of the slope signal, the user code check if a new minimum has been found and stores the position and amplitude of a new minimum. The algorithm checks if the determine PSA parameter is outside the signal boundaries after all processing is done.

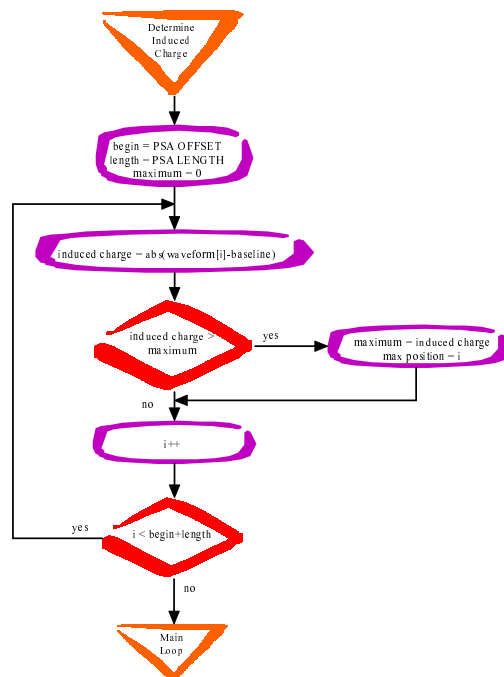


**Figure C.7:** The algorithm for the segment with no net charge extracts the induced charge by subtracting the baseline value from the waveform between the two positions set with the PSA OFFSET and LENGTH parameters and taking the absolute value. If a new maximum is found, the amplitude and position are stored and the maximum amplitude  $q^{max}$  of the segment will be returned to the XIA code.

The DGF-4C module has not enough channels to readout a full MINIBALL detector, and consequently the detector signals (six segments plus one signal from the core) a distributed over two DGF-4C modules. If the core signal is not available on one of these DGF modules, another method applies to determine the begin and end of the segment signal. In this case, these parameters have to be set by the user to an average value and consequently the average end position and the average position of the beginning of the signal has to be determined by the user by inspecting the PSA parameters  $T_0$  and  $T_{90}$ . If these parameters are not correctly set, the PSA will fail. The PSA algorithm is shown in figure C.8 and the setup of the DSP code parameters will be presented in one of the following sections.

### Processing Time

The behavior of the DSP is predictive in the way that the execution of an instruction does not depend on a successful cache access or the result of a previous instruction, since DSP has no cache and the computational units work without pipelining. Therefore each instruction or multi-instruction is executed in 25 ns if the DSP is clocked with 40 MHz. Therefore an estimate of the processing time can be achieved by counting the number of instructions per module assuming a risetime of 400 ns

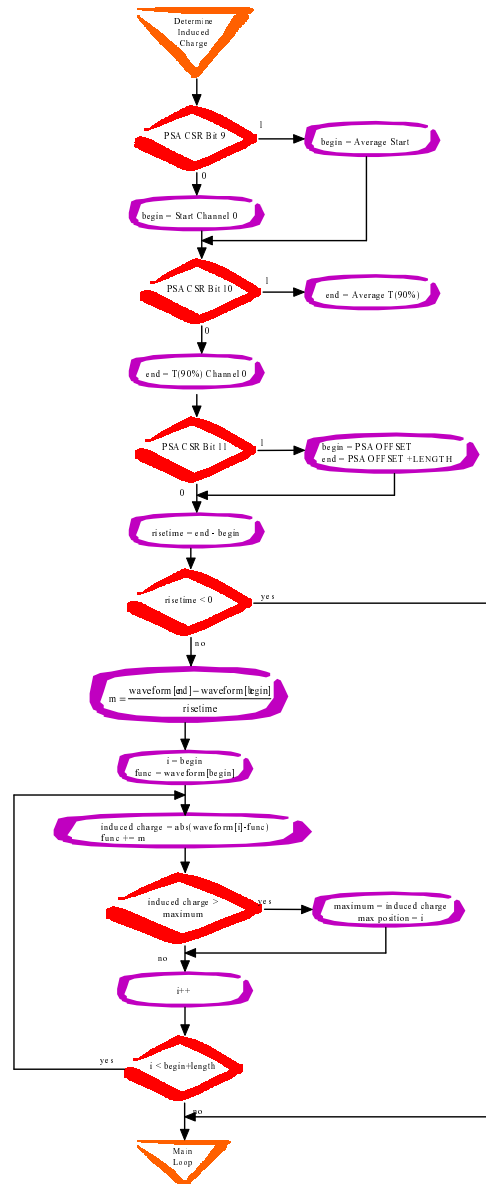


**Figure C.8:** The code first determines which parameters should be used as a reference for the start and end time of the segment signal. The user can decide if the result of the PSA of DGF channel 0 will be used, which is recommended if channel 0 is connected to the core of a MINIBALL detector or if the average  $t_0$  and  $t_{90}$  values or the PSA OFFSET and LENGTH parameters will be used. The next step is the determination of the slope of the leading edge, which uses the risetime information and the amplitude information. A linear rising signal using the previously derived slope is then subtracted from the detector signal, resulting in the (approximated) induced signal. Then the same operations as in case of no net charge can be used to determine the maximum amplitude  $q^{max}$  of the mirror charge.

- Baseline: 0.5  $\mu\text{s}$  (8 samples)
- $t_{50}, t_{90}$ : 1.0  $\mu\text{s}$  (without interpolation)
- $t_0$ : 1.125  $\mu\text{s}$  (without interpolation)
- $t_{ss}$ : 3.25  $\mu\text{s}$  (without interpolation)
- Mirror Charge: 2.95  $\mu\text{s}$  (without net charge signal)
- Mirror Charge: 4.75  $\mu\text{s}$  (with net charge signal)
- Linear Interpolation: 0.85  $\mu\text{s}$

In case the energy is below the threshold value the total processing time for PSA is as low as 3.5  $\mu\text{s}$ , but for a channel with an energy above the threshold the processing time can be as high as about 15  $\mu\text{s}$  if all PSA algorithms are enabled.

## C.2 Input Format

An array of 16 words was reserved for the configuration of the user DSP code from the host computer. The USERIN array is located in the parameter memory space of the DGF-4C. The current usage of the USERIN array is shown in table C.1. Table C.2 summarizes the expected data formats of the user code parameters.

One of the most important parameters of the USERIN array is the CSR parameter, which controls the user DSP code by en-/disabling subroutines and PSA algorithms. The usage of the PSA CSR is shown in table C.3.

A deliberate configuration of the user DSP code is mandatory for proper operation.

## C.3 Output Format

Finally, after all PSA modules finished successfully their event processing the results of the PSA algorithms are copied into the URETVAL array from which the XIA DSP code transfers the data into the channel header in the list mode buffer for each event. The final contents of the channel header in DGF-4C list mode buffer is explained in table C.4. Table C.5 explains the meaning of the individual bits in the error code word.

## C.4 Configuration Software for the User DSP Code

Before the user code can be enabled by setting MODSCR bit 0 and CHANCSR bit 0, the code has to be configured to the needs of the experiment. For this the USERIN array has to be set correctly, which will be explained in this section. The structure of the DGF-4C DSP code can be seen from the dgfcode.map file which reports the usage of the DSP memory and the mapping of the DSP modules into the available memory of the DSP (as defined in the dgfcode.ach file).

```
0000 - 1FFF [ 8192.] pm ram code PROGRAM
2000 - 2BFF [ 3072.] pm ram code USERPROGRAM
0000 - 019F [ 416.] dm ram data DGF_PARAMS
01A0 - 3B93 [ 14836.] dm ram data DMDATA
3B94 - 3FDF [ 1100.] dm ram data USERDATA
```

Offset	Parameter Name	Description
0	BASELINE0/1/2/3	Length $2^n$ of Baseline Average
1	ENERGY THRESH0/1	Threshold for net charge presence
2	ENERGY THRESH2/3	Threshold for net charge presence
3	TRIGGER THRESH0/1	Threshold for software LE trigger
4	TRIGGER THRESH2/3	Threshold for software LE trigger
5	$t_{90}$ THRESH0/1/2/3	Threshold for software LE trigger
6	PSA CSR CHN0	Control and Status Register for PSA Channel 0
7	PSA CSR CHN1	Control and Status Register for PSA Channel 1
8	PSA CSR CHN2	Control and Status Register for PSA Channel 2
9	PSA CSR CHN3	Control and Status Register for PSA Channel 3
10	PSA LENGTH0/1	Number of samples used for PSA
11	PSA LENGTH2/3	Number of samples used for PSA
12	PSA OFFSET0/1	Offset with respect to start of waveform
13	PSA OFFSET2/3	Offset with respect to start of waveform
14	REFT0	Reference $t_0^{\text{ef}} = t_0^{\text{ave}}$
15	REFT90	Reference $t_{90}^{\text{ef}} = t_{90}^{\text{ave}}$

**Table C.1:** Usage of the USERIN data array. The data is ordered with respect to the address offset relative to the address of USERIN.

Parameter	Function	Size	Format	USERIN
BASELEN	Length of MA	4	int	0
E_THRESH	Defines energy deposition	8	int	2/1
LE_THREH	Trigger Threshold	8	int	4/3
T90_THRESH	Fraction for Discriminator	4	int	5
PSA_CSR	Control and Status Register	1	bit	9/6
PSA_LENGTH	Number of samples used for PSA	8	int	11/10
PSA_OFFSET	Start bin for PSA	8	int	13/12
$t_0^{\text{ave}}$	Average start bin	16	8.8	14
$t_{90}^{\text{ave}}$	Average $t_{90}$ bin	16	8.8	15

**Table C.2:** Size and position in the USERIN array of the user code parameters.

Index	Module	Name	Description
0	MB PSA	$t_0$	Enables EBC algorithm
1	MB PSA	$t_{90}$	Determine end of signal risetime
2	MB PSA	$t_{ss}$	Determine position of steepest slope
3	MB PSA	Mirror Charge	Determine height of mirror charge
4	TFA	Energy Threshold	User energy threshold for TFA
5	TFA	Enable TFA	Enable TFA module
6	TFA	TFA	-
7	Averaging	Force Average Timing	Execute PSA with averaged signal
8	Averaging	Enable Averaging	Enable signal averaging
9	Averaging	Use $t_0^{ave}$	Use as reference time
10	Averaging	Use $t_{90}^{ave}$	Use as reference time
11	Averaging	Offset and Length used as $t^{ref}$	Use as reference time
12	MB PSA	Enable $\frac{f'}{f''}$	Q-EBC instead of L-EBC
13	MB PSA	Enable Interpolation for $t_0/t_{ss}$	perform interpolation
14	MB PSA	Overwrite GSLT	return 6 PSA parameter
15	MB PSA	Enable Interpolation for $t_{50}/t_{90}$	perform interpolation

**Table C.3:** Usage of the PSA Control and Status Register (CSR).

Index	XIA Code	Description	User Code	Description
0	NDATA	Number of Words	NDATA	same
1	TRIGTIME	Fast Trigger Time	TRIGTIME	same
2	ENERGY	Energy	ENERGY	same
3	XIAPSA	XIA PSA value	$t_0$	Position of the signal begin
4	USERPSA	User PSA value	$t_{ss}$	Position of the steepest slope
5	GSLTHI	GSLT time stamp	$\max q_{mirror} $	Maximum height of mirror charge
6	GSLTMI	GSLT time stamp	$t_{qmax}$	Position of mirror charge maximum
7	GSLTLO	GSLT time stamp	Error Code	PSA Error Code
8	REALTIMEHI	High Word Real Time	$t_{90}$	Position of signal end

**Table C.4:** Usage of the Channel Header information for the User code compared with that of the original XIA DSP code. For  $COMPRESSION > 1$  only a fraction of PSA parameters will be included into the header information. Similarly, if bit 1 of CHANCSRB is zero, the XIA PSA parameter is not overwritten and included into the channel header. Similarly, if PSA[0] is zero, the  $t_0$  parameter is replaced by the XIA PSA result (a constant fraction time  $t_{xx}$ ).

Bit	Name	Description
0	ERR_T50	Indicates an unrecoverable error in the $t_{50}$ module
1	ERR_T90	Indicates an unrecoverable error in the $t_{90}$ module
2	ERR_T0	Indicates an unrecoverable error in the $t_0$ module
3	ERR_TSLOPE	Indicates an unrecoverable error in the $t_{ss}$ module
15	BAD_ENERGY	DGF-4C indicates a bad energy measurement

**Table C.5:** Interpretation of the PSA error codes.

The memory that has been reserved for the parameters (DGF\_PARAMS) is located at the beginning of the data memory (dm) space. In order to access the data memory via CAMAC transfers an offset of 0x4000 has to be added to the TSAR<sup>3</sup> of the DGF-4C. The USERIN array can be found at a relative offset of 48 (= 0x30) and a total of 16 memory locations were reserved. The offset for the USEROUT array is 288.

```
0030 - 003F [ 16.] dm ram      variable USERIN of INTVECT
0120 - 012F [ 16.] dm ram      variable USEROUT of INTVECT
```

Because of the limited amount of memory reserved for the USERIN array, the parameters have to be compressed to fit into the available space, i.e. parameters can be accessed byte, nibble or bit wise. If four channels have to fit into one 16 bit word, only four bits are available per channel and similarly if 8 bits are reserved for the parameter, two channels fit into one memory location. In the former case, one parameter has to be shifted before addition, i.e. channel 1  $\times$  256 + channel 0. In the latter case, the computation is channel 3  $\times$  2<sup>12</sup> + channel 2  $\times$  2<sup>8</sup> + channel 1  $\times$  2<sup>4</sup> + channel 0. Clearly, the individual parameters have to stay inside their 4 or 8 bit boundaries. Table C.2 summarizes the properties of the user code parameters in the USERIN array. If it is desired to set the average start and end time ( $T_0^{ave}$  and  $T_{90}^{ave}$ ), it will be necessary to get the offset for these variables from the dgfcode.map file and set the timing information (in the 8.8 fractional format) with a CAMAC access as shown in the following pseudo code example

```
OFFSET_DSP = 0x4000;
/* get address offset of STARTAVE0/1/2/3 from dgfcode.map file */
OFFSET_START_AVE = 0x3dc1;
VALUE_START_AVE = 3072; /* 3072/256 = 12.0 */
CAMAC_WriteTSAR(OFFSET_DSP+OFFSET_START_AVE); /* set Transfer Start Address Register */
for(i=0;i<4;i++) CAMAC_WriteDSP(VALUE_START_AVE); /* 4 channels */

/* get address offset of TENDAVE0/1/2/3 from dgfcode.map file */
OFFSET_END_AVE=0x3dc6;
VALUE_END_AVE=6912; /* 6912/256 = 27.0*/
CAMAC_WriteTSAR(OFFSET_DSP+OFFSET_END_AVE); /* set Transfer Start Address Register */
for(i=0;i<4;i++) CAMAC_WriteDSP(VALUE_END_AVE);
```

In the latest DSP code release these parameters can be set using the USERIN14 and USERIN15 parameters of the DGF.

In order to mimic the memoryview() command of the IGOR shell, the user program has to read the full data memory starting at the data memory offset. It is also possible to read out the circular and the linear data buffers. The offsets can be obtained from the dgfcode.map file

```
0800 - 0FFB [ 2044.] dm ram circ variable EVENTBUFFER of INTVECT
0FFC - 2FFB [ 8192.] dm ram      variable BUFFER of INTVECT
```

## C.5 Fixed Point Data Formats

The DSP supports only fixed point computations in hardware. In order to understand the computations of the user code, the representation of a fractional number in the fixed point format is required. The radix point in fixed point computation defines the dynamic range and the precision that can be achieved. Some examples of fixed point formats are compiled in table C.6. For the computation with binary numbers ( $b = \sum_n c_n 2^n$ ) similar rules apply as for the computation with decimal numbers ( $d = \sum_n c_n 10^n$ ). For the multiplication and division of two fractional numbers  $F_1 = I_1.F_1$  and  $F_2 = I_2.F_2$

---

<sup>3</sup>Transfer Start Address Register

Format	DR Unsigned	LSB	DR Signed	LSB
16.0	[0, 65535]	1	[-32768, 32767]	1
8.8	[0., 256[	0.0039	[-128., 128[	0.0039
1.15	[0.,2[	0.0000306	[-1., 1[	0.0000306
0.16	[0, 1[	0.0000153	-	-

**Table C.6:** Dynamic range (DR) and the size of the LSB for three fixed point data formats. The  $,x[$  stands for  $, (x\text{-LSB}) ]$ .

with  $I$  being the integer part and  $F$  being the fractional part of the representation the following rules are obtained

$$\begin{aligned} I_1.F_1 \cdot I_2.F_2 &= (I_1 + I_2).(F_1 + F_2) \\ I_1.F_1 \div I_2.F_2 &= (I_1 - I_2 + 1).(F_1 - F_2 - 1) \end{aligned}$$

For example the multiplication of a 24.0 with a 0.24 number yields a 24.24 number, while the multiplication of a 16.0 with a 8.8 number gives a 24.8 number. For the division of a 32.0 by a 16.0 number, the 32.0 number has to be shifted into a 31.1 format first. Then  $31.1 \div 16.0$  yields a 16.0 number. Usually, a certain output format is desired and the format of the divisor is fixed. Therefore the dividend is shifted such as to achieve the proper result.

## C.6 Event Trigger

An amplitude and risetime compensated (ARC) constant fraction discriminator (CFD) [111, 112] was added to the FPGA code of the DGF-4C [113] in addition to the previously existing leading edge trigger.

The CFD module was implemented in an efficient way, using many of the existing modules in the FPGA. The fast filter trapezoidal shaper was used for the CFD algorithm, replacing the additional timing filter amplifier (TFA) circuit, which is usually used in analog setups. The trapezoidal shaper is used to differentiate the ADC signal, ensuring that the signal quickly returns to the baseline after a  $\gamma$  event. The time constant of the differentiation can be adjusted, preserving the signal amplitude in case of a large time constant. A subsequent integration improves the signal to noise ratio before the leading edge and constant fraction discriminator algorithms are applied.

The constant fraction discriminator consists of a delay line and an attenuation network. The zero crossing is determined by the condition that the amplitude of the delayed signal equals a fraction of the signal amplitude. Clearly, this approximation is only valid inside a certain range of the signal, the compensation range [29], where variations in the signal shapes are small. Consequently, the CFD delay has to be adjusted with care in order to ensure operation of the CFD inside the compensation range<sup>4</sup>.

A schematic of the CFD implementation is shown in C.9. The additional delay after the CFD shaper was added instead of a slow risetime rejection circuit. If the leading edge discriminator crosses its threshold after the constant fraction discriminator fires, then the time of the trigger is determined by the LE discriminator. In order to ensure

<sup>4</sup>In the case of a linear signal the CFD triggers at  $t = \frac{K}{1-2^{-n}}$  [29].

CFDREG Parameter	Fraction	FWHM [ns]	RMS [ns]
0x3fef	0.5	119.0	69.5
0x7fef	0.25	81.5	55.5
0xbfef	0.125	72.5	54.0
0x3fef	0.5	81.1	50.8
0x7fef	0.25	58.5	31.7
0xbfef	0.125	55.3	30.3

**Table C.7:** Time resolution obtained with the CFD trigger implemented in the DGF-4C FiPPI. A fraction of 25 % is advisable in order to get a good time resolution. Decreasing the fraction to 12.5 % doesn't improve the time resolution further, even though an optimal fraction of 10 % was reported for certain detectors. The upper rows were obtained if an energy of 344 keV was required for detector B and no requirements were set for detector C. The lower three rows show the time resolution for a true coincidence measurement requiring 344 and 779 keV in detector B and C, respectively.

that the trigger is generated by the CFD only, even in the case of late LE triggers, the CFD output can be delayed by up to 400 ns. Instead of rejecting slow risetime events, i.e. late LE triggers, it was tried to recover a proper CFD operation in this case. However, the operation of the additional delay was not tested.

The time resolution of the CFD was measured for three different attenuations by irradiating the MINIBALL cluster detector with a  $^{152}\text{Eu}$  source. The operation of the CFD is controlled by a single parameter only, which is called CFDREG.

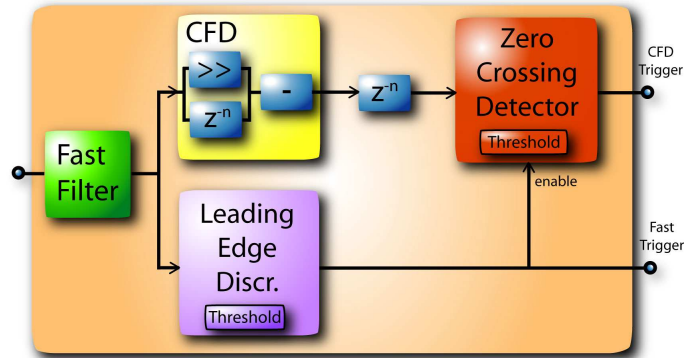
The threshold of the zero crossing detector can be adjusted to achieve minimum walk. However, the implementation supports *negative* thresholds only and for the measurement the CFD was set to the largest value supported, which represents  $-1^5$ . Five bits (of 16) were reserved for the discriminator threshold.

The delay of the CFD is can be adjusted over a 400 ns range, however the minimum delay is likely to be 75 ns which is due to additional delays in the implementation. Consequently, a delay less than 75 ns cannot be achieved. The inherit delay could be determined with a simulation of the CFD algorithm, but this was not supported.

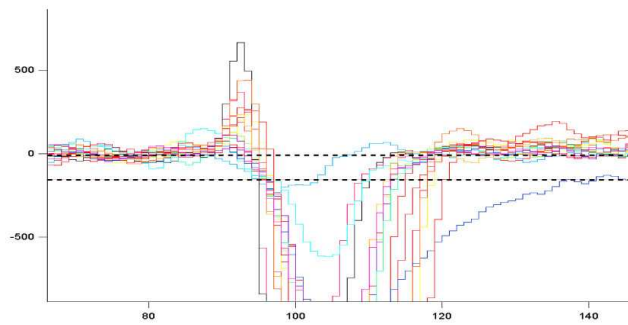
For the measurements the CFD delay was set to 25 ns, i.e 100 ns in total. The additional trigger delay was set to 0 ns. The results are compiled in table C.7. For a coincidence measurement a time resolution of about 60 ns was obtained, which is slightly more than twice the sampling period of the DGF-4C. This could be improved further if the trigger would be generated with the sample which is closest to the zero crossing instead of the sample after the zero crossing.

However, since a better time resolution can be achieved with the subsequent pulse shape analysis, the time resolution of the CFD is less important than the amplitude dependence, which causes an energy dependent time resolution as shown in C.9. In panel (c) the time difference between two detectors is plotted versus the energy deposition in detector C, while an energy of 344 keV was required for detector B. Below 300 keV in detector C the time difference between the two detectors increases, indicating that the CFD is not independent of the signal amplitude in this region due to the small slope of the low energy signals and the insufficient sampling rate.

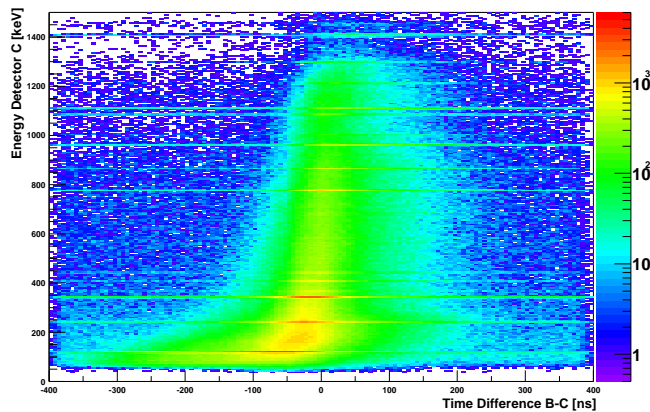
<sup>5</sup>The lower three bits (3 LSBs) of the CFD data are ignored by the discriminator.



(a) Schematic of the CFD implementation.



(b) Threshold adjustment for walk compensation.



(c) Energy dependence of the time resolution.

**Figure C.9:** The implemented constant fraction discriminator is shown in (a). The ADC data is first routed through the fast filter, which is a trapezoidal shaper, resulting in a differentiated and subsequently smoothed signal. Then the signal path is split, the fast filter output is connected directly to the leading edge discriminator, whose output is used to enable the zero crossing detector of the CFD, and also to the CFD circuits which implements the CFD pulse shaping based on delay elements and attenuation. Below the usage of a non-zero threshold to reduce the time walk is indicated. A typical time difference spectrum of the hardware CFD trigger using a fraction of 25 % plotted as a function of the energy deposition in one detector is shown in (c). Below 400 keV the time difference is still strongly dependent on the energy, i.e. amplitude of the signal, showing that the CFD cannot ensure an amplitude and risetime independent trigger for low energy signals.



## Appendix D

# Contents of the CD-ROM

The CD-ROM contains four folders.

- The folder *DGF* contains the user DSP code for the pulse shape analysis in various versions.
- The folder *GRT4* contains the full XILINX WebPACK project for the GRT4 module.
- The folder *DDC* contains a more efficient implementation of the MWD due to increased use of pipelining.
- The folder *CC32* contains the RPC CAMAC server and the ROOT client software.
- The folder *LaTeX* contains the source of this thesis including all pictures and plots, the thesis as PDF and PS file



# Acknowledgments

”When we long for a life with no difficulties, remind us that oaks grow strong in contrary winds, and diamonds are made under pressure.” - Peter Marshall

Many people contributed and helped on the way to complete this thesis.

My advisers Dr. Heiko Scheit and Prof. Dr. Dirk Schwalm contributed with many ideas and discussions. Without their help and the working environment provided this thesis would not have been possible.

I want to thank both present and former members of the CB group for the various contributions and discussions. Especially I want to mention Vinzenz Bildstein, Hans Boie, Joerg Fitting, Dr. Christoph Gund, Dr. Frank Koeck and Oliver Niedermaier.

I am grateful to Ian Lazarus for the collaboration on the development of the GRT4 module and the many discussions concerning FPGAs and the GRT4 module.

I am grateful to Dr. Michael Momayezi for the help in debugging my DSP code. I thank Jack Harris for an interesting night in the Yosemite National Park.

I am grateful to the comp.arch.fpga newsgroup and the many contributors.

Finally I want to thank my family and friends for their continuous and unwearied support. Especially I want to mention my girlfriend Anke, my sister Eva and also Andreas, Barbara, Christoph, Eric, Holger, Mathias and Uwe.



# Bibliography

- [1] GSI Future Project, <http://www.gsi.de/zukunftsprojekt/>
- [2] The ISOLDE Facility Homepage, <http://isolde.web.cern.ch/isolde/>
- [3] H. G. Thomas et al., *Encapsulated Ge detectors: development and first tests*, Nucl. Instr. Meth. A 369 (1996) 135
- [4] *Kapsel für einen im Ultrahochvakuum arbeitenden Detektor*, Deutsches Patentamt Offenlegungsschrift DE 43 24 709 A1, 23.07.1993  
*Verfahren zur Herstellung eines gekapselten Detektors*, Deutsches Patentamt Offenlegungsschrift DE 43 24 710 A1, 23.07.1993
- [5] *Halbleiterdetektor aus hochreinem Grundmaterial, insbesondere Germanium*, Deutsches Patentamt Offenlegungsschrift DE 29 24 569 C2, 19.06.1979
- [6] C. P. Cork et al., *Encapsulation of germanium detectors for space flight*, IEEE Trans. Nuc. Sci. NS-43, No.3 (1996) 1463
- [7] EUROBALL Homepage, <http://nnsa.dl.ac.uk/euroball-home/>
- [8] I. Y. Lee, *The Gammasphere*, Nucl. Phys. A 520 (1990) 641c.
- [9] G. J. Schmid et al., *Gamma-ray polarization sensitivity of the Gammasphere segmented germanium detectors*, Nucl. Instr. and Meth. in Phys. Res. A 417 (1998) 95-110
- [10] J. Eberth et al., Prog. Part. Nucl. Phys. 46 (2001) 389-398
- [11] D. Habs et al., *The REX-ISOLDE Project*, Nucl. Instr. Meth. A616 (1997) 29c-38c
- [12] W. F. Mueller et al., *Thirty-two-fold segmented germanium detectors to identify gamma rays from intermediate-energy exotic beams*, Nucl. Instr. Meth. A 466 (2001) 492
- [13] X-ray Instrumentation Associates, <http://www.xia.com>
- [14] I-Yang Lee, *An "Ultimate" Gamma Ray Detector*, LBL, 1994
- [15] K. Vetter et al., *Three-dimensional position resolution in two-dimensionally segmented HP-Ge detectors*, Nucl. Instr. and Meth. A 452 (2000) 223-238
- [16] The Advanced Gamma-Tracking array AGATA, <http://agata.pd.infn.it/index.html>

- [17] K. Vetter et al., *Gamma-ray imaging with position-sensitive HPGe detectors*, Nucl. Instr. Meth. A, in press
- [18] L. Mihailescu, *Principles and Methods for  $\gamma$ -Ray Tracking with large volume Germanium Detectors*, PhD Thesis, Forschungszentrum Juelich, 2000
- [19] GRETA Newsletter Number 3, July 2004, <http://radware.phy.ornl.gov/greta/news3/>
- [20] GRETA-Module Proposal, <http://greta.lbl.gov>
- [21] Luis Palafox Gamir, *A New Method for the Determination of the Entry Position of  $\gamma$ -rays in HPGe Detectors by Current Analysis*, PhD Thesis, University of Heidelberg, 1997
- [22] Christoph Gund, *The Sixfold Segmented MINIBALL Module Simulation and Experiment*, PhD Thesis, University of Heidelberg, 2000
- [23] Dirk Weisshaar, PhD thesis, Institut für Kernphysik (IKP), University of Cologne, 2003
- [24] M. Lauer, *Implementierung von Algorithmen zur Echtzeitpulsformanalyse von HPGe Detektorsignalen*, Diploma Thesis, Universität Heidelberg, 2000
- [25] J. Fitting, *Messung und Pulsformanalyse an einem MINIBALL-Cluster-Detektor*, Diploma Thesis, University of Heidelberg, 2002
- [26] E. E. Haller, *Detector Materials: Germanium and Silicon*, IEEE Trans. Nucl. Sci. NS-29 (1982), 1109
- [27] P. Sangsingkeow et al., *Advances in germanium detector technology*, Nucl. Instr. Meth. A 505 (2003), 183-186
- [28] J. Gerl, *Gamma-ray detector design*, [http://www-gsi-vms.gsi.de/eb/docs/eb\\_design.ps-gz](http://www-gsi-vms.gsi.de/eb/docs/eb_design.ps-gz)
- [29] H. Spieler, *Radiation Detectors and Signal Processing*, presented at University of Heidelberg, Oct. 8-12, 2001, [http://www-physics.lbl.gov/~spieler/Heidelberg\\_Notes/index.html](http://www-physics.lbl.gov/~spieler/Heidelberg_Notes/index.html)
- [30] V. Radeka, *Low-Noise Techniques in Detectors*, Ann. Rev. of Nucl. Part. Sci. 29, 1, 1982, p.764-768
- [31] Th. Kröll et al., *Gamma-ray Tracking With The MARS Detector*, AIP Conference Proceedings Vol 656(1) pp. 357-364. March 3, 2003
- [32] Glenn F. Knoll, *Radiation Detection and Measurement*, John Wiley & Sons, Inc., 1989
- [33] F. S. Goulding and D. A. Landis, *Signal Processing for Semiconductor Detectors*, IEEE Trans. Nucl. Sci. NS-29 (1982), p.1125-1141
- [34] Product Description, The Digital Gamma Finder DGF-4C (1999), [www.xia.com](http://www.xia.com)

- [35] F. Hilsenrath, H. D. Voss, and J. C. Bakke, *A Single Chip Pulse Processor for Nuclear Spectroscopy*, IEEE Trans. Nucl. Sci. NS-32 (1985) 145
- [36] A. Georgiev and W. Gast, *Digital pulse processing in high resolution, high throughput, gamma-ray spectroscopy*, IEEE Trans. Nucl. Sci. Vol. NS-40 (1993) 770-779
- [37] Valentin T. Jordanov and Glenn F. Knoll, *Digital synthesis of pulse shapes in real time for high resolution radiation spectroscopy*, Nucl. Instr. Meth. A345 (1994), 337-345
- [38] Werner Gast et al, *Schaltungsanordnung für die digitale Verarbeitung von Halbleiterdetektorsignalen*, Patentschrift DE 42 26 175 C2, 17.06.1993
- [39] J. Stein et al., *X-ray detectors with digitized preamplifiers*, Nucl. Instr. Meth. B 113 (1994) 141-145
- [40] A. Georgiev, W. Gast and R. M. Lieder, *An analog-to-digital conversion based on a moving window deconvolution*, IEEE Trans. Nucl. Sci. Vol. NS-41 (1994), 1116-1124
- [41] Valentin T. Jordanov, *Deconvolution of pulses from a detector-amplifier configuration*, Nucl. Instr. Meth. A351(1994), 592-594
- [42] Valentin T. Jordanov, *Digital techniques for real-time pulse shaping in radiation measurements*, Nucl. Instr. Meth. A353 (1994), 261-264
- [43] B. Hubbard-Nelson, M. Momayezi and W. K. Warburton, *A module for energy and pulse shape data acquisition*, Nucl. Instr. and Meth. A422 (1999) 411
- [44] Warburton et al., *Method and apparatus for digitally based high speed x-ray spectrometer*, United States Patent 5,684,850, November 4, 1997
- [45] Warburton et al., *Method and apparatus for digitally based high speed x-ray spectrometer for direct coupled use with continuous discharge preamplifiers*, United States Patent 5,774,522, June 30, 1998
- [46] Warburton et al., *Method and Apparatus for combinatorial logic signal processor in a digitally based high speed x-ray spectrometer*, United States Patent 5,873,054, Feb. 16 1999
- [47] Warburton et al., *Method and apparatus for analog signal conditioner for high speed, digital x-ray spectrometer*, United States Patent 5,870,051 , February 9, 1999
- [48] T. Kihm et al., *A digital multi-channel spectroscopy system with 100 MHz ADC module for the GENIUS-TF and GENIUS projects*, Nucl. Instr. Meth. A 498 (2003) 333-339
- [49] G. P. Westpfahl, *Adaptive Digital Filter for High-Rate High-Resolution Gamma Spectroscopy*, IEEE Trans. Nucl. Sc. Vol. 48, No. 3 (2001)
- [50] T. Lakatos et al., *Signal processing method for nuclear spectrometers*, United States Patent 5,005,146, Apr. 2 1991

- [51] B. Jaehne, *Digitale Bildverarbeitung*, Springer-Verlag, 1997
- [52] P. W. Nicholson, *Nuclear Electronics*, John Wiley & Sons, 1974
- [53] Z. H. Cho and R. L. Chase, *Comparative Study of the Timing Techniques currently employed with Ge detectors*, Nucl. Instr. Meth. 98 (1972) 335-347
- [54] M. Descovich, *Improving the position resolution of Highly Segmented HPGe Detectors using Pulse Shape Analysis Methods*, PhD thesis, University of Liverpool, 2002
- [55] T. Blu, P. Thevenaz and M. Unser, *Linear Interpolation Revitalized*, IEEE Transactions on Image Processing, Vol. 13, (2004), 710-719
- [56] Hans Boie, *Aufbau eines Experiments zur Messung der Emissionswahrscheinlichkeit von Bremsstrahlung im  $\alpha$ -Zerfall von  $^{210}\text{Po}$* , Diploma Thesis, Universität Heidelberg, 2002
- [57] W. Gast et al., *Digital signal processing and algorithms for  $\gamma$ -ray tracking*, IEEE Trans. Nuc. Sci. 48 (2001) 2380-2384
- [58] GRT4 Web Page, <http://nnsa.dl.ac.uk/GRT/>
- [59] Ian Lazarus et al., Poster presented at the Nuclear Science Symposium October 20-24, 2003, IEEE Trans. Nucl. Sci. Vol. NS-51 (2004) 1353-1357
- [60] Analog Devices Web Page, <http://www.analog.com>
- [61] XILINX Web Page, <http://www.xilinx.com>
- [62] Altera Corporation Web Page, <http://www.altera.com>
- [63] Open Cores Web Page, <http://www.opencores.org>
- [64] Texas Instruments, *Understanding Data Converters*, Application Note, [www.ti.com](http://www.ti.com)
- [65] Norbert Bulian, private communication
- [66] HAMEG Instruments Web Page, [www.hameg.de](http://www.hameg.de)
- [67] IEEE Std 301-1988, *IEEE Standard Test Procedures for Amplifiers and Preamplifiers used with Detectors of Ionizing Radiation - Description*
- [68] E. Fairstein, *Amplifier Test Standard*, IEEE Trans. Nucl. Sci. Vol. NS-32 (1985)
- [69] R. Venturelli et al., *On the linearity of the sampling electronics used by MARS*, LNL Annual Report 2001
- [70] Analog Devices Application Note AN-410, <http://www.analog.com>
- [71] E. G. Soenen, *An Architecture and An Algorithm for fully digital Correction of Monolithic Pipelined ADC's*, IEEE Transaction on circuits and systems II, Signal Processing Vol. 42, No.3, 1995

- [72] J. Elbornsson and J.-E. Eklund, *Histogram Based Correction of Matching Errors in Subranged ADC*, Proceedings of ESSCIRC2001, Villach, Austria, pp. 552-555, Sep 2001
- [73] Jan-Erik Eklund, *Blind Estimation applied to A/D Converters*, Ericsson Microelectronics
- [74] Wojtek Skulski, private communication
- [75] Jean-Francois Loude, *Energy Resolution in Nuclear Spectroscopy*, IPHE 2000-022, 10 October 2000
- [76] Ian Lazarus, private communication
- [77] Nallatech Inc., <http://www.nallatech.com/>
- [78] PET Imaging, Medical Imaging Group at University of Liverpool, <http://ns.ph.liv.ac.uk/~hcs/Petimaging.html>
- [79] A. N. Ostrowski et al., *CD: A double sided silicon strip detector for radioactive nuclear beam experiments*, Nucl. Instr. Meth. A 480 (2002) 448 - 455
- [80] A. V. Oppenheim and R. W. Schaffer, *Zeitdiskrete Signalverarbeitung*, R. Oldenburg Verlag, 1999
- [81] S. D. Stearns, *Digital Signal Analysis*, Prentice Hall, 1990
- [82] Richard G. Lyons, *Understanding Digital Signal Processing*, Addison-Wesley Longman, Inc., Reading, MA, 1997
- [83] R. W. Hamming, *Numerical methods for scientists and engineers*, Dover Publications, 1987
- [84] F. B. Hildebrand, *Introduction to numerical analysis*, Dover Publications, 1987
- [85] Steven W. Smith, *The Scientist and Engineer's Guide to Digital Signal Processing*, California Technical Publishing, <http://www.dsppguide.com>
- [86] W. Lechner and N. Lohl, *Analyse digitaler Signale*, Vieweg Verlag, Braunschweig, 1990
- [87] V. Radeka, *Trapezoidal Filtering of Signals from Large Germanium Detectors at High Rates*, IEEE Trans. Nuc. Sci. NS-19, No. 1, 412 (1972)
- [88] F. S. Goulding, *Pulse-Shaping in Low-Noise Nuclear Amplifiers: A Physical Approach to Noise Analysis*, Nucl. Instr. Meth. 100 (1972), 493-504
- [89] F. S. Goulding, *Analysis of noise in energy-dispersive spectrometers using time-domain methods*, Nucl. Instr. Meth. A 485 (2002) 653-660
- [90] M. Eschenauer et al., *Resolution enhancement of gamma-spectroscopy data from neutron-damaged coaxial n-type HPGe-detectors*, Nucl. Instr. Meth. A 340 (1994), 364

- [91] Julius Orion Steven III Home Page, <http://www-ccrma.stanford.edu/~jos/>
- [92] M. Unser, Biomedical Imaging Group Homepage, <http://bigwww.epfl.ch/index.html>
- [93] P. Thevenaz, T. Blu and M. Unser, *Image Interpolation and Resampling*, Handbook of Medical Imaging, Processing and Analysis, I.N. Bankman, Ed., Academic Press, San Diego CA, USA, pp. 393-420, 2000, <http://bigwww.epfl.ch/publications/thevenaz9901.pdf>
- [94] Handel-C Web Page, <http://www.celoxica.com>
- [95] XILINX Core Generator Web Page, <http://www.xilinx.com/products/logiccore/coregen>
- [96] Simulink Web Page, <http://www.mathworks.com/products/simulink>
- [97] System Generator for DSP Web Page, [http://www.xilinx.com/xlnx/xil\\_prodcat\\_product.jsp?title=system\\_generator](http://www.xilinx.com/xlnx/xil_prodcat_product.jsp?title=system_generator)
- [98] National Instruments LabView, <http://www.ni.com>
- [99] Free ISE WebPACK, [http://www.xilinx.com/xlnx/xil\\_prodcat\\_landingpage.jsp?title=ISE+WebPack](http://www.xilinx.com/xlnx/xil_prodcat_landingpage.jsp?title=ISE+WebPack)
- [100] DX Designer (based on ViewDraw) <http://www.mentor.com/dxdesigner/>
- [101] G. Lehmann, B. Wunder and M. Selz, *Schaltungsdesign mit VHDL: Synthese, Simulation und Dokumentation digitaler Schaltungen*, <http://www.itiv.uni-karlsruhe.de/opencms/opencms/de/study/vhdl/index.html>
- [102] XILINX Library Guide, [http://www.xilinx.com/support/software\\_manuals.htm](http://www.xilinx.com/support/software_manuals.htm)
- [103] ELNEC s.r.o. Web Page, <http://www.elnec.com>
- [104] Sallen-Key Low-Pass Filter, <http://www.ecircuitcenter.com/Circuits/opsalkey1/opsalkey1.htm>
- [105] AD Interactive Design Tools: Active Filter Synthesis, [http://www.analog.com/Analog\\_Root/static/techSupport/designTools/interactiveTools/filter/filter.html](http://www.analog.com/Analog_Root/static/techSupport/designTools/interactiveTools/filter/filter.html)
- [106] Two's Complement, <http://www.duke.edu/~twf/cps104/twoscomp.html>
- [107] GRT4 Users Manual, <http://nnsa.dl.ac.uk/GRT/>
- [108] Berkeley Nucleonics Corporation, <http://www.berkeleyelectronics.com>
- [109] W.Skulski, *Digital Signal Processing Electronics for Nuclear Physics Applications*, GRETINA Electronics Workshop, Argonne, 24-25 July 2004
- [110] Wavemetrics Inc. Web Page, <http://www.wavemetrics.com>

- [111] D. A. Gedcke, *A constant fraction of pulse height trigger for optimum time resolution*, Nucl. Instr. Meth. 55(1967), 377-380
- [112] Z. H. Cho and J. Llacer, *Timing with high purity germanium coaxial detector*, Nucl. Instr. Meth. 98 (1972) 461-466
- [113] M. Lauer, *Description of hardware CFD*, Manual, 2002